Natural Balancing Mechanisms in Converters

by

Johannes Wilhelm (Wim) van der Merwe

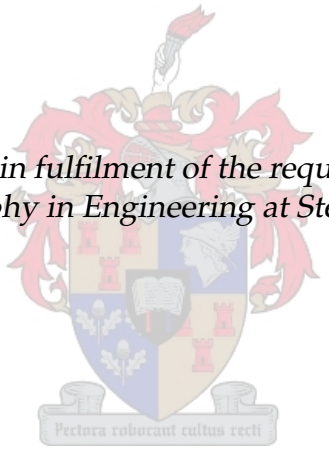

Dissertation presented in fulfilment of the requirements for the degree of Doctor of Philosophy in Engineering at Stellenbosch University

Department of Electric and Electronic Engineering
University of Stellenbosch
Private Bag X1, 7602 Matieland, South Africa

Promoter: Prof Hendrik du Toit Mouton

March 2011

Declaration

By submitting this dissertation electronically, I declare that the entirety of the work contained therein is my own, original work, that I am the owner of the copyright thereof (unless to the extent explicitly otherwise stated) and that I have not previously in its entirety or in part submitted it for obtaining any qualification.

March 2011

Abstract

Natural Balancing Mechanisms in Converters

J.W. van der Merwe

Department of Electric and Electronic Engineering
University of Stellenbosch
Private Bag X1, 7602 Matieland, South Africa

Dissertation: PhD(Eng) (E&E)

March 2011

This thesis investigates the natural balancing mechanisms in multilevel and modular converters using phase shifted carrier pulse width modulation. Two groups of mechanisms are identified; a weak balancing mechanism that is only present when the switching functions are interleaved and a strong mechanism that occurs irrespective of the interleaving of the switching functions. It is further shown that the strong balancing mechanism can be divided into a balancing mechanism that depends on the direct exchange of unbalance energy and a loss based balancing mechanism. Each of the mechanisms is discussed and analysed using a converter where the specific mechanism dominates as example. Emphasis is placed on the calculation of the rebalancing time constant following a perturbation. Closed form expressions for the rebalancing time constants for each of the analysed converters are presented.

Uittreksel

Natuurlike Balansering Meganismes in Omsetters

("Natural Balancing Mechanisms in Converters")

J.W. van der Merwe

Departement Elektries en Elektroniese Ingenieurswese
Universiteit van Stellenbosch
Privaatsak X1, 7602 Matieland, Suid Afrika

Proefskrif: PhD(Ing) (E&E)

Maart 2011

Hierdie proefskrif handel oor die natuurlike balanserings meganismes van veelvlakkige en modulêre omsetters wat fase-skuif dragolf puls wydte modulasie gebruik. Die meganismes kan in twee hoof groepe verdeel word: 'n swak balanserings meganisme wat afhanklik is van die oorvleuling van die skakelfunksies en 'n sterk meganisme wat voorkom ongeag of die skakelfunksies oorvleul al dan nie. Die sterk meganisme verdeel verder in twee subgroepe, 'n direkte oordrag van onbalans energie en 'n meganisme wat afhang van die verliese in die stelsel. Elkeen van die meganismes word aan die hand van 'n omsetter topologie waarin die spesifieke meganisme oorheers beskryf en ontleed. In die ondersoek word klem geplaas op die daarstelling van uitdrukkings om die tydskonstantes van herbalansering na 'n afwyking vir elk van die omsetter toplologieë te beskryf.

Acknowledgements

I would like to express my sincere gratitude to the following people and organisations who have contributed to making this work possible:

- My promoter Prof. H. du T. Mouton. Thank you for the opportunities you afforded me. I am grateful of all I learnt and for the time you invested in this work. I am especially thankful for the considerable time you invested in helping me to express my work in a readable mathematical format.
- The South African National Energy Research Institute (SANERI), the National Research Foundation (NRF) and the Stellenbosch University merit bursary program for their financial support.
- The MSc(Eng) students that worked with me on the SST project: Marko Wolf, Francois Breet and Louis Schietekat.
- The rest of the power electronic research group and the workshop personnel.
- Steven Thielemans for his help with the practical measurements of the flying capacitor converter.
- Prof. Andrè Weideman and Prof. C. Lance for their insight and guidance.
- Prof. Braham Ferreira of TU Delft for the opportunity to spend two months at TU Delft and his help with the design of the SST high frequency transformer.
- The open source community. This study was done without the use of any proprietary software. Software that was used include: Ubuntu Linux, LaTeX and Python with Numpy and Scipy for all numerical calculations and simulations.
- My parents for their support and the foundation they have given me.
- My friends for their support.
- I would like to thank God for granting me the academic ability to complete this dissertation.

Dedications

Hierdie proefskrif word opgedra aan my eggenote,
Ira van der Merwe,
vir haar ondersteuning, gebed, en liefde.

Contents

List of Figures

List of Tables

Summary of Presented Papers

Conference Papers

1. J.W. van der Merwe and H. du T. Mouton: "Balancing of a 2-Cell Modular Input-Series-Output-Parallel Converter with Common Duty Ratio Control under Converter Mismatch", 18^{th} South African Universities Power Engineering Conference (SAUPEC), Stellenbosch, South Africa, January 2009.

2. J.W. van der Merwe and H. du T. Mouton: "Solid-state transformer topology selection", IEEE International Conference on Industrial Technology, pp. 1-6, Churchill, Australia, February 2009.

3. J.W. van der Merwe and H. du T. Mouton: "Natural balancing of the two-cell back-to-back multilevel converter with specific application to the solid-state transformer concept", 4^{th} IEEE Conference on Industrial Electronics and Applications (ICIEA), pp. 2955-2960, Xi'An, China, June 2009.

4. J.W. van der Merwe and H. du T. Mouton: "The solid-state transformer concept: A new era in power distribution", Conference Record of the 9th IEEE AFRICON, Nairobi Kenya, September 2009.

5. J.W. van der Merwe and H. du T. Mouton: "The Effect of the Filter Inductor ESR on the Natural Balancing Time Constant of the Flying Capacitor Converter", IEEE International Symposium on Industrial Electronics (ISIE), Bari, Italy, July 2010.

6. J.W. van der Merwe and H. du T. Mouton: "An Investigation of the Natural Balancing Mechanisms of Cascaded Active-Rectifiers", 14^{th} International Power Electronics and Motion Control Conference (EPE-PEMC), Ohrid, Republic of Macedonia, September 2010.

7. J.W. van der Merwe and H. du T. Mouton: "An Investigation of the Natural Balancing Mechanisms of Modular Input-Series-Output-Series DC-DC Converters", 2^{nd} Energy Conversion Congress and Expo (ECCE), Atlanta, USA, September 2010.

Journal Papers

1. J.W. van der Merwe and H. du T. Mouton: "Lyapunov Stability of the Flying Capacitor Converter Natural Voltage Balancing Mechanism", submitted for review.

2. J.W. van der Merwe, H. du T. Mouton and S. Thielemans: "Calculating Boundaries for the Natural Voltage Balancing Time-Constant of the Constant Duty Cycle Flying Capacitor Converter", submitted for review.

Nomenclature

Abbreviations

AC	Alternating Current
CARC	Cascaded Active Rectifier Converter
CCM	Continuous Conduction Mode
DC	Direct Current
DCM	Discontinuous Conduction Mode
DFT	Discrete Fourier Transform
ESR	Equivalent Series Resistance
FCC	Flying Capacitor Converter
IPOP	Input-Parallel-Output-Parallel (Converter)
IPOS	Input-Parallel-Output-Series (Converter)
ISOP	Input-Series-Output Parallel (Converter)
ISOS	Input-Series-Output-Series (Converter)
LHS	Left Hand Side (of equation)
PEBB	Power Electronic Building Block
PWM	Pulse Width Modulation
RHS	Right Hand Side (of equation)
SST	Solid State Transformer

Constants

π	3.141 592 653 589 793 238 462 643 383 279 5
e	2.718 281 828 459 045 235 360 287 471 352 6
∞	Infinity

Variables

C	Capacitance [F]
C_o	Output filter capacitance [F]
$C_{a(n)}$	Fourier series coefficients of switching function $s_a(t)$
$C_{0(n)}$	Fourier series coefficients of the reference switching function
I	Current [A]
L	Inductance [H]

N	Number of cells
Q	Quality factor, defined for filter circuits
R	Resistance [Ω]
V	Voltage [V]
T_s	Switching period [s]
X	Reactance [Ω]
Z	Impedance, $Z = R + jX$ [Ω]
a	Transformer turns ratio
d	Duty cycle
d_{eff}	Equivalent balancing duty cycle, modulated FCC
$d_{eff\ rms}$	Equivalent balancing duty cycle, RMS approach
f_s	Switching frequency [Hz]
j	Imaginary number, $j = \sqrt{-1}$
m_a	The amplitude modulation index [0,1]
m_f	The frequency modulation index
$\mathbf{y}$	Eigenvector
Ψ	Exponential Fourier series coefficients
$\mathbf{\Lambda}$	Characteristic rebalancing matrix, $\mathbf{\Lambda} \in \mathbb{R}^{n \times n}$
$\mathbf{\Lambda_s}$	Symmetric part of $\mathbf{\Lambda}$
$\mathbf{\Lambda_{sk}}$	Skew-symmetric part of $\mathbf{\Lambda}$
δ	Product of turns ratio and duty cycle (defined for ISOP)
ζ	de Moivre numbers (N roots of -1)
ζ_n	Sequence of de Moivre numbers, $\zeta_n = e^{-j2\pi n\frac{1}{N}}$
ζ_n^a	Indexed sequence de Moivre numbers, $\zeta_n^a = e^{-j2\pi n\frac{a}{N}}$
φ	Eigenvalue
ξ	Summation variable
τ	Time constant [s]
τ_{max}	Maximum bound to FCC voltage rebalancing time constant [s]
τ_{maxA}	Approximated value of τ_{max} [s]
τ_{maxV}	Maximum voltage balancing time constant [s]
ω	Radian frequency [rad$\cdot$s^{-1}]
ω_s	Switching radian frequency, $\omega_s = 2\pi f_s$ [rad$\cdot$s^{-1}]

Mathematical Operators

$\propto$	Proportional to
$\Leftrightarrow$	Material equivalence, (if and only if)
$\forall$	For all; for any
$\sigma(\mathbf{A})$	Spectrum of matrix $\mathbf{A}$, set of all eigenvalues, $\sigma(\mathbf{A}) = \{\varphi_1, \varphi_2, \ldots, \varphi_N\}$
$\sigma_n(\mathbf{A})$	Any specific eigenvalue in spectrum of $\mathbf{A}$, $\sigma_n(\mathbf{A}) = \varphi_n$

$\sigma_{max}(\mathbf{A})$ Largest eigenvalue of $\mathbf{A}$ where $\sigma(\mathbf{A}) \subset \mathbb{R}$
$\sigma_{min}(\mathbf{A})$ Smallest eigenvalue of $\mathbf{A}$ where $\sigma(\mathbf{A}) \subset \mathbb{R}$
$\mathrm{Re}\{z\}$ Real part of complex number z
$\mathrm{Im}\{z\}$ Imaginary part of complex number z
$J_n(x)$ Bessel function of the first kind
$\zeta_R(x)$ Riemann zeta function defined as $\zeta_R(x) = \sum_{n=1}^{\infty} \frac{1}{n^x}$
A^* Complex conjugate of A
$A * B$ Convolution of A and B
$\langle \mathbf{x}, \mathbf{x} \rangle$ Inner product of two vectors
$\mathbf{x} \perp \mathbf{y}$ The vectors $\mathbf{x}$ and $\mathbf{y}$ are orthogonal
$\mathbb{R}$ Real numbers
$j\mathbb{R}$ Imaginary numbers
$\mathbb{C}$ Complex numbers
$\mathbb{F}$ $\mathbb{R}$ or $\mathbb{C}$
$\mathbb{Z}$ Integers

Subscripts

d Difference
t Total
τ Originating from total circuit
δ Originating from difference circuit

Notation Conventions

$\mathbf{A}$ Boldface capital letters denote matrices
$\mathbf{x}$ Boldface lowercase letters denote vectors
$\tilde{x}$ The ˜ superscript denotes modulated duty cycle
$\hat{x}$ The ˆ superscript denotes the time-averaged value over a switching period

Chapter 1

Introduction

The quest for energy efficiency and the incorporation of so-called green energy sources into the grid has fuelled much interest in power electronic systems during the last 20 years. This growing demand called not only for improvements in power semiconductors but also for novel topologies and control methods. However, although power semiconductor efficiency and reliability has increased markedly, voltage blocking and current ratings have not increased much. Therefore, increasing system voltage and current requirements must be met by means of changes in the topology and control methodology.

At device level, the blocking voltage can be increased through a series connection of switches, while a parallel connection can be used to increase the current carrying ability. However, due to variations in device characteristics, the sharing of the stresses among the devices must be addressed. In general, the current handling abilities of semiconductor devices are sufficient for many applications, and most innovations have so far focused on increasing the converter operating voltage. The best-known variants of multi level converters are the flying capacitor, diode clamped, and cascaded converters.

On a system level, the need for higher power ratings can also be met in a similar manner through the series and parallel connection of complete converter units, often termed cells. This modularisation of converters is often referred to as the power electronic building block, or PEBB, concept. However, as with the interconnection of switching devices, care must be taken to ensure the sharing of voltage and current stresses among the different cells. In general, modular converters are created through either a series or parallel connection of converters on the input side and likewise on the output side. Examples would be the input-series-output-parallel (ISOP) and input-series-output-series (ISOS) converters.

Two distinct avenues of balancing multilevel and modular converters exist: it can either be done by actively measuring and controlling the switch stresses (active balancing), or, by relying upon the inherent interactions of the converter states to balance the system naturally under certain operating conditions (natural balancing).

1.1 Research Statement

This study focuses on the natural balancing of converters. Two natural balancing mechanisms are identified, namely weak and strong. The distinction between the mechanisms hinges on the requirement that the converter switching signals must be interleaved. The weak balancing mechanism is only present when interleaved switching (where the switching signals of different cells are phase shifted with respect to one another) is used. Conversely, the strong balancing mechanism is present both when interleaved switching and ordinary switching (where the cells operate with the same switching signals) is used. Furthermore, the strong balancing mechanism consists of two sub-mechanisms: a fast acting direct exchange of unbalance energy between the cells and a slower rebalancing that occurs due to the different losses experienced by converters or switches that operate with unequal voltages and/or currents.

Natural balancing can be used for many converter topologies. Most topologies exhibit a combination of the two strong mechanisms and the weak mechanism. This study aims to introduce the three balancing mechanisms in terms of their respective methods of operation and their limitations. Each mechanism will be introduced by analysing a converter topology where the discussed mechanism is either the only mechanism or the dominant mechanism.

It will be shown that the natural balancing mechanisms will balance the converters in the steady state. Furthermore, the rebalancing of converters following external perturbations will be investigated. Time constants that describe the rebalancing process will be presented. These time constants can be used in the design of converters that operate by using natural balancing.

1.2 Research Methodology

The frequency domain method will be used as a starting point to investigate all balancing mechanisms. With this method of analysis as a starting point, it will be shown that the time domain method using time averaged circuit parameters can be used to identify the strong balancing mechanisms.

The exponential Fourier series will be used to represent all switching functions in the frequency domain, since the equivalence between multiplication in the time domain and convolution in the frequency domain strictly only holds for the exponential Fourier series.

From previous studies, it is known that the frequency domain expressions that describe the mechanisms, especially the weak mechanism, tend to be complicated and difficult to work with. These expressions can typically only be evaluated using numerical methods. In this study, therefore, a concerted effort will be made to simplify all expressions as much as possible by using the characteristics of the switching functions. In some cases, the resulting expressions can be simplified further by means of certain assumptions regarding the nature of the load at the switching frequency and above.

The expressions are simplified as much as possible to yield expressions for the time constant that can be evaluated without using numerical methods.

The method of describing the circuits in terms of difference and total parameters will be used throughout this study. For each discussed converter, an equivalent circuit in terms of the total and difference parameters will be presented. This alternate representation of the circuit operation is beneficial, as it allows for a clear and intuitive understanding of the balancing process.

1.3 Thesis Outline

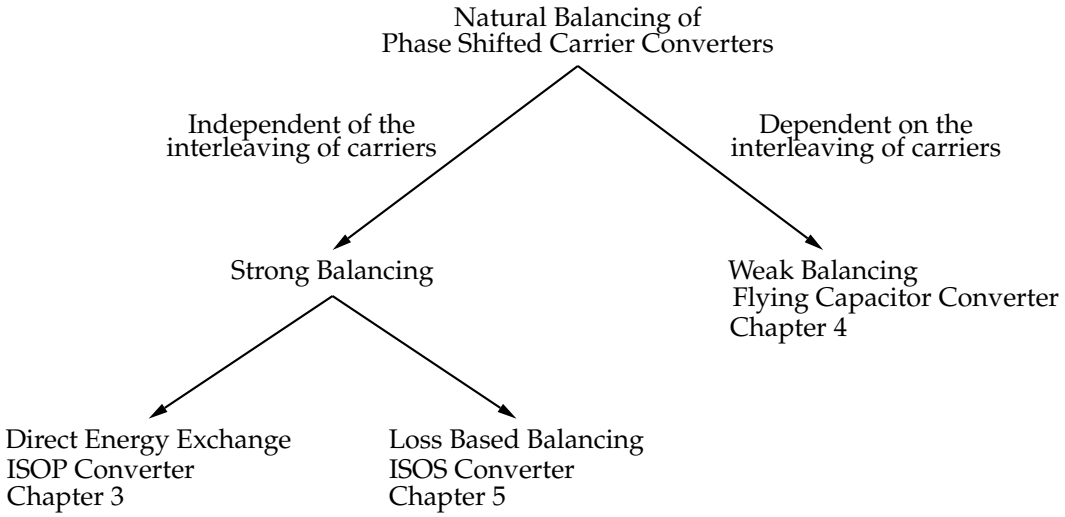

Figure 1.1: Thesis outline in terms of the different balancing mechanisms

Firstly, in Chapter 2, an introductory overview of multilevel and modular converters will be presented. In addition, an overview will be presented of the different balancing theories to describe the weak balancing mechanism of the flying capacitor converter.

Three converters are identified in each of which one of the three mechanisms dominate. In Chapters 3, 4 and 5, the mechanisms are introduced through analysis of these converters.

The direct strong balancing mechanism is introduced in Chapter 3 in which the modular ISOP DC-DC converter is analysed. It will be shown that, although the weak mechanism does theoretically have an influence, the strong mechanism dominates. The balancing process will be discussed and it is shown that the converter balances in the steady state. Furthermore, accurate time constants and an equivalent circuit describing the rebalancing process following perturbation are presented. The converter will also balance when non-similar cells are used, although the steady state balance will reflect the mismatch. Again, time constants and an equivalent circuit that describes the process will be presented. Furthermore, it will be shown that this strong balancing method can also be identified and described by using time averaging methods. In conclusion, it is revealed that the use of passive rectifiers alters the balancing mechanism. It will be shown that the strong mechanism still functions when the direct energy exchange between the cells

is prohibited. The operation of this strong mechanism differs in every respect from the situation where a direct exchange is possible, but it is still a strong mechanism as it is independent of the switching mechanism used. An equivalent rebalancing circuit describing the rebalancing of this modified circuit will be presented.

The weak balancing mechanism is introduced in Chapter 4 by analysing the flying capacitor converter (FCC). It will be shown that the weak balancing mechanism depends on the interleaving of the switching signals. Furthermore, the time constants for both the 2-cell and 3-cell converters can be determined directly. Although the complete expressions for these time constants require the evaluation of an infinite series, it is possible to simplify the expressions considerably by using approximations of the load at the frequencies of interest. When these approximations of the load are used, the resulting expressions for the time constant resemble the expressions found by means of the time domain method. Furthermore, the system matrix for the N-cell converter naturally decomposes into symmetric and skew symmetric parts. This decomposition will be used in conjunction with Lyapunov's theorem to prove that the system is stable. Furthermore, it will be shown that the eigenvalues of the symmetric part of the decomposition can be used to determine a maximum bound on the rebalancing time constant. It is possible, by using assumptions regarding the nature of the load at the switching frequency and above, to factorise the matrix in such a way that this can be calculated by using a closed form expression and a value from a reference table. Finally, the results for the constant duty cycle case will show that the same methods can be used to determine a maximum bound on the rebalancing time constant for the modulated duty cycle converter.

In Chapter 5, the discussion of the ISOS DC-DC converter introduces the loss-based strong balancing mechanism. According to analysis in the frequency domain the weak balancing mechanism is active in this converter and the strong balancing mechanism that relies on direct energy exchange is not. This result is confirmed in time domain simulations, where balancing occurs only when interleaved switching is used. However, in practical systems, balancing occurs irrespective of the switching regime used. It will be shown that the cells experience different losses when the system is unbalanced. The unbalance dependent losses serve as the balancing mechanism.

1.3.1 Theory Verification

Throughout this study the presented theory will be verified through comparison with detailed time simulations and in some cases practical measurements. In an effort to improve the readability of the text these results are included in the text and not in a separate chapter.

For some topologies only measured results are used while other topologies are investigated using only simulations. The following points are noted in an effort to address this discrepancy:

1. In many of the investigated topologies precise knowledge of the converter is needed to describe the natural balancing properties accurately. This is especially true for the weak balancing mechanism. By investigating the balancing

mechanisms through simulation all parameters are implicitly known and the mathematical model can be compared to the simulation result to verify the model.

2. Once the mathematical model is verified against the simplified equivalent circuit, that was used for the time domain simulation, the accuracy of the assumptions in deriving the equivalent circuit can be tested through comparison of the mathematical model to practical measurements. This approach was followed in the investigation of the weak balancing mechanism in the FCC.

3. For some topologies it was not possible to follow both approaches, notably for the different ISOP DC-DC converter topologies. For the converter with active rectifiers only simulation results are presented. The reason for this is twofold: no experimental converter was available and secondly the balancing mechanism is such that the risk of modelling errors is low. Conversely, for the converter with passive rectifiers only measured results are presented. Every effort was made to simulate the converter, however a stable and reliable model that describes the results could not be found. It is believed that this failure is due to the highly non linear behaviour of the system, the currents are in discontinuous conduction mode, and the large differences in the circuit time constants that are of concern.

4. A short description and photographs of the practical hardware are included in Appendix D.

5. Python script files that was used for the time domain simulations are included in Appendix C.

1.4 Summary of Contributions

The main contributions of this study to the body of knowledge are:

1. A model for the balancing of non-similar cells connected in input-series-output-parallel is presented.

2. The effects of passive rectification on the balancing of the ISOP converter are investigated. A model for the rebalancing of the converter is presented.

3. Simple expressions for the rebalancing time constant for the 2-cell FCC are presented. The expressions were derived by using frequency domain methods but they resemble the expressions found through time domain analysis.

4. It is shown that the time constants for the 3-cell FCC can also be written down directly, for most loads.

5. For the N-cell FCC, it is shown that:

    a) The system matrix decomposes naturally into the sum of a symmetric matrix and a skew-symmetric matrix.

b) Using Lyapunov's theorem it is proven that the FCC is stable. Previous studies used a stability model that was inferred from the system operation.

c) The eigenvalues of the symmetric matrix can be used to describe a maximum bound on the rebalancing time constant of the FCC.

d) The symmetric matrix can be factorised using assumptions regarding the nature of the load at the switching frequency and above. Using this factorisation it is possible to formulate a closed form expression for the maximum rebalancing time constant that can be calculated by using a look-up table.

e) The rebalancing time constant depends on the characteristics of the load, and specifically the ratio $Re\{Z(\omega)\}/|Z(\omega)|^2$ at the multiples of the switching frequency.

6. It is shown that the ISOS converter balances naturally, in contrast to previous studies concluded that the ISOS converter cannot balance naturally.

7. It is shown that switching losses and other voltage dependent losses have a natural balancing influence.

Although not described in this thesis, the following contributions were also made:

1. A model for the natural balancing of a 2-cell back-to-back active rectifier and DC-DC converter connected in cascaded input parallel output was developed. This model is described in detail in [1]. This model was used to construct a 3.8 kV to 800 V (AC to DC) converter as part of a solid-state transformer prototype.

2. A model for the natural balancing of the cascaded active rectifier was developed [2]. The model is able to describe the effect of non-similar loads on the steady-state voltages.

3. A balancing scheme for a modular three-phase solid-state transformer prototype was developed that relies on natural balancing. This scheme will be described in a later publication.

Chapter 2

The Power Electronic Building Block, Multilevel Converters and the Balancing Problem

The quest for converters operating at higher voltage and power levels gave rise to the investigation of multilevel and modular converters. Multilevel converters, such as the diode clamped converter, the flying capacitor converter (also known as the capacitor clamped or multi-cell converter), can operate at voltages higher than the ratings of the individual switches [3; 4]. Another advantage of multilevel converters is that the output generates a stepped voltage when the switching functions of the switches in a phase leg are interleaved. This interleaving not only reduces the harmonic content of the output voltage, but also reduces the output filter requirements [5]. Multilevel converters, including cascaded converters, are often used in drive applications [6; 7; 8].

The output power of a converter can also be increased by operating many similar converters in parallel, such as in the inter-cell flyback converter [9]. However, it is also possible to increase both operating voltage and current by combining many similar modules both in series and in parallel. The use of several similar converters together is the cornerstone of the power electronic building block (PEBB) concept. Apart from the increase in current and voltage ratings, the use of smaller similar modules can also increase the reliability of the total system through the inclusion of redundant modules. Other advantages include the reduction of harmonic content through interleaving of the cell switching information and a decrease in costs achieved by mass manufacturing of smaller modules and reduced maintenance requirements. The modular approach is currently used in industry for very large converters, such as a 63 MVA electromagnetic aircraft launch system demonstrator built by ABB [10]. The modular approach is also used in railroad applications due to the high power requirements [11; 12; 13] as well as in high power drives [14; 15].

The solid-state transformer (SST), concept is another candidate where the modular converter concept can be used effectively. Due to its high voltage rating requirements the SST must consist of either traditional multilevel converters [16; 17] or a modular arrangement [18; 1; 19; 20; 21; 22; 23]. It is also possible to use a combination of the two systems [24], among others.

In both multilevel and modular converters, the voltage balancing among the different levels (or cells) and current balancing in the case of modular converters is of concern. Many different active balancing methods for the different converters can be found in the literature. However, these methods require complicated measuring circuits, and they need to manipulate the switching functions of individual cells or switches to achieve and maintain converter balance. Conversely, it is true that most converters exhibit some natural balancing (also called self-balancing) characteristics. These balancing methods have been described for the FCC [25; 26; 27; 28], the diode clamped converter [29; 30], the modular DC-DC converter topologies [31] and the series stacked series injection power quality converter [32; 33] to name a few.

The study of natural balancing in converters is not only important when the natural balancing method is considered as primary converter balancing mechanism, but also when active balancing is considered. The study of natural balancing reveals the interactions between the cell voltages (and currents in some converter topologies), the switching functions and the rest of the converter state variables. Manipulation of the switching functions during active balancing without considering these interactions can lead to unanticipated interactions and even system instability.

Two avenues of analysing natural balancing characteristics exist, involving analysis in either the frequency domain or the time domain. Some converters, such as the ISOP converter, exhibit a strong balancing method where the unbalance energy can be exchanged directly between the different cells. This method will be described in detail in Chapter 3. The strong mechanism can be identified by using circuit averaging techniques and analysis in the time domain. However, another weak balancing method exists where an exchange of energy occurs through the interactions between the load current and the switching functions used. Originally, these interactions were solely studied in the frequency domain but, more recently, a method was developed to study these interactions in the time domain.

The remainder of this literature review will be devoted to a discussion of the different methods used to identify and analyse the weak balancing mechanism. The FCC has only the weak balancing mechanism and is therefore the converter analysed during this discussion.

2.1 Analysis of the FCC in the Frequency Domain

2.1.1 Meynard *et al.*

The assumptions and definitions are [34]:

1. All switches are ideal, with the on state voltage, the off state current, as well as both the switching time and delays, all equal to zero.

2. The switching function applied to switch k is defined as $s_k(t) \in 0, 1$.

3. The voltage variations of both the floating capacitor voltages and the source are so small that they can be regarded as a constant over a switching period.

4. The load has a time constant much larger than the switching period so that, at each switching period, the load current is in the steady state.

5. The voltage state vector is defined by the voltages of the flying capacitors,

$$\mathbf{v} = \begin{bmatrix} v_1 & v_2 & \dots & v_{N-1} \end{bmatrix}^T. \tag{2.1.1}$$

6. The switching function of the k^{th} switch is defined as a duty cycle d_k with a phase shift ϕ_k.

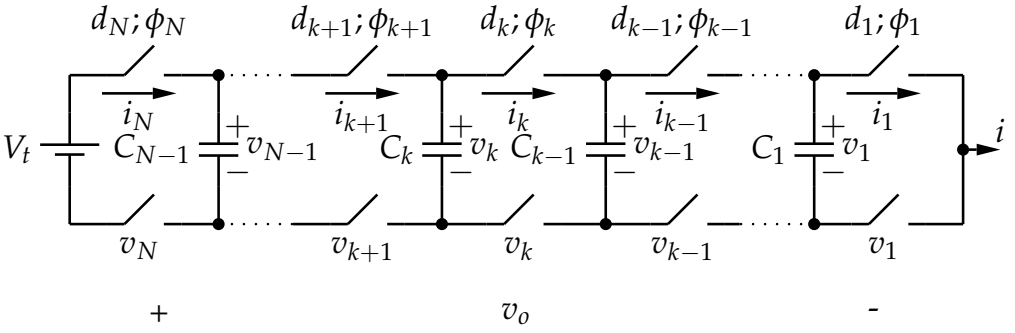

Figure 2.1: Circuit definitions used in the Meynard model

The balancing model is generated by following the steps below:

1. Given the state of the system as vector **v**, the source V_t and the control signals (d_n and ϕ_n), determine the amplitude and voltage harmonics across the k^{th} bottom switch, $V_{sk(n)}$, $1 \leq k \leq N$.

2. The unfiltered output voltage v_o is the sum of the voltages across the bottom switches. Each harmonic of this output voltage is calculated and written as $V_{o(n)}$.

3. Using the unfiltered output voltage and knowledge of the load, the output current harmonics magnitude I_n at an angle ψ_n can be calculated.

4. The average current over a switching period in each switch, $\hat{i}_k$ can be calculated as a function of the phase shift between the control signal and the current harmonic.

5. The average current in the flying capacitor is the difference between the average current in two adjoining switches.

6. The variation in the state vector can be calculated by using the value of the flying capacitors and the average current through them.

The model can be calculated for any harmonic n by using the switching function of the k^{th} switch given as

$$S_{k(n)} = \frac{1}{2\pi} \sin(n\pi d_k) e^{jn\phi_k}. \tag{2.1.2}$$

The voltage across switch k is equal to $v_k - v_{k-1}$ when in the off state and equal to zero when conducting. Therefore, the unfiltered output voltage, which is found as the sum of the voltages across the N switches, can be written as

$$V_{o(n)} = \sum_{k=1}^{N} S_{k(n)} \left(v_k - v_{k-1} \right), \tag{2.1.3}$$

or in matrix form

$$V_{o(n)} = 2 \left[\begin{array}{cccc} S_{1(n)} - S_{2(n)} & S_{1(n)} - S_{2(n)} & \cdots & S_{N(n)} - S_{N-1(n)} \end{array} \right] \left[\begin{array}{c} v_1 \\ v_2 \\ \vdots \\ v_{N-1} \end{array} \right] + 2 S_{N(n)} V_t. \tag{2.1.4}$$

The load current at the n^{th} harmonic is found as

$$I_n = \frac{V_{o(n)}}{Z_n} = |I_n| e^{j\psi_n}. \tag{2.1.5}$$

This current generates a current through the k^{th} bottom switch that depends on the switching function. The average current in the switch is therefore

$$\begin{aligned} \hat{i}_{k(n)} &= \frac{1}{2\pi} \int_{-\phi_k - d_k\pi}^{-\phi_k + d_k\pi} |I_n| \cos(n\xi + \psi_n) d\xi \\ &= \frac{|I_n|}{2n\pi} \Big\{ \sin(-n\phi_k + n d_k \pi + \psi_n) - \sin(-n\phi_k - n d_k \pi + \psi_n) \Big\} \\ &= \frac{|I_n|}{n\pi} \sin(n d_k \pi) \cos(n\phi_k - \psi_n) \\ &= Re \left\{ S^*_{k(n)} I_n \right\}. \end{aligned} \tag{2.1.6}$$

Since the change in the state vector due to the current generated by switching harmonic n can be found as

$$C_k \frac{d}{dt} v_{k(n)} = I_{k+1(n)} - I_{k(n)}, \tag{2.1.7}$$

the following is true

$$\frac{d}{dt} \mathbf{v_n} = Re \left\{ \left[\begin{array}{c} \frac{1}{C_1} \left(S^*_{2(n)} - S^*_{1(n)} \right) \\ \frac{1}{C_2} \left(S^*_{3(n)} - S^*_{2(n)} \right) \\ \vdots \\ \frac{1}{C_{N-1}} \left(S^*_{N(n)} - S^*_{N-1(n)} \right) \end{array} \right] I_n \right\}. \tag{2.1.8}$$

Substituting the definition of I_n back yields

$$\frac{d}{dt} \mathbf{v_n} = \mathbf{A_n} \mathbf{v_n} + \mathbf{b_n} V_t, \tag{2.1.9}$$

where

$$\mathbf{A_n} = 2Re\left\{\begin{bmatrix} \frac{1}{C_1}\left(S^*_{2(n)} - S^*_{1(n)}\right) \\ \frac{1}{C_2}\left(S^*_{3(n)} - S^*_{2(n)}\right) \\ \vdots \\ \frac{1}{C_{N-1}}\left(S^*_{N(n)} - S^*_{N-1(n)}\right) \end{bmatrix} \frac{1}{Z_n}\mathbf{s_n}\right\}$$

$$\mathbf{s_n} = \begin{bmatrix} S_{1(n)} - S_{2(n)} & S_{1(n)} - S_{2(n)} & \dots & S_{N(n)} - S_{N-1(n)} \end{bmatrix}$$

$$\mathbf{b_n} = 2Re\left\{\begin{bmatrix} \frac{1}{C_1}\left(S^*_{2(n)} - S^*_{1(n)}\right) \\ \frac{1}{C_2}\left(S^*_{3(n)} - S^*_{2(n)}\right) \\ \vdots \\ \frac{1}{C_{N-1}}\left(S^*_{N(n)} - S^*_{N-1(n)}\right) \end{bmatrix} \frac{1}{Z_n}S_{N(n)}\right\}$$

When the first Q harmonics are taken into account, the total average current through the flying capacitors can be found as

$$\hat{\mathbf{i}} = \frac{d}{dt}\mathbf{v} = \sum_{n=1}^{Q} \mathbf{A_n}\mathbf{v_n} + \mathbf{b_n}V_t. \tag{2.1.10}$$

This can be rewritten as

$$\dot{\mathbf{v}} = \mathbf{A}\mathbf{v} + \mathbf{b}V_t \tag{2.1.11}$$

where

$$\mathbf{A} = -2Re\{\mathbf{CD}\}$$

$$\mathbf{b} = 2Re\{\mathbf{Ce}\}$$

$$\mathbf{C} = \begin{bmatrix} \frac{S^*_{1(1)} - S_{2(1)}}{C_1} & \frac{S^*_{1(2)} - S_{2(2)}}{C_1} & \dots & \frac{S^*_{1(Q)} - S_{2(Q)}}{C_1} \\ \frac{S^*_{2(1)} - S_{3(1)}}{C_2} & \frac{S^*_{2(2)} - S_{3(2)}}{C_2} & \dots & \frac{S^*_{2(Q)} - S_{3(Q)}}{C_2} \\ \vdots & \vdots & \ddots & \vdots \\ \frac{S^*_{N-1(1)} - S_{N(1)}}{C_{N-1}} & \frac{S^*_{N-1(2)} - S_{N(2)}}{C_{N-1}} & \dots & \frac{S^*_{N-1(Q)} - S_{N(Q)}}{C_{N-1}} \end{bmatrix}$$

$$\mathbf{D} = \begin{bmatrix} \frac{S_{1(1)} - S_{2(1)}}{Z_1} & \frac{S_{2(1)} - S_{3(1)}}{Z_1} & \dots & \frac{S_{N-1(1)} - S_{N(1)}}{Z_1} \\ \frac{S_{1(2)} - S_{2(2)}}{Z_2} & \frac{S_{2(2)} - S_{3(2)}}{Z_2} & \dots & \frac{S_{N-1(2)} - S_{N(2)}}{Z_2} \\ \vdots & \vdots & \ddots & \vdots \\ \frac{S_{1(Q)} - S_{2(Q)}}{Z_Q} & \frac{S_{2(Q)} - S_{3(Q)}}{Z_Q} & \dots & \frac{S_{N-1(Q)} - S_{N(Q)}}{Z_Q} \end{bmatrix}$$

$$\mathbf{e} = \begin{bmatrix} \frac{S_{N(1)}}{Z_1} & \frac{S_{N(2)}}{Z_2} & \dots & \frac{S_{N(Q)}}{Z_Q} \end{bmatrix}^T$$

The characteristics of the flying capacitor balancing process can be studied through numerical analysis of the presented model. The main conclusions and recommendations are:

1. The natural balancing process has been identified. It has been shown that the balancing process depends on:

a) The interleaving of the cells.

b) The interactions of the current harmonics and the switching functions.

c) The requirement that all switches operate with the same duty cycle. Operating two or more cells at different duty cycles results in unbalance.

2. The accuracy of the model does not increase significantly when the number of harmonics is increased beyond a certain point. It is suggested that this point lies somewhere between the number of cells used and 10.

3. The balance booster has been identified. It has been shown that the balance booster decreases the impedance at a specific frequency, thus resulting in an increased current ripple and faster rebalancing.

4. The FCC balances naturally for both constant and modulated duty cycle.

5. The model can be used to design and model active balancing mechanisms [35].

2.1.2 Yuan, Stemmler and Barbi

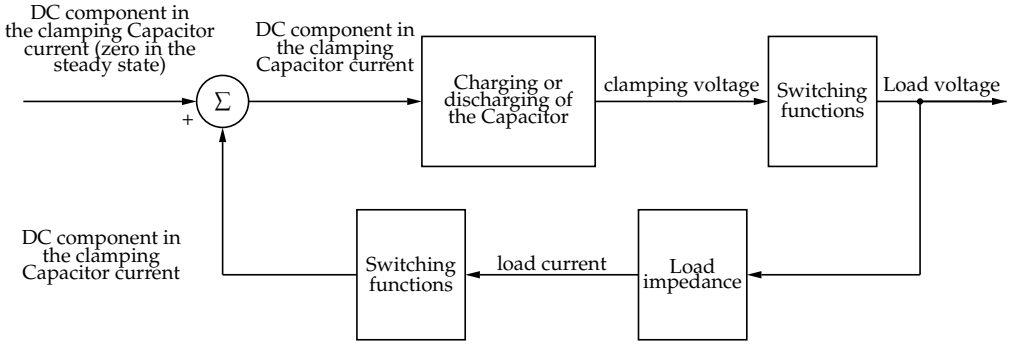

Figure 2.2: Spontaneous clamping capacitor current control loop in a 2-cell FCC

The model explains the natural balancing with the aid of a spontaneous clamping capacitor control loop, shown in Fig. 2.2. The model is developed in full for 2-cell and 3-cell converters although it could theoretically be extended to any number of cells. The method used for the 2-cell is discussed here.

The main assumptions and definitions are:

1. The converter operating with a modulated duty cycle is studied.

2. The switching functions are defined as $s(t) \in \{0, 1\}$.

3. The charge balance in the flying capacitors is studied.

4. The PWM signals are created by comparing triangular carriers with frequency f_c and a reference signal with frequency f_r.

The switching functions are expressed in the frequency domain by using the double Fourier series with positive frequency entries as:

$$\begin{aligned}
s_1(t) &= \frac{1}{2} + \frac{m_a}{2}\sin(\omega_m t) + \sum_{m=1,3,5}^{\infty} (-1)^{\frac{m+1}{2}} \frac{2J_0(\frac{mm_a\pi}{2})}{m\pi}\sin(m\omega_c t) \\
&\quad + \sum_{m=1,3,5}^{\infty}\sum_{n=\pm1,\pm3}^{\pm\infty} \frac{2J_n(mm_a\pi)}{m\pi}\sin\left(\frac{m\pi}{2}\right)\cos(m\omega_c t + n\omega_r t - m\pi) \\
&\quad + \sum_{m=2,4}^{\infty}\sum_{n=\pm1,\pm3}^{\pm\infty} \frac{2J_n(mm_a\pi)}{m\pi}\cos\left(\frac{m\pi}{2}\right)\sin(m\omega_c t + n\omega_r t - m\pi) \\
s_2(t) &= \frac{1}{2} + \frac{m_a}{2}\sin(\omega_m t) - \sum_{m=1,3,5}^{\infty} (-1)^{\frac{m+1}{2}} \frac{2J_0(\frac{mm_a\pi}{2})}{m\pi}\sin(m\omega_c t) \\
&\quad - \sum_{m=1,3,5}^{\infty}\sum_{n=\pm1,\pm3}^{\pm\infty} \frac{2J_n(mm_a\pi)}{m\pi}\sin\left(\frac{m\pi}{2}\right)\cos(m\omega_c t + n\omega_r t - m\pi) \\
&\quad + \sum_{m=2,4}^{\infty}\sum_{n=\pm1,\pm3}^{\pm\infty} \frac{2J_n(mm_a\pi)}{m\pi}\cos\left(\frac{m\pi}{2}\right)\sin(m\omega_c t + n\omega_r t - m\pi)
\end{aligned}$$

The unfiltered output voltage is

$$\begin{aligned}
v_o &= s_2 v_1 + s_1(V_t - v_1) - \frac{V_t}{2} \\
&= \frac{V_t}{2}(s_1 - s_2 - 1) + (s_1 - s_2)\left(\frac{V_t}{2} - \hat{v}_1\right) + (s_1 - s_2)\left(\hat{v}_1 - v_1\right), \qquad (2.1.12)
\end{aligned}$$

where $\hat{v}_1$ is the DC average of the flying capacitor voltage. Let Δv_1 denote the variation of the flying capacitor voltage from the steady state, then the corresponding variation in output voltage is

$$\begin{aligned}
\Delta v_0 =& \Delta v_1 \Bigg\{ \sum_{m=1,3,5}^{\infty} (-1)^{\frac{m+1}{2}} \frac{4J_0(\frac{mm_a\pi}{2})}{m\pi}\sin\left(m\omega_c t - \frac{\pi}{2}\right) \\
&+ \sum_{m=1,3,5}^{\infty}\sum_{n=\pm2,\pm4}^{\pm\infty} \frac{4J_n(mm_a\pi)}{m\pi}\sin\left(\frac{m\pi}{2}\right)\cos(m\omega_c t + n\omega_r t - m\pi)\Bigg\}. \qquad (2.1.13)
\end{aligned}$$

If the load impedance can be described as $Z(\omega)\angle\theta(\omega)$ at all relevant frequencies, then the variation in load current can be found from the expression describing the variation in output voltage. This load current variation is reflected back as a variation in flying capacitor current, i_c as

$$\Delta i_c = \Delta I_{load}(s_1 - s_2), \qquad (2.1.14)$$

with DC component

$$\Delta i_{c(DC)} = \Delta v_1 G$$
$$G = \frac{1}{2}\sum_{m=1,3,5}^{\infty}\left\{\left((-1)^{\frac{m+1}{2}}\frac{4J_0(\frac{mm_a\pi}{2})}{m\pi}\right)^2\frac{1}{Z(m\omega_c)}\cos(\theta(m\omega_c)\right\}$$
$$+\frac{1}{2}\sum_{m=1,3,5}^{\infty}\sum_{n=\pm2,\pm4}^{\pm\infty}\left\{\left(\frac{4J_n(mm_a\pi)}{m\pi}\sin\left(\frac{m\pi}{2}\right)\right)^2\frac{1}{Z(m\omega_c+n\omega_r)}\cos(\theta(m\omega_c+n\omega_r)\right\}. \tag{2.1.15}$$

The rebalancing time constant is therefore

$$\tau = \frac{C}{G}. \tag{2.1.16}$$

The main conclusions and recommendations are:

1. The FCC rebalances when the load is not purely reactive.
2. When more cells are used, the spontaneous clamping capacitor current loop changes to allow for coupling between the different current loops.
3. The balancing time constant increases, as the capacitance of the flying capacitor, the load impedance amplitude and the load impedance angle are increased. The balancing time constant decreases with modulation index.
4. Slight unbalances might exist in the steady state when asymmetries in the system are taken into account.
5. Due to the natural balancing mechanism, the FCC may work without active control of the clamping voltages. However, a pseudo load might be needed to deal with light or reactive loads.

2.1.3 Wilkinson and Mouton

The main assumptions and definitions are [26; 36; 28]:

1. All switches are ideal, with the on state voltage and the off state current, as well as both the switching time and delays all equal to zero.
2. The switches in each cell are operated as a complementary pair.
3. The switching function applied to switch k is $s_k(t) \in \{-1, 1\}$.
4. The FCC is modelled in terms of total and difference parameters. The same approach is also used in this thesis.
5. The 'integrals over groups of harmonics' method is used to analyse the system.

The positive frequency double Fourier series is used to describe the switching functions in the frequency domain. The switching function of the k^{th} cell is

$$s_k(t) = A_{00} + \sum_{m=1}^{\infty} \left\{ A_{m0} \cos\left(m\omega_s t - \frac{2m\pi k}{N} \right) + B_{m0} \left(m\omega_s t - \frac{2m\pi k}{N} \right) \right\} + \sum_{m=1}^{\infty} \sum_{n=1}^{\infty} \left\{ A_{mn} \cos\left(m\omega_s t + n\omega_r t - \frac{2m\pi k}{N} \right) + B_{mn} \sin\left(m\omega_s t + n\omega_r t - \frac{2m\pi k}{N} \right) \right\} \tag{2.1.17}$$

where

$$A_{mn} + jB_{mn} = \begin{cases} \frac{2j}{m\pi} J_n\left(\frac{m\pi m_a}{2}\right)(1 + e^{jm\pi}) & \text{for } m \neq 0 \text{ and } n \text{ odd} \\ \frac{2}{jm\pi} J_n\left(\frac{m\pi m_a}{2}\right)(1 - e^{jm\pi}) & \text{for } m \neq 0 \text{ and } n \text{ even} \\ jm_a & \text{for } m = 0 \text{ and } n = 1 \\ 0 & \text{otherwise.} \end{cases}$$

When the total and difference switching functions are investigated, the 'integrals over groups of harmonics' concept shows that the difference switching functions interact with one another. No interaction between the total and difference switching functions is found

$$|S_t(\omega)||S_{di}(\omega)| \approx 0 \text{ for } i = 1, 2, \ldots, N-1, \tag{2.1.18}$$

when the switching frequency is sufficiently larger than the modulation frequency. The interactions between the individual difference switching functions can be described by investigating the integral over the harmonic groups. Since it is true that

$$|S_{d1}(\omega)| = |S_{d2}(\omega)| = |S_{di}(\omega)|, \tag{2.1.19}$$

these interactions can be described by using similar variables, for $q \in \{0, 1, 2, \ldots\}$

$$\begin{aligned} \lambda_0 &= \int_{m=qN} \frac{|S_{d1}(\xi)|^2}{Z(\xi)} d\xi = 0 \\ \lambda_1 &= \int_{m=qN+1} \frac{|S_{d1}(\xi)|^2}{Z(\xi)} d\xi \\ &\vdots \\ \lambda_{N-1} &= \int_{m=qN+(N-1)} \frac{|S_{d1}(\xi)|^2}{Z(\xi)} d\xi. \end{aligned} \tag{2.1.20}$$

Using these descriptions, the circuit operation is described in the form

$$\frac{d}{dt}\mathbf{v_d} = -\frac{1}{C} 2Re\{\mathbf{A}\}\,\mathbf{v_d}, \tag{2.1.21}$$

where

$$\mathbf{A} = \begin{bmatrix} \sum_{i=1}^{N-1} \lambda_i & \sum_{i=1}^{N-1} \lambda_i e^{j\frac{2\pi i}{N}} & \cdots & \sum_{i=1}^{N-1} \lambda_i e^{j\frac{2\pi(N-2)i}{N}} \\ \sum_{i=1}^{N-1} \lambda_i e^{j\frac{2\pi(N-1)i}{N}} & \sum_{i=1}^{N-1} \lambda_i & \cdots & \sum_{i=1}^{N-1} \lambda_i e^{j\frac{2\pi(N-3)i}{N}} \\ \vdots & \vdots & \ddots & \vdots \\ \sum_{i=1}^{N-1} \lambda_i e^{j\frac{2\pi(N-2)i}{N}} & \sum_{i=1}^{N-1} \lambda_i e^{j\frac{2\pi(N-3)i}{N}} & \cdots & \sum_{i=1}^{N-1} \lambda_i \end{bmatrix}$$

$$\mathbf{v_d} = \begin{bmatrix} v_{d1} & v_{d2} & \cdots & V_{d(N-1)} \end{bmatrix}^T.$$

The system can be studied by numerically constructing $\mathbf{A}$ and extracting the location of the system roots. The main conclusions and recommendations are:

1. There are values of constant duty cycle and N where $\det(2Re\{\mathbf{A}\}) = 0$. Since the determinant of a matrix is the product of the eigenvalues, this implies that one or more eigenvalues are equal to zero. It is possible that the system will not rebalance in this case.

2. The locations of the eigenvalues were estimated by calculating the spectral radius of $\mathbf{A}$ and using Gerschgorin circles. However, for systems with $N > 2$, the spectral radius and the entries of $\mathbf{A}$ used to construct the Gerschgorin circles must be calculated numerically. Once $\mathbf{A}$ is constructed, it is trivial to calculate the exact location of the eigenvalues by using Python or MATLAB. Furthermore, the intersection of the Gerschgorin circle and the spectral radius often included part of the right hand side of the complex plane.

3. The inductor ESR was not modelled.

4. There are specific values of constant duty cycle where unbalance can occur.

5. Natural balance will occur when all of the following are true:

   a) When modulated duty cycle is used, or constant duty cycle where $\det(2Re\{\mathbf{A}\}) \neq 0$.

   b) When the load is such that $Re\{Z(\omega)\} > 0$.

   c) When there is no overlapping of the switching frequency harmonics, $|S_{d1}(\omega)||S_t(\omega)| = 0$.

2.1.4 McGrath and Holmes

The unique model definitions are [25; 37; 38]:

1. The number N is defined as the number of levels and not the number of cells.

2. The switching functions are defined as $S_n(t) \in \{0, 1\}$.

From the circuit operation, the flying capacitor current is given by

$$C_n \frac{dv_n(t)}{dt} = (S_{n+1}(t) - S_n(t))\, i_o(t) \tag{2.1.22}$$

for $n = 0, 1, \ldots, N-2$. The load current, $i_o(t)$ is determined from the output voltage of the converter as

$$\left(R + L\frac{d}{dt}\right) = \Big(2S_N(t) - 1\Big)\frac{V_t}{2} - \sum_{n=1}^{N-2}\Big(S_{n+1}(t) - S_n(t)\Big)v_n(t). \tag{2.1.23}$$

The double Fourier series, with positive frequency entries, is used to describe the switching functions in the frequency domain. The switching function is defined as:

$$S_n(t) = \frac{1}{2} + \frac{m_a}{2}\cos(\omega_0 t) + \sum_{k=1}^{\infty}\sum_{m=-\infty}^{\infty} C_{km}\cos(k\omega_s t + k\phi_s + m\omega_0 t) \tag{2.1.24}$$

$$C_{km} = \frac{2}{k\pi}\sin\left((k+m)\frac{\pi}{2}\right) J_m\left(k\frac{\pi}{2}m_a\right) \tag{2.1.25}$$

When the switching signals are interleaved, the switching signal phase shift of the n^{th} cell is

$$\phi_{s,n} = \frac{2\pi(n-1)}{N-1}. \tag{2.1.26}$$

The results are combined to yield the following combined switching functions, with reference to (2.1.23):

$$S_{n+1}(t) - S_n(t) = \sum_{k=1}^{\infty}\sum_{m=1}^{\infty} A_{km}\cos(\omega_{km}t + \theta_{n,k}) \tag{2.1.27}$$

$$2S_{N-1}(t) - 1 = m_a\cos(\omega_0 t) + \sum_{k=1}^{\infty}\sum_{m=-\infty}^{\infty} B_{km}\cos(\omega_{km}t + \gamma_k) \tag{2.1.28}$$

$$\omega_{km} = k\omega_s + m\omega_0 \tag{2.1.29}$$

$$A_{km} = 2\sin\left(\frac{k\pi}{N-1}\right) C_{km}$$

$$B_{km} = 2C_{km} \tag{2.1.30}$$

$$\gamma_k = \frac{2k(N-2)\pi}{N-1} \tag{2.1.31}$$

$$\theta_{n,k} = k\frac{(2n-1)\pi}{N-1} + \frac{\pi}{2} \tag{2.1.32}$$

The model first considers a single harmonic frequency ω_{km}. If the load is defined as

$$Z_{km} = |Z_{km}|e^{j\psi_{km}}, \tag{2.1.33}$$

the output current at the frequency can be found as

$$i_{o,km}(t) = \frac{B_{km}}{|Z_{km}|}\cos(\omega_{km}t + \gamma_k - \psi_{km})\frac{V_t}{2} - \sum_{n-1}^{N-2}\frac{A_{km}}{|Z_{km}|}\cos(\omega_{km}t + \theta_{nk} - \psi_{km})v_n(t). \tag{2.1.34}$$

The flying capacitor current is found by substituting (2.1.34) and (2.1.27) into (2.1.23). This result depends on the multiplication of two sinusoids with the same frequency and yields a DC term and a double frequency harmonic. Since only the low frequency effects are of interest, only the DC term is used. The change in the flying capacitor voltage due to the current harmonic at ω_{km} can therefore be described as

$$C_n \frac{dn_{n,km}(t)}{dt} = A_{km}B_{km}Re\left\{\frac{e^{j\gamma_k}e^{-j\theta_{nk}}}{4Z_k}\right\}V_t - \sum_{i=1}^{N-2} A_{km}^2 Re\left\{\frac{e^{j\theta_{lk}}e^{-j\theta_{nk}}}{2Z_{km}}\right\}V_i(t), \quad (2.1.35)$$

or in matrix form as

$$\dot{\mathbf{v}}_{\mathbf{km}}(t) = \mathbf{A_{km}}\mathbf{v}(t) + \mathbf{B_{km}}V_t \quad (2.1.36)$$

where

$$\mathbf{v}(t) = \begin{bmatrix} v_1(t) & v_2(t) & \cdots & v_{N-2}(t) \end{bmatrix}^T \quad (2.1.37)$$

$$\mathbf{A_{km}} = -Re\left\{\frac{\mathbf{C}^{-1}\mathbf{\Lambda}_{\mathbf{km}}^{*}\mathbf{\Lambda}_{\mathbf{km}}^{\mathbf{T}}}{2Z(j\omega_{km})}\right\} \quad (2.1.38)$$

$$\mathbf{B_{km}} = Re\left\{\frac{\mathbf{C}^{-1}\mathbf{\Lambda}_{\mathbf{km}}^{*}\mathbf{\Psi}_{\mathbf{km}}^{\mathbf{T}}}{4Z(j\omega_{km})}\right\} \quad (2.1.39)$$

$$\mathbf{\Lambda_{km}} = A_{km}\begin{bmatrix} e^{\theta_{1,k}} & e^{\theta_{2,k}} & \cdots & e^{\theta_{N-2,k}} \end{bmatrix}^T \quad (2.1.40)$$

$$\mathbf{\Psi_{km}} = B_{km}e^{j\gamma_k} \quad (2.1.41)$$

$$\mathbf{C} = \begin{bmatrix} C_1 & 0 & \cdots & 0 \\ 0 & C_2 & \cdots & 0 \\ \vdots & \vdots & \ddots & \vdots \\ 0 & 0 & \cdots & C_{N-2} \end{bmatrix}. \quad (2.1.42)$$

The contribution of the different harmonics can be summed together to create a linearised model

$$\dot{\mathbf{v}}(t) = \mathbf{A}\mathbf{v}(t) + \mathbf{B}V_t \quad (2.1.43)$$

where

$$\mathbf{A} = \sum_{k=1}^{\infty}\sum_{m=-\infty}^{\infty}\mathbf{A_{km}} \quad (2.1.44)$$

$$\mathbf{B} = \sum_{k=1}^{\infty}\sum_{m=-\infty}^{\infty}\mathbf{B_{km}}. \quad (2.1.45)$$

This is a noteworthy result in that the representation of two signals multiplied in the time domain typically requires the evaluation of the convolution of the frequency domain representations over all frequencies. The representation of the convolution in terms of an infinite summation will be used extensively in this thesis.

This linearised model is used extensively by McGrath and Holmes. The model is applied to different FCC topologies and applications. In general, linear systems analysis techniques such as the root locus are used to investigate the balancing behaviour. The eigenvalues are calculated through numerical processes by using the presented linearised model. The main conclusions and recommendations are:

1. The balancing process is driven by output current ripple. Hence, the system poles depend on switching frequency, modulation index and load.

2. The locations of the poles in the complex plane depends on the ratio of the inductance and resistance, for LR-type loads. However, as the pole locations are calculated numerically, no closed form expression to explain this dependence is presented.

3. The skin- and proximity effects play a significant role in the balancing process.

4. The order of interleaving influences the balancing process. The locations of the poles are not affected by changing the interleaving order, but the locations of the zeros are altered significantly.

5. A model is developed for three phase drive applications where the output current from phases b and c can influence the balancing dynamics of phase a.

6. The effect of the induction machine slip is negligible and can be ignored. This implies that the balancing properties are independent of the mechanical load.

7. The induction machine parameters must be adjusted to account for skin- and proximity effects as well as for the dependence of motor leakage inductance on excitation frequency.

8. Near perfect pole-zero cancellation occurs in constant Volts/Hertz drive applications resulting in an apparent order reduction.

9. There is a trade-off between the rebalancing time constant and the steady-state balance booster loss when designing the balance booster resistance.

10. It is possible to preserve the natural balancing properties by using modulation schemes other than phase shifted interleaving. The phase disposition method or centred space vector PWM methods can be used with the benefit of decreased output voltage THD. However, state machines are required to ensure that the switching pulses are distributed equally among the cells [38].

2.2 Analysis of the FCC in the Time Domain

The approach of the analysis of switched systems [39] requires the description of m continuous-time systems by:

$$\dot{\mathbf{x}}(t) = \mathbf{f}_i(\mathbf{x}(t)),\ i = 1, \ldots, m, \tag{2.2.1}$$

where $\mathbf{x}(\cdot) \in \mathbb{R}^n$ is the state vector and $\mathbf{f}_i(\cdot) : \mathbb{R}^n \to \mathbb{R}^n$ describes the circuit dynamics. A switched system is a mathematical model in the form:

$$\dot{\mathbf{x}}(t) = \mathbf{f}_{s(t)}(\mathbf{x}(t)), \tag{2.2.2}$$

where $s(\cdot) \in \{1, \ldots, m\}$ is the switching law. By using this approach, it is possible to model a system that switches between m subsystems or states. The switching

law depends on the control algorithm or strategy used, as well as on the type of modulator and the states of the controlled circuit parameters. However, in open loop systems it is possible to generate a function, $s(t)$, that describes which subsystem is active at which time.

This method of describing a switching system is well known and is often used as a departure point in the generation of a small-signal model by using state-space averaging [40]. This description is also used for time domain simulations; all simulation results presented in this thesis were obtained by using this method or some derivative of it.

For time domain simulations, the system is described by using (2.2.2) and ignoring non-linear terms; in other words, all the subsystems are linear. If all the subsystems are linear, then the derivative of the state vector can be expressed as:

$$\dot{\mathbf{x}}(t) = \begin{cases} \mathbf{A}_1\mathbf{x}(t) + \mathbf{b}_1 g(t) & 0 \leq t < t_1 \\ \mathbf{A}_2\mathbf{x}(t) + \mathbf{b}_2 g(t) & t_1 < t \leq t_2 \\ \vdots & \vdots \end{cases} \tag{2.2.3}$$

Here $g(t)$ describes external influences that are invariant on the state vector, i.e. sources. The solution can be found, with a time step of Δt as [40]:

$$\mathbf{x}(t) = \mathbf{x}(t - \Delta t) + \int_{t-\Delta t}^{t} \mathbf{A}_i(\xi)\mathbf{x}(\xi) + \mathbf{b}_i(\xi)g(\xi)d\xi \tag{2.2.4}$$

where ξ is an integration variable. Although the circuit description changes abruptly during switching, the state variables typically have relatively long time constants, thus ensuring low current and voltage ripple (which is true for practical converters). Therefore the solution at $t = t_1^-$ is used as an initial condition to calculate the solution at $t > t_1$, thereby *stitching* together the solutions of the different switched subsystems.

The primary argument for the analysis of the FCC in the time domain is that, even if all subsystems are linear, i.e. in the form of (2.2.3), the solutions might demonstrate highly non-linear behaviour [41], suggesting that frequency domain methods might not be applicable. The time domain analysis considers the analytical solutions for the m linear differential equations corresponding to the m different switching states. By combining the different solutions according to the switching law, certain deductions and conclusions can be made from the resulting time domain expression.

The analytical solution can be found by applying one of the fundamental theorems of linear systems with constant coefficients. If at time $t = \tau$ the state vector is $\mathbf{x}(\tau)$ and assuming the i^{th} switching state to be active, then it follows that [41] (and with a constant source, i.e. $g(t) = V$)

$$\mathbf{x}(t) = e^{\mathbf{A}_i(t-\tau)}\mathbf{x}(\tau) + \mathbf{c}_i(t - \tau), \tag{2.2.5}$$

where

$$\mathbf{c}_i(t - \tau) = V \int_{\tau}^{t} e^{\mathbf{A}_i(t-\xi)}\mathbf{b}_i d\xi. \tag{2.2.6}$$

In the ideal case, where the switching law can be explicitly defined, the switching law will be periodic with some frequency. In the case of PWM converters operating with a constant duty cycle, the switching law will be periodic with a period that is a multiple of the switching period. When the duty cycle is modulated, as in the case of inverters, the switching law will be periodic with a period that is a multiple of the modulation period, if the switching frequency is a integer multiple of the modulation frequency. If the switching frequency is not an integer multiple of the modulation frequency, the switching law could have a period many times larger than the modulation function's or, in the case of a non-rational multiple, the switching law could be non-periodic.

If the switching law is periodic, then the solution of (2.2.5) can be applied repeatedly. Let t_i denote the switching times, i.e. the instants in time where the switching takes place. Let the switching law be periodic with a period of t_m and let it switch through the m states in sequence. The length of time that each subsystem is active is defined as Δt_i and it is further defined as $\Delta t_i = t_i - t_{i-1}$ such that $t_m = \sum_{i=1}^{m} \Delta t_i$. Using (2.2.5) the solutions for the state vector at the switching transitions can be found as:

$$\begin{aligned}
\mathbf{x}(t_1) =& e^{\mathbf{A}_1 \Delta t_1}\mathbf{x}(0) + \mathbf{c}_1(\Delta t_1) \\
\mathbf{x}(t_2) =& e^{\mathbf{A}_2 \Delta t_2}\mathbf{x}(t_1) + \mathbf{c}_2(\Delta t_2) \\
\mathbf{x}(t_3) =& e^{\mathbf{A}_3 \Delta t_3}\mathbf{x}(t_2) + \mathbf{c}_3(\Delta t_3) \\
&\vdots \\
\mathbf{x}(t_m) =& e^{\mathbf{A}_m \Delta t_m}\mathbf{x}(t_{m-1}) + \mathbf{c}_m(\Delta t_m) \\
\mathbf{x}(t_{m+1}) =& e^{\mathbf{A}_1 \Delta t_1}\mathbf{x}(t_m) + \mathbf{c}_1(\Delta t_1) \\
&\vdots
\end{aligned} \tag{2.2.7}$$

Combining the first m equations yields

$$\mathbf{x}(t_m) = \mathbf{\Phi}\mathbf{x}(0) + \mathbf{b}, \tag{2.2.8}$$

where

$$\mathbf{\Phi} = \prod_{i=1}^{m} e^{A_i \Delta t_i} \tag{2.2.9}$$

and

$$\mathbf{b} = \sum_{i=1}^{m} \left(\mathbf{c}_i(\Delta t_i) \cdot \prod_{k=i+1}^{m} e^{A_k \Delta t_k} \right). \tag{2.2.10}$$

Since the switching law is periodic, the solution at multiples of t_m can be found as:

$$\mathbf{x}(t_{m(k+1)}) = \mathbf{\Phi}\mathbf{x}(t_{mk}) + \mathbf{b}, \;\; k = 1, 2, \ldots \tag{2.2.11}$$

The matrix $\mathbf{\Phi}$ is called the fundamental matrix, and it contains all the information required to solve (2.2.2) with any initial conditions at time instants that are multiples of the switching law period. However, it is difficult to find an analytical expression for $\mathbf{\Phi}$ except for simple circuit configurations and converters operating under the condition where the number of different subsystems, or m, is low or repeating often, and the switching law period is small.

The earliest documented use that could be found of this method to study natural balancing was used to analyse a series stacked power quality conditioner [33]. However, mostly because the system in question was operational with modulated duty cycle, an analytical expression for $\mathbf{\Phi}$ was not forthcoming. However, by investigating certain special cases and using Floquet theory, several insightful observations regarding the natural balancing method could be made.

It is possible to calculate the fundamental matrix $\mathbf{\Phi}$ numerically. The rebalancing time constants could also be extracted from this matrix. However, no real understanding of the balancing process or information to enable the design of systems with enhanced natural balancing properties is forthcoming out of such a numerical calculation. At best, such a calculation would provide the same insight as a time-domain simulation, albeit much faster than using circuit based time domain integration methods [33].

The 2-cell FCC operating with a LR load and with constant duty cycle, was analysed using this method [41]. Under these conditions, there are only four subsystems, of which two are equivalent, and two state variables namely the flying capacitor voltage and the load inductor current. In this case, it is possible to find an analytical expression for $\mathbf{\Phi}$. The eigenvalues of the matrix are related to the balancing time constants as

$$\tau_i = \frac{t_m}{\ln \varphi_i}, \tag{2.2.12}$$

where t_m is the switching law period and φ_i are the eigenvalues of $\mathbf{\Phi}$.

2.2.1 2-Cell Example

Consider the 2-cell FCC presented in Fig. 2.3. Four switching states can be identified as described in Table 2.1. Using the circuit and the switching states, the state variables, i_o and v_1, can now be described during each state. During the following discussion, it will be assumed that the duty ratio is higher than 50%, or equivalently, that two triangular carriers with bounds at +1 and -1 are used and that the reference function has a positive value. In this case, switching state s_3 does not occur. The switching states will occur in the sequence $\ldots, s_1, s_2, s_1, s_4, \ldots$ The system will be described, for each of the unique states, as a linear time invariant system by using the form

$$\mathbf{x}(t) = \begin{bmatrix} i_o(t) \\ v_1(t) \end{bmatrix} \tag{2.2.13}$$

$$\mathbf{x}(t) = \mathbf{A}(t)\mathbf{x}(t_0) + \mathbf{b}(t)\frac{V_t}{2}, \tag{2.2.14}$$

where the initial value of the state vector is described by $\mathbf{x}(t_0)$.

2.2.1.1 Description of the System during State 1

During switching state 1, the capacitor is completely disconnected from the system and the circuit operation can be described as in Fig. 2.4. Let the system enter state

Table 2.1: Different switching states for the 2-cell FCC: Example of time domain analysis

Switching state	Switches on
s_1	S_0+ and S_1+
s_2	S_0+ and S_1-
s_3	S_0- and S_1-
s_4	S_0- and S_1+

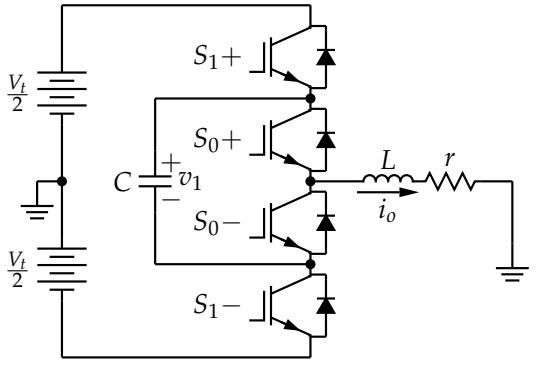

Figure 2.3: Two cell FCC: Example of time domain analysis

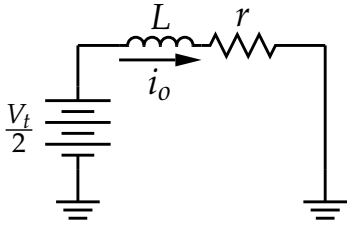

Figure 2.4: The 2-cell FCC during switching state 1

1 at time t_0, then the state variables during this state can be described by

$$\mathbf{x}(t) = \mathbf{A_1}(t)\mathbf{x}(t_0) + \mathbf{b_1}(t)\frac{V_t}{2}$$

$$\mathbf{A_1}(t) = \begin{bmatrix} e^{\frac{-tr}{L}} & 0 \\ 0 & 1 \end{bmatrix} \tag{2.2.15}$$

$$\mathbf{b_1}(t) = \begin{bmatrix} \frac{1}{r}\left(1 - e^{\frac{-tr}{L}}\right) \\ 0 \end{bmatrix} \tag{2.2.16}$$

2.2.1.2 Description of the System during State 2

During state 2, the system can be described by means of the circuit of Fig. 2.5. During this state, the system would exhibit the oscillatory response of a LCR circuit. Although the resistor r will influence the oscillation frequency, it is assumed that, if the resistor is small enough, then this variation will be negligible and that it can be ignored. Let the system enter state 2 at time t_1, then the state variables during

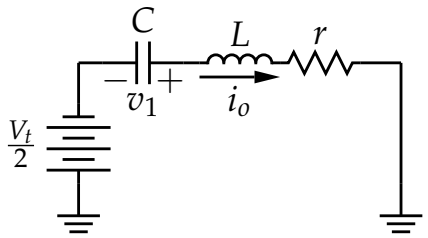

Figure 2.5: The 2-cell FCC during switching state 2

this state can be described by

$$\mathbf{x}(t) = \mathbf{A_2}(t)\mathbf{x}(t_1) + \mathbf{b_2}(t)\frac{V_t}{2}$$

$$\mathbf{A_2}(t) = e^{-\alpha t}\begin{bmatrix} \cos(\omega_0 t) - \frac{\alpha}{\omega_0}\sin(\omega_0 t) & \frac{1}{\omega_0 L}\sin(\omega_0 t) \\ -\frac{1}{\omega_0 C}\sin(\omega_0 t) & \cos(\omega_0 t) + \frac{\alpha}{\omega_0}\sin(\omega_0 t) \end{bmatrix} \tag{2.2.17}$$

$$\mathbf{b_2}(t) = \begin{bmatrix} -\frac{1}{\omega_0 L}e^{\alpha t}\sin(\omega_0 t) \\ -e^{-\alpha t}\left(\frac{\alpha}{\omega_0}\sin(\omega_0 t) + \cos(\omega_0 t)\right) + 1 \end{bmatrix}, \tag{2.2.18}$$

where

$$\alpha = \frac{r}{2L} \tag{2.2.19}$$

$$\omega_0 = \frac{1}{\sqrt{LC}} \tag{2.2.20}$$

$$\omega = \sqrt{\omega_0^2 - \alpha^2} \tag{2.2.21}$$

$$r \ll 2\sqrt{\frac{L}{C}} \Longrightarrow \omega \approx \omega_0. \tag{2.2.22}$$

2.2.1.3 Description of the System during State 4

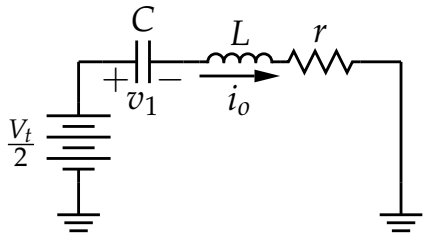

Figure 2.6: The 2-cell FCC during switching state 4

The circuit response of state 4 is similar to that of state 2. Let the system enter

state 4 at time t_3, then the state variables during this state can be described by

$$\begin{aligned}
\mathbf{x}(t) =& \mathbf{A_4}(t)\mathbf{x}(t_3) + \mathbf{b_4}(t)\frac{V_t}{2} \\
\mathbf{A_4}(t) =& e^{-\alpha t}\begin{bmatrix} \cos(\omega_0 t) - \frac{\alpha}{\omega_0}\sin(\omega_0 t) & -\frac{1}{\omega_0 L}\sin(\omega_0 t) \\ \frac{1}{\omega_0 C}\sin(\omega_0 t) & \cos(\omega_0 t) + \frac{\alpha}{\omega_0}\sin(\omega_0 t) \end{bmatrix} \qquad (2.2.23) \\
\mathbf{b_4}(t) =& \begin{bmatrix} \frac{1}{\omega_0 L}e^{\alpha t}\sin(\omega_0 t) \\ -e^{-\alpha t}\left(\frac{\alpha}{\omega_0}\sin(\omega_0 t) + \cos(\omega_0 t)\right) + 1 \end{bmatrix}. \qquad (2.2.24)
\end{aligned}$$

2.2.1.4 Description of the State-Variables at the Switching Instants

The state variables can be described at the switching instants by using the defined circuit descriptions and the method discussed in Section 2.2. Let the term Δt_1 describe the length of time the system spends in state 1, then it is true that

$$\begin{aligned}
t_1 &= \Delta t_1 + t_0 \\
t_2 &= \Delta t_2 + \Delta t_1 + t_0 \\
t_3 &= \Delta t_3 + \Delta t_2 + \Delta t_1 + t_0 \\
t_4 &= \Delta t_4 + \Delta t_3 + \Delta t_2 + \Delta t_1 + t_0 = T_{pwm} + t_0. \qquad (2.2.25)
\end{aligned}$$

The state variables can now be described, at the switching instants, as

$$\begin{aligned}
\mathbf{x}(t_1) =& \mathbf{A_1}(\Delta t_1)\mathbf{x}(t_0) + \mathbf{b_1}(\Delta t_1)\frac{V_t}{2} \\
\mathbf{x}(t_2) =& \mathbf{A_2}(\Delta t_2)\mathbf{x}(t_1) + \mathbf{b_2}(\Delta t_2)\frac{V_t}{2} \\
\mathbf{x}(t_3) =& \mathbf{A_1}(\Delta t_3)\mathbf{x}(t_2) + \mathbf{b_1}(\Delta t_3)\frac{V_t}{2} \\
\mathbf{x}(t_4) =& \mathbf{A_4}(\Delta t_4)\mathbf{x}(t_3) + \mathbf{b_4}(\Delta t_4)\frac{V_t}{2} \\
\mathbf{x}(t_5) =& \mathbf{A_1}(\Delta t_1)\mathbf{x}(t_4) + \mathbf{b_1}(\Delta t_1)\frac{V_t}{2}.
\end{aligned}$$

By combining the solutions, an expression can be found to describe the state variables at multiples of the switching law period as

$$\begin{aligned}
\mathbf{x}(t + T_{pwm}) &= \mathbf{A}\mathbf{x}(t) + \mathbf{b}\frac{V_t}{2} \qquad (2.2.26) \\
\mathbf{A} &= \mathbf{A_4}(\Delta t_4)\mathbf{A_1}(\Delta t_3)\mathbf{A_2}(\Delta t_2)\mathbf{A_1}(\Delta t_1) \qquad (2.2.27) \\
\mathbf{b} &= \mathbf{A_4}(\Delta t_4)\Big\{\mathbf{A_1}(\Delta t_3)\Big\{\mathbf{A_2}(\Delta t_2)\mathbf{b_1}(\Delta t_1) + \mathbf{b_2}(\Delta t_2)\Big\} \\
&\qquad + \mathbf{b_1}(\Delta t_3)\Big\} + \mathbf{b_4}(\Delta t_4). \qquad (2.2.28)
\end{aligned}$$

2.2.2 The Balancing Model

By defining the different switching times, $\Delta t_1, \ldots, \Delta t_4$ as a function of the duty cycle, the fundamental matrix becomes a function of the duty cycle and (2.2.26)

becomes

$$\mathbf{x}(t + T_{pwm}) = \mathbf{A}(d)\mathbf{x}(t) + \mathbf{b}(d)\frac{V_t}{2}. \tag{2.2.29}$$

The changes in the system can be approximated by using this representation of the circuit by averaging the derivative of the state variables over a switching law period. Therefore

$$\frac{d}{dt}i_o(t + T_{pwm}) \approx \frac{i_o(t + T_{pwm}) - i_o(t)}{T_{pwm}} \tag{2.2.30}$$

$$\frac{d}{dt}v_1(t + T_{pwm}) \approx \frac{v_1(t + T_{pwm}) - v_1(t)}{T_{pwm}}. \tag{2.2.31}$$

Using these averaged derivatives, the averaged FCC differential equation system can be written as

$$\frac{d}{dt}\mathbf{x} = \frac{1}{T_{pwm}}\Big\{\mathbf{A}(d) - \mathbf{I}\Big\}\mathbf{x} + \frac{1}{T_{pwm}}\mathbf{b}(d)\frac{V_t}{2}. \tag{2.2.32}$$

Describing the circuit in this manner is analogous to circuit averaging. This representation will not reflect switching voltage and current ripples that occur within a switching law period.

It is stated in [27] that the fundamental matrix **A** can be created by using any of the states as a starting point, and therefore yielding four different state matrices. However, the matrices are similar, in that they share the same characteristic polynomial and eigenvalues.

Once a symbolic expression for the fundamental matrix has been generated, expressions for the eigenvalues can be extracted by using the characteristic polynomial. This method is described in detail for the 2-cell case in [41]. It is not a simple process, though, and geometric series expansions for $\sin(x)$, $\cos(x)$, e^x, $\sqrt{1+x}$ and $\ln(1+x)$ are needed. By using these series expansions, and simplifying, the time constants of the system can be approximated as

$$\tau_1 \approx \frac{L}{r} \tag{2.2.33}$$

$$\tau_2(D) \approx \frac{48L^2C}{r(1-D)^2(1+2D)T_{pwm}^2} \text{ for } 0 \leq D \leq 1, \tag{2.2.34}$$

where D is an alternate expression for the duty cycle such that $-1 \leq D \leq 1$.

For modulated duty cycle systems, it is assumed that the system components are dimensioned in such a way that the system is in a quasi steady state. Furthermore, if the modulation frequency, f_m, is much faster than the balancing behaviour of the FCC, it is possible to average the time constant over a modulation period. Using this approach, the flying capacitor rebalancing time constant can be expressed as

$$\tau_2(m_a) \approx \frac{48L^2C}{r\left(1 - \frac{3}{2}m_a^2 + \frac{8}{3\pi}m_a^3\right)T_{pwm}^2}, \tag{2.2.35}$$

with the requirement that

$$T_0 \gg T_m \tag{2.2.36}$$

where $T_m = 1/f_m$ and

$$\frac{1}{T_0} = \frac{1}{T_m}\int_0^{T_m} \frac{1}{\tau_2(t)}dt. \tag{2.2.37}$$

The main conclusions from the time domain studies are:

1. By making suitable approximations, simple expressions for the rebalancing time constants can be found. These expressions give a designer who wishes to exploit natural balancing in a FCC, enough information to optimise the design.

2. The method requires a symbolic expression for the fundamental matrix to express the characteristic equation symbolically. If the load complexity increases, the number of state variables increases and therefore the size of the fundamental matrix increases. This increase implies that the order of the characteristic polynomial will increase. It thus becomes even more difficult to calculate symbolic expressions for the roots of a polynomial as the order increase; in fact, according to Abel's impossibility theorem no general algebraic solution for the roots of polynomials with order 5 or higher exists [42, p. 211]. For systems where the order is higher than 4, educated guesses must be made to find one of the roots and to factorise the polynomial to reduce the order.

3. The time domain method had been used to describe FCC converters with RL loads, as shown in Fig. 2.3 or with pure resistive loads up to 5-levels [43; 44]. It was also used to describe H-bridge FCC converters up to 5-levels per leg, also with RL loads [45; 46].

Chapter 3

The Strong Balancing Mechanism: Input-Series-Output-Parallel Modular DC-DC Converter

The strong balancing mechanism occurs irrespective of the interleaving between the different switches. Since the interleaving does not play an active role, the strong balancing mechanism can be identified and described by using circuit averaging techniques.

The ISOP modular DC-DC converter is identified as a converter where the strong balancing mechanism dominates. In keeping with the method used throughout this thesis, namely, of analysing the balancing mechanisms in the frequency domain, the ISOP converter is analysed in the frequency domain and a rebalancing equivalent circuit is presented. It is shown that the ISOP shares both the input voltage and the output current equally among the cells. The converter will return to this balanced state should some disturbance occur. This rebalancing is associated with a large rebalancing current that might be harmful to the system, should the unbalanced state be forced through an external disturbance. An equivalent circuit that describes the balancing process is presented. The balancing time constant can be calculated by means of this circuit.

Taking the theory further, the balancing of non-similar converters is discussed. It is shown that, should two cells with slight variations be used, the cells still share the input voltage and output current. However, this sharing will reflect the mismatch. The equivalent balancing circuit is adapted to allow for variations in the effective duty cycle of the cells.

The described strong balancing mechanism is modified when passive rectification is used on the secondary side of the isolation barrier, as the rectifier diodes prohibit energy exchange from one cell to another through the output. The rebalancing of this circuit is discussed, and an equivalent rebalancing circuit is presented.

The theory presented for the active rectified circuit is verified through comparison with detailed time simulations. In the case of passive rectification, the theory is developed and verified by using measured values as reference.

3.1 Development of the ISOP Equivalent Circuit

Consider the 2-cell converter shown in Fig. 3.1. The following assumptions and approximations are made:

1. The source resistance and other interconnection resistances are lumped into r_s.
2. The winding resistance of the transformer and filter inductor ESR are lumped into r.
3. The switches are assumed to be ideal, implying that the on-state voltage, off-state current as well as the switching times and delays are all zero.
4. All capacitors are assumed to be ideal and linear with no ESR. The cell bus capacitors are equal with value C.
5. The cells are assumed to be similar in all respects, notably in terms of the transformer turns ratio and the value of r and L.
6. The magnetising inductance of the transformers are assumed to be large enough to have negligible influence.

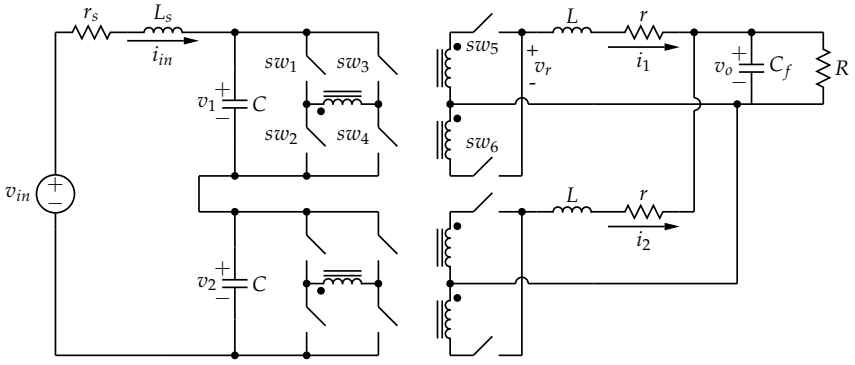

Figure 3.1: General figure of a two cell ISOP converter

The full bridge converters can be approximated by ideal, non saturable, transformers with a time dependent turns ratio, as used in [47]. It is important to note that the turns ratio in this application is not the time averaged value of the duty cycle. In Fig. 3.1 the switches of the topmost converter are labelled 1-6. If each of the converters is substituted by an ideal transformer, the operation of the circuit can be described without any loss of information, as long as the switching functions s_1, and s_2 are complete representations of the switching behaviour of the respective converters.

The switching function of the topmost converter, with reference to the switching behaviour of the respective switches, is indicated in Table 3.1. Let a denote the turns ratio of the isolation transformer and assume that all switches are in the off-state unless mentioned otherwise. Four switching states can be identified, two energy

transfer states (1,4,5 on) and (2,3,6 on) and two free-flow states (1,3,5,6 on) and (2,4,5,6 on).

When either of the energy transfer states are selected the voltage v_r as indicated in Fig. 3.1 will have a value of av_1. Since each of the energy transfer states are selected once in a switching period the rectified output has a frequency equal to twice the switching frequency.

The definitions in Table 3.1 can be adjusted to accommodate any other switching scheme. As mentioned, it is important to note that the effective frequency of the full bridge switching function is twice that of the individual switches. The information presented can be extended to s_2.

Table 3.1: Definition of switching functions

Switch Information	s_1
1,4,5 (on)	a
2,3,6 (on)	a
1,3,5,6 (on)	0
2,4,5,6 (on)	0

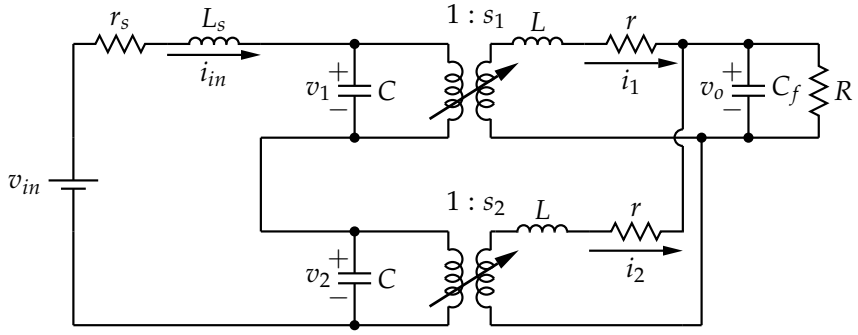

Figure 3.2: The two cell ISOP circuit expressed in terms of the two port circuits

With the switching functions defined, the circuit of Fig 3.1 can be redrawn with the converters replaced with ideal, variable turns ratio transformers, as indicated in Fig. 3.2. Using this representation, the system of differential equations describing the operation of the converter can be expressed as:

$$\frac{d}{dt}\begin{bmatrix} L_s \cdot i_{in} \\ C \cdot v_1 \\ C \cdot v_2 \\ L \cdot i_1 \\ L \cdot i_2 \\ C_f \cdot v_o \end{bmatrix} = \begin{bmatrix} -r_s & -1 & -1 & 0 & 0 & 0 \\ 1 & 0 & 0 & -s_1 & 0 & 0 \\ 1 & 0 & 0 & 0 & -s_2 & 0 \\ 0 & s_1 & 0 & -r & 0 & -1 \\ 0 & 0 & s_2 & 0 & -r & -1 \\ 0 & 0 & 0 & 1 & 1 & \frac{-1}{R} \end{bmatrix} \begin{bmatrix} i_{in} \\ v_1 \\ v_2 \\ i_1 \\ i_2 \\ v_o \end{bmatrix} + \begin{bmatrix} v_{in} \\ 0 \\ 0 \\ 0 \\ 0 \\ 0 \end{bmatrix} \tag{3.1.1}$$

The following variables are defined in order to study the unbalance in the circuit:

$$\begin{aligned} s_d &= \frac{s_1 - s_2}{2} & s_t &= \frac{s_1 + s_2}{2} \\ v_d &= v_1 - v_2 & v_t &= v_1 + v_2 \\ i_d &= i_1 - i_2 & i_t &= i_1 + i_2 \end{aligned} \tag{3.1.2}$$

Equation (3.1.1) can be rewritten in terms of the definitions in (3.1.2), as shown in detail in Appendix A.5.1, resulting in:

$$\frac{d}{dt}\begin{bmatrix} L_s \cdot i_{in} \\ C \cdot v_t \\ C \cdot v_d \\ L \cdot i_t \\ L \cdot i_d \\ C_f \cdot v_o \end{bmatrix} = \begin{bmatrix} -r_s & -1 & 0 & 0 & 0 & 0 \\ 2 & 0 & 0 & -s_t & -s_d & 0 \\ 0 & 0 & 0 & -s_d & -s_t & 0 \\ 0 & s_t & s_d & -r & 0 & -2 \\ 0 & s_d & s_t & 0 & -r & 0 \\ 0 & 0 & 0 & 1 & 0 & \frac{-1}{R} \end{bmatrix} \begin{bmatrix} i_{in} \\ v_t \\ v_d \\ i_t \\ i_d \\ v_o \end{bmatrix} + \begin{bmatrix} v_{in} \\ 0 \\ 0 \\ 0 \\ 0 \\ 0 \end{bmatrix} \tag{3.1.3}$$

The circuit of the two-cell series stacked converter in terms of d and t parameters can be expressed, as shown in Fig. 3.3. The proposed circuit is equivalent to the original circuit of Fig. 3.1, but the bus voltages and currents are expressed in terms of total and difference values. This representation allows for a clear understanding of the balancing process.

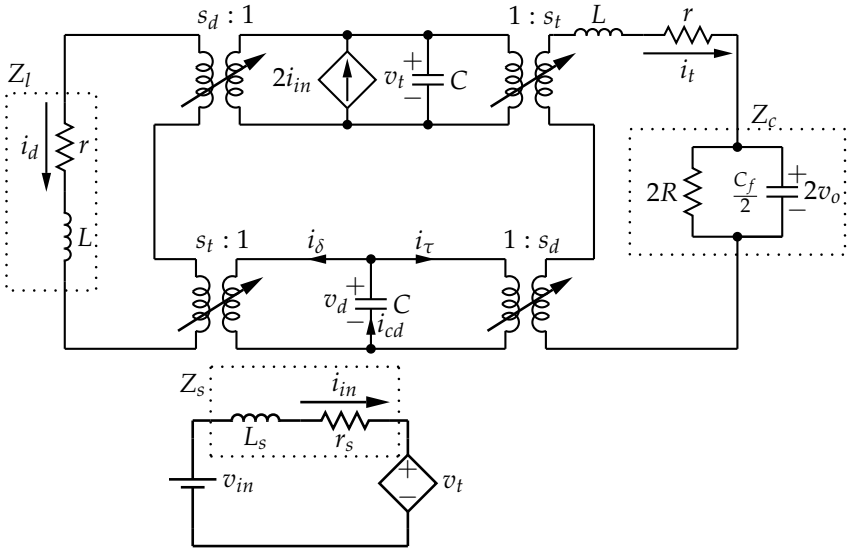

Figure 3.3: 2-Level ISOP converter in terms of d and t parameters

3.2 Analysis of the Converter in the Frequency Domain

The converter can be analysed, in terms of the defined d and t parameters, using the proposed model of (3.1.3) and Fig. 3.3. The circuit will be analysed in the frequency domain.

The following assumptions are made:

1. The two cells are operating at the same switching frequency.
2. The PWM signals are generated by comparing a PWM reference signal with a sawtooth carrier.
3. The two cells operate with interleaved switching whereby the carrier functions are phase shifted by 180°. Two such interleaved sawtooth carriers with a period of T_c are depicted in Fig. 3.4.
4. The PWM reference signals of the two cells are equal.
5. The full-bridge converters are operating at a constant duty cycle, defined as d.
6. The isolation transformer turns ratio is assumed to be 1:1.

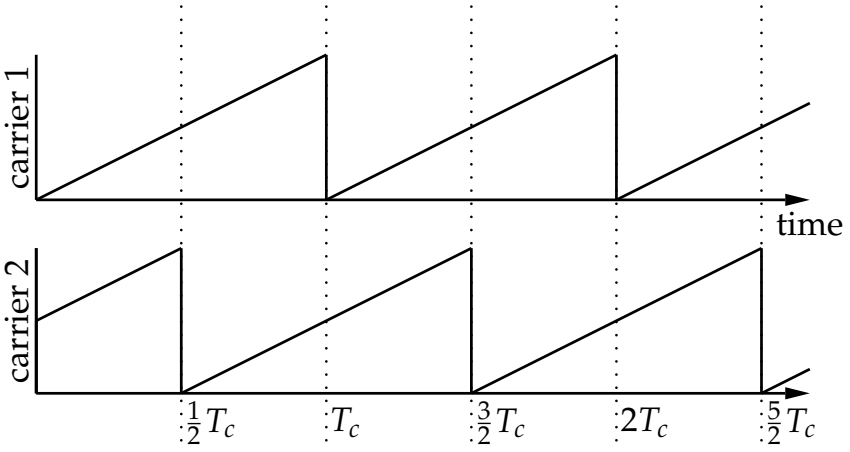

Figure 3.4: Two sawtooth carriers interleaved by 180°.

The exponential Fourier series can be used to represent the harmonic content of the signal. The switching function $s_1(t)$ can be expressed in exponential Fourier series form as [48]:

$$s_1(t) = \sum_{n=-\infty}^{\infty} C_{1(n)} e^{jn\omega_s t} \tag{3.2.1}$$

where,

$$C_{1(n)} = \frac{1}{T_s} \int_{t_0}^{t_0+T_s} s_1(t) e^{-jn\omega_s t} dt. \tag{3.2.2}$$

Similarly switching function s_2 maps to coefficients $C_{2(n)}$. The Fourier series coefficients of the two interleaved converters, for a duty cycle d, can be expressed as

$$C_{1(n)} = \Psi(n) \tag{3.2.3}$$

$$C_{2(n)} = -1^n \Psi(n), \tag{3.2.4}$$

where $\Psi(n)$ is the constant duty cycle exponential Fourier series coefficients, defined as:

$$\Psi(n) = \begin{cases} \frac{j}{2\pi n}\left(e^{-j2\pi nd} - 1\right) & \text{for } n \neq 0 \\ d & \text{for } n = 0 \end{cases} \tag{3.2.5}$$

A formal derivation of the Fourier series coefficients is included in Appendix A.6.1 on p.177.

The frequency ω_s in this case denotes the effective radian frequency at the output of the rectifier, or double the switching frequency of the switching elements.

Assuming that the cell bus capacitance is large enough, the harmonic content of the cell voltages can be neglected. It is furthermore assumed that, due to the large cell bus capacitance, even when the cell bus voltages change in time the rest of the converter is in the steady state. With reference to Fig. 3.3, the currents $I_t(\omega)$ and $I_d(\omega)$ can be found as

$$I_t(\omega) = \frac{1}{Z_t(\omega)}\left(V_t S_t(\omega) + V_d S_d(\omega)\right) \tag{3.2.6}$$

$$I_d(\omega) = \frac{1}{Z_l(\omega)}\left(V_t S_d(\omega) + V_d S_t(\omega)\right) \tag{3.2.7}$$

Where, with reference to the definitions in Fig. 3.3,

$$Z_l(\omega) = j\omega L + r \tag{3.2.8}$$

$$Z_c(\omega) = \frac{2R}{j2\omega C_f R + 1} \tag{3.2.9}$$

$$Z_s(\omega) = r_s + j\omega L_s \tag{3.2.10}$$

$$Z_t(\omega) = Z_l(\omega) + Z_c(\omega). \tag{3.2.11}$$

Let $I_{cd}(\omega)$ denote the current through the C_d capacitor, as shown in Fig. 3.3. An expression for $I_{cd}(\omega)$ can be found as

$$\begin{aligned} I_{cd}(\omega) &= I_\delta(\omega) + I_\tau(\omega) \\ &= S_t(\omega) * I_d(\omega) + S_d(\omega) * I_t(\omega), \end{aligned} \tag{3.2.12}$$

where $*$ denotes the convolution operator.

The average current, or the DC component in other words, can be found by evaluating (3.2.12) at $\omega = 0$. Substitution of (3.2.7) and (3.2.6) into (3.2.12) and rearranging yields, at $\omega = 0$

$$I_{cd} = AV_d + BV_t \tag{3.2.13}$$

where

$$A = \left(\frac{S_t(\omega)}{Z_l(\omega)} * S_t(\omega) + \frac{S_d(\omega)}{Z_t(\omega)} * S_d(\omega)\right)\Bigg|_{\omega=0} \tag{3.2.14}$$

and

$$B = \left(\frac{S_d(\omega)}{Z_l(\omega)} * S_t(\omega) + \frac{S_t(\omega)}{Z_t(\omega)} * S_d(\omega)\right)\Bigg|_{\omega=0}. \tag{3.2.15}$$

The assumption that the cell capacitors are sufficiently large to allow the voltage ripple at the switching frequency to be neglected does not imply that the cell

voltages cannot slowly vary over time. Equation (3.2.13) can be rewritten to allow for this slow variation over time as

$$-C\frac{d}{dt}v_d(t) = i_{cd}(t) = Av_d(t) + BV_t(t). \tag{3.2.16}$$

3.2.1 Convolution Properties

At $\omega = 0$ the convolution of two frequency domain signals, expressed in exponential Fourier series form, can be found as [49, p. 23]:

$$\Big(F(\omega) * G(\omega)\Big)\Big|_{\omega=0} = \sum_{\xi=-\infty}^{\infty} F_{(\xi)}G_{(-\xi)} \tag{3.2.17}$$

This convolution expression gives the average value of the time domain multiplication of two periodic signals evaluated over a complete period. A proof is included in Lemma 1 on p.160.

Investigation of (3.2.15) reveals that the B term depends on the convolution of $S_t(\omega)$ and the impedance modified $S_d(\omega)$. Substituting (3.1.2) and (3.2.3) into (3.2.17) and using the identity that $C^*_{(\xi)} = C_{(-\xi)}$ (since all switching functions are real valued) [50, p. 237] yields

$$\begin{aligned}
\frac{S_d(\omega)}{Z_l(\omega)} * S_t(\omega)\Big|_{\omega=0} &= \sum_{\xi=-\infty}^{\infty} \frac{C_{1(-\xi)} - C_{2(-\xi)}}{4Z_l(\xi\omega_s)}\Big(C_{1(\xi)} + C_{2(\xi)}\Big) \\
&= \sum_{\xi=-\infty}^{\infty} \frac{\Psi(\xi) - (-1)^{\xi}\Psi(\xi)}{4Z_l(\xi\omega_s)}\Big(\Psi(-\xi) + (-1)^{-\xi}\Psi(-\xi)\Big) \\
&= \sum_{\xi=-\infty}^{\infty} \frac{\Psi(\xi)\left(1 - (-1)^{\xi}\right)}{4Z_l(\xi\omega_s)}\Psi(-\xi)\Big(1 + (-1)^{-\xi}\Big) \\
&= \sum_{\xi=-\infty}^{\infty} \frac{|\Psi(\xi)|^2}{4Z_l(\xi\omega_s)}\Big(1 - (-1)^{\xi}\Big)\Big(1 + (-1)^{-\xi}\Big) \\
&= \sum_{\xi=-\infty}^{\infty} \frac{|\Psi(\xi)|^2}{4Z_l(\xi\omega_s)}0 = 0.
\end{aligned} \tag{3.2.18}$$

This result is repeated in the list of Lemmas as Lemma 15 on p.172.

The same methodology can be used to derive an expression for the convolution

of S_d with itself:

$$\begin{aligned}
\left.\frac{S_d(\omega)}{Z_t(\omega)} * S_d(\omega)\right|_{\omega=0} &= \sum_{\xi=-\infty}^{\infty} \frac{C_{1(\xi)} - C_{2(\xi)}}{4Z_t(\xi\omega_s)} \left(C_{1(-\xi)} - C_{2(-\xi)}\right) \\
&= \sum_{\xi=-\infty}^{\infty} \frac{\Psi(\xi) - (-1)^{\xi}\Psi(\xi)}{4Z_t(\xi\omega_s)} \left(\Psi(-\xi) - (-1)^{\xi}\Psi(-\xi)\right) \\
&= \sum_{\xi=-\infty}^{\infty} \frac{\Psi(\xi)\left(1 - (-1)^{\xi}\right)}{4Z_t(\xi\omega_s)} \Psi(-\xi) \left(1 - (-1)^{-\xi}\right) \\
&= \sum_{\xi=-\infty}^{\infty} \frac{|\Psi(\xi)|^2}{4Z_t(\xi\omega_s)} \left(1 - (-1)^{\xi}\right)^2 \\
&= \sum_{\xi=-\infty}^{\infty} \frac{|\Psi(\xi)|^2}{2Z_t(\xi\omega_s)} \left(1 - (-1)^{\xi}\right) \qquad (3.2.19)
\end{aligned}$$

The sum can be simplified by adding the positive and negative parts of the sum together. The term $1 - (-1)^{\xi} = 0$ for all even values of ξ:

$$\begin{aligned}
\left.\frac{S_d(\omega)}{Z_t(\omega)} * S_d(\omega)\right|_{\omega=0} &= \sum_{\xi=1,3,5}^{\infty} \left(\frac{|\Psi(\xi)|^2}{Z_t(\xi\omega_s)} + \frac{|\Psi(-\xi)|^2}{Z_t(-\xi\omega_s)}\right) \\
&= \sum_{\xi=1,3,5}^{\infty} \frac{|\Psi(\xi)|^2 Z_t(-\xi\omega_s) + |\Psi(\xi)|^2 Z_t(\xi\omega_s)}{|Z_t(\xi\omega_s)|^2} \\
&= 2\sum_{\xi=1,3,5}^{\infty} \frac{|\Psi(\xi)|^2}{|Z_t(\xi\omega_s)|^2} \mathrm{Re}\{Z_t(\xi\omega_s)\} \qquad (3.2.20)
\end{aligned}$$

This result is repeated in the list of Lemmas as Lemma 16 on p.173.

For the convolution of S_t with itself:

$$\begin{aligned}
\left.\frac{S_t(\omega)}{Z_l(\omega)} * S_t(\omega)\right|_{\omega=0} &= \sum_{\xi=-\infty}^{\infty} \frac{C_{1(\xi)} + C_{2(\xi)}}{4Z_l(\xi\omega_s)} \left(C_{1(-\xi)} + C_{2(-\xi)}\right) \\
&= \sum_{\xi=-\infty}^{\infty} \frac{\Psi(\xi) + (-1)^{\xi}\Psi(\xi)}{4Z_l(\xi\omega_s)} \left(\Psi(-\xi) + (-1)^{\xi}\Psi(-\xi)\right) \\
&= \sum_{\xi=-\infty}^{\infty} \frac{|\Psi(\xi)|^2}{4Z_l(\xi\omega_s)} \left(1 + (-1)^{\xi}\right)^2 \\
&= \sum_{\xi=-\infty}^{\infty} \frac{|\Psi(\xi)|^2}{2Z_l(\xi\omega_s)} \left(1 + (-1)^{\xi}\right) \\
&= \frac{\Psi(0)^2}{Z_l(0)} + \sum_{\xi=2,4,6}^{\infty} \left(\frac{|\Psi(\xi)|^2}{Z_l(\xi\omega_s)} + \frac{|\Psi(-\xi)|^2}{Z_l(-\xi\omega_s)}\right) \\
&= \frac{d^2}{Z_l(0)} + \sum_{\xi=2,4,6}^{\infty} \frac{|\Psi(\xi)|^2 Z_l(-\xi\omega_s) + |\Psi(\xi)|^2 Z_l(\xi\omega_s)}{|Z_l(\xi\omega_s)|^2} \\
&= \frac{d^2}{Z_l(0)} + 2\sum_{\xi=2,4,6}^{\infty} \frac{|\Psi(\xi)|^2}{|Z_l(\xi\omega_s)|^2} \mathrm{Re}\{Z_l(\xi\omega_s)\} \qquad (3.2.21)
\end{aligned}$$

This result is repeated in the list of Lemmas as Lemma 17 on p.173.

Substitution of these results into (3.2.14) and (3.2.15) yields:

$$A = \frac{d^2}{Z_l(0)} + 2\sum_{\xi=2,4,6}^{\infty} \frac{|\Psi(\xi)|^2}{|Z_l(\xi\omega_s)|^2}\mathrm{Re}\{Z_l(\xi\omega_s)\} + 2\sum_{\xi=1,3,5}^{\infty} \frac{|\Psi(\xi)|^2}{|Z_t(\xi\omega_s)|^2}\mathrm{Re}\{Z_t(\xi\omega_s)\} \tag{3.2.22}$$

$$B = 0 \tag{3.2.23}$$

3.2.2 Contribution of Harmonic Content

The convolution operation is evaluated at $\omega = 0$ through summation over all frequencies. Investigation of (3.2.5) shows that the magnitude in the harmonics of the switching functions decreases with increasing frequency. The filter elements in the circuit, especially the large bus capacitors, will further act to suppress the harmonic content at the switching frequency and higher.

In general the filter capacitor C_f is large. Therefore at the switching frequency and higher $\mathrm{Re}\{Z_c\} \approx 0$. In most systems it is possible to approximate $Z_t(\omega)$ at the frequencies of interest as:

$$Z_t(\omega) \approx Z_l(\omega) \text{ for } \omega \geq \omega_s \tag{3.2.24}$$

Substitution of this approximation into (3.2.22) yields

$$A = \frac{d^2}{Z_l(0)} + 2\sum_{\xi=1}^{\infty} \frac{|\Psi(\xi)|^2}{|Z_l(\xi\omega_s)|^2}\mathrm{Re}\{Z_l(\xi\omega_s)\}. \tag{3.2.25}$$

At $\omega = 0$ it is true that $Z_l = r$. With the assumption that the inductor is manufactured with Litz wire and a winding structure such that the skin and proximity effects are negligible, at $\omega \geq \omega_s$

$$Re\{Z_l(\omega)\} \approx r \tag{3.2.26}$$

$$|Z_l(\omega)| \approx \omega L. \tag{3.2.27}$$

Therefore, with substitution of (3.2.5):

$$A = \frac{d^2}{r} + \sum_{\xi=1}^{\infty} \frac{|e^{-j2\pi\xi d} - 1|^2 r}{2\xi^4\pi^4 f_s^2 L^2} \tag{3.2.28}$$

Using the relation that $\left|e^{-j2\pi nd} - 1\right| \leq 2$, the contribution of the harmonic content can be estimated as:

$$\begin{aligned}
\sum_{\xi=1}^{\infty} \frac{|e^{-j2\pi\xi d} - 1|^2 r}{2\xi^4\pi^4 f_s^2 L^2} &< \sum_{\xi=1}^{\infty} \frac{2r}{\xi^4\pi^4 f_s^2 L^2} \\
&< \frac{2r}{\pi^4 f_s^2 L^2} \sum_{\xi=1}^{\infty} \frac{1}{\xi^4} \\
&< \frac{2r}{\pi^4 f_s^2 L^2} \zeta_R(4) \\
&< 0.0222 \frac{r}{f_s^2 L^2}
\end{aligned} \tag{3.2.29}$$

Where ζ_R is the Riemann zeta function [51, p.1]. $\zeta_R(4) = 1.0823$. Under most conditions it is true that:

$$\frac{d^2}{r} \ggg 0.0222\frac{r}{f_s^2 L^2} \tag{3.2.30}$$

and therefore

$$A \approx \frac{d^2}{r}. \tag{3.2.31}$$

Using this approximation A is independent on the interleaving between the different cells. However, the right-hand side of (3.2.30) depends on the interleaving, as will be shown later in this study, and this determines the weak rebalancing mechanism. The balancing process in the ISOP is dominated by the strong mechanism to such an extent that the effects of the weak mechanism can safely be ignored.

Under some conditions, especially at very low values of d, (3.2.30) might not hold. Under these conditions the weak balancing mechanism will have a noticeable influence, this is investigated further in Section 3.4.3.

3.3 Balancing of Similar Cells

A 2-cell ISOP is balanced when the input voltage and output currents of the two cells are equal. In other words, both v_d and i_d must be zero. Substituting (3.2.31) into (3.2.16) yields:

$$-C\frac{d}{dt}v_d(t) = \frac{d^2}{r}v_d(t) \tag{3.3.1}$$

It is clear that any unbalance in the voltage v_d will be dissipated since the pole of the equation is always in the left-hand half of the complex plane.

With reference to Fig. 3.3 the currents i_δ and i_τ can be defined as, with incorporation of (3.2.18):

$$I_\delta(\omega) = V_d\frac{S_t(\omega)}{Z_l(\omega)} * S_t(\omega) \tag{3.3.2}$$

$$I_\tau(\omega) = V_d\frac{S_d(\omega)}{Z_t(\omega)} * S_d(\omega) \tag{3.3.3}$$

Using the results from Section 3.2.2, it follows that

$$I_\delta \gg I_\tau. \tag{3.3.4}$$

Rewriting (3.3.2) using only the DC coupling, when $\omega \to 0$, yields:

$$I_\delta(\omega) = \frac{d^2 V_d(\omega)}{Z_l(\omega)} \tag{3.3.5}$$

When $\omega = 0$ it follows that $Z_l(0) = r$. However, during transient response the system states vary over time, therefore an assumption that $\omega = 0$ would be an over simplification. It is however true that the frequencies of interest during the rebalancing process are orders of magnitude smaller than the switching frequency and thus the interactions between them can safely be ignored.

An equivalent circuit describing the rebalancing process can be constructed by using the presented theory. The results of the preceding discussion can be summarised as:

$$\frac{d}{dt}v_d(t) = -\frac{1}{C}i_\delta(t) \tag{3.3.6}$$

$$I_\delta(\omega) = \frac{d^2 V_d(\omega)}{r + j\omega L} \tag{3.3.7}$$

The d^2 term represents the referral of the impedance from the secondary side of the converter to the primary side. Using an ideal transformer the equivalent rebalancing circuit in Fig. 3.5 is constructed.

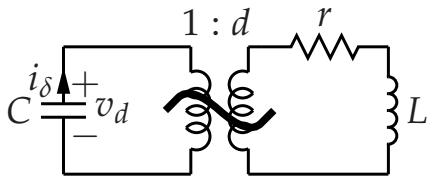

Figure 3.5: Equivalent rebalancing circuit

The balancing process can thus be expressed as:

$$0 = L'\frac{di}{dt} + r'i + \frac{1}{C}\int_0^t i d\tau \tag{3.3.8}$$

where

$$L' = \frac{L}{d^2}\ ,\ r' = \frac{r}{d^2} \tag{3.3.9}$$

$$i(0) = dI_d(0)\ ,\ v(0) = v_d(0) \tag{3.3.10}$$

The homogeneous equation can be expressed by using the Laplace transform as

$$L's^2 + r's + \frac{1}{C} = 0, \tag{3.3.11}$$

with roots

$$s_1 = -\frac{r'}{2L'} + \sqrt{\left(\frac{r'}{2L'}\right)^2 - \frac{1}{L'C}} \tag{3.3.12}$$

$$s_1 = -\frac{r'}{2L'} - \sqrt{\left(\frac{r'}{2L'}\right)^2 - \frac{1}{L'C}}. \tag{3.3.13}$$

In general the bus capacitance is large, but normally

$$C < \frac{4d^2 L}{r^2}, \tag{3.3.14}$$

Table 3.2: Circuit values used for the ISOP simulations

Item	Value	
Sec. Filter Inductor	L	1 mH
Lumped Sec. Resistance	r	0.5 Ω
Bus Capacitors	C	500 μF
Output Capacitor	C_f	4 700 μF
Load resistance	R	300 Ω
Input Inductor	L_s	50 nH
Input Resistance	r_s	0.2 Ω
Total Voltage	V_t	1 600 V
Switching frequency	$\frac{\omega_c}{2\pi}$	25 kHz
Duty cycle	d	80 %

implying that the system will be underdamped. Therefore

$$Re\{s_1\} = Re\{s_2\} = -\frac{r}{2L}. \tag{3.3.15}$$

It follows that, for ISOP circuits where (3.3.14) holds, the rebalancing time constant is found as

$$\tau = \frac{2L}{r}. \tag{3.3.16}$$

3.4 Results

The theory presented is validated and investigated further through comparison with a simulation. The simulation script, listed in Appendix C, is written in Python and makes use of the `scipy.integrate.odeint` function. The odeint function in turn makes use of the LSODA function in the ODEPACK collection of solvers that was written in FORTRAN 77 by Alan Hindmarsh and Linda Petzhold of Lawrence Livermore National Labs. It is a very robust adaptive step-size solver that automatically switches to a BDF (backward differential formula) multi-step method if the system is deemed stiff [52].

Unless stated differently, the circuit values tabulated in Table 3.2 are used in the following discussion.

3.4.1 Time Constant

The circuit of Fig. 3.1 is simulated with the indicated component values. The system is allowed to reach steady state before unbalance of 200 V in the cell voltages v_1 and v_2 is introduced. The approximation boundary (3.3.14) evaluates to

$$C = 500\ \mu\text{F} < 10.24\ \text{mF}, \tag{3.4.1}$$

therefore the approximation (3.3.16) holds. The result is indicated in Fig. 3.6.

The rebalancing is very rapid especially considering that 200 V unbalance represents an unbalance energy of 10 J. The time constant, from (3.3.16), is 4 ms. The removal of 67% of the unbalance energy within τ s represents a 1 675 W power

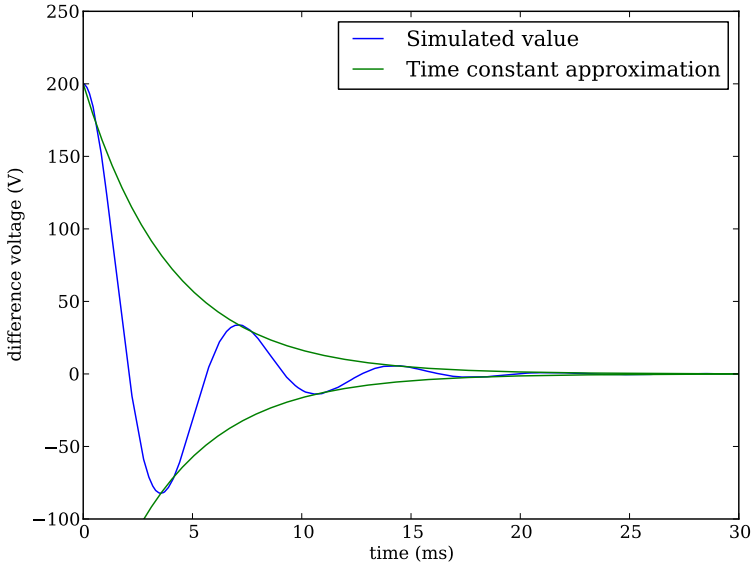

Figure 3.6: Difference voltage following perturbation

flow from C_d resulting in very large rebalancing currents. The currents i_1 and i_2 corresponding to Fig. 3.6 are shown in Fig. 3.7.

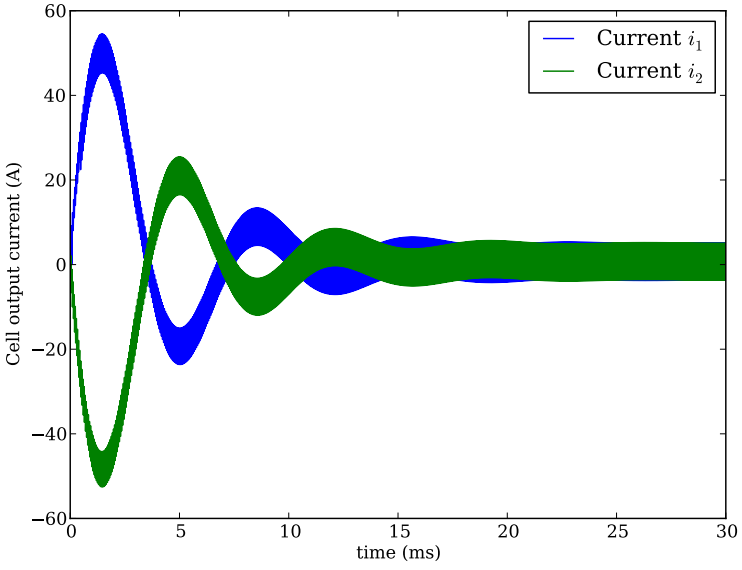

Figure 3.7: Cell currents following perturbation

It is interesting to note that all the unbalance energy is dissipated in the resistance r. Fig. 3.8 shows that the total energy dissipated in r at $t = 15$ ms is around

10 J, which is equal to the initial unbalance energy. The slight increase in dissipated energy after rebalancing is due to the ripple current.

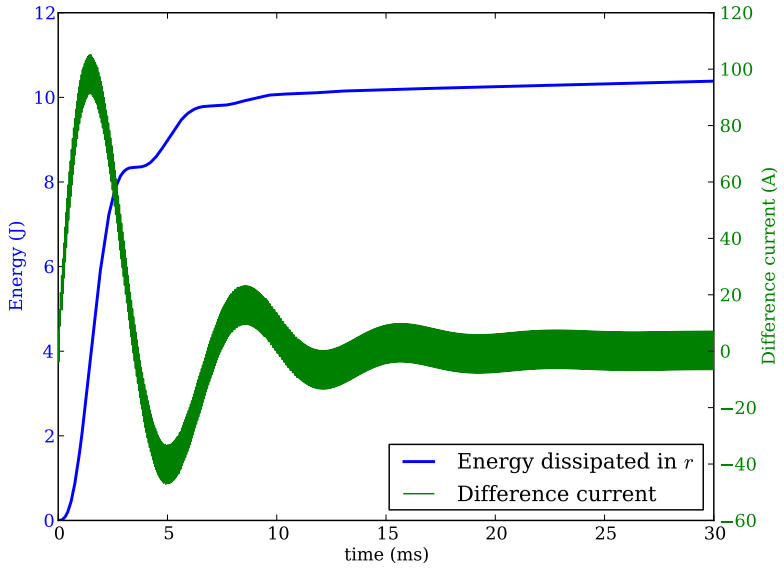

Figure 3.8: Energy dissipated in r and the difference current during rebalancing

3.4.2 Existence of the Circulating Current

The strong rebalancing mechanism results in very quick rebalancing of the circuit. Under most circumstances, this would be desirable, as it ensures balance between the cells. However, under certain circumstances the large rebalancing current can lead to system failure if the unbalance persists. This is similar to connecting two power transformers in parallel in the presence of conversion ratio mismatches. In Fig. 3.9 the system is allowed to reach steady state before a 200 V unbalance is introduced at 50 ms. The unbalance is forced by modelling the capacitors C_1 and C_2 as batteries. It is clear that the unbalance circulating current is many times larger than the operating current of the converter cells.

According to the equivalent circuit in d and t parameters (see Fig 3.3), the unbalanced current is isolated from the load. Therefore, the load voltage is invariant of the existence of circulating currents. The output voltage v_o corresponding to Fig 3.9 is shown in Fig. 3.10 and confirms this result.

3.4.3 The Weak Balancing Mechanism in the ISOP Converter

Although the strong balancing mechanism dominates, the interaction of the harmonics (i.e. the weak balancing mechanism) does theoretically play a role. Using

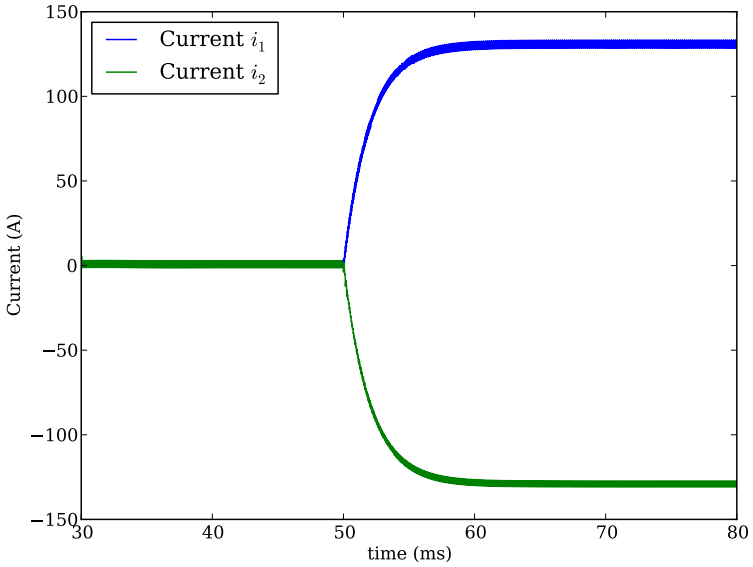

Figure 3.9: Circulating current in the ISOP should the unbalance persist

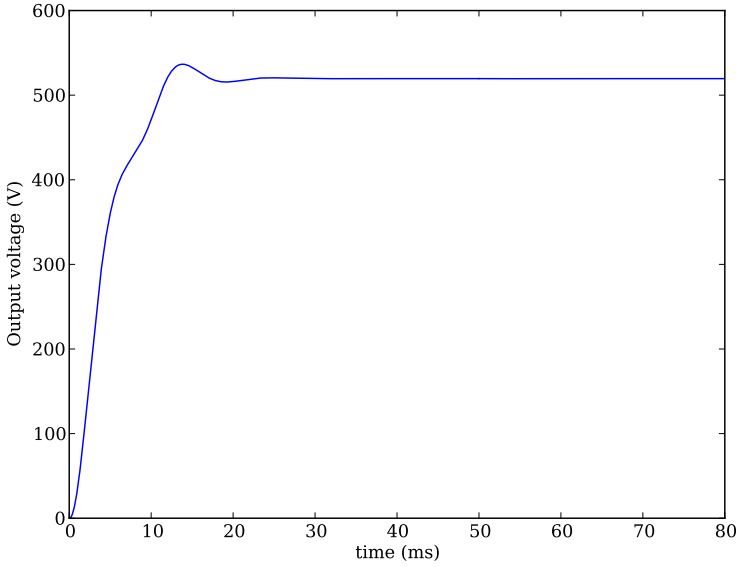

Figure 3.10: Output voltage invariance to circulating current

(3.2.30) as basis, the strengths of the mechanisms can be estimated as:

$$\text{Strong Balancing} \propto \frac{d^2}{r} \tag{3.4.2}$$

$$\text{Weak Balancing} \propto \frac{r}{f_s^2 L^2} \tag{3.4.3}$$

If the respective estimated strengths are expressed as a ratio:

$$\frac{\text{Weak Balancing}}{\text{Strong Balancing}} \propto \frac{r^2}{d^2 f_s^2 L^2} \tag{3.4.4}$$

With the circuit values used the right-hand side of the equation evaluates to 0.00016. In Fig. 3.11, the circuit is simulated both with interleaved switching and ordinary or non-interleaved switching. If the weak balancing mechanism plays any significant role, the rebalancing using interleaved switching should be faster than with ordinary switching. However, the only noticeable difference is a pronounced voltage ripple with ordinary switching. It is clear that the weak balancing mechanism has very little influence on the rebalancing process.

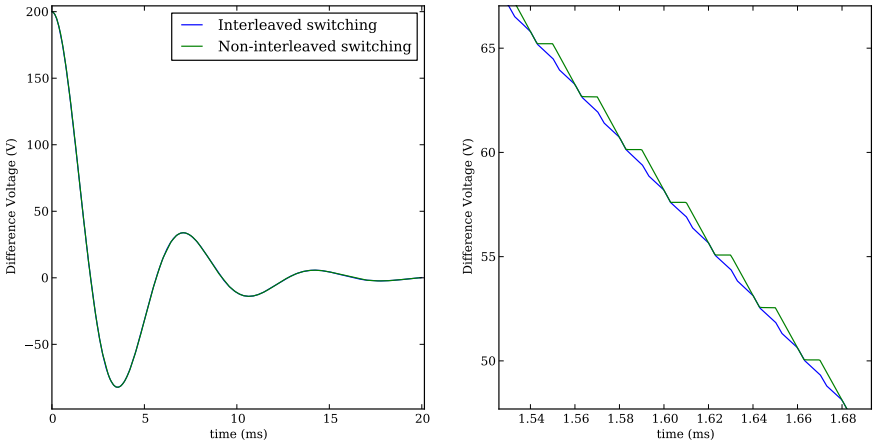

Figure 3.11: Comparison of the strong and weak mechanisms in the ISOP

From (3.4.4) it can be seen that the relative strength of the weak balancing mechanism depends on the magnitude of the current ripple. If the circuit parameters are changed to a hypothetical scenario where the current ripple is very large, the relative strength of the weak balancing mechanism will increase. Using $f_s = 10$ kHz, $L = 100$ μH and $d = 10$ %, the right-hand side of (3.4.4) evaluates to 6.25. Theoretically, the weak balancing mechanism should be 40 000 times stronger relative to the strong balancing mechanism than would be the case with the original circuit values. The result is shown in Fig 3.12. However, although the converter is operating with a current ripple of 2 700 %, the weak balancing mechanism is still negligible.

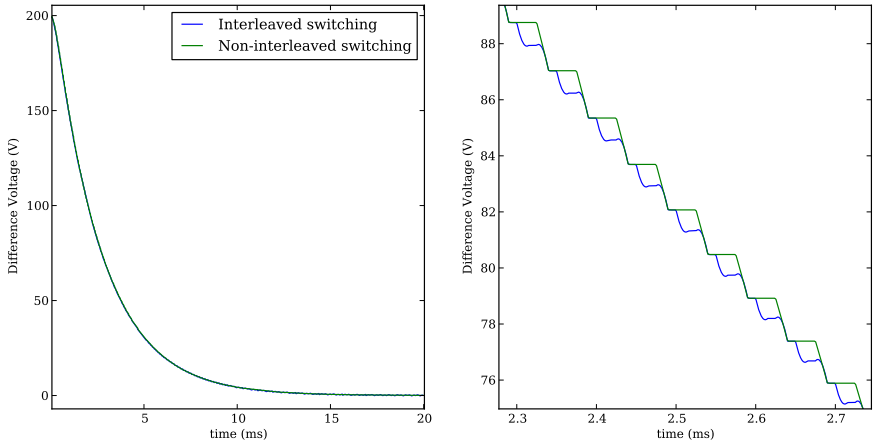

Figure 3.12: Comparison of the strong and weak mechanisms in the ISOP cont.

3.4.4 Weak Balancing in ISOP Converters Used in Series Stacked Power Conditioners

The natural balancing mechanisms of the ISOP as used in series stacked power conditioners was studied in [33]. An equivalent d and t parameter circuit similar to Fig. 3.3 was used to analyse the balancing.

The main differences between the circuit used in [33] and the DC-DC ISOP converter used here are:

1. The cells are operational with sinusoidal modulation.
2. The switching frequency is low, $f_s = 1\,000$ Hz.
3. The filters are dimensioned for high power applications. The fundamental component of the load is 50 Hz and therefore influences the filter realisation.

In contrast to the results of the investigation of the DC-DC ISOP, as discussed in the previous Section, the study of the modulated duty cycle ISOP [33] concluded that, although the strong balancing mechanism dominates the weak mechanism does have a measurable influence. The difference in results between the two studies can be attributed to the following:

1. When the modulated duty cycle is used, the lowest harmonic of the switching function occurs at the reference frequency [5]. A complete discussion of the harmonics of modulated duty cycle is included in Chapter 4. With reference to Fig. 3.3, the magnitude of i_δ is limited by $\frac{1}{r+j2\pi 50L}$ and not $\frac{1}{r}$ as in the DC case.
2. The lower switching frequency implies that the first effective switching frequency occurs at 2 000 Hz. It was shown in (3.4.4) that the strength of the weak balancing mechanism is inversely proportional to f_s.

3. The dimensioning of the filter components, in [33] $\omega_s L = 1.88\ \Omega$, while the DC-DC converter yields $\omega_s L = 157\ \Omega$.

3.5 Balancing of Non-Similar Cells

It was proven that a converter consisting of 2 similar cells would balance both the input voltage and the output current between the two modular converters, with each taking half. In [31] it had been stated, although not rigorously proven, that two non-similar cells in an ISOP configuration would still balance the voltage and current, although they would do so in a ratio that reflects the effective duty cycle.

In general, the variations between the cells can be attributed to three degrees of variance: transformer turns ratio, duty cycle and variations in component values. Furthermore, slight mismatches in component values are generally expected, while duty cycle and turns ratio mismatches are less frequent. However, in keeping with the cell mismatch criteria used in [31], mismatch in either duty cycle or transformer turns ratio will be used here.

From the definition of the switching functions and the derivation of the equivalent circuit it could be shown that for cell 1 with a transformer turns ratio of a_1 and a duty cycle d_1

$$C_{1(0)} = \delta_1 \text{ where } \delta_1 = a_1 d_1 \tag{3.5.1}$$

and similarly for cell 2.

Using the circuit of Fig. 3.3, the same methodology can be followed as for similar cells. Using (3.2.13), repeated for convenience

$$I_{cd} = AV_d + BV_t,$$

and (3.2.14) and (3.2.15) and ignoring the contribution of the harmonic content, it can be shown that:

$$V_d \frac{\delta_1^2 + \delta_2^2 + 2\delta_1\delta_2}{4r} = -V_t \frac{\delta_1^2 - \delta_2^2}{4r} \tag{3.5.2}$$

$$V_d = -V_t \frac{\delta_1^2 - \delta_2^2}{\delta_1^2 + \delta_2^2 + 2\delta_1\delta_2} = -V_t \frac{\delta_d}{\delta_t} \tag{3.5.3}$$

where

$$\delta_d = \delta_1 - \delta_2,\ \delta_t = \delta_1 + \delta_2. \tag{3.5.4}$$

It can be seen that the cell voltages will reflect the mismatch in the converters. However, the converters will share the total output current, since from (3.2.7)

$$\begin{aligned} I_d(\omega)|_{\omega=0} &= \frac{\delta_d V_t + \delta_t V_d}{2r} \\ &= \frac{\delta_d V_t - \delta_t \frac{\delta_d}{\delta_t} V_t}{2r} = 0. \end{aligned} \tag{3.5.5}$$

3.5.1 Rebalancing Mechanism of Non-Similar Cells

Having established that the cell voltages will be balanced in steady state the circuit response to an external perturbation can be investigated.

Let $I_\tau(\omega)$ and $I_\delta(\omega)$ be the reflected currents of $I_t(\omega)$ and $I_d(\omega)$ as indicated in Fig. 3.3. The currents can be expressed as:

$$I_\tau(\omega) = \left(\frac{V_t S_t(\omega) + V_d S_d(\omega)}{Z_t(\omega)} \right) * S_d(\omega) \tag{3.5.6}$$

$$I_\delta(\omega) = \left(\frac{V_t S_d(\omega) + V_d S_t(\omega)}{Z_l(\omega)} \right) * S_t(\omega) \tag{3.5.7}$$

As discussed in the previous section the source V_t determines the final value, or steady state value, of the cell voltages but plays no part in the rebalancing process. Using the results of the previous sections the expressions can be rewritten as:

$$I_\tau(\omega)|_{\omega=0} = -V_d \frac{\delta_1^2 + \delta_2^2 - 2\delta_1\delta_2}{2R + r} \tag{3.5.8}$$

$$I_\delta(\omega)|_{\omega=0} = -V_d \frac{\delta_1^2 + \delta_2^2 + 2\delta_1\delta_2}{r} \tag{3.5.9}$$

$$= -V_d \frac{\delta_t^2}{r} \tag{3.5.10}$$

Since $R \gg r$ and $\delta_1^2 + \delta_2^2 - 2\delta_1\delta_2 < \delta_1^2 + \delta_2^2 + 2\delta_1\delta_2$ it is clear that $I_\delta \gg I_\tau$.

With reference to Fig. 3.3, the balancing process via the i_d sub-circuit of the converter is governed by a RLC circuit described by C, L and r. By using of time averaging, the rebalancing equivalent circuit can be created (see Fig. 3.13). The balancing process can be expressed as:

$$0 = L' \frac{di}{dt} + r' i + \frac{1}{C} \int_0^t i d\tau \tag{3.5.11}$$

where

$$L' = \frac{L}{\delta_t^2}\ ,\ r' = \frac{r}{\delta_t^2} \tag{3.5.12}$$

$$i(0) = \delta_t I_d(0)\ ,\ v(0) = v_d(0) \tag{3.5.13}$$

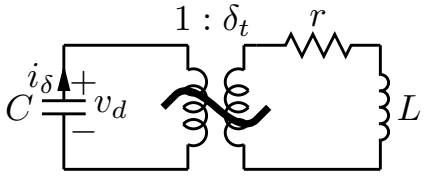

Figure 3.13: Equivalent rebalancing circuit

The second order ordinary differential equation (ODE), with the indicated boundary conditions, that describes the rebalancing RLC circuit can be analysed analytically.

3.5.2 Results

The theory presented was tested by comparing the predicted results with the results of a detailed simulation. The parameter values used in the simulation are summarised in Table 3.3. Initially the two cells were operating at the same duty cycle, but at $t = 2$ ms the duty cycles of cell 1 and cell 2 were changed to 75% and 85% respectively. According to the theory presented, the cell voltages will reflect this mismatch and the steady state difference voltage should be

$$V_d = \frac{\delta_d}{\delta_t} V_t = \frac{0.05}{0.8} 2000 = 125\ V. \tag{3.5.14}$$

However, the output currents will remain balanced in the steady state despite the mismatch.

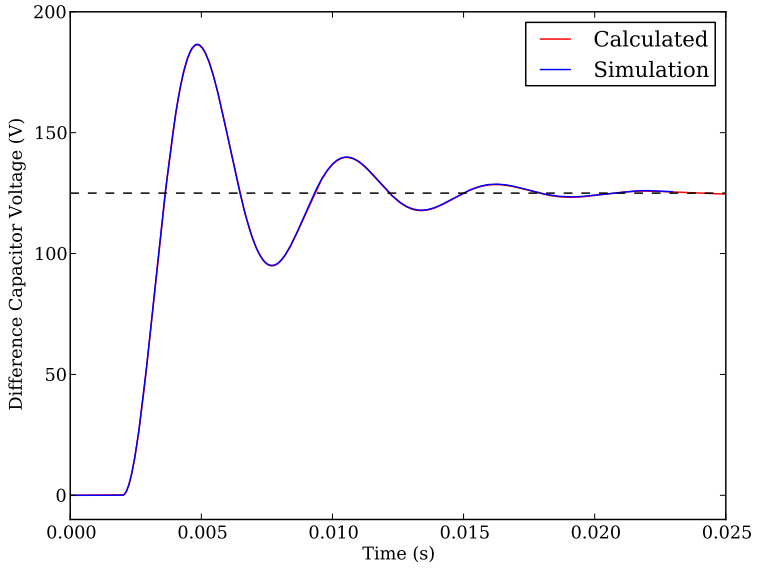

Figure 3.14: Voltage v_d after introduction of converter mismatch

Fig. 3.14 compares the v_d voltage during rebalancing found through detailed simulation to the solution found to the ODE described in (3.5.11) - (3.5.13) with an external 125 V source. It is clear that the difference voltage stabilises at the predicted 125 V level. The corresponding waveforms of the difference current (i_d) are shown in Fig. 3.15. The output current sharing is clear.

The cell voltages and the output currents, as defined in Fig. 3.1, are shown in Fig. 3.16. The output currents in steady state are equal, since the input voltage corresponding to the cell with the high duty cycle (v_2 in this case) is lower than v_1.

Table 3.3: Circuit values used

Item	Value	
Sec. Filter Inductor	L	1 mH
Lumped Sec. Resistance	r	0.5 Ω
Bus Capacitors	C	500 μF
Input Inductor	L_s	50 nH
Input Resistance	r_s	0.2 Ω
Total Voltage	V_t	2 000 V
Switching frequency	$\frac{\omega_c}{2\pi}$	50 kHz
Initial duty cycle	d_1,d_2	80 %
Duty cycle 1, $t > 2$ ms	d_1	75 %
Duty cycle 2, $t >$ 2 ms	d_2	85 %

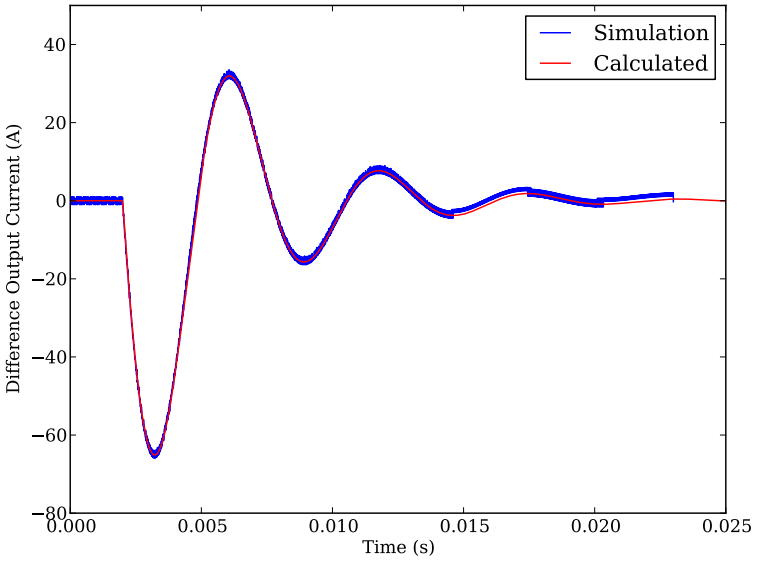

Figure 3.15: Current i_d after introduction of converter mismatch

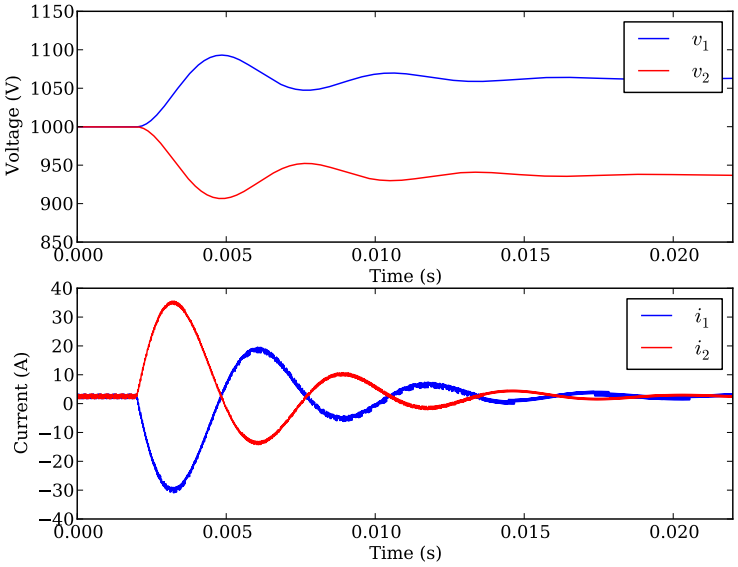

Figure 3.16: Voltages v_1 and v_2 and currents i_1 and i_2 after introduction of converter mismatch

3.6 Analysis Using a Circuit Averaging Technique

The strong rebalancing mechanism is fairly well known, since it is possible to identify its existence by using an averaging technique. The time averaged 2-cell ISOP circuit using the average switch method [47, Chapter 7.4] is shown in Fig. 3.17.

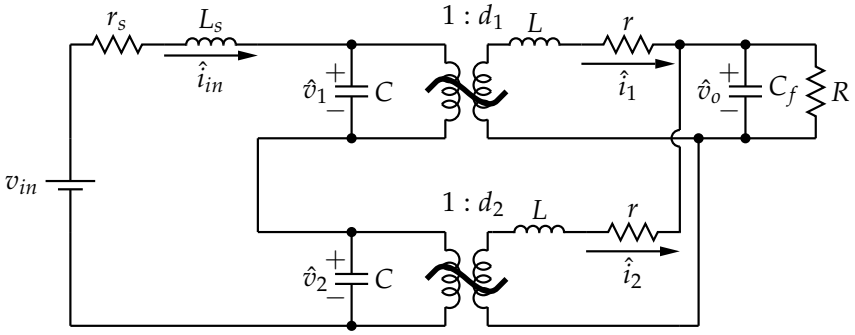

Figure 3.17: 2-Cell time averaged ISOP circuit

Assuming that $d_1 = d_2 = d$ the following is true, where $\hat{i}_1$ is the time averaged value of i_1, or alternately stated the average value of i_1 within one switching cycle,

i.e. neglecting the effect of the switching ripple components:

$$\hat{i}_1 = \frac{d\hat{v}_1 - \hat{v}_o}{r} \tag{3.6.1}$$

$$\hat{i}_2 = \frac{d\hat{v}_2 - \hat{v}_o}{r} \tag{3.6.2}$$

$$C\frac{d\hat{v}_1}{dt} = \hat{i}_{in} - \frac{\hat{i}_1}{d} \tag{3.6.3}$$

$$C\frac{d\hat{v}_2}{dt} = \hat{i}_{in} - \frac{\hat{i}_2}{d} \tag{3.6.4}$$

It is clear that should $\hat{v}_1 > \hat{v}_2$ then

$$\hat{i}_1 > \hat{i}_2 \Rightarrow \frac{d\hat{v}_1}{dt} < 0 \text{ and } \frac{d\hat{v}_2}{dt} > 0. \tag{3.6.5}$$

From this it is clear that the system would naturally balance. Rewriting the equations describing the circuit operation in terms of d and t parameters, it is possible to arrive at the circuit structure of Fig. 3.3, albeit with time averaged values.

3.7 ISOP with Passive Rectifiers

When the ISOP operates with passive rectification the operation of the diode rectifier limits the magnitude of the i_d current. With reference to Fig. 3.18, the rectifier diodes prevents negative currents, therefore

$$i_1 \geq 0 \text{ and } i_2 \geq 0. \tag{3.7.1}$$

If the currents are positive it is true that

$$\begin{aligned} |i_1 - i_2| &\leq i_1 + i_2 \\ |i_d| &\leq i_t. \end{aligned} \tag{3.7.2}$$

The fast rebalancing times typical to the strong rebalancing mechanism is due to a large i_d current. However, even though the diodes limit the magnitude of the i_d current, the strong balancing mechanism is still present.

Although it is theoretically possible to analyse the circuit behaviour in the frequency domain, the presence of discontinuous conduction mode (DCM) complicates this approach. DCM alters the effective duty cycle and the phase displacement of the switching functions. Since the ISOP circuit balancing process can also be identified and described by using time averaging techniques, this simpler method is used.

To aid this discussion, measurements from an experimental setup are presented. Two cells with the parameters indicated in Table 3.4 were forced into unbalance through manipulation of the duty cycles, as indicated. Fig. 3.19 shows that the voltages rebalance as soon as the two duty cycles are equal.

It is immediately obvious that the circuit of Fig. 3.3 is not directly applicable, as the equivalent circuit does not make allowance for the effects of (3.7.2). The circuit also suggests that i_{in} is invariant to changes in v_d since it was proven in Section 3.2.1

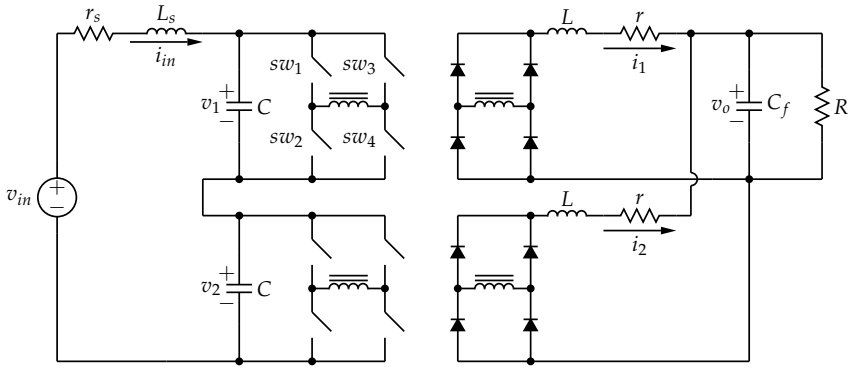

Figure 3.18: 2-Cell ISOP converter with passive rectifiers

Table 3.4: Circuit values used in experiment

Item	Value	
Sec. Filter Inductor	L	4 mH
Lumped Sec. Resistance, $f \geq f_s$	r	14 Ω
Bus Capacitors	C	50 μF
Output Filter Capacitor	C_f	1 600 μF
Load Resistor	R	193 Ω
Total Voltage	V_t	508 V
Switching frequency	$\frac{\omega_c}{2\pi}$	25 kHz
Steady state duty cycle	d_1,d_2	80 %
Modified duty cycle 1, $t <$ 0 s	d_1	74 %
Modified duty cycle 2, $t <$ 0 s	d_2	86 %

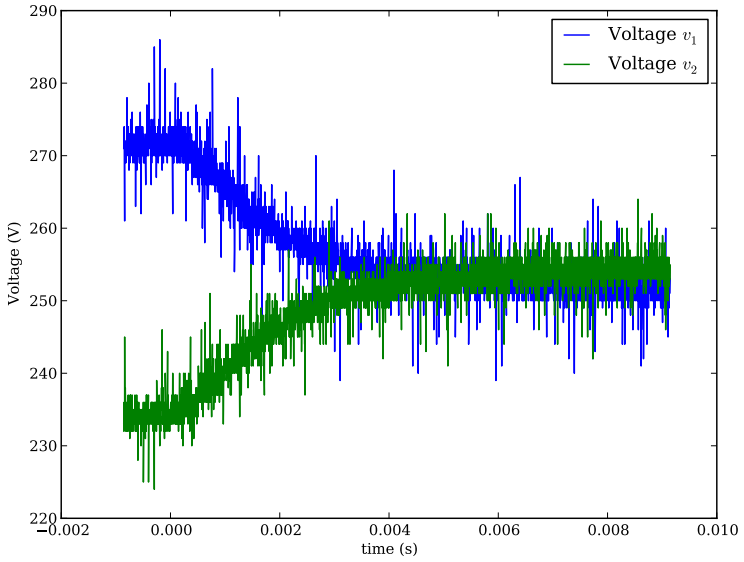

Figure 3.19: Voltage rebalancing of the ISOP with passive rectifiers

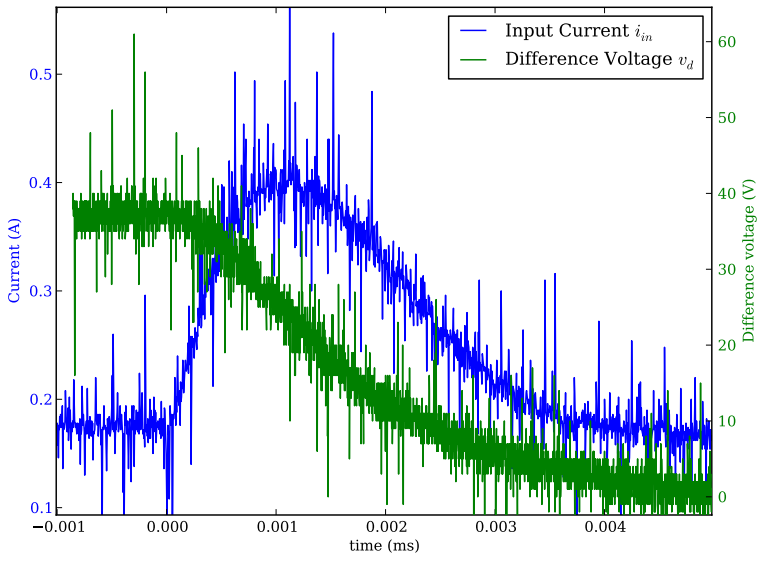

Figure 3.20: Input current and difference voltage during rebalancing of the ISOP with passive rectifiers

that the DC component of the convolution of S_t and S_d is always zero. However in Fig. 3.20, it can be seen that the input current changes as the system rebalances. This suggests that the system rebalances through a different mechanism.

As shown in Section 3.4.1 and Fig. 3.8, the unbalance energy is dissipated in the parasitic resistance when active rectification is used. The output voltage of the system with passive rectifiers during rebalancing is shown in Fig. 3.21. For the sake of clarity, the signal was filtered with a zero phase (forwards and backwards) 3^{rd} order Butterworth filter with a cut-off frequency at 12 500 Hz. It can be seen that the output voltage changes and some extra energy is dissipated in R. The extra energy stored in C_f can be found as

$$\begin{aligned}\Delta E &= \frac{1}{2}C_f\left(126.52^2 - 125.35^2\right) \\ &= 0.243\,\text{J} \gg \frac{1}{2}Cv_d(0)^2 = 0.034\,\text{J}.\end{aligned} \tag{3.7.3}$$

This is more than the initial unbalance energy! It follows that the majority of the unbalance energy is dissipated in the load. Clearly, the rebalancing mechanism differs from that of active rectification.

Ignoring the effect of the source inductance and resistance it follows that

$$C\frac{dv_1}{dt} = -C\frac{dv_2}{dt}. \tag{3.7.4}$$

If α is defined as the product of the effective duty cycle and the transformer turns

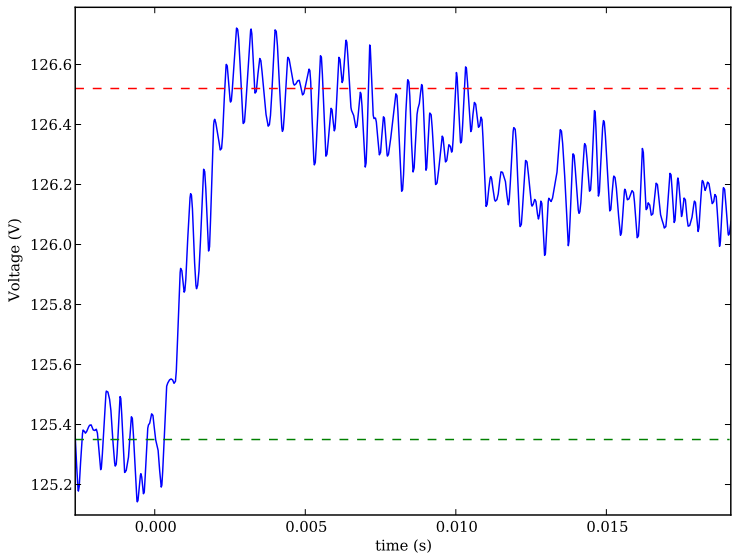

Figure 3.21: Output voltage during rebalancing of the ISOP with passive rectifiers

ratio, it can be seen that:

$$i_{c1} = i_{in} - \alpha i_1 \tag{3.7.5}$$

$$i_{c2} = i_{in} - \alpha i_2 \tag{3.7.6}$$

The capacitor currents are shown in Fig. 3.22. The constant α for the measured results is estimated from the requirement that $\frac{1}{T}\int_T i_c dt = 0$ in the steady state. The value for α is estimated to be 0.58.

A good approximation of the rebalancing process can be found by assuming that $i_2 = 0$ while $v_1 > v_2$. Under these circumstances:

$$C\frac{dv_2}{dt} = i_{in} = -C\frac{dv_1}{dt} \tag{3.7.7}$$

$$C\frac{dv_1}{dt} = i_{in} - \alpha i_1 \tag{3.7.8}$$

$$C\frac{dv_1}{dt} = C\frac{dv_2}{dt} - \alpha i_1 \tag{3.7.9}$$

$$2C\frac{dv_1}{dt} = -\alpha i_1 \tag{3.7.10}$$

$$C\frac{dv_d}{dt} = -\alpha i_1 \tag{3.7.11}$$

Since $i_2 = 0$ it follows that $i_d = i_1$. If the current i_1 is defined as

$$i_1(t) = \hat{i}_1 + \Delta i_1(t), \tag{3.7.12}$$

the transient current Δi_1 can be found by using the equivalent circuit of Fig. 3.23. The capacitor C_f is initially uncharged. The current found by using the equivalent circuit is compared to the measured current in Fig. 3.24.

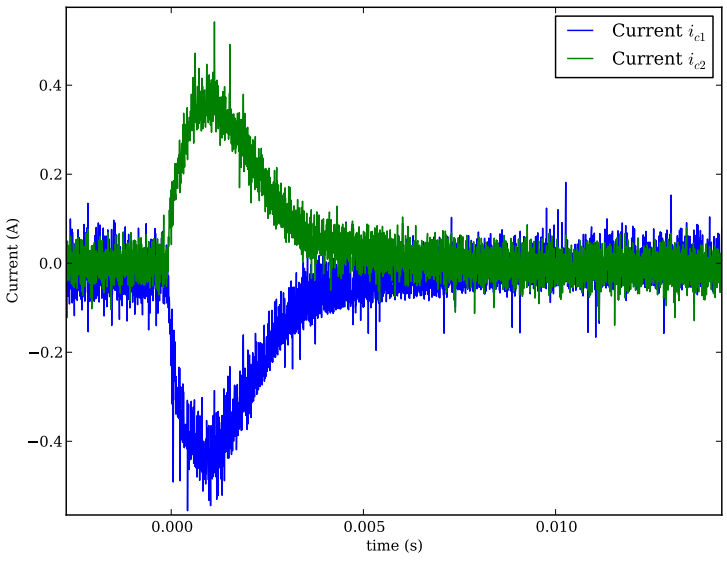

Figure 3.22: Capacitor currents during rebalancing of the ISOP with passive rectifiers

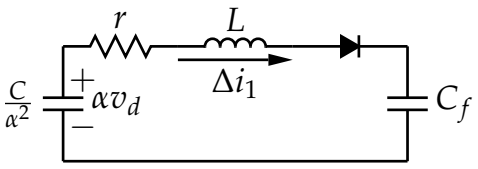

Figure 3.23: Equivalent rebalancing circuit of the ISOP with passive rectifiers

The comparison between the resulting v_d approximation and the measured value is shown in Fig. 3.25. Although, the approximation resembles the measured value, it is not a perfect fit. This can be attributed to the assumption that $i_2 = 0$ during rebalancing. The currents i_1 and i_2 during rebalancing are shown in Fig. 3.26. It is clear that i_2 starts flowing before $v_1 = v_2$.

It is possible to refine the presented theory to account for the variations in i_2 during the rebalancing process. However, the accuracy of this approximation is good, a more accurate model would add much complexity.

3.8 Conclusion

Modular converters had been the subject of vigorous research in recent times. To increase the modularity of the system, it is desirable to control the total converter by means of a common duty cycle control scheme. For the ISOP DC-DC converter it is accepted in the literature that two similar converters operating under such a control scheme will share both input voltage and output current equally, however, a rigorous proof was still lacking. The effect of converter mismatch was also largely unexplored.

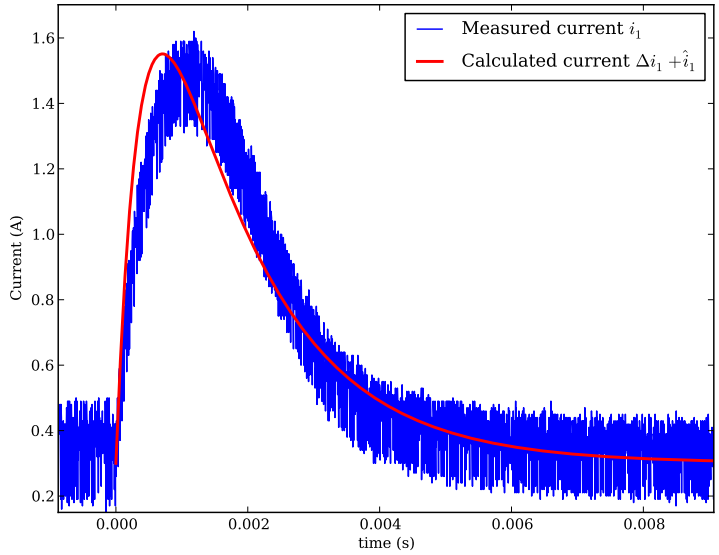

Figure 3.24: The i_1 current during rebalancing of the ISOP converter with passive rectifiers

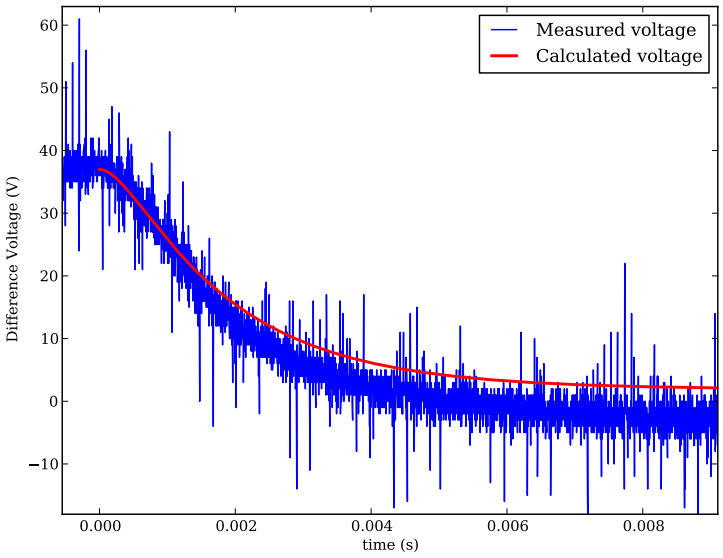

Figure 3.25: Comparison of the measured and estimated difference voltage

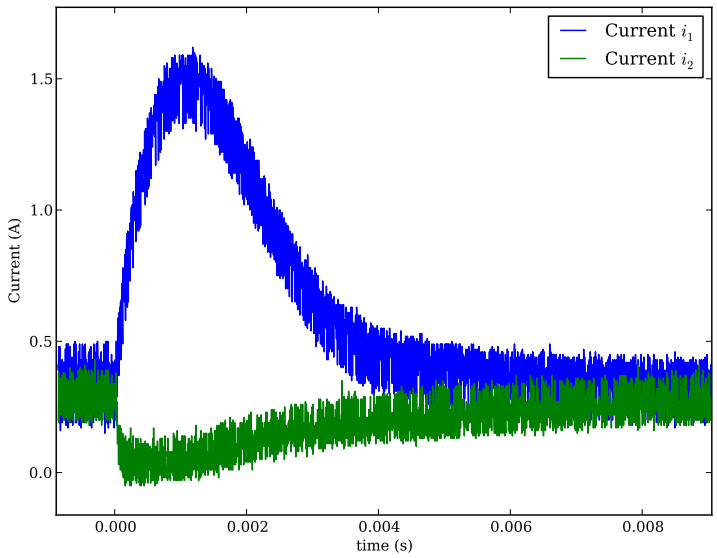

Figure 3.26: The i_1 and i_2 currents during rebalancing of the ISOP with passive rectifiers

In this chapter, the two-cell ISOP converter, with synchronous rectification, was investigated. An equivalent circuit of the system in terms of d and t parameters was developed. With the aid of this circuit, it was proven that the system, using two similar converters, will be balanced in steady state. The effect of converter mismatch in terms of duty cycle and transformer turns ratio mismatches was also investigated. It was proven that the output current would be shared equally by the two converters despite the mismatch, although the input voltage would reflect the mismatch.

The transient behaviour of the system, as response either to a perturbation or to the introduction of converter mismatch, was investigated, and an equivalent circuit describing the rebalancing of the circuit was developed. The results of both the steady state and transient behaviour of the system were compared with detailed simulations and thus validated.

Finally, the effect of passive rectification on the rebalancing process was investigated. The system rebalances in this configuration, although it does so by means of a completely different method. With synchronous rectification, the unbalance energy is dissipated in the inductor ESR, whereas the energy is dissipated in the load when passive rectifiers are used. The method of rebalancing was investigated and an equivalent rebalancing circuit was proposed. The theory presented was compared and verified through comparison with measured results.

Chapter 4

The Weak Balancing Mechanism: Flying Capacitor Converter

The weak balancing mechanism occurs exclusively when the different switches or cells are interleaved. Since the balancing method depends on the interleaving, the weak balancing mechanism cannot be identified or described using circuit averaging techniques. Consequently, the weak balancing method is relatively unknown.

The flying capacitor converter (FCC) is identified as a converter that exhibits only the weak balancing mechanism. Two distinct avenues of analysing the natural balancing mechanism of the FCC are used in the literature: analysis in either the frequency or the time domain. Studies in the frequency domain proved that the FCC voltages will balance naturally for any number of levels under sinusoidal modulation, and the existence of a quantifiable balancing time constant was identified [25; 37; 34; 38; 26; 36; 53] among others. However, the derived expressions for the time constant are complicated and they rely on the evaluation of a convolution sum over all frequency.

Studies in the time domain resulted in a clear and concise expression to approximate the balancing time constant [27; 41; 54; 55; 56]. However, the time domain approach requires closed form solutions to a specific topology, and repeating the method for a different load or a higher number of levels is complex and time consuming.

In this chapter, firstly the two-cell FCC operating with constant duty cycle is considered and it is proven that the FCC will balance naturally. The rebalancing process is discussed, and a clear and readily interpreted expression for the rebalancing time constant is presented. The circuit attributes that influences the balancing time constant are identified and discussed. A good approximation is presented of the time constant that can be calculated using only a pocket calculator. The constant duty cycle theory is used to provide a description of the rebalancing that occurs when sinusoidal modulation is used.

Secondly, the theory developed for the 2-cell FCC is applied to the 3-cell FCC. It is shown that the rebalancing time constants for the 3-cell FCC can also be determined analytically.

Thirdly, the natural balancing of the N-cell FCC operating with constant duty cycle is discussed. Using Lyapunov methods it is proven that the system will be

stable. The dissipation of the unbalance energy is discussed.

When the expressions that describe the characteristic matrix of the system are simplified it is shown that the matrix decomposes naturally into a symmetric and a skew symmetric part. By using Lyapunov's method it is shown that the system stability can be determined from the characteristics of the symmetric part of the matrix. A proof is provided that the matrix is positive definite and the system therefore Lyapunov stable. Previous studies of the balancing mechanism inferred stability from the circuit operation.

Furthermore, it is shown that the eigenvalues of the symmetric matrix can be used to determine a bound on the eigenvalues of the characteristic matrix and hence the rebalancing time constants. It is shown that the expression for the symmetric matrix is such that, with the use of a approximation regarding the nature of the load at the frequencies of interest, the eigenvalues can be approximated using a closed form expression and a reference table.

Finally, the sinusoidally modulated FCC is considered. Methods for analysis are presented using the double Fourier series representation of the switching functions. By using the theory developed for the constant duty cycle case, it is possible to formulate a method of approximating the maximum time constant in a similar manner, using a reference table.

Should more accurate expressions for the maximum rebalancing time constant be needed, Python script files are included in Appendix C. These files use the presented theory to accurately calculate the maximum voltage rebalancing time constant for any FCC.

The presented theory is verified throughout by means of comparison with detailed time domain simulations. The theory is also compared with the practical measurements of a system located at Gent University in Belgium. The author wishes to take this opportunity to thank Mr. Steven Thielemans for his help and assistance in this regard.

4.1 The 2-Cell FCC and Equivalent Circuit

The circuit of the 2-Cell FCC, with the inductor ESR indicated as r, is shown in Fig. 4.1. To analyse the circuit the switching functions, $s_0(t)$ and $s_1(t)$ are defined as:

$$s_0(t) = \begin{cases} 1 & \text{if } S_0+ \text{ is closed} \\ -1 & \text{if } S_0- \text{ is closed} \end{cases} \tag{4.1.1}$$

$$s_1(t) = \begin{cases} 1 & \text{if } S_1+ \text{ is closed} \\ -1 & \text{if } S_1- \text{ is closed} \end{cases} \tag{4.1.2}$$

For the analysis of the FCC the reference switching function is chosen as S_0 and not S_1 as is the case with the ISOP and ISOS converters. This choice is made to simplify the expressions when the N-cell case is considered.

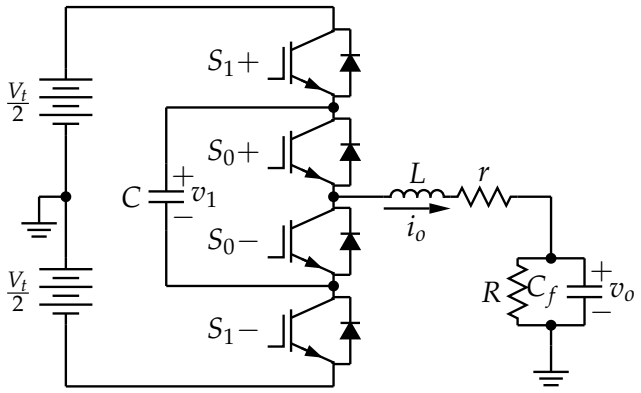

Figure 4.1: 2-Cell Flying Capacitor Converter

The system of differential equations describing the converter operation is:

$$2C\frac{dv_1}{dt} = \{s_1(t) - s_0(t)\}i_o(t) \tag{4.1.3}$$

$$L\frac{di_o}{dt} = \frac{1}{2}V_t \cdot s_1(t) + \frac{1}{2}v_1(t)\{s_0(t) - s_1(t)\} - v_o(t) - r \cdot i_o(t) \tag{4.1.4}$$

$$C_f\frac{dv_o}{dt} = i_o(t) - \frac{v_o(t)}{R} \tag{4.1.5}$$

In order to study the natural balancing mechanisms, it is convenient to define the total and difference parameters of the circuit descriptors:

$$s_t = \frac{1}{2}(s_0 + s_1)$$
$$s_d = \frac{1}{2}(s_1 - s_0)$$
$$v_d = \frac{V_t}{2} - v_1$$

The system of differential equations can be rewritten in terms of the defined d and t parameters as [28]:

$$C\frac{dv_d}{dt} = -s_d(t) \cdot i_o(t) \tag{4.1.6}$$

$$L\frac{di_o}{dt} = \frac{1}{2}V_t \cdot s_t(t) + v_d(t) \cdot s_d(t) - v_o(t) - r \cdot i_o(t) \tag{4.1.7}$$

$$C_f\frac{dv_o}{dt} = i_o(t) - \frac{v_o(t)}{R} \tag{4.1.8}$$

By using of a transformer model, with a variable turns-ratio, an equivalent circuit of the FCC can be redrawn in terms of d and t parameters, see Fig. 4.2. This equivalent circuit lends itself to a clear representation of the balancing process.

By using the equivalent circuit, it can be seen that the current through the flying capacitor can be given as

$$i_d(t) = i_o(t) \cdot s_d(t). \tag{4.1.9}$$

However, solving the problem in the time domain presents several obstacles, most of which can be circumvented by moving to the frequency domain.

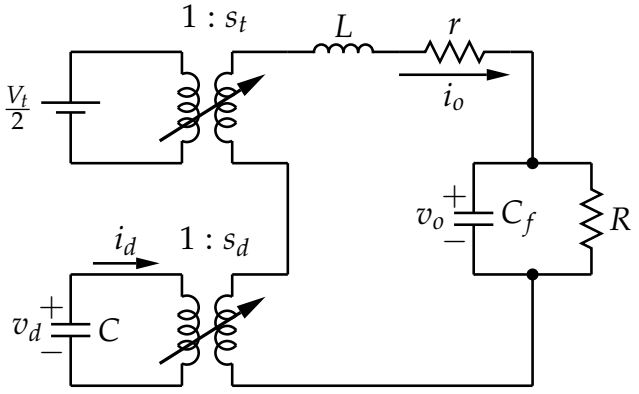

Figure 4.2: 2-Cell FCC circuit in terms of d and t parameters

4.1.1 Harmonic Information

It is assumed that the two cells of the FCC converter are operating with constant duty-cycle and a constant switching frequency, and that the switching signals of the two cells are interleaved. Let the switching PWM function be created through comparison of the reference signal f_r and a triangle carrier signal with frequency ω_c. A triangular carrier is used in lieu of a sawtooth carrier since the triangular carrier results in lower harmonic distortion at the output voltage, especially in three phase inverters [5].

For the FCC the switching functions have a value of either -1 or 1 and are derived in the following manner, for the reference switching function $s_0(t)$ the phase shift is chosen as $\theta_c = -\frac{\pi}{2}$:

$$f_r = 2d - 1$$
$$f_c = \frac{2}{\pi}\arcsin(\sin(\omega_c + \theta_c))$$
$$s(t) = \begin{cases} 1, \text{ for } f_r \geq f_c(t) \\ -1, \text{ for } f_r < f_c(t) \end{cases}$$

The switching functions of the two cells, assuming cell 0 to be the reference cell, can be represented in the frequency domain, where $\Psi(n)$ is the exponential Fourier coefficients and d denotes the duty-cycle, as:

$$s_0(t) = \sum_{n=-\infty}^{\infty} C_{0(n)} e^{jn\omega_s t} \tag{4.1.10}$$
$$C_{0(n)} = \Psi(n) \tag{4.1.11}$$
$$C_{1(n)} = (-1)^n \Psi(n) \tag{4.1.12}$$
$$\Psi(n) = \begin{cases} \frac{2}{\pi n}\sin(\pi n d) & \text{for } n \neq 0 \\ 2d - 1 & \text{for } n = 0 \end{cases} \tag{4.1.13}$$

A derivation of the exponential Fourier series coefficients is included in Appendix A.6.2 on p.179.

4.1.2 The Balancing Equation

The balancing mechanisms of the FCC can now be investigated by assuming that that C is sufficiently large so that the switching frequency voltage ripple on v_1 is negligible. It is furthermore assumed that the capacitance is large enough that the capacitor voltage vary slow enough with time that the rest of the converter can be regarded as being in the steady state.

In the frequency domain the DC component of (4.1.9) can be found as:

$$I_d(\omega)|_{\omega=0} = \frac{V_t}{2}\left.\frac{S_t(\omega)}{Z(\omega)} * S_d(\omega)\right|_{\omega=0} + v_d \left.\frac{S_d(\omega)}{Z(\omega)} * S_d(\omega)\right|_{\omega=0} \tag{4.1.14}$$

As shown in Section 3.2.1 and proven in Lemma 15 on p.172, it is true that:

$$\left.\frac{S_t(\omega)}{Z(\omega)} * S_d(\omega)\right|_{\omega=0} = 0 \tag{4.1.15}$$

Likewise, with reference to Lemma 16 on p. 173:

$$\left.\frac{S_d(\omega)}{Z(\omega)} * S_d(\omega)\right|_{\omega=0} = 2\sum_{\xi=1,3}^{\infty} \frac{|\Psi(\xi)|^2}{|Z(\xi\omega_s)|^2}\mathrm{Re}\{Z(\xi\omega_s)\} \tag{4.1.16}$$

Substitution of (4.1.15) into (4.1.14) yields:

$$I_d(\omega)|_{\omega=0} = v_d \left.\frac{S_d(\omega)}{Z(\omega)} * S_d(\omega)\right|_{\omega=0} \tag{4.1.17}$$

From (4.1.16) it is clear that the convolution sum will always yield a positive value and hence the pole of

$$C\frac{dv_d}{dt} = -\ I_d(\omega)|_{\omega=0} = -v_d \left.\frac{S_d(\omega)}{Z(\omega)} * S_d(\omega)\right|_{\omega=0} \tag{4.1.18}$$

will always be in the left-hand half of the complex plane, implying that the voltage unbalance will decay towards $v_d = 0$ in the steady-state.

4.2 The Effect of the Filter Inductor ESR

With reference to Fig. 4.2 the impedance $Z(\omega)$ can be found, for systems with a resistive load, as:

$$Z(\omega) = \frac{R + r + j\omega L + j\omega C_f Rr - \omega^2 RLC_f}{1 + j\omega C_f R} \tag{4.2.1}$$

In general, the filter components are chosen such that the cut-off frequency of the LC_f is lower than the switching frequency, normally less than one-half; the capacitance C_f is chosen such that $\frac{1}{RC_f} \ll 2\pi f_s$. The component values for a 1 kW FCC, with a higher than normal ESR, are shown in Table 4.1

Neglecting the influence of the skin effect and the proximity effect on the inductor ESR at multiples of the switching frequency, the real and imaginary parts of

Table 4.1: Component values for a typical FCC

V_t	100 V	C	40 μF
L	153 μH	C_f	50 μF
r	0.8 Ω	f_s	5 kHz
R	10 Ω		

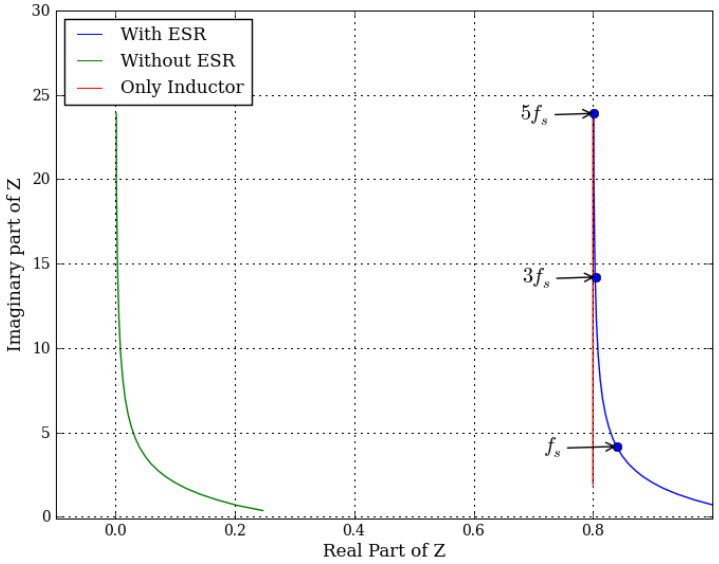

Figure 4.3: Re$\{Z(\omega)\}$ vs Im$\{Z(\omega)\}$ for a range of frequencies

$Z(\omega)$ are plotted against one another for $\frac{1}{2}f_s < f < 5f_s$, Fig. 4.3. The summation points of (4.1.16) are shown as dots on the trace containing information on the ESR influence. The effect of using only an inductor with ESR is also shown; it is clear that its effect dominates the impedance at these frequencies.

The capacitor ESR and the on-state resistance of the switch MosFet, or equivalent resistance in the case of an IGBT switch, will also influence the real part of the impedance. Due to the switching behaviour, a part of the switch conduction losses could be added to the inductor ESR, but as some switch current conducts through the flying capacitor, deriving an exact expression for this portion falls outside the scope of this study.

The following assumptions are made:

1. The effect of the other series resistances are neglected, or equivalently lumped in r.

2. The inductor is designed with Litz-wire and constructed in such a manner that the effect of the skin- and proximity effects are negligible.

3. The filter capacitance C_f is large.

Based on these assumptions it is true that the characteristics of the inductor dominate the behaviour of $Z(\omega)$ at the frequencies of interest. The filter capacitor size assumption is important. With reference to Fig. 4.3 and (4.2.1), a large filter capacitor effectively masks the effect of R at the frequencies of interest, making the assumption of $Z(\omega) = r + j\omega_s L$ feasible. Using this simplification (4.1.16) can be rewritten, with substitution of (4.1.13) and assuming that $r \ll \omega L$ as:

$$\frac{S_d(\omega)}{Z(\omega)} * S_d(\omega)\bigg|_{\omega=0} = 2\sum_{\xi=1,3}^{\infty} \frac{|\Psi(\xi)|^2}{4\xi^2\pi^2 f_s^2 L^2} r \tag{4.2.2}$$

An expression for $|\Psi(\xi)|^2$ can be found through investigation of (4.1.13). It follows that, for $\xi \neq 0$

$$|\Psi(\xi)|^2 = \frac{4\sin^2(\pi\xi d)}{\pi^2\xi^2}. \tag{4.2.3}$$

It is interesting to note that if a sawtooth carrier is used the definition of $\Psi(n)$ changes to

$$\Psi(n) = \begin{cases} \frac{j}{\pi n}\left(e^{-j\pi n d} - 1\right) & \text{for } n \neq 0 \\ 2d - 1 & \text{for } n = 0. \end{cases} \tag{4.2.4}$$

Using this definition it is true that

$$|\Psi(\xi)| = |\frac{1}{\pi\xi}||e^{-j2\pi\xi d} - 1|, \tag{4.2.5}$$

and with reference to Fig. 4.4

$$\begin{aligned} |e^{-j2\pi\xi d} - 1|^2 &= (1 - \cos(2\pi\xi d))^2 + \sin^2(2\pi\xi d) \\ &= \cos^2(2\pi\xi d) - 2\cos(2\pi\xi d) + 1 + \sin^2(2\pi\xi d) \\ &= 2\left(1 - \cos(2\pi\xi d)\right). \end{aligned} \tag{4.2.6}$$

Furthermore the definition of $|\Psi(\xi)|^2$ is invariant on the choice of sawtooth or triangular carrier, since

$$|\Psi(\xi)|^2 = \frac{2(1 - \cos(2\pi\xi d)}{\pi^2\xi^2} \tag{4.2.7}$$

$$= \frac{4\sin^2(\pi\xi d)}{\pi^2\xi^2}. \tag{4.2.8}$$

Substituting the value of $|\Psi(\xi)|^2$ into (4.2.2) yields:

$$\frac{S_d(\omega)}{Z(\omega)} * S_d(\omega)\bigg|_{\omega=0} = \sum_{\xi=1,3}^{\infty} \frac{1 - \cos(2\pi\xi d)}{\xi^4\pi^4 f_s^2 L^2} r \tag{4.2.9}$$

However, the ξ^4 term dominates the summation, to such an extent that, with reference to Fig. 4.5:

$$\sum_{\xi=1,3}^{\infty} \frac{1 - \cos(2\pi\xi d)}{\xi^4} \approx 1 - \cos(2\pi d) \tag{4.2.10}$$

$$\therefore \frac{S_d(\omega)}{Z(\omega)} * S_d(\omega)\bigg|_{\omega=0} \approx \frac{1 - \cos(2\pi d)}{\pi^4 f_s^2 L^2} r \tag{4.2.11}$$

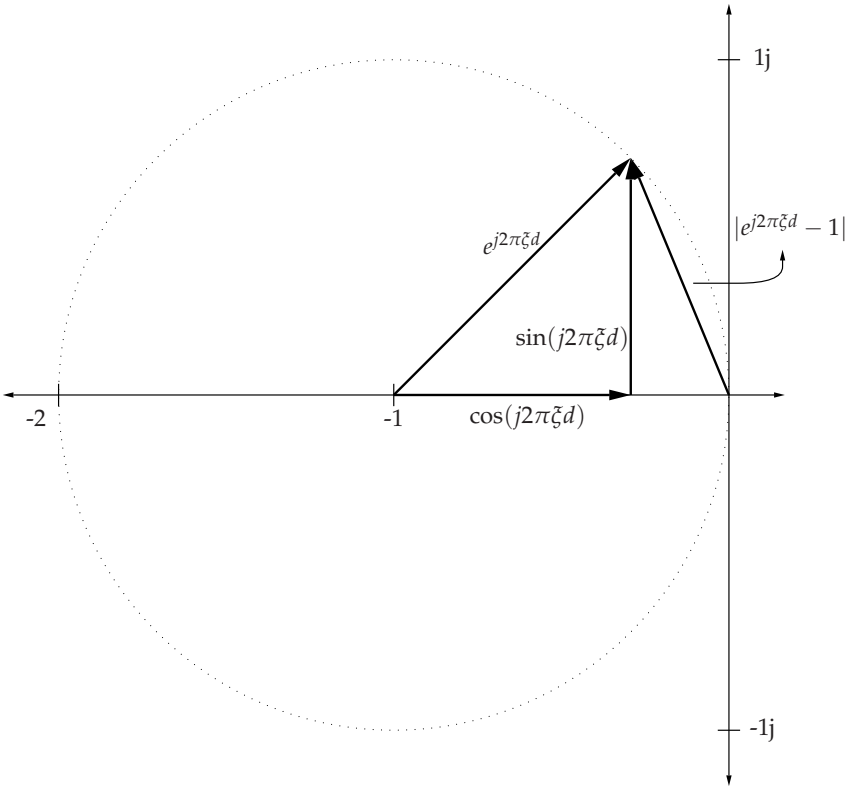

Figure 4.4: Graphical calculation of $|\Psi(\xi)|$ on the complex plane

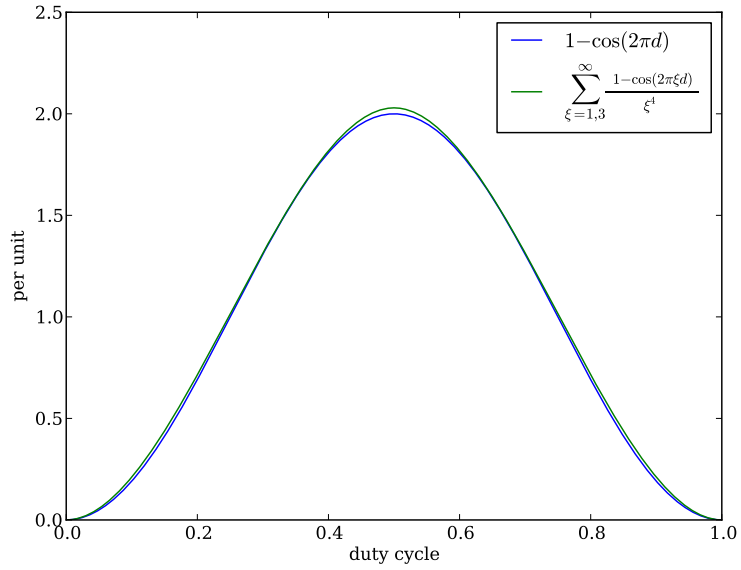

Figure 4.5: Estimation of the $\sum_{\xi=1,3}^{\infty} \frac{1-\cos(2\pi\xi d)}{\xi^4}$ term

Using this approximation, (4.1.18) can be rewritten as:

$$C\frac{dv_d}{dt} = -v_d\frac{1-\cos(2\pi d)}{\pi^4 f_s^2 L^2}r \tag{4.2.12}$$

with solution, for a given initial condition $v_d(0)$:

$$v_d(t) = v_d(0)e^{\frac{-t}{\tau}} \tag{4.2.13}$$

$$\tau = \frac{C\pi^4 f_s^2 L^2}{r\,(1-\cos(2\pi d))} \tag{4.2.14}$$

When the filter capacitance is not large enough, or for loads where the assumptions do not hold, a better approximation of τ can be found through

$$\tau = \frac{C}{4\sum\limits_{\xi=1,3}^{\infty}\frac{1-\cos(2\pi\xi d)}{\pi^2\xi^2|Z(\xi\omega_s)|^2}\mathrm{Re}\{Z(\xi\omega_s)\}}. \tag{4.2.15}$$

It is clear that the balancing time constant depends on the duty cycle. Furthermore the time constant also depends on the flying capacitor capacitance and the characteristics of the total load. The influence of the load on the time constant will be discussed in the next Section.

4.3 Discussion

4.3.1 Purely Resistive Load

Investigation of the hypothetical situation where a purely resistive load is connected to the FCC yields considerable insight into the natural balancing process. With $Z(\omega) = r$ the expression for the time-constant in (4.2.15) can be rewritten as:

$$\begin{aligned}\tau &= \frac{C}{\sum\limits_{\xi=1,3}^{\infty}\frac{1-\cos(2\pi\xi d)}{\pi^2\xi^2 r^2}r} \\ &= \frac{Cr}{f(d)}\end{aligned} \tag{4.3.1}$$

$$f(d) = \sum_{\xi=1,3}^{\infty}\frac{1-\cos(2\pi\xi d)}{\pi^2\xi^2} \tag{4.3.2}$$

Cr is the familiar time-constant for a RC circuit, while the function $f(d)$ is a Fourier series representation of a triangular function, where:

$$\sum_{\xi=1,3}^{\infty}\frac{1-\cos(2\pi\xi d)}{\pi^2\xi^2} = \begin{cases}\frac{1}{2}d & \text{for } 0 \le d \le 0.5 \\ \frac{1}{4}-\frac{1}{2}d & \text{for } 0.5 < d \le 1\end{cases} \tag{4.3.3}$$

It is clear that the unbalance energy in the capacitor C is dissipated in the load resistance. The time-constant is modified by a function of the duty-cycle. $f(d)$

reaches a maximum at $d = 50\%$, resulting in the fastest time constant. Conversely, when $f(0) = f(1) = 0$ no rebalancing is possible. However, these work points correspond to the trivial cases where the converter switches the load to either $+\frac{V_t}{2}$ or $-\frac{V_t}{2}$. Investigation of Fig. 4.1 under these conditions shows that no current can flow through C, making it impossible to balance the capacitor voltage.

Taking this argument further to consider a load as shown in Fig. 4.1 and investigating (4.2.15), it is clear that the unbalance energy in the capacitor is dissipated in the real part of the load at the odd-harmonics of the switching frequency. For example, increasing the inductance decreases the current ripple and hence the current at the odd switching frequency harmonics. This results in a lower current through the load at these harmonics and hence a slower dissipation of the unbalance energy in the real part of the load, i.e. a longer time-constant.

4.3.2 Decreasing the Time-Constant Through the Inclusion of a Balance Booster

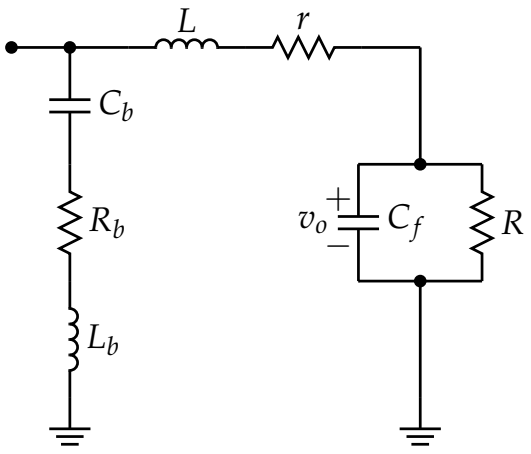

Figure 4.6: A balance booster

Table 4.2: Component values for the Balance Booster

L_b	210 μH	R_b	2 Ω
C_b	3 μF		

The impedance ratio of $\frac{\mathrm{Re}\{Z(\omega)\}}{|Z(\omega)|^2}$ at the switching frequency harmonics determines the time constant for all duty-cycles. A balance booster [34; 28; 37] is a LCR notch filter tuned to the switching frequency, or it can consist of several balance boosters tuned to the odd multiples of the switching frequency, that is included in parallel to $Z(\omega)$ to improve the natural balancing. A balance booster consisting of C_b, L_b and R_b is shown in Fig. 4.6. The balance booster provides a low and nearly real impedance path for the current at the switching frequency, allowing the unbalance energy to be dissipated in the balance booster resistance. In Fig. 4.7

the parametric curves of the load impedance $Z(\omega)$ are compared on the range $0.5f_s \leq f \leq 5f_s$ both with and without a balance booster. It is clear that the inclusion of the balance booster alters the impedance at the switching frequency to a nearly real value.

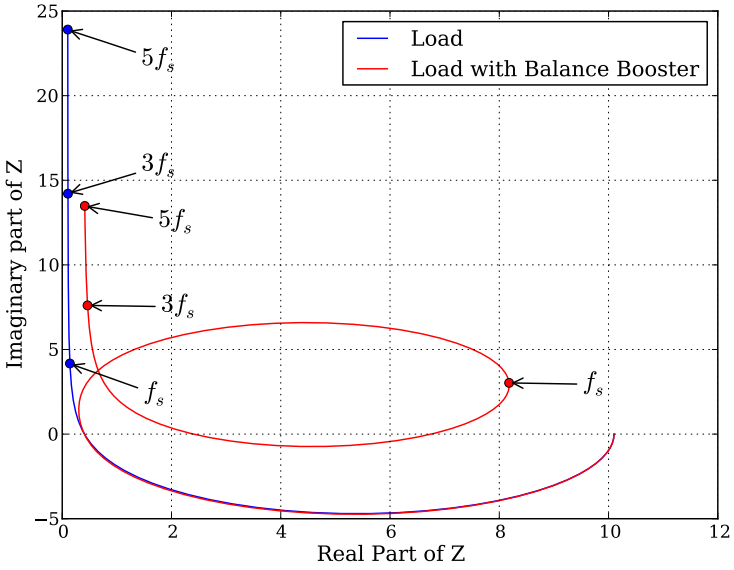

Figure 4.7: Re$\{Z(\omega)\}$ vs Im$\{Z(\omega)\}$ for a range of frequencies; effect of the balance booster

The advantage of the balance booster circuit is that due to the interleaving of the carriers the effective output frequency of the FCC is twice the switching frequency [4]. The balance booster tuned to the switching frequency thus conducts very little current under normal conditions, and only conducts current originating from the unbalance in C.

A Python script is included in Appendix C.2.4 to aid in the design of the balance booster, using a parametric plot similar to Fig. 4.7. If the balance booster is well tuned, it is possible to approximate the load as

$$Z(\omega_s) \approx r_{eq}, \tag{4.3.4}$$

where r_{eq} is the effective resistance of the balance booster circuit at the switching frequency. A rough approximation of the balance time constant can be found using the discussion in Section 4.3.1 and (4.3.1).

Theoretically, the balancing time-constant could also be improved using an inductor with a higher ESR, especially at the switching frequency. An inductor wound with a single large diameter wire will result in a low DC ESR but a higher AC resistance due to the skin effect. An inductor core geometry that results in a winding structure containing many winding layers will also result in a large AC resistance due to the proximity effect. However, this results in higher losses and lower efficiency.

Finally, as stated previously, due to the interleaving of the cells, the effective output frequency of the converter is twice the switching frequency. If the output filter cut-off frequency is increased by reducing the capacitor size, the impedance ratio will also decrease, hence improving the time-constant. This can be more effectively exploited when the FCC has more cells, hence operating at a higher effective switching frequency. However, under these conditions the accuracy of the approximated time constant using (4.2.15) will decrease, since some unbalance energy will be dissipated in the load.

4.3.3 Comparison to the Expression Derived Through Time Domain Analysis

Analysis of the FCC in the time domain yields the following estimation for the time constant [41]:

$$\tau \approx \frac{48}{r} L^2 C f_s^2 \frac{1}{(1-D)^2(1+2D)} \tag{4.3.5}$$

The descriptor D was used for the duty cycle in lieu of d; as the duty cycle was defined differently in [41], the conversion can be found as $D = 2d - 1$. The use of (4.3.5) yields very similar results to (4.2.14). However, the time domain study assumed a load consisting of only an inductor and resistance. Using (4.3.5) for more complex loads, such as the inclusion of a balance booster, is not possible. Also, when $r > 2\pi f_s L$ using either (4.3.5) or (4.2.14) yields time constants much lower than those found by using (4.2.15), for example with $L = 0$, both methods yield $\tau = 0$ in comparison with (4.3.1).

In Fig. 4.8, the three different approximations for the time-constant are compared on the range $\frac{1}{2} \leq d \leq 1$, using the parameters from Table 4.1. It is clear that the approximations of (4.2.14) and (4.3.5) are similar.

4.4 Simulation Studies

The 2-Cell FCC was simulated under start-up conditions with the parameters indicated in Table 4.1. This implies that the flying capacitor is initially uncharged and that it should in steady state (for the cell-voltages to be balanced) attain a voltage of 50 V. Alternatively, this problem represents an initial value of $v_d(0) = 50$ V. In the following figures the simple approximation curve was obtained by using (4.2.14) and the full approximation through (4.2.15). As a base case, the simulated system was operating with $d = 0.3$, shown in Fig. 4.9

It was stated that the approximation of (4.2.14) is more accurate when the filter capacitance is large. This is indicated in Fig. 4.10, where the filter capacitance is increased from 50 μF to 150 μF.

The presented theory also states that the balancing time constant should decrease with an increase in inductor ESR. In Fig. 4.11 the ESR is increased from 0.8 Ω to 5 Ω. An assumption in the derivation of (4.2.14) was that $r \ll 2\pi f_s L$. It follows that the accuracy of the approximated time constant will be lower, since in this case the ESR approach the inductive reactance at the switching frequency. The time constant found by (4.2.14) is faster under these conditions than in the case both with the time simulation and that found through (4.2.15).

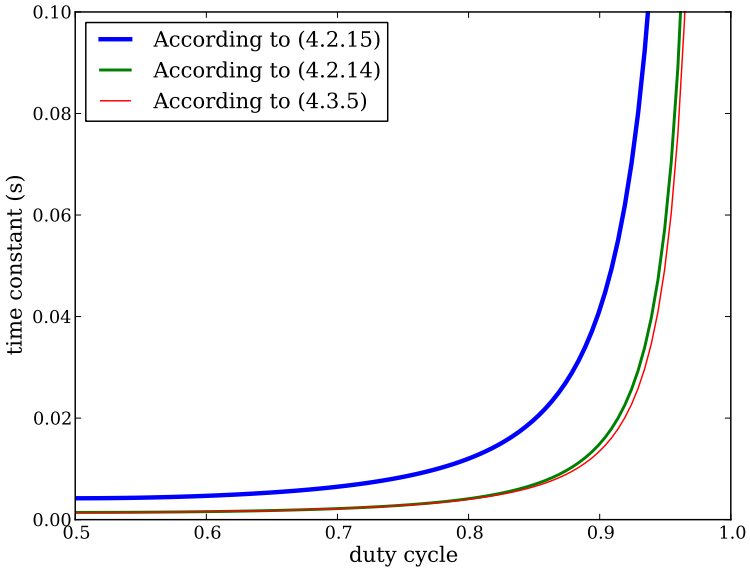

Figure 4.8: Comparison of the different time-constant approximations

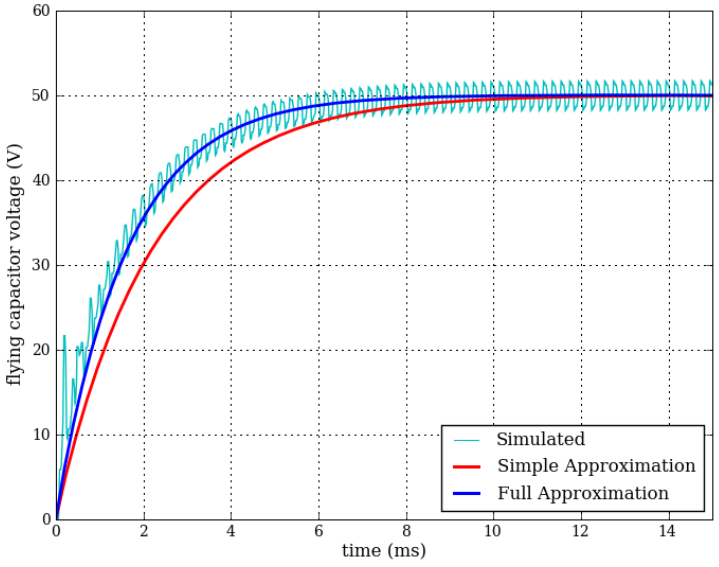

Figure 4.9: Simulation of FCC, base-case with $d = 30\%$

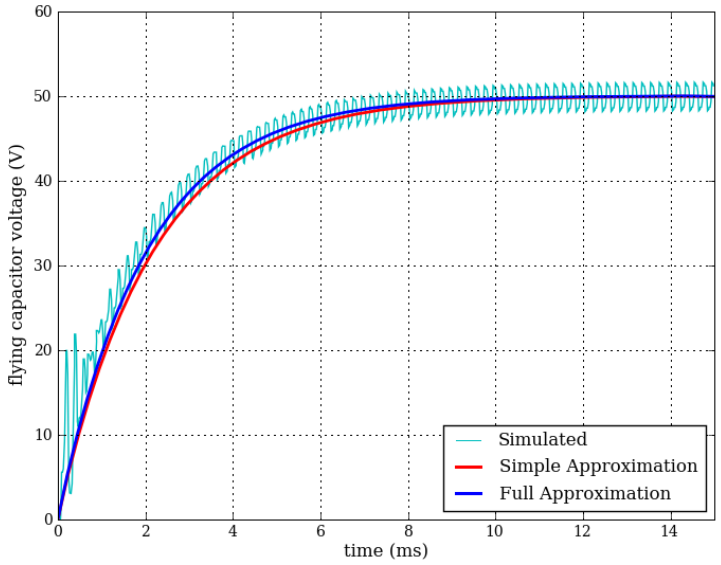

Figure 4.10: Simulation of FCC, larger capacitance with $d = 30\%$ and $C = 150\ \mu$F

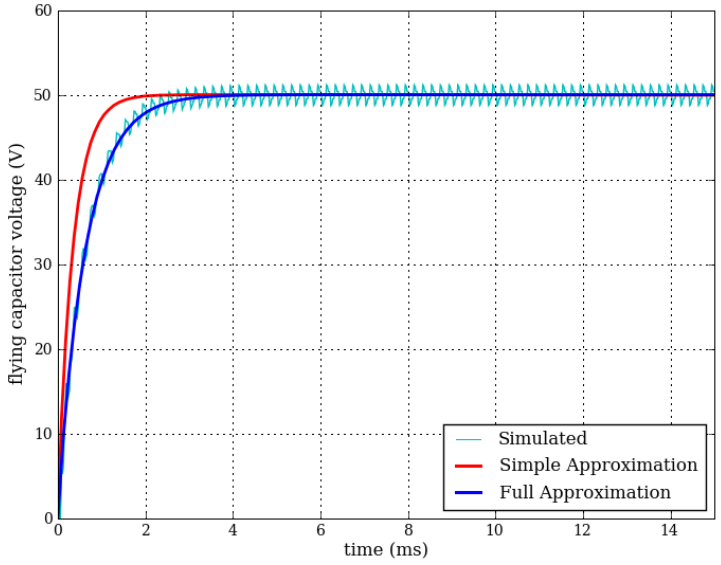

Figure 4.11: Simulation of FCC, larger ESR with $d = 30\%$ and $r = 5\ \Omega$

Finally, the influence of the duty is investigated by changing the duty cycle from 30 % to 15 %. According to (4.2.14), this should result in a larger balancing time constant. The simulation waveforms are shown in Fig 4.12.

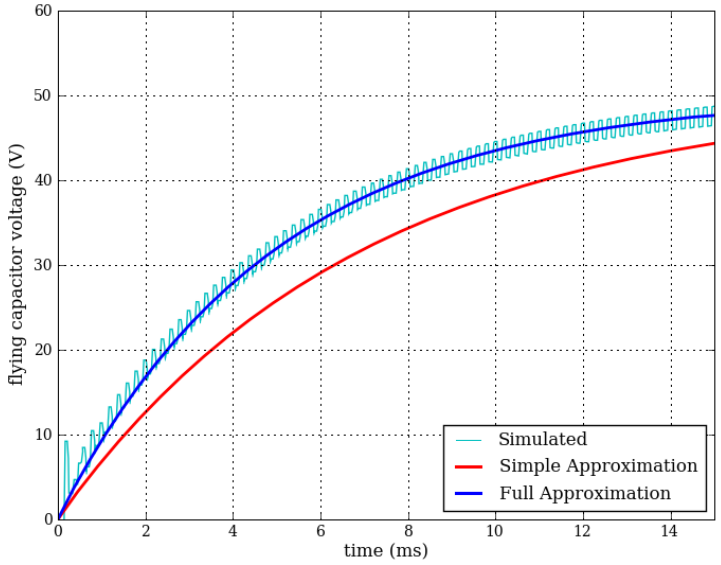

Figure 4.12: Simulation of FCC, lower duty-cycle with $d = 15\%$

4.5 Balancing of Modulated Duty Cycle

The FCC is often used as an inverter where the duty cycle is modulated to provide a time varying, most often sinusoidal, output.

Using a carrier, f_c and a reference signal f_r

$$f_c(t) = \frac{2}{\pi}\arcsin(\sin(\omega_s t)) \tag{4.5.1}$$

$$f_r(t) = m_a \sin(\omega_r t) \tag{4.5.2}$$

and assuming that $\omega_s \gg \omega_r$ the duty cycle of the previous discussion can be approximated by:

$$d(t) \approx 0.5 + \frac{m_a}{2}\sin(\omega_r t) \tag{4.5.3}$$

Using the assumptions stated in Section 4.2, which is, in essence, that the effect of the filter inductor dominates $Z(\omega)$, the expression for the approximated time constant (4.2.14) can be rewritten as a function of time as:

$$\tau(t) = \frac{C\pi^4 f_s^2 L^2}{r\left(1 - \cos(2\pi(\frac{1}{2} + \frac{m_a}{2}\sin(\omega_r t)))\right)} \tag{4.5.4}$$

If the time constant is slow enough relative to the period of the modulating function a time average of the time constant can be used to approximate the balancing of the system. Isolating the time varying term and calculating the time average yields:

$$\begin{aligned}\alpha &= \frac{1}{\pi}\int_0^{\pi}\Big(1-\cos(\pi+\pi m_a\sin(t))\Big)dt \\ &= 1+\frac{1}{\pi}\int_0^{\pi}\cos(\pi m_a\sin(t))dt \\ &= 1+J_0(\pi m_a)\end{aligned} \tag{4.5.5}$$

Where $J_n(x)$ is the Bessel function of the first kind defined as [5, p.632]:

$$J_n(x) = \frac{1}{\pi}\int_0^{\pi}\cos(nt - x\sin(t))dt \tag{4.5.6}$$

Using this time averaged expression, an average, or equivalent, time constant can be found by using:

$$\tau_{eq}(m_a) = \frac{C\pi^4 f_s^2 L^2}{r(1+J_0(\pi m_a))} \tag{4.5.7}$$

The averaged time constant of the modulated duty cycle case corresponds to an equivalent constant duty cycle, such that:

$$\begin{aligned}1+J_0(\pi m_a) &= 1-\cos(2\pi d_{eff}) \\ d_{eff} &= \frac{\cos^{-1}\left(-J_0(\pi m_a)\right)}{2\pi}\end{aligned} \tag{4.5.8}$$

Another approximation of the equivalent constant duty cycle that corresponds well for $0 \leq m_a \leq 0.5$ can be found through a rms approximation of the reference sinusoid. With reference to Fig. 4.5, the time constant is symmetrical around $d = 50$ %. Modulation of the output requires that the output be biased at $d = 50$ % and that the duty cycle be modulated to swing in both the positive and negative direction around this bias point. The duty cycle can be approximated, neglecting the discrete nature of the duty cycle, as:

$$d(t) \approx \frac{1}{2} + \frac{m_a}{2}\sin(\omega_r t) \tag{4.5.9}$$

with rms value of

$$d_{eff\ rms} \approx \frac{1}{2} \pm \frac{m_a}{2\sqrt{2}}. \tag{4.5.10}$$

The equivalent constant duty cycles found by means of these two methods are compared in Fig. 4.13. It is clear that the rms approximation corresponds well for $m_a < 0.5$.

4.5.1 Simulation Studies

The FCC of Table 4.3 was simulated with the resultant flying capacitor voltage waveform indicated in Fig. 4.14. The approximations were made using (4.5.7) as

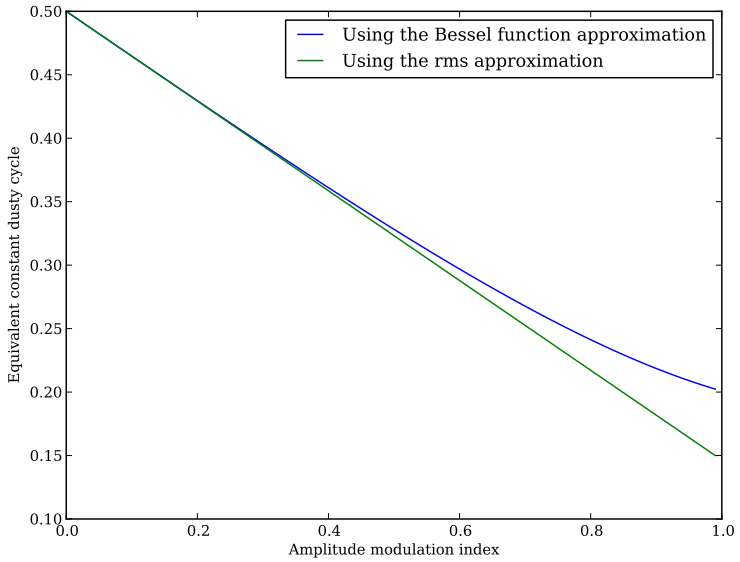

Figure 4.13: Comparison of the different equivalent duty cycle approximations

Table 4.3: Component values for a typical FCC, modulated duty cycle

V_t	100 V	C	40 μF
L	153 μH	C_f	150 μF
r_{dc}	0.8 Ω	f_s	5 kHz
R	10 Ω	m_a	0.8

the simple approximation and (4.5.8) in conjunction with (4.2.15) as the full approximation. The modulation frequency was set at 20 Hz to accentuate the varying nature of the effective rebalancing time constant. Both approximations are accurate. Changing the reference frequency to 150 Hz and the modulation index to 0.4 yields the result of Fig. 4.15.

The same constraints with regard to the accuracy of the simple approximation of the time constant holds as discussed in Section 4.4. That is mainly the requirement of a large filter capacitor, such that the characteristics of the filter inductor dominate the impedance $Z(\omega)$ at the frequencies of interest.

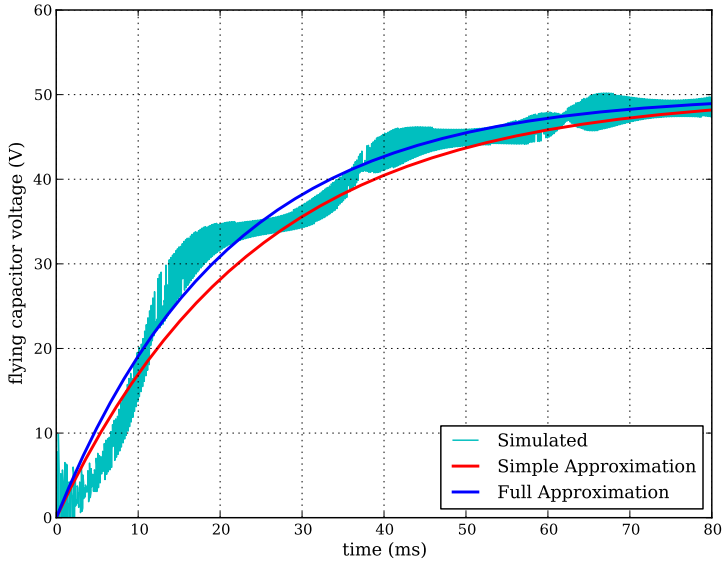

Figure 4.14: Simulation of modulated FCC

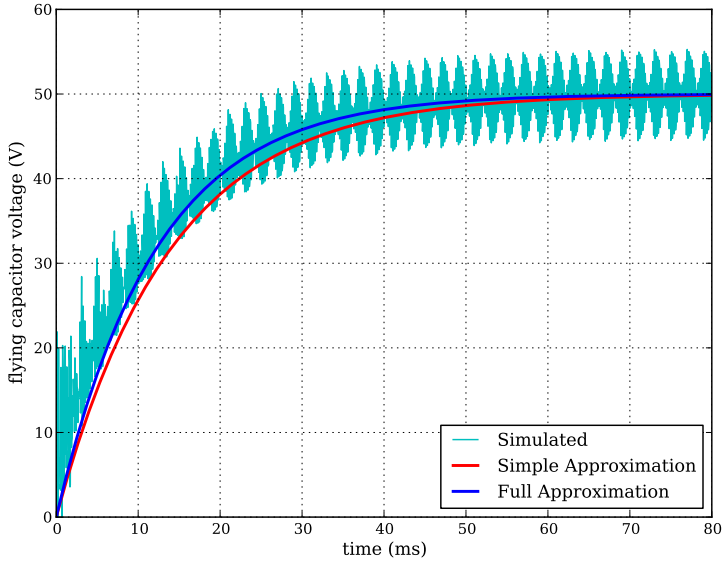

Figure 4.15: Simulation of modulated FCC, $f_r = 150$ Hz, $m_a = 0.4$

4.6 The 3-Cell FCC

The rebalancing time constant of the 3-cell FCC can also be found directly. To analyse the circuit the switching functions, $s_0(t)$, $s_1(t)$ and $s_2(t)$ are defined as:

$$s_0(t) = \begin{cases} 1 & \text{if } S_0+ \text{ is closed} \\ -1 & \text{if } S_0- \text{ is closed} \end{cases}$$
$$s_1(t) = \begin{cases} 1 & \text{if } S_1+ \text{ is closed} \\ -1 & \text{if } S_1- \text{ is closed} \end{cases}$$
$$s_2(t) = \begin{cases} 1 & \text{if } S_2+ \text{ is closed} \\ -1 & \text{if } S_2- \text{ is closed} \end{cases} \tag{4.6.1}$$

From the circuit of Fig. 4.16, the system of differential equations describing the circuit operation can be found as:

$$\frac{d}{dt}\begin{bmatrix} 2C \cdot v_1 \\ 2C \cdot v_2 \\ L \cdot i_o \\ C_f \cdot v_o \end{bmatrix} = \begin{bmatrix} 0 & 0 & s_1 - s_0 & 0 \\ 0 & 0 & s_2 - s_1 & 0 \\ \frac{1}{2}(s_0 - s_1) & \frac{1}{2}(s_1 - s_2) & -r & -1 \\ 0 & 0 & 1 & \frac{-1}{R} \end{bmatrix} \begin{bmatrix} v_1 \\ v_2 \\ i_o \\ v_o \end{bmatrix} + \begin{bmatrix} 0 \\ 0 \\ s_2 \\ 0 \end{bmatrix} \frac{V_t}{2} \tag{4.6.2}$$

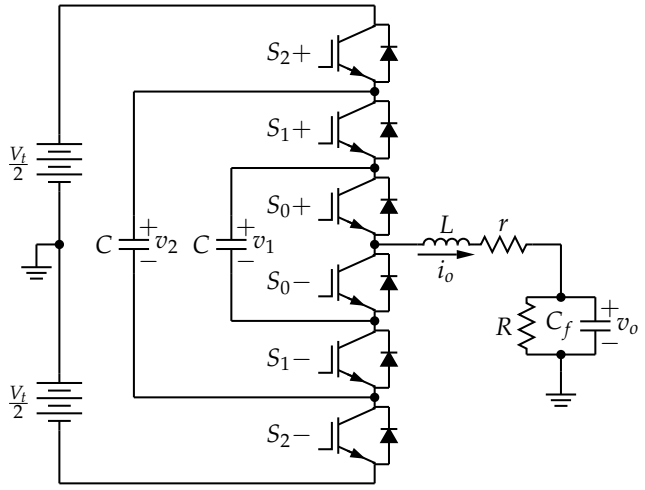

Figure 4.16: 3-Cell flying capacitor converter

The following difference and total parameters are defined:

$$
\begin{aligned}
s_t &= \frac{1}{2}(s_1 + s_2 + s_3) \\
s_{d1} &= \frac{1}{2}(s_1 - s_0) \\
s_{d2} &= \frac{1}{2}(s_2 - s_1) \\
v_{d1} &= \frac{V_t}{3} - v_1 \\
v_{d2} &= \frac{2V_t}{3} - v_2
\end{aligned}
$$

The system of differential equations can be rewritten in terms of the defined d and t parameters as [28]:

$$
\frac{d}{dt}\begin{bmatrix} C \cdot v_{d1} \\ C \cdot v_{d2} \\ L \cdot i_o \\ C_f \cdot v_o \end{bmatrix} = \begin{bmatrix} 0 & 0 & -s_{d1} & 0 \\ 0 & 0 & -s_{d2} & 0 \\ s_{d1} & s_{d2} & -r & -1 \\ 0 & 0 & 1 & \frac{-1}{R} \end{bmatrix} \begin{bmatrix} v_1 \\ v_2 \\ i_o \\ v_o \end{bmatrix} + \begin{bmatrix} 0 \\ 0 \\ s_t \\ 0 \end{bmatrix} \frac{V_t}{3} \tag{4.6.3}
$$

By using the variable turns-ratio transformer model, an equivalent circuit of the FCC can be redrawn in terms of d and t parameters (see Fig. 4.17).

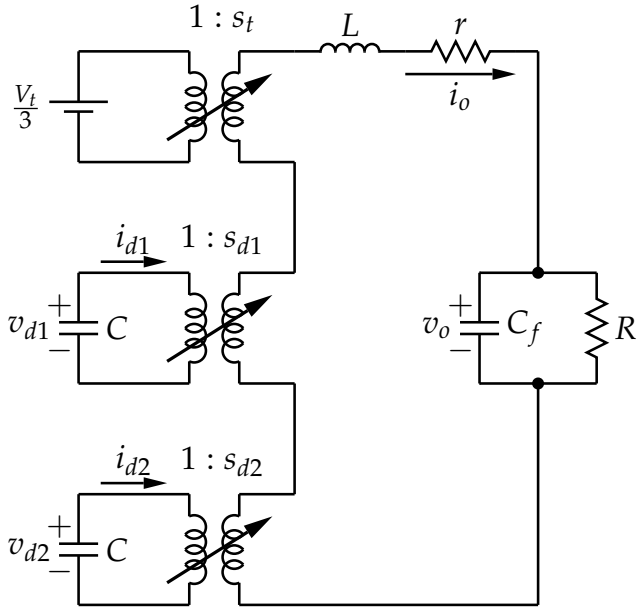

Figure 4.17: 3-Cell FCC in terms of d and t parameters

From Section 4.1.1 and as derived in Appendix A.6.2 the exponential Fourier

series coefficients of switching functions for the 3-cell FCC are

$$C_{0(n)} = \Psi(n) \tag{4.6.4}$$

$$C_{1(n)} = \Psi(n)e^{-j2\pi n\frac{1}{3}} = \Psi(n)\zeta_n^1 \tag{4.6.5}$$

$$C_{2(n)} = \Psi(n)e^{-j2\pi n\frac{2}{3}} = \Psi(n)\zeta_n^2 \tag{4.6.6}$$

$$\Psi(n) = \begin{cases} \frac{2}{\pi n}\sin(\pi n d) & \text{for } n \neq 0 \\ 2d-1 & \text{for } n = 0. \end{cases} \tag{4.6.7}$$

The function ζ_n^a is defined as $\zeta_n^a = e^{-j2\pi n\frac{a}{N}}$, where $N = 3$ for the 3-cell case.

4.6.1 Balancing Equation

Using the same assumptions as with the 2-cell case, namely, that the flying capacitor, C is large enough so that the switching frequency voltage ripple on v_1 and v_2 is negligible and that the capacitance is large enough that the capacitor voltage vary slow enough with time that the rest of the converter can be regarded as being in the steady state, the expressions for the averaged flying capacitor currents can be found as:

$$i_{d1} = \frac{V_t}{3}\left.\frac{S_t(\omega)}{Z(\omega)} * S_{d1}(\omega)\right|_{\omega=0} + V_{d1}\left.\frac{S_{d1}(\omega)}{Z(\omega)} * S_{d1}(\omega)\right|_{\omega=0} + V_{d2}\left.\frac{S_{d2}(\omega)}{Z(\omega)} * S_{d1}(\omega)\right|_{\omega=0} \tag{4.6.8}$$

$$i_{d2} = \frac{V_t}{3}\left.\frac{S_t(\omega)}{Z(\omega)} * S_{d2}(\omega)\right|_{\omega=0} + V_{d1}\left.\frac{S_{d1}(\omega)}{Z(\omega)} * S_{d2}(\omega)\right|_{\omega=0} + V_{d2}\left.\frac{S_{d2}(\omega)}{Z(\omega)} * S_{d2}(\omega)\right|_{\omega=0} \tag{4.6.9}$$

From previous discussions and as proven in Lemma 10 on p. 167:

$$\left.\frac{S_t(\omega)}{Z(\omega)} * S_{d1}(\omega)\right|_{\omega=0} = \left.\frac{S_t(\omega)}{Z(\omega)} * S_{d2}(\omega)\right|_{\omega=0} = 0 \tag{4.6.10}$$

Also,

$$\begin{aligned}
\frac{S_{d1}(\omega)}{Z(\omega)} * S_{d2}(\omega)\Big|_{\omega=0} &= \sum_{\xi=-\infty}^{\infty} \frac{S_{d1(\xi)}}{Z(\xi\omega_s)} S_{d2(-\xi)} \\
&= \sum_{\xi=-\infty}^{\infty} \frac{C_{1(\xi)} - C_{0(\xi)}}{4Z(\xi\omega_s)} \left(C_{2(-\xi)} - C_{1(-\xi)}\right) \\
&= \sum_{\xi=-\infty}^{\infty} \frac{\Psi(\xi)\left(\zeta_\xi^1 - \zeta_\xi^0\right)}{4Z(\xi\omega_s)} \Psi^*(\xi)\left(\zeta_{-\xi}^2 - \zeta_{-\xi}^1\right) \\
&= \sum_{\xi=-\infty}^{\infty} \frac{|\Psi(\xi)|^2}{4Z(\xi\omega_s)} \left(\zeta_\xi^1 - \zeta_\xi^0\right)\left(\zeta_\xi^{-2} - \zeta_\xi^{-1}\right) \\
&= \sum_{\xi=-\infty}^{\infty} \frac{|\Psi(\xi)|^2}{4Z(\xi\omega_s)} \left(\zeta_\xi^{-1} - \zeta_\xi^{-2} - \zeta_\xi^0 + \zeta_\xi^{-1}\right) \\
&= \sum_{\xi=-\infty}^{\infty} \frac{|\Psi(\xi)|^2}{4Z(\xi\omega_s)} \left(-\zeta_\xi^{-2} + 2\zeta_\xi^{-1} - \zeta_\xi^0\right) \\
&= \sum_{\xi=-\infty}^{\infty} \frac{|\Psi(\xi)|^2}{4Z(\xi\omega_s)} \zeta_\xi^{-1}\left(2 - \zeta_\xi^{-1} - \zeta_\xi^1\right) \\
&= \sum_{\xi=-\infty}^{\infty} \frac{|\Psi(\xi)|^2}{2Z(\xi\omega_s)} \left(1 - Re\left\{\zeta_\xi\right\}\right) \zeta_\xi^{-1} = \lambda_{12} \qquad (4.6.11)
\end{aligned}$$

and likewise:

$$\frac{S_{d1}(\omega)}{Z(\omega)} * S_{d1}(\omega)\Big|_{\omega=0} = \sum_{\xi=-\infty}^{\infty} \frac{|\Psi(\xi)|^2}{2Z(\xi\omega_s)} \left(1 - Re\left\{\zeta_\xi\right\}\right) = \lambda_{11} \qquad (4.6.12)$$

$$\frac{S_{d2}(\omega)}{Z(\omega)} * S_{d2}(\omega)\Big|_{\omega=0} = \sum_{\xi=-\infty}^{\infty} \frac{|\Psi(\xi)|^2}{2Z(\xi\omega_s)} \left(1 - Re\left\{\zeta_\xi\right\}\right) = \lambda_{22} = \lambda_{11} \qquad (4.6.13)$$

$$\frac{S_{d2}(\omega)}{Z(\omega)} * S_{d1}(\omega)\Big|_{\omega=0} = \sum_{\xi=-\infty}^{\infty} \frac{|\Psi(\xi)|^2}{2Z(\xi\omega_s)} \left(1 - Re\left\{\zeta_\xi\right\}\right) \zeta_\xi^1 = \lambda_{21} \qquad (4.6.14)$$

The expression for λ_{ab} is derived in Lemma 12 on p.170. The balancing equation can now be written as

$$-C\frac{d}{dt}\begin{bmatrix} v_{d1} \\ v_{d2} \end{bmatrix} = \begin{bmatrix} \lambda_{11} & \lambda_{12} \\ \lambda_{21} & \lambda_{11} \end{bmatrix} \begin{bmatrix} v_{d1} \\ v_{d2} \end{bmatrix}, \qquad (4.6.15)$$

or more compactly as:

$$C\dot{\mathbf{v}}_\mathbf{d} = -\mathbf{\Lambda}\mathbf{v}_\mathbf{d} \qquad (4.6.16)$$

4.6.2 Balancing of the 3-cell FCC

If φ_1 and φ_2 are the eigenvalues of $\mathbf{\Lambda}$ with corresponding eigenvectors $\mathbf{y_1}$ and $\mathbf{y_2}$, then the solution of (4.6.16) is [57, p.371] and [58, p. 184] (assuming that $\mathbf{\Lambda}$ is simple, or equivalently that no eigenvalue is repeated):

$$\mathbf{v}_\mathbf{d} = A\mathbf{y_1}e^{-\frac{\varphi_1}{C}t} + B\mathbf{y_2}e^{-\frac{\varphi_2}{C}t} \qquad (4.6.17)$$

with A and B constants corresponding to the initial values of the system.

Investigation of (4.6.17) reveals:

1. Should either φ_1 or φ_2 have a negative real part the system will be unbalanced.
2. The time constants of the system are given by $\tau_1 = C/Re\{\varphi_1\}$ and $\tau_2 = C/Re\{\varphi_2\}$.
3. If both eigenvalues are positive and real the smallest eigenvalue will correspond to the largest time constant.

Using the characteristic equation [59, p. 307] to calculate the eigenvalues implies finding all scalars φ for which the equation

$$(\mathbf{\Lambda} - \varphi\mathbf{I})\mathbf{y} = \mathbf{0} \tag{4.6.18}$$

has nontrivial solutions. This is equivalent to finding all φ such that the matrix $(\mathbf{\Lambda} - \varphi\mathbf{I})$ is not invertible, or

$$\det(\mathbf{\Lambda} - \varphi\mathbf{I}) = 0. \tag{4.6.19}$$

The determinant is found as:

$$\begin{aligned}\det(\mathbf{\Lambda} - \varphi\mathbf{I}) &= \det\begin{bmatrix} \lambda_{11} - \varphi & \lambda_{12} \\ \lambda_{21} & \lambda_{11} - \varphi \end{bmatrix} \\ &= (\lambda_{11} - \varphi)^2 - \lambda_{12}\lambda_{21} \\ &= \varphi^2 - 2\lambda_{11}\varphi + \lambda_{11}^2 - \lambda_{12}\lambda_{21}\end{aligned}$$

Setting $\det(\mathbf{\Lambda} - \varphi\mathbf{I}) = 0$, and solving the quadratic equation , yields the eigenvalues as:

$$\begin{aligned}\varphi_1, \varphi_2 &= \frac{2\lambda_{11} \pm \sqrt{(2\lambda_{11})^2 - 4(\lambda_{11}^2 - \lambda_{12}\lambda_{21})}}{2} \\ &= \lambda_{11} \pm \frac{1}{2}\sqrt{\lambda_{12}\lambda_{21}}\end{aligned} \tag{4.6.20}$$

4.6.2.1 Relationship Between λ_{12} and λ_{21}

The expression for λ_{12} (4.6.11) can be rewritten by combining the sum for positive and negative values of ξ, and realising that $Re\left\{\zeta_{\xi}\right\} = 1$ when $\xi = 0$, as:

$$\begin{aligned}
\lambda_{12} &= \sum_{\xi=-\infty}^{\infty} \frac{|\Psi(\xi)|^2}{2Z(\xi\omega_s)} \left(1 - Re\left\{\zeta_{\xi}\right\}\right) \zeta_{\xi}^{-1} \\
&= \sum_{\xi=1}^{\infty} \frac{|\Psi(\xi)|^2}{2Z(\xi\omega_s)} \left(1 - Re\left\{\zeta_{\xi}\right\}\right) \zeta_{\xi}^{-1} + \sum_{\xi=1}^{\infty} \frac{|\Psi(\xi)|^2}{2Z(-\xi\omega_s)} \left(1 - Re\left\{\zeta_{-\xi}\right\}\right) \zeta_{-\xi}^{-1} \\
&= \sum_{\xi=1}^{\infty} |\Psi(\xi)|^2 \left(1 - Re\left\{\zeta_{\xi}\right\}\right) \left(\frac{\zeta_{\xi}^{-1}}{2Z(\xi\omega_s)} + \frac{\zeta_{-\xi}^{-1}}{2Z(-\xi\omega_s)}\right) \\
&= \sum_{\xi=1}^{\infty} \frac{|\Psi(\xi)|^2}{|Z(\xi\omega_s)|^2} \left(1 - Re\left\{\zeta_{\xi}\right\}\right) Re\left\{Z(\xi\omega_s)\zeta_{\xi}^{1}\right\} \qquad (4.6.21) \\
&= \sum_{\xi=1}^{\infty} \frac{|\Psi(\xi)|^2}{|Z(\xi\omega_s)|^2} \left(1 - Re\left\{\zeta_{\xi}\right\}\right) \alpha_{12} \qquad (4.6.22)
\end{aligned}$$

Similarly, the expression for λ_{21}, (4.6.14), can be rewritten as:

$$\begin{aligned}
\lambda_{21} &= \sum_{\xi=1}^{\infty} \frac{|\Psi(\xi)|^2}{|Z(\xi\omega_s)|^2} \left(1 - Re\left\{\zeta_{\xi}\right\}\right) Re\left\{Z(\xi\omega_s)\zeta_{\xi}^{-1}\right\} \qquad (4.6.23) \\
&= \sum_{\xi=1}^{\infty} \frac{|\Psi(\xi)|^2}{|Z(\xi\omega_s)|^2} \left(1 - Re\left\{\zeta_{\xi}\right\}\right) \alpha_{21} \qquad (4.6.24)
\end{aligned}$$

This derivation for an alternate expression for λ_{ab} is generalised and proven in Lemma 14 on p.171.

The only variation between λ_{12} and λ_{21} is the α term. Furthermore, it is true that for all $\xi \in \mathbb{Z}$

$$\frac{|\Psi(\xi)|^2}{|Z(\xi\omega_s)|^2} \left(1 - Re\left\{\zeta_{\xi}\right\}\right) > 0. \qquad (4.6.25)$$

The α_{12} term can be rewritten as:

$$\begin{aligned}
\alpha_{12} &= Re\left\{Z(\xi\omega_s)\zeta_{\xi}^{-1}\right\} \\
&= Re\left\{Z(\xi\omega_s)\right\} Re\left\{\zeta_{\xi}^{-1}\right\} - Im\left\{Z(\xi\omega_s)\right\} Im\left\{\zeta_{\xi}^{-1}\right\} \qquad (4.6.26)
\end{aligned}$$

likewise

$$\alpha_{21} = Re\left\{Z(\xi\omega_s)\right\} Re\left\{\zeta_{\xi}^{1}\right\} - Im\left\{Z(\xi\omega_s)\right\} Im\left\{\zeta_{\xi}^{1}\right\}. \qquad (4.6.27)$$

For most load and filter combinations it is true that the impedance of the filter inductance dominates the load impedance at the switching frequency and higher. This is especially true for systems with a LC output filter. However, in certain drive applications, especially with a low switching frequency, this statement will not be true. Assuming that the statement hold, it is true that $Re\left\{Z(\omega)\right\} \ll Im\left\{Z(\omega)\right\}$ at the frequencies of interest and therefore only the $Im\left\{Z(\xi\omega_s)\right\} Im\left\{\zeta_{\xi}^{1}\right\}$ part of the expression for α will be considered.

It is true that when ξ is an integer multiple of 3

$$\left(1 - Re\left\{\zeta_{\xi}\right\}\right) = 0. \tag{4.6.28}$$

Furthermore for ξ is not an integer multiple of 3

$$\begin{aligned} Im\left\{\zeta_{\xi}^{-1}\right\} &= Im\left\{e^{j\frac{\xi}{3}}\right\} \\ &= -Im\left\{e^{-j\frac{\xi}{3}}\right\} = -Im\left\{\zeta_{\xi}^{1}\right\}, \end{aligned} \tag{4.6.29}$$

and therefore

$$\alpha_{12} > 0 \Longleftrightarrow \alpha_{21} < 0. \tag{4.6.30}$$

It is therefore true that

$$\lambda_{12}\lambda_{21} < 0. \tag{4.6.31}$$

4.6.2.2 Rebalancing Time Constant

If the result of (4.6.31) is introduced into the expression for the eigenvalues, (4.6.20), the eigenvalues are found as

$$\varphi_1, \varphi_2 = \lambda_{11} \pm j\frac{1}{2}\sqrt{\lambda_{12}\lambda_{21}}, \tag{4.6.32}$$

and therefore,

$$Re\left\{\varphi_1\right\} = Re\left\{\varphi_2\right\} = \lambda_{11}. \tag{4.6.33}$$

Using the method of combining the sum for positive and negative values of ξ used to derive alternate expressions for λ_{12} and λ_{21} the expression

$$\lambda_{11} = \sum_{\xi=-\infty}^{\infty} \frac{|\Psi(\xi)|^2}{2Z(\xi\omega_s)}\left(1 - Re\left\{\zeta_{\xi}\right\}\right),$$

can be rewritten as

$$\lambda_{11} = \sum_{\xi=1}^{\infty} \frac{|\Psi(\xi)|^2}{|Z(\xi\omega_s)|^2}\left(1 - Re\left\{\zeta_{\xi}\right\}\right) Re\left\{Z(\xi\omega_s)\right\}. \tag{4.6.34}$$

It is clear that

$$\lambda_{11} > 0 \tag{4.6.35}$$

when $Re\left\{Z(\xi\omega_s)\right\} > 0$, consistent with non-regenerative loads.

Using this proof that $Re\left\{\varphi_1\right\} > 0$ and $Re\left\{\varphi_2\right\} > 0$, it is clear that the system will always rebalance with time constant

$$\tau = \frac{C}{\lambda_{11}}. \tag{4.6.36}$$

The expression for the time constant can be rewritten, using the same methodology as in Section 4.2. Using (4.2.7), repeated for convenience as

$$|\Psi(\xi)|^2 = \frac{2(1 - \cos(2\pi\xi d)}{\pi^2\xi^2},$$

and assuming that the filter inductor characteristics dominates $Z(\omega)$, (4.6.34) can be rewritten as:

$$\lambda_{11} = \sum_{\xi=1}^{\infty} \frac{(1-\cos(2\pi\xi d)r}{2\pi^4 f^2 L^2 \xi^4} \left(1 - Re\left\{\zeta_\xi\right\}\right) \tag{4.6.37}$$

This is equivalent to (4.2.9) found for the 2-cell case; where, for the 2-cell case $\zeta_\xi = (-1)^\xi$.

In the 2-cell case, with reference to Fig. 4.5, it was possible to approximate the sum using only the first term, (4.2.10) repeated as

$$\sum_{\xi=1,3}^{\infty} \frac{1-\cos(2\pi\xi d)}{\xi^4} \approx 1 - \cos(2\pi d).$$

However, since $\zeta_\xi \neq (-1)^\xi$ for a higher numbers of cells, the accuracy of this approximation diminishes as the number of cells increases. For the 3-cell case this approximation is still usable, especially at duty cycles around 50%, as shown in Fig. 4.18. However, as the duty cycle approaches either 0% or 100%, the error becomes high, up to 30%, as shown in the second part of Fig. 4.18.

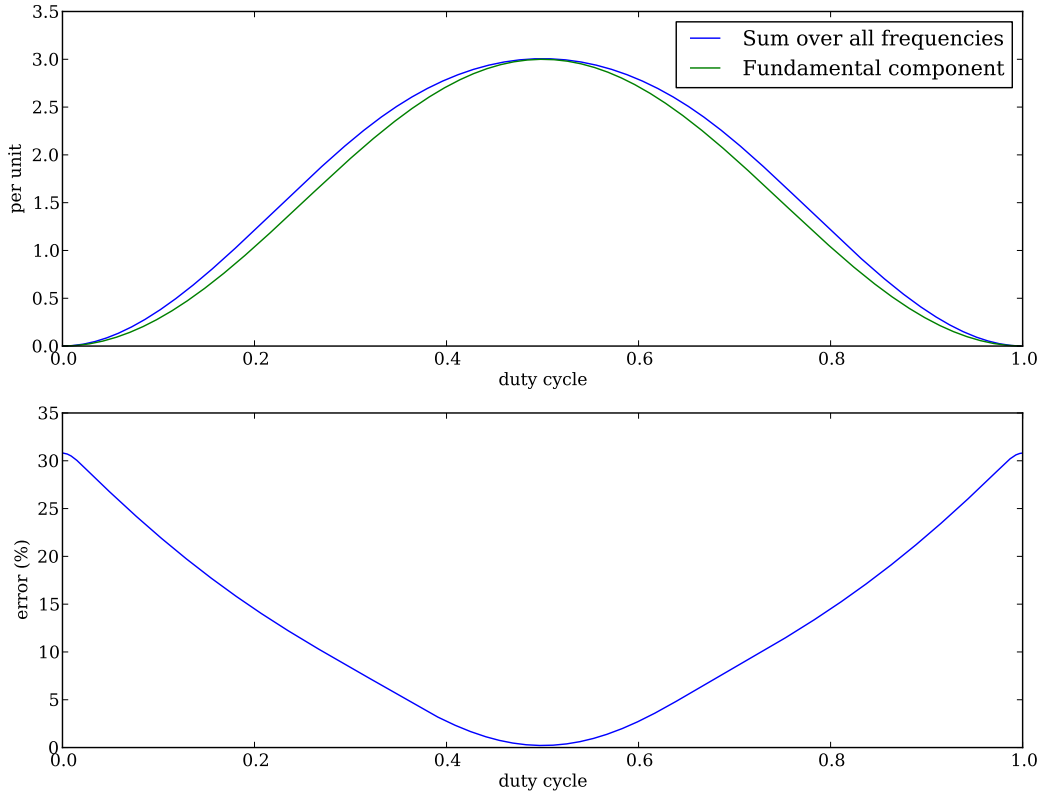

Figure 4.18: Approximation of $\sum_{\xi=1}^{\infty} \frac{(1-\cos(2\pi\xi d)}{\xi^4} \left(1 - Re\left\{\zeta_\xi\right\}\right)$

Therefore using

$$\sum_{\xi=1}^{\infty} \frac{(1-\cos(2\pi\xi d)}{\xi^4}\left(1-Re\left\{\zeta_\xi\right\}\right) \approx (1-\cos(2\pi d))\left(1-\cos\left(\frac{2}{3}\pi\right)\right), \quad (4.6.38)$$

the time constant can be approximated as:

$$\tau = \frac{2\pi^4 f^2 L^2 C}{(1-\cos(2\pi d))(1-\cos(2\pi/3))r} \quad (4.6.39)$$

Although this yields a fast approximation, the error at extreme values of the duty cycle is high. Using the sum over all frequencies, the time constant can be more accurately approximated as

$$\begin{aligned}\tau &= \frac{C}{\frac{r}{f^2L^2}\sum_{\xi=1}^{\infty}\frac{(1-\cos(2\pi\xi d)}{2\pi^4\xi^4}\left(1-Re\left\{\zeta_\xi\right\}\right)} \\ &= \frac{f^2L^2C}{r}\tau_r \end{aligned} \quad (4.6.40)$$

where,

$$\tau_r = \left(\sum_{\xi=1}^{\infty}\frac{(1-\cos(2\pi\xi d)}{2\pi^4\xi^4}\left(1-Re\left\{\zeta_\xi\right\}\right)\right)^{-1}. \quad (4.6.41)$$

The value of τ_r is independent of the circuit parameters. This approximation is accurate and can be used when:

1. The behaviour of $Z(\omega)$ at the switching frequency and higher is dominated by the filter inductor.

2. The inductor is manufactured in such a way that the skin- and proximity effects are negligible.

The values for τ_r are tabulated for different duty cycles in Appendix E, Table E.1. It is therefore possible to approximate the time constant accurately for any 3-cell FCC when the values of r, L, C and f are known, by using (4.6.40) and the value of τ_r corresponding to the operating duty cycle.

Under conditions where the filter inductor does not dominate the behaviour of the load at the switching frequency the time constant can be calculated using

$$\tau = \frac{C}{\sum_{\xi=1}^{\infty}\frac{(1-\cos(2\pi\xi d)}{|Z(\xi\omega_s)|^2}\left(1-Re\left\{\zeta_\xi\right\}\right)Re\left\{Z(\xi\omega_s)\right\}}. \quad (4.6.42)$$

4.7 N-Cell FCC with Constant Duty Cycle

From the circuit of Fig. 4.19, the system of differential equations describing the circuit operation can be found as:

$$\frac{d}{dt}\begin{bmatrix} 2C\cdot v_1 \\ 2C\cdot v_2 \\ \vdots \\ 2C\cdot v_{N-1} \\ L\cdot i_o \\ C_f\cdot v_o \end{bmatrix} = \begin{bmatrix} 0 \\ 0 \\ \vdots \\ 0 \\ s_{N-1} \\ 0 \end{bmatrix}\frac{V_t}{2} + \begin{bmatrix} 0 & 0 & \dots & 0 & s_1-s_0 & 0 \\ 0 & 0 & \dots & 0 & s_2-s_1 & 0 \\ \vdots & \vdots & \ddots & \vdots & \vdots & \vdots \\ 0 & 0 & \dots & 0 & s_{N-1}-s_{N-2} & 0 \\ \frac{1}{2}(s_0-s_1) & \frac{1}{2}(s_1-s_2) & \dots & \frac{1}{2}(s_{N-2}-s_{N-1}) & -r & -1 \\ 0 & 0 & \dots & 0 & 1 & \frac{-1}{R} \end{bmatrix}\begin{bmatrix} v_1 \\ v_2 \\ \vdots \\ v_{N-1} \\ i_o \\ v_o \end{bmatrix} \tag{4.7.1}$$

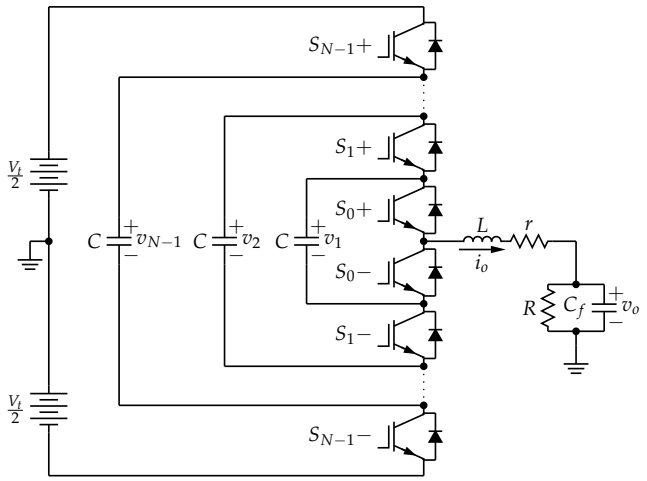

Figure 4.19: N-Cell flying capacitor converter

The following difference and total parameters are defined:

$$s_t = \frac{1}{2}\sum_{n=0}^{N-1} s_n$$

$$s_{dn} = \frac{1}{2}(s_n - s_{n-1}) \qquad \text{for } n = 1,\dots,N-1$$

$$v_{dn} = \frac{nV_t}{N} - v_n \qquad \text{for } n = 1,\dots,N-1$$

The system of differential equations can be rewritten in terms of the defined d and t parameters as [28, Section 2.11]:

$$\frac{d}{dt}\begin{bmatrix} C\cdot v_{d1} \\ C\cdot v_{d2} \\ \vdots \\ C\cdot v_{d(N-1)} \\ L\cdot i_o \\ C_f\cdot v_o \end{bmatrix} = \begin{bmatrix} 0 & 0 & \dots & 0 & -s_{d1} & 0 \\ 0 & 0 & \dots & 0 & -s_{d2} & 0 \\ \vdots & \vdots & \ddots & \vdots & \vdots & \vdots \\ 0 & 0 & \dots & 0 & -s_{d(N-1)} & 0 \\ s_{d1} & s_{d2} & \dots & s_{d(N-1)} & -r & -1 \\ 0 & 0 & \dots & 0 & 1 & \frac{-1}{R} \end{bmatrix} \begin{bmatrix} v_{d1} \\ v_{d2} \\ \vdots \\ v_{d(N-1)} \\ i_o \\ v_o \end{bmatrix} + \begin{bmatrix} 0 \\ 0 \\ \vdots \\ 0 \\ s_t \\ 0 \end{bmatrix} \frac{V_t}{N} \tag{4.7.2}$$

By using of the variable turns-ratio transformer model, an equivalent circuit of the FCC can be redrawn in terms of d and t parameters, Fig. 4.20.

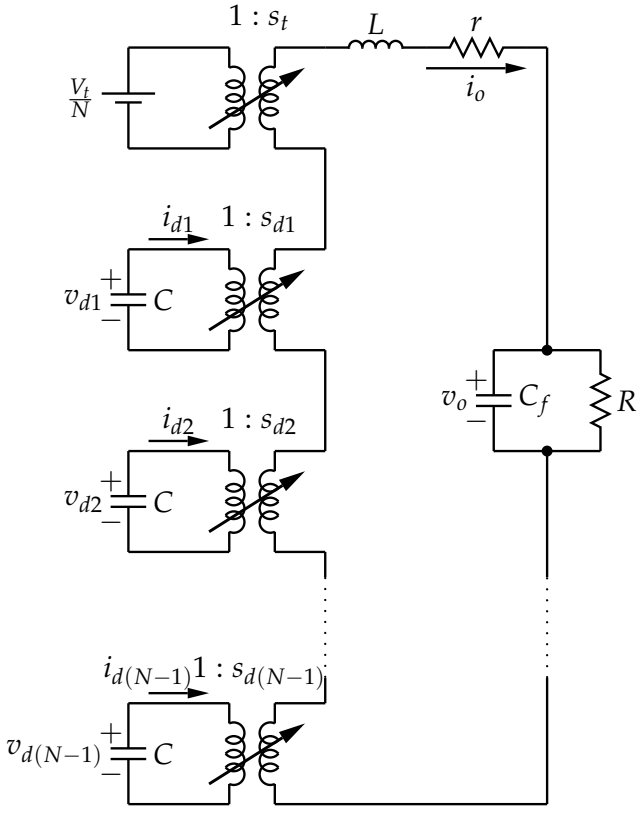

Figure 4.20: N-Cell FCC in terms of d and t parameters

From Section 4.1.1 and as derived in Appendix A.6.2 the exponential Fourier series coefficients of switching functions for the N-cell FCC are

$$C_{0(n)} = \Psi(n) \tag{4.7.3}$$

$$C_{x(n)} = \Psi(n)e^{-j2\pi n\frac{x}{N}} = \Psi(n)\zeta_n^x \tag{4.7.4}$$

$$\Psi(n) = \begin{cases} \frac{2}{\pi n}\sin(\pi n d) & \text{for } n \neq 0 \\ 2d-1 & \text{for } n = 0. \end{cases} \tag{4.7.5}$$

The function ζ_n^a is defined as $\zeta_n^a = e^{-j2\pi n\frac{a}{N}}$.

4.7.1 Balancing Equation

The same assumptions as with the 2- and 3-cell cases are used. It is assumed that that C is sufficiently large that the switching frequency voltage ripple on the flying capacitor is negligible. It is furthermore assumed that the capacitance is large enough that the capacitor voltage vary slow enough with time that the rest of the converter can be regarded as being in the steady state. An expression for the average current through the flying capacitor of cell a where $0 \leq a \leq N-1$ can be found as

$$i_{da} = \frac{V_t}{N}\left.\frac{S_t(\omega)}{Z(\omega)} * S_{da}(\omega)\right|_{\omega=0} + \sum_{n=1}^{N-1} V_{dn}\left.\frac{S_{dn}(\omega)}{Z(\omega)} * S_{da}(\omega)\right|_{\omega=0}. \tag{4.7.6}$$

It is shown in Lemma 15 on p.172 that

$$\frac{V_t}{N}\left.\frac{S_t(\omega)}{Z(\omega)} * S_{dn}(\omega)\right|_{\omega=0} = 0. \tag{4.7.7}$$

Rewriting this in matrix form, the balancing equation can be expressed as:

$$-\frac{d}{dt}C\begin{bmatrix} Vd_1 \\ Vd_2 \\ \vdots \\ Vd_{N-1}\end{bmatrix} = \begin{bmatrix} \lambda_{11} & \lambda_{12} & \cdots & \lambda_{1(N-1)} \\ \lambda_{21} & \lambda_{22} & \cdots & \lambda_{2(N-1)} \\ \vdots & \vdots & \ddots & \vdots \\ \lambda_{(N-1)1} & \lambda_{(N-1)2} & \cdots & \lambda_{(N-1)(N-1)}\end{bmatrix}\begin{bmatrix} Vd_1 \\ Vd_2 \\ \vdots \\ Vd_{N-1}\end{bmatrix} \tag{4.7.8}$$

where

$$\lambda_{ab} = \left.\frac{S_{db}(\omega)}{Z(\omega)} * S_{da}(\omega)\right|_{\omega=0}. \tag{4.7.9}$$

The value for λ_{ab} can be found for any value of $1 \leq a, b \leq N-1$ as

$$\lambda_{ab} = \sum_{\xi=-\infty}^{\infty} \frac{|\Psi(\xi)|^2}{2Z(\xi\omega_s)}\left(1 - Re\left\{\zeta_\xi\right\}\right)\zeta_\xi^{b-a},$$

by realising that $\zeta_{-n}^x = \zeta_n^{-x}$. This result is proven in Lemma 12 on p.170. The ζ_ξ^{b-a} term is the only variation between the different entries. In fact, the periodic nature of ζ_ξ^{b-a} gives the $b-a$ term a modulus of N resulting in N distinct entries, and therefore $\mathbf{\Lambda}$ has a Toeplitz structure [60, p.1] [1].

The balancing equation can be rewritten as:

$$C\dot{\mathbf{v}}_\mathbf{d} = -\mathbf{\Lambda}\mathbf{v}_\mathbf{d} \tag{4.7.10}$$

where

$$\mathbf{\Lambda} = \begin{bmatrix} z_0 & z_1 & z_2 & \cdots & z_{N-2} \\ z_{N-1} & z_0 & z_1 & \cdots & z_{N-3} \\ z_{N-2} & z_{N-1} & z_0 & \cdots & z_{N-4} \\ \vdots & \vdots & \vdots & \ddots & \vdots \\ z_2 & z_3 & z_4 & \cdots & z_0\end{bmatrix} \tag{4.7.11}$$

[1] A short overview of matrix types is included in Appendix A.2 on p. 159

$$z_a = \sum_{\xi=-\infty}^{\infty} \frac{|\Psi(\xi)|^2}{2Z(\xi\omega_s)} \left(1 - Re\left\{\zeta_\xi\right\}\right) \zeta_\xi^a. \tag{4.7.12}$$

4.7.2 Characteristics of the Λ Matrix

As proven in Lemma 14 on p.171, the expression for z_a can be rewritten as

$$\begin{aligned} z_a &= \sum_{\xi=1}^{\infty} \frac{|\Psi(\xi)|^2}{2|Z(\xi\omega_s)|^2} \left(1 - Re\left\{\zeta_\xi\right\}\right) \left(Re\left\{Z(\xi\omega_s)\right\} Re\left\{\zeta_\xi^a\right\} - Im\left\{Z(\xi\omega_s)\right\} Im\left\{\zeta_{-\xi}^a\right\}\right) \\ &= x_a + y_a, \end{aligned} \tag{4.7.13}$$

where

$$x_a = \sum_{\xi=1}^{\infty} \frac{|\Psi(\xi)|^2}{|Z(\xi\omega_s)|^2} \left(1 - Re\left\{\zeta_\xi\right\}\right) Re\left\{Z(\xi\omega_s)\right\} Re\left\{\zeta_\xi^a\right\} \tag{4.7.14}$$

$$y_a = \sum_{\xi=1}^{\infty} \frac{|\Psi(\xi)|^2}{|Z(\xi\omega_s)|^2} \left(1 - Re\left\{\zeta_\xi\right\}\right) Im\left\{Z(\xi\omega_s)\right\} Im\left\{\zeta_\xi^a\right\}. \tag{4.7.15}$$

Theorem 1. *Every square matrix* $\mathbf{A}$ *can be written uniquely as the sum of a symmetric matrix,* $\mathbf{A_s}$*, and a skew-symmetric matrix* $\mathbf{A_{sk}}$*, where [61, p. 151]:*

$$\begin{aligned} \mathbf{A} &= \mathbf{A_s} + \mathbf{A_{sk}} \\ \mathbf{A_s} &= \frac{\mathbf{A} + \mathbf{A}^\mathbf{T}}{2} \\ \mathbf{A_{sk}} &= \frac{\mathbf{A} - \mathbf{A}^\mathbf{T}}{2} \end{aligned}$$

In the case of (4.7.11), $\mathbf{\Lambda}$ decomposes naturally into symmetric and skew-symmetric parts as:

$$\mathbf{\Lambda} = \mathbf{\Lambda_s} + \mathbf{\Lambda_{sk}}, \tag{4.7.16}$$

where

$$\mathbf{\Lambda_s} = \begin{bmatrix} x_0 & x_1 & x_2 & \cdots & x_{N-2} \\ x_{N-1} & x_0 & x_1 & \cdots & x_{N-3} \\ x_{N-2} & x_{N-1} & x_0 & \cdots & x_{N-4} \\ \vdots & \vdots & \vdots & \ddots & \vdots \\ x_2 & x_3 & x_4 & \cdots & x_0 \end{bmatrix} \tag{4.7.17}$$

and

$$\mathbf{\Lambda_{sk}} = \begin{bmatrix} y_0 & y_1 & y_2 & \cdots & y_{N-2} \\ y_{N-1} & y_0 & y_1 & \cdots & y_{N-3} \\ y_{N-2} & y_{N-1} & y_0 & \cdots & y_{N-4} \\ \vdots & \vdots & \vdots & \ddots & \vdots \\ y_2 & y_3 & y_4 & \cdots & y_0 \end{bmatrix}. \tag{4.7.18}$$

4.7.2.1 Characteristics of the $\mathbf{\Lambda_s}$ Matrix

Using (4.7.17) and (4.7.14) it is true that

$$\mathbf{\Lambda_s} = \sum_{n=1}^{\infty} \mathbf{\Lambda_{s(n)}} \tag{4.7.19}$$

where

$$\mathbf{\Lambda_{s(n)}} = \begin{bmatrix} x_0(n) & x_1(n) & x_2(n) & \cdots & x_{N-2}(n) \\ x_{N-1}(n) & x_0(n) & x_1(n) & \cdots & x_{N-3}(n) \\ x_{N-2}(n) & x_{N-1}(n) & x_0(n) & \cdots & x_{N-4}(n) \\ \vdots & \vdots & \vdots & \ddots & \vdots \\ x_2(n) & x_3(n) & x_4(n) & \cdots & x_0(n) \end{bmatrix} \tag{4.7.20}$$

and

$$x_a(n) = \frac{|\Psi(n)|^2}{|Z(n\omega_s)|^2} \left(1 - Re\left\{\zeta_n\right\}\right) Re\left\{Z(n\omega_s)\right\} Re\left\{\zeta_n^a\right\}. \tag{4.7.21}$$

Using (4.7.21) it is possible to rewrite (4.7.20) as:

$$\mathbf{\Lambda_{s(n)}} = \alpha(n) \begin{bmatrix} 1 & \cos(2\pi n \frac{1}{N}) & \cos(2\pi n \frac{2}{N}) & \cdots & \cos(2\pi n \frac{N-2}{N}) \\ \cos(2\pi n \frac{N-1}{N}) & 1 & \cos(2\pi n \frac{1}{N}) & \cdots & \cos(2\pi n \frac{N-3}{N}) \\ \cos(2\pi n \frac{N-2}{N}) & \cos(2\pi n \frac{N-1}{N}) & 1 & \cdots & \cos(2\pi n \frac{N-4}{N}) \\ \vdots & \vdots & \vdots & \ddots & \vdots \\ \cos(2\pi n \frac{2}{N}) & \cos(2\pi n \frac{3}{N}) & \cos(2\pi n \frac{4}{N}) & \cdots & 1 \end{bmatrix} \tag{4.7.22}$$

$$\alpha(n) = \frac{|\Psi(n)|^2}{|Z(n\omega_s)|^2} \left(1 - Re\left\{\zeta_n\right\}\right) Re\left\{Z(n\omega_s)\right\} \tag{4.7.23}$$

It is true that

$$\cos\left(2\pi n \frac{a}{N}\right) = \cos\left(2\pi n \frac{N-a}{N}\right), \tag{4.7.24}$$

therefore rewriting (4.7.22) yields:

$$\mathbf{\Lambda_{s(n)}} = \alpha(n) \begin{bmatrix} 1 & \cos(2\pi n \frac{1}{N}) & \cos(2\pi n \frac{2}{N}) & \cdots & \cos(2\pi n \frac{2}{N}) \\ \cos(2\pi n \frac{1}{N}) & 1 & \cos(2\pi n \frac{1}{N}) & \cdots & \cos(2\pi n \frac{3}{N}) \\ \cos(2\pi n \frac{2}{N}) & \cos(2\pi n \frac{1}{N}) & 1 & \cdots & \cos(2\pi n \frac{4}{N}) \\ \vdots & \vdots & \vdots & \ddots & \vdots \\ \cos(2\pi n \frac{2}{N}) & \cos(2\pi n \frac{3}{N}) & \cos(2\pi n \frac{4}{N}) & \cdots & 1 \end{bmatrix} \tag{4.7.25}$$

It is clear that $\mathbf{\Lambda_{s(n)}}$ is a symmetric matrix since

$$\mathbf{\Lambda_{s(n)}} = \mathbf{\Lambda_{s(n)}}^{\mathbf{T}}. \tag{4.7.26}$$

Due to the infinite summation $\mathbf{\Lambda_s}$ will only exist when

$$\sum_{n=1}^{\infty} \alpha(n) \tag{4.7.27}$$

converges. Using $Z(n\omega_s) = |Z(n\omega_s)|\angle\theta_n$, where $Re\{Z(n\omega_s)\} > 0$, and the expression for the Fourier series coefficients it is true that:

$$\begin{aligned}\sum_{n=1}^{\infty} \alpha(n) &= \sum_{n=1}^{\infty} \left(1 - Re\left\{\zeta_{\xi}^{n}\right\}\right) \frac{4\sin^2(\pi n d)\cos(\theta_n)|Z(n\omega_s)|}{\pi^2 n^2 |Z(n\omega_s)|^2} \\ &\leq \frac{8}{\pi^2} \sum_{n=1}^{\infty} \frac{1}{n^2 |Z(n\omega_s)|}\end{aligned}$$

Let $\varepsilon \in \mathbb{R}$ and $\varepsilon \geq 0$. It is true that the series

$$\sum_{n=1}^{\infty} \frac{1}{\varepsilon n^2} = \frac{\pi^2}{6\varepsilon} \tag{4.7.28}$$

converges absolutely. Furthermore, when $Re\{Z(n\omega_s)\} \geq \varepsilon$ for all n, it is true that

$$\left|\frac{1}{\varepsilon n^2}\right| \geq \left|\frac{1}{n^2 |Z(n\omega_s)|}\right|. \tag{4.7.29}$$

Therefore, according to the direct comparison test, the convergence of (4.7.28) implies that (4.7.27) converges absolutely when $Re\{Z(n\omega_s)\} > 0$.

Furthermore, the same series are used for the diagonal entries of $\mathbf{\Lambda_s}$. It is also true that the function $\mathbf{A} \mapsto \mathbf{A^T}$ is continuous. Therefore the matrix $\mathbf{\Lambda_s}$ will be symmetric and

$$\mathbf{\Lambda_s} = \mathbf{\Lambda_s^T}. \tag{4.7.30}$$

4.7.2.2 Characteristics of the $\mathbf{\Lambda_{sk}}$ Matrix

Using (4.7.18) and (4.7.15) it is true that

$$\mathbf{\Lambda_{sk}} = \sum_{n=1}^{\infty} \mathbf{\Lambda_{sk(n)}} \tag{4.7.31}$$

where

$$\mathbf{\Lambda_{sk(n)}} = \begin{bmatrix} y_0(n) & y_1(n) & y_2(n) & \cdots & y_{N-2}(n) \\ y_{N-1}(n) & y_0(n) & y_1(n) & \cdots & y_{N-3}(n) \\ y_{N-2}(n) & y_{N-1}(n) & y_0(n) & \cdots & y_{N-4}(n) \\ \vdots & \vdots & \vdots & \ddots & \vdots \\ y_2(n) & y_3(n) & y_4(n) & \cdots & y_0(n) \end{bmatrix} \tag{4.7.32}$$

and

$$y_a(n) = \frac{|\Psi(n)|^2}{|Z(n\omega_s)|^2} \left(1 - Re\{\zeta_n\}\right) Im\{\zeta_n^a\} Im\{Z(n\omega_s)\}. \tag{4.7.33}$$

Using (4.7.33) it is possible to rewrite (4.7.32) as:

$$\mathbf{\Lambda_{sk(n)}} = \beta(n) \begin{bmatrix} 0 & \sin(2\pi n\frac{1}{N}) & \sin(2\pi n\frac{2}{N}) & \cdots & \sin(2\pi n\frac{N-2}{N}) \\ \sin(2\pi n\frac{N-1}{N}) & 0 & \sin(2\pi n\frac{1}{N}) & \cdots & \sin(2\pi n\frac{N-3}{N}) \\ \sin(2\pi n\frac{N-2}{N}) & \sin(2\pi n\frac{N-1}{N}) & 0 & \cdots & \sin(2\pi n\frac{N-4}{N}) \\ \vdots & \vdots & \vdots & \ddots & \vdots \\ \sin(2\pi n\frac{2}{N}) & \sin(2\pi n\frac{3}{N}) & \sin(2\pi n\frac{4}{N}) & \cdots & 0 \end{bmatrix} \tag{4.7.34}$$

$$\beta(n) = \frac{|\Psi(n)|^2}{|Z(n\omega_s)|^2}\left(1 - Re\left\{\zeta_n\right\}\right) Im\left\{Z(n\omega_s)\right\} \tag{4.7.35}$$

It is true that

$$\sin\left(2\pi n\frac{a}{N}\right) = -\sin\left(2\pi n\frac{N-a}{N}\right), \tag{4.7.36}$$

therefore rewriting (4.7.34) yields:

$$\mathbf{\Lambda_{sk(n)}} = \beta(n) \begin{bmatrix} 0 & \sin(2\pi n\frac{1}{N}) & \sin(2\pi n\frac{2}{N}) & \cdots & -\sin(2\pi n\frac{2}{N}) \\ -\sin(2\pi n\frac{1}{N}) & 0 & \sin(2\pi n\frac{1}{N}) & \cdots & -\sin(2\pi n\frac{3}{N}) \\ -\sin(2\pi n\frac{2}{N}) & -\sin(2\pi n\frac{1}{N}) & 0 & \cdots & -\sin(2\pi n\frac{4}{N}) \\ \vdots & \vdots & \vdots & \ddots & \vdots \\ \sin(2\pi n\frac{2}{N}) & \sin(2\pi n\frac{3}{N}) & \sin(2\pi n\frac{4}{N}) & \cdots & 0 \end{bmatrix} \tag{4.7.37}$$

It is clear that $\mathbf{\Lambda_{sk(n)}}$ is a skew-symmetric matrix since,

$$\mathbf{\Lambda_{sk(n)}} = -\mathbf{\Lambda_{sk(n)}}^{\mathbf{T}}. \tag{4.7.38}$$

Using the same reasoning as with $\mathbf{\Lambda_s}$ it is true that the infinite summation of $\beta(n)$ converges and since the same series are used for the different entries of $\mathbf{\Lambda_{sk(n)}}$ and that the function $\mathbf{A} \mapsto -\mathbf{A^T}$ is continuous it follows that $\mathbf{A_{sk}}$ is skew-symmetric and

$$\mathbf{\Lambda_{sk}} = -\mathbf{\Lambda_{sk}^T}. \tag{4.7.39}$$

It was shown that $\mathbf{\Lambda}$ decomposes naturally into the sum of two matrices $\mathbf{\Lambda_s}$ and $\mathbf{\Lambda_{sk}}$. Furthermore it was shown that $\mathbf{\Lambda_s}$ is symmetric and $\mathbf{\Lambda_{sk}}$ is skew symmetric. According to Theorem 1 the decomposition of a square matrix into the sum of a symmetric, skew-symmetric matrix pair is unique and therefore apart from the original expressions for $\mathbf{\Lambda_s}$ and $\mathbf{\Lambda_{sk}}$, equations (4.7.17) and (4.7.18), the matrices can also from Theorem 1 be written by using the definition of $\mathbf{\Lambda}$ in (4.7.11) as

$$\mathbf{\Lambda_s} = \frac{\mathbf{\Lambda} + \mathbf{\Lambda^T}}{2} \tag{4.7.40}$$

$$\mathbf{\Lambda_{sk}} = \frac{\mathbf{\Lambda} - \mathbf{\Lambda^T}}{2}. \tag{4.7.41}$$

4.7.3 Stability Analysis

Having proven that $\mathbf{\Lambda}$ can be decomposed into the sum of two (one symmetric and the other skew-symmetric) matrices, it is possible to investigate the system's stability. First an intuitive feel for the balancing equation using an analogous example from non-rigid body dynamics will be presented.

4.7.3.1 Equivalence to Mechanical Systems

The following example from [63] gives insight into the rebalancing behaviour of the FCC.

Let $\mathbf{f} : \mathbb{R}^n \mapsto \mathbb{R}^n$ be any differentiable function, choosing an $\mathbf{x_0} \in \mathbb{R}^n$ and using Taylor's theorem

$$\mathbf{f}(\mathbf{x}) = \mathbf{f}(\mathbf{x_0}) + \frac{d}{dt}\mathbf{f}(\mathbf{x_0})\Delta\mathbf{x} + \text{higher order terms.} \tag{4.7.42}$$

Neglecting the higher order terms and using

$$\frac{d}{dt}\mathbf{f}(\mathbf{x_0}) = \mathbf{A}\mathbf{f}(\mathbf{x_0}), \tag{4.7.43}$$

where $\mathbf{A}$ can be decomposed into a symmetric part $\mathbf{A_s}$ and a skew-symmetric part $\mathbf{A_{sk}}$, yields

$$\mathbf{f}(\mathbf{x}) \approx \mathbf{f}(\mathbf{x_0}) + \mathbf{A_s}\mathbf{f}(\mathbf{x_0})\Delta\mathbf{x} + \mathbf{A_{sk}}\mathbf{f}(\mathbf{x_0})\Delta\mathbf{x}. \tag{4.7.44}$$

This decomposition corresponds to the following theorem:

Theorem 2 (Theorem of Helmholtz)**.** *The most general motion of a sufficiently small non-rigid body can be represented as the sum of:*

1. *A translation, that is the* $\mathbf{f}(\mathbf{x_0})$ *part.*
2. *A rotation, that is the skew-symmetric part of the derivative acting on* Δx *or* $\mathbf{A_{sk}}\mathbf{f}(\mathbf{x_0})$*.*
3. *A expansion or contraction in three mutually orthogonal directions, that is the symmetric part or* $\mathbf{A_s}\mathbf{f}(\mathbf{x_0})$*.*

It is possible to generalise this representation further, from [64] it is possible to express a general second order time-invariant system as:

$$(\mathbf{M} + \mathbf{L})\ddot{\mathbf{x}}(t) + (\mathbf{D} + \mathbf{G})\dot{\mathbf{x}}(t) + (\mathbf{K} + \mathbf{C})\mathbf{x}(t) = \mathbf{P}(t) \tag{4.7.45}$$

where for mechanical systems:

M The symmetric inertia matrix.

D The symmetric damping matrix.

K The symmetric stiffness matrix.

G The skew-symmetric gyroscopic matrix.

C The skew-symmetric circulatory matrix.

Translation of this result to the balancing equation, repeated as:

$$C\frac{d}{dt}\mathbf{v_d} = -\mathbf{\Lambda_s}\mathbf{v_d} - \mathbf{\Lambda_{sk}}\mathbf{v_d}$$

gives the following insights:

1. The unbalance in the system, expressed as $\mathbf{v_d}$ can be viewed as a volume in $N-1$ dimensions. When no unbalance is present, this volume would have zero size.

2. Since the $\mathbf{\Lambda_s}$ matrix is symmetric, the $\mathbf{\Lambda_s v_d}$ term corresponds to the contraction of the unbalance volume (or equivalently to the expansion of the volume, if the system is unstable).

3. Since $\mathbf{\Lambda_{sk}}$ matrix is skew-symmetric, the $\mathbf{\Lambda_{sk} v_d}$ term corresponds to the rotation of the unbalance volume. Practically this rotation corresponds to the exchange of the unbalance voltage between the different cells. This unbalance is evident in the simulation results presented in Section 4.8, e.g. Fig. 4.23. This rotation does not dissipate any of the unbalance energy, but merely shifts it from one cell to another.

4.7.3.2 Inferred Stability Theorem

Previous studies of the FCC showed that the FCC will in general balance naturally when constant duty cycle modulation is used and the load is not purely reactive. The studies proved that the point $\mathbf{v_d} = \mathbf{0}$ is a stability point and inferred stability from the circuit operation. It was also shown [28] that there are unique combinations of the number of cells and duty ratio where balancing is impossible.

System stability can be inferred from the equivalent circuit of the FCC using total and difference parameters, Fig. 4.20. The following observations can be made from the circuit:

1. Under balanced conditions the voltages v_{d1} to $v_{d(N-1)}$ will be equal to zero. If this is true the voltage across the load will be equal to $V_t \cdot s_t(t)$. Therefore, due to the interleaving of the switching functions the first switching harmonic of this voltage will be at Nf_s.

2. Therefore, since the load is linear, the load current frequency spectrum will consist of multiples of Nf_s when the system is balanced.

3. The current through an unbalanced cell capacitor, say i_{da} can be written as the interaction between the load current and the relevant switching function, $i_{da}(t) = i_o(t) \cdot s_{da}(t)$. However, it was proven in Lemma 10, on p. 167, that the average value of this current is zero.

4. An unbalance voltage in any difference cell, say v_{da} will create an additional voltage $v_{da} \cdot s_{da}(t)$ across the load (with the assumption that the switching ripple across the flying capacitor is small enough to be ignored). The frequency spectrum of switching function s_{da} consists of all switching harmonics that are not a multiple of N.

5. Under unbalanced conditions the load voltage frequency spectrum will therefore consist of all multiples of f_s. Since the load is linear, the load current spectrum will also consist of all the harmonics of f_s.

6. If the load is dissipative any increase in load current harmonics will be associated with increased losses.

7. The current through any other flying capacitor, say $i_{db}(t)$ can therefore be written as $i_o(t) \cdot s_{db}(t)$. It was proven in Lemma 12, on p. 170, that this current does have a DC component.

8. These interactions between the load current harmonics and the difference cell switching functions are described by the matrix $\mathbf{\Lambda}$. The system can be described by
$$\dot{\mathbf{v}}_\mathbf{d} = \mathbf{\Lambda} \mathbf{v}_\mathbf{d}, \tag{4.7.46}$$
with solution, when $\mathbf{\Lambda}$ is non-singular
$$\mathbf{v}_\mathbf{d} = \sum_{n=1}^{N-1} A_n \mathbf{y}_\mathbf{n} e^{-\varphi_n t/C}, \tag{4.7.47}$$
where $\mathbf{y}_\mathbf{n}$ is an eigenvector of $\mathbf{\Lambda}$ with associated eigenvalue φ_n.

9. A negative real valued eigenvalue of $\mathbf{\Lambda}$ is associated with the dissipation of a cell's unbalance energy in the load. This dissipation occurs through an increased load current ripple.

10. A complex valued eigenvalue pair is associated with the exchange of unbalanced energy between two cells. If, hypothetically, the eigenvalues are purely imaginary this exchange of unbalance energy will be loss less. However, this exchange must occur via the interactions of the load current ripple with the switching functions. If the load is not purely reactive this ripple current will be associated with some loss and therefore the eigenvalue pair can not be purely imaginary and will have a negative real part.

11. From [28] it is known that unique points exists where the interactions between the switching functions and the load current ripple is such that no exchange is possible. Under these conditions $\mathbf{\Lambda}$ will have an eigenvalue of zero.

The inferred stability theorem therefore relies on two facts. Firstly, all energy exchange must occur via the load current. Any increase in the load current ripple will result in increased losses and therefore a reduction in the total unbalance energy. Secondly, due to the interleaving of the switching functions no energy exchange between the source V_t and any cell is possible. However, a rigorous proof of system stability was still lacking.

4.7.3.3 Stability Using Lyapunov's Method

The system stability can be investigated using Lyapunov's method, which states:

Theorem 3 (Lyapunov's Theorem)**.** *Consider the system* $\dot{\mathbf{x}} = \mathbf{A}\mathbf{x}$ *where* $\mathbf{A} \in \mathbb{R}^{n \times n}$. *Define* $\mathbf{W} = \mathbf{A}^\mathbf{T}\mathbf{B} + \mathbf{B}\mathbf{A}$ *with the requirement that* $\mathbf{B}$ *is positive definite. The following statements hold [66, Corollary 11.8.8]:*

1. *The system is Lyaponov stable if and only if* $\mathbf{W}$ *is negative-semidefinite.*
2. *The system is asymptotically stable if and only if* $\mathbf{W}$ *is negative definite.*

Definition 1. *The inner product of two vectors vector* $\mathbf{x}$ *and* $\mathbf{y}$ *written as* $\langle \mathbf{x}, \mathbf{y} \rangle$ *is defined by the relation [58, p. 14]*

$$\begin{aligned} \langle \mathbf{x}, \mathbf{y} \rangle &= \sum_{i=1}^{N} x_i y_i \\ &= \mathbf{x}^{\mathbf{T}} \mathbf{y}. \end{aligned}$$

The following are properties of the inner product:

1. $\langle \mathbf{x}, \mathbf{y} \rangle = \langle \mathbf{y}, \mathbf{x} \rangle$
2. $\langle \mathbf{x} + \mathbf{y}, \mathbf{z} \rangle = \langle \mathbf{x}, \mathbf{z} \rangle + \langle \mathbf{y}, \mathbf{z} \rangle$
3. $\langle k\mathbf{x}, \mathbf{y} \rangle = k\langle \mathbf{x}, \mathbf{y} \rangle$ *(k is a real number)*
4. $\langle \mathbf{x}, \mathbf{x} \rangle \geq 0$ *(*$= 0$ *iff* $\mathbf{x} = \mathbf{0}$*)*
5. *If* $x \neq \mathbf{0}$ *and* $y \neq \mathbf{0}$ *then* $\langle \mathbf{x}, \mathbf{y} \rangle = 0 \iff \mathbf{x} \perp \mathbf{y}$

Definition 2. *The spectrum of a* $m \times m$ *square matrix* $\mathbf{A}$ *is the set of all its eigenvalues [66, Definition 4.4.3], and is written as follows:*

$$\sigma(\mathbf{A}) = \{\varphi_1, \varphi_2, \ldots, \varphi_n\}$$

furthermore any eigenvalue in the spectrum of $\mathbf{A}$ *is written as*

$$\sigma_n(\mathbf{A}) = \varphi_n \text{ where } 1 \leq n \leq m.$$

Theorem 4. *For a symmetric matrix* $\mathbf{A_s} \in \mathbb{R}^{n \times n}$ *and a skew-symmetric matrix* $\mathbf{A_{sk}} \in \mathbb{R}^{n \times n}$ *the following is true about the eigenvalues [58]:*

$$\begin{aligned} \sigma_n(\mathbf{A_s}) &\subset \mathbb{R} \\ \sigma_n(\mathbf{A_{sk}}) &\subset j\mathbb{R} \end{aligned}$$

Definition 3. *A* $n \times n$ *real symmetric matrix* $\mathbf{A}$ *is positive definite if, for any non-zero vector* $\mathbf{x} \in \mathbb{R}^n$ *[67, p. 396-9]*

$$\mathbf{x}^{\mathbf{T}} \mathbf{A} \mathbf{x} > 0,$$

and positive-semidefinite if

$$\mathbf{x}^{\mathbf{T}} \mathbf{A} \mathbf{x} \geq 0.$$

Furthermore, since $\sigma(\mathbf{A}) \subset \mathbb{R}$*, it is true that*

$$\mathbf{x}^{\mathbf{T}} \mathbf{A} \mathbf{x} > 0 \iff \sigma(\mathbf{A}) > 0,$$

and

$$\mathbf{x}^{\mathbf{T}} \mathbf{A} \mathbf{x} \geq 0 \iff \sigma(\mathbf{A}) \geq 0.$$

Corollary 1. *The identity matrix* $\mathbf{I}$ *is positive definite since* $\sigma(\mathbf{I}) = \{1\}$

Applying Lyapunov's second theorem, Theorem 3, to the balancing equation, repeated as

$$C\frac{d}{dt}\mathbf{v_d} = -\mathbf{\Lambda_s}\mathbf{v_d} - \mathbf{\Lambda_{sk}}\mathbf{v_d},$$

and choosing $\mathbf{B} = \mathbf{I}$ yields the following expression for $\mathbf{W}$:

$$\begin{aligned}\mathbf{W} &= (-\mathbf{\Lambda_s} - \mathbf{\Lambda_{sk}})^{\mathbf{T}}\mathbf{I} + \mathbf{I}(-\mathbf{\Lambda_s} - \mathbf{\Lambda_{sk}}) \\ &= -\mathbf{\Lambda_s^T} - \mathbf{\Lambda_{sk}^T} - \mathbf{\Lambda_s} - \mathbf{\Lambda_{sk}} \\ &= -2\mathbf{\Lambda_s} + \mathbf{\Lambda_{sk}} - \mathbf{\Lambda_{sk}} \\ &= -2\mathbf{\Lambda_s} \end{aligned} \tag{4.7.48}$$

According to Theorem 3, the system will be globally stable if $-2\mathbf{\Lambda_s}$ is negative definite or equivalently if all eigenvalues of $-2\mathbf{\Lambda_s}$ are in the left-hand half of the complex plane.

4.7.3.4 Proof that Λ_s is Positive Semidefinite

An expression for $\mathbf{\Lambda_s}$ was derived in Section 4.7.2.1. The expression is repeated for convenience

$$\mathbf{\Lambda_s} = \sum_{n=1}^{\infty} \mathbf{\Lambda_{s(n)}}$$

where

$$\mathbf{\Lambda_{s(n)}} = \alpha(n)\mathbf{R_{(n)}}$$

$$\mathbf{R_{(n)}} = \begin{bmatrix} 1 & \cos(2\pi n\frac{1}{N}) & \cos(2\pi n\frac{2}{N}) & \cdots & \cos(2\pi n\frac{N-2}{N}) \\ \cos(2\pi n\frac{N-1}{N}) & 1 & \cos(2\pi n\frac{1}{N}) & \cdots & \cos(2\pi n\frac{N-3}{N}) \\ \cos(2\pi n\frac{N-2}{N}) & \cos(2\pi n\frac{N-1}{N}) & 1 & \cdots & \cos(2\pi n\frac{N-4}{N}) \\ \vdots & \vdots & \vdots & \ddots & \vdots \\ \cos(2\pi n\frac{2}{N}) & \cos(2\pi n\frac{3}{N}) & \cos(2\pi n\frac{4}{N}) & \cdots & 1 \end{bmatrix}$$

$$\alpha(n) = \frac{|\Psi(n)|^2}{|Z(n\omega_s)|^2}\left(1 - Re\left\{\zeta_n\right\}\right) Re\left\{Z(n\omega_s)\right\}$$

Theorem 5. *Let $\mathbf{x_1}, \mathbf{x_2}, \ldots, \mathbf{x_n} \in \mathbb{F}^n$, and define $\mathbf{A} \in \mathbb{F}^{n\times n}$ by the fact that the entry (i, j) of $\mathbf{A}$ is equal to $\mathbf{x_i^* x_j}$. Furthermore define a matrix $\mathbf{B} = [\mathbf{x_1}\ \mathbf{x_2}\ \ldots\ \mathbf{x_n}]$. Then $\mathbf{A} = B^*B$. Consequently $\mathbf{A}$ is positive definite [66, Fact 8.7.36]. Here, $\mathbb{F}$ denotes either $\mathbb{R}$ or $\mathbb{C}$ and in the case of complex numbers $\mathbf{A}^*$ denotes the conjugate transpose (Hermitian conjugate) of $\mathbf{A}$.*

Theorem 6. *The sum of two positive definite matrices of the same size is positive definite. More generally, any non-negative linear combination of positive definite matrices is positive definite [67, Observation 7.1.3]*

It is possible o prove that $\mathbf{\Lambda_s}$ is positive semidefinite through the use of Theorems 5 and 6.[2]

[2]The proof was suggested by Prof. C. Lance, University of Leeds, UK (private communication).

By defining

$$\theta = 2\pi\frac{1}{N} \tag{4.7.49}$$

it is possible to rewrite the definition of $\mathbf{R}_{(\mathbf{n})}$ as

$$\mathbf{R}_{(\mathbf{n})} = \begin{bmatrix} 1 & \cos(n\theta) & \cos(2n\theta) & \cdots & \cos(\{N-2\}n\theta) \\ \cos(n\theta) & 1 & \cos(n\theta) & \cdots & \cos(\{N-3\}n\theta) \\ \cos(2n\theta) & \cos(n\theta) & 1 & \cdots & \cos(\{N-4\}n\theta) \\ \vdots & \vdots & \vdots & \ddots & \vdots \\ \cos(\{N-2\}n\theta) & \cos(\{N-3\}n\theta) & \cos(\{N-4\}n\theta) & \cdots & 1 \end{bmatrix}. \tag{4.7.50}$$

Define the following two $1 \times N-1$ matrices

$$\mathbf{Q}_{\mathbf{p}(\mathbf{n})} = \begin{bmatrix} 1 & e^{jn\theta} & e^{jn2\theta} & \ldots & e^{jn(N-2)\theta} \end{bmatrix} \tag{4.7.51}$$

and

$$\mathbf{Q}_{\mathbf{n}(\mathbf{n})} = \begin{bmatrix} 1 & e^{-jn\theta} & e^{-jn2\theta} & \ldots & e^{-jn(N-2)\theta} \end{bmatrix}. \tag{4.7.52}$$

It is now true that

$$\mathbf{Q}^*_{\mathbf{p}(\mathbf{n})}\mathbf{Q}_{\mathbf{p}(\mathbf{n})} = \begin{bmatrix} 1 & e^{jn\theta} & e^{jn2\theta} & \cdots & e^{jn(N-2)\theta} \\ e^{-jn\theta} & 1 & e^{jn\theta} & \cdots & e^{jn(N-3)\theta} \\ e^{-jn2\theta} & e^{-jn\theta} & 1 & \cdots & e^{jn(N-4)\theta} \\ \vdots & \vdots & \vdots & \ddots & \vdots \\ e^{-jn(N-2)\theta} & e^{-jn(N-3)\theta} & e^{-jn(N-4)\theta} & \cdots & 1 \end{bmatrix} \tag{4.7.53}$$

and likewise

$$\mathbf{Q}^*_{\mathbf{n}(\mathbf{n})}\mathbf{Q}_{\mathbf{n}(\mathbf{n})} = \begin{bmatrix} 1 & e^{-jn\theta} & e^{-jn2\theta} & \cdots & e^{-jn(N-2)\theta} \\ e^{jn\theta} & 1 & e^{-jn\theta} & \cdots & e^{-jn(N-3)\theta} \\ e^{jn2\theta} & e^{jn\theta} & 1 & \cdots & e^{-jn(N-4)\theta} \\ \vdots & \vdots & \vdots & \ddots & \vdots \\ e^{jn(N-2)\theta} & e^{jn(N-3)\theta} & e^{jn(N-4)\theta} & \cdots & 1 \end{bmatrix} \tag{4.7.54}$$

where $\mathbf{A}^*$ denotes the complex conjugate transpose of $\mathbf{A}$. Using the identity that

$$\frac{1}{2}\left(e^{j\vartheta} + e^{-j\vartheta}\right) = \cos(\vartheta) \tag{4.7.55}$$

it follows that

$$\frac{1}{2}\left(\mathbf{Q}^*_{\mathbf{p}(\mathbf{n})}\mathbf{Q}_{\mathbf{p}(\mathbf{n})} + \mathbf{Q}^*_{\mathbf{n}(\mathbf{n})}\mathbf{Q}_{\mathbf{n}(\mathbf{n})}\right) = \mathbf{R}_{(\mathbf{n})}. \tag{4.7.56}$$

From Theorem 5 it follows that both $\mathbf{Q}^*_{\mathbf{p}(\mathbf{n})}\mathbf{Q}_{\mathbf{p}(\mathbf{n})}$ and $\mathbf{Q}^*_{\mathbf{n}(\mathbf{n})}\mathbf{Q}_{\mathbf{n}(\mathbf{n})}$ are positive-semidefinite. Furthermore from Theorem 6 it is true that $\mathbf{R}_{(\mathbf{n})}$ is positive-semidefinite.

Recall from (4.7.22) that

$$\alpha(n) = \frac{|\Psi(n)|^2}{|Z(n\omega_s)|^2}\left(1 - Re\left\{\zeta^n\right\}\right) Re\left\{Z(n\omega_s)\right\}.$$

It is clear that $\alpha(n)$ is positive for all values of n if $Re\{Z(n\omega_s)\} \geq 0$. When $\alpha(n)$ is positive for all n it follows that $\mathbf{\Lambda_{s(n)}}$ is also positive-semidefinite.

It was shown earlier that the series

$$\sum_{n=1}^{\infty} \mathbf{\Lambda_{s(n)}}$$

converges to $\mathbf{\Lambda_s}$. Furthermore since the function $\mathbf{A} \mapsto \mathbf{x^T A x}$ is continuous it follows from Theorem 6 that $\mathbf{\Lambda_s}$ is positive-semidefinite. It is also possible to rewrite the infinite series as a sum of N matrices by realising that due to the definition of θ the set $\{n \in \mathbb{Z}^+ : \mathbf{A_{r(n)}}\}$ consists of N elements.

In the theoretical case where the load is purely reactive, in other words when $Re\{Z(n\omega_s)\} = 0$, it is true, for all n, that $\alpha(n) = 0$. In this case $\mathbf{\Lambda_s}$ will be a zero matrix and no rebalancing is possible. This result is consistent with the results of previous studies [26; 34].

4.7.4 Dissipation of the Unbalance Energy

The unbalance energy contained in the system can be expressed as:

$$\begin{aligned} E &= \frac{1}{2}C\left(v_{d1}^2 + v_{d2}^2 + \ldots + v_{d(N-1)}^2\right) \\ &= \frac{1}{2}C\langle \mathbf{v_d}, \mathbf{v_d} \rangle \end{aligned} \tag{4.7.57}$$

Differentiating yields:

$$\begin{aligned} \frac{d}{dt}E &= \frac{1}{2}C\left(\langle \dot{\mathbf{v}}_\mathbf{d}, \mathbf{v_d} \rangle + \langle \mathbf{v_d}, \dot{\mathbf{v}}_\mathbf{d} \rangle\right) \\ &= \frac{1}{2}C\left(\dot{\mathbf{v}}_\mathbf{d}^\mathbf{T}\mathbf{v_d} + \mathbf{v_d^T}\dot{\mathbf{v}}_\mathbf{d}\right) \\ &= \frac{1}{2}C\Big(\frac{-1}{C}\left(\mathbf{\Lambda v_d}\right)^\mathbf{T}\mathbf{v_d} + \frac{-1}{C}\mathbf{v_d^T \Lambda v_d}\Big) \\ &= -\frac{1}{2}\left(\mathbf{v_d^T \Lambda^T v_d} + \mathbf{v_d^T \Lambda v_d}\right) \end{aligned} \tag{4.7.58}$$

Using the fact that $\mathbf{\Lambda_s}$ is symmetric and $\mathbf{\Lambda_{sk}}$ is skew-symmetric yields:

$$\begin{aligned} \frac{d}{dt}E &= -\frac{1}{2}\Big(\mathbf{v_d^T}\left(\mathbf{\Lambda_s} + \mathbf{\Lambda_{sk}}\right)^\mathbf{T}\mathbf{v_d} + \mathbf{v_d^T}\left(\mathbf{\Lambda_s} + \mathbf{\Lambda_{sk}}\right)\mathbf{v_d}\Big) \\ &= -\frac{1}{2}\Big(\mathbf{v_d^T \Lambda_s v_d} - \mathbf{v_d^T \Lambda_{sk} v_d} + \mathbf{v_d^T \Lambda_s v_d} + \mathbf{v_d^T \Lambda_{sk} v_d}\Big) \\ &= -\mathbf{v_d^T \Lambda_s v_d} \end{aligned} \tag{4.7.59}$$

Theorem 7. *The eigenvectors associated with distinct eigenvalues of a real symmetric matrix* $\mathbf{A_s}$ *are orthogonal [58, p. 36].*

Proof. Using two eigenvectors, $\mathbf{x}$ and $\mathbf{y}$, of $\mathbf{A_s}$

$$\begin{aligned} \mathbf{A_s x} &= \alpha \mathbf{x} \\ \mathbf{A_s y} &= \beta \mathbf{y} \end{aligned}$$

$\alpha \neq \beta$, it is true that

$$\langle \mathbf{y}, \mathbf{A_s x} \rangle = \alpha \langle \mathbf{y}, \mathbf{x} \rangle$$
$$\langle \mathbf{x}, \mathbf{A_s y} \rangle = \beta \langle \mathbf{x}, \mathbf{y} \rangle.$$

Since $\langle \mathbf{x}, \mathbf{A_s y} \rangle = \langle \mathbf{A_s x}, \mathbf{y} \rangle = \langle \mathbf{y}, \mathbf{A_s x} \rangle$, subtraction yields

$$0 = (\alpha - \beta) \langle \mathbf{x}, \mathbf{y} \rangle$$

Hence $\langle \mathbf{x}, \mathbf{y} \rangle = 0$ which implies that $\mathbf{x} \perp \mathbf{y}$. □

According to Theorem 7, the eigenvectors of the real symmetric matrix $\mathbf{\Lambda_s}$, without repeated eigenvalues, are orthogonal. As all orthogonal vectors are per definition also linearly independent, $\mathbf{\Lambda_s}$ can therefore, according to Theorem 8, be factorised as

$$\mathbf{\Lambda_s} = \mathbf{Y D Y^{-1}}, \tag{4.7.60}$$

where

$$\mathbf{Y} = \begin{bmatrix} \mathbf{y_1} & \mathbf{y_2} & \cdots & \mathbf{y_{N-1}} \end{bmatrix} \tag{4.7.61}$$

$$\mathbf{D} = \begin{bmatrix} \varphi_1 & 0 & \cdots & 0 \\ 0 & \varphi_2 & \cdots & 0 \\ \vdots & \vdots & \ddots & \vdots \\ 0 & 0 & \cdots & \varphi_{N-1} \end{bmatrix} \tag{4.7.62}$$

and $\mathbf{y_n}$ is an eigenvector of $\mathbf{\Lambda_s}$ with associated eigenvalue φ_n.

Theorem 8 (Diagonalisation Theorem)**.** *A $n \times n$ matrix $\mathbf{A}$ is diagonalisable in the form*

$$\mathbf{A = Y D Y^{-1}}$$

where $\mathbf{Y}$ is a $n \times n$ matrix with columns $\mathbf{y_1}, \ldots, \mathbf{y_n}$, the n eigenvectors of $\mathbf{A}$, and $\mathbf{D}$ is a diagonal matrix with diagonal entries $\varphi_1, \ldots, \varphi_n$, the eigenvalues of $\mathbf{A}$, if and only if the n eigenvectors of $\mathbf{A}$ are linearly independent [59, p. 314].

When all the eigenvectors are normalised, i.e. unit vectors, $\mathbf{Y}$ will be an orthonormal matrix and it is true that

$$\mathbf{Y Y^T = Y^T Y = I} \tag{4.7.63}$$
$$\therefore \mathbf{Y^T = Y^{-1}}. \tag{4.7.64}$$

Furthermore, orthonormal matrices preserve the inner product [66] in that for a orthonormal matrix $\mathbf{Q}$ and any vectors $\mathbf{x}$ and $\mathbf{y}$

$$\langle \mathbf{Qx}, \mathbf{Qy} \rangle = \langle \mathbf{x}, \mathbf{y} \rangle.$$

The unbalance voltage state vector can be expressed in terms of the $N-1$ orthogonal eigenvectors $\mathbf{y_n}$ of $\mathbf{\Lambda_s}$ and using w_n as the different weighting factors, as

$$\begin{aligned} \mathbf{v_d} &= \sum_{n=1}^{N-1} w_n \mathbf{y_n} \\ &= \mathbf{Yw}, \end{aligned} \tag{4.7.65}$$

where

$$\mathbf{w} = \begin{bmatrix} w_1 & w_2 & \cdots & w_{N-1} \end{bmatrix}^T. \tag{4.7.66}$$

Using this representation of $\mathbf{v_d}$ the unbalance energy is found as

$$\begin{aligned} E &= \frac{1}{2}C\langle \mathbf{v_d}, \mathbf{v_d} \rangle \\ &= \frac{1}{2}C\langle \mathbf{Yw}, \mathbf{Yw} \rangle \\ &= \frac{1}{2}C\langle \mathbf{w}, \mathbf{w} \rangle \\ &= \frac{1}{2}C\sum_{n=1}^{N-1} w_n^2. \end{aligned} \tag{4.7.67}$$

The RHS of (4.7.59) can be rewritten using the same definition of $\mathbf{v_d}$ as:

$$\begin{aligned} \frac{d}{dt}E &= -\mathbf{v_d^T}\mathbf{\Lambda_s}\mathbf{v_d} \\ &= -(\mathbf{Yw})^{\mathbf{T}}\mathbf{\Lambda_s}\mathbf{Yw} \\ &= -\mathbf{w^T}\mathbf{Y^T}\mathbf{\Lambda_s}\mathbf{Yw} \end{aligned}$$

using Theorem 8

$$\begin{aligned} \frac{d}{dt}E &= -\mathbf{w^T}\mathbf{Y^T}\mathbf{\Lambda_s}\mathbf{Yw} \\ &= -\mathbf{w^T}\mathbf{Y^T}\mathbf{YD}\mathbf{Y^T}\mathbf{Yw} \\ &= -\mathbf{w^T}\mathbf{Dw} \\ &= -\sum_{n=1}^{N-1} w_n^2\varphi_n. \end{aligned} \tag{4.7.68}$$

The following observations can be made:

1. According to the stability criteria by using Lyapunov's Second Method (in Section 4.7.3.3), $-\mathbf{\Lambda_s}$ must be negative definite. This corresponds to the result of (4.7.68), as the unbalance energy will decay to zero if all the eigenvalues of $-\mathbf{\Lambda_s}$ are negative.

2. From the discussion in Section 4.7.3.2 it is possible to deduce from the equivalent circuit of Fig. 4.20 that the unbalance energy will be dissipated in the load under most conditions.

3. Furthermore, it was proven in Section 4.7.3.3 that $\mathbf{\Lambda_s}$ is in fact positive semidefinite. There are unique operational points where the unbalance energy will remain constant in a specific cell, corresponding to $\mathbf{\Lambda_s}$ having an eigenvalue equal to zero. These points of operation are identified in [28] and briefly discussed in Section 4.7.7.

4. The requirement that $\mathbf{\Lambda_s}$ is simple, i.e. not having repeated eigenvalues, does not limit the applicability of this discussion. All eigenvectors of real symmetric matrices are linearly independent [58], therefore Theorem 8 holds for all real symmetric matrices. This discussion and the conclusions are therefore applicable even if $\mathbf{A_s}$ is not simple.

4.7.5 Approximation of the Eigenvalues of $\mathbf{\Lambda_s}$

The following two sections introduces a method of estimating the maximum rebalancing time constants from the characteristics of $\mathbf{\Lambda}$. It is true that $\mathbf{\Lambda}$ is Toeplitz. In the asymptotic case where $N \to \infty$ certain conclusions and bounds on the spectrum of a Toeplitz matrix $\mathbf{A} \in \mathbb{R}^{K\times K}$ can be made by using an approximating circulant matrix $\mathbf{A_c} \in \mathbb{R}^{(K+1)\times(K+1)}$ [60]. However, the voltage rating requirements of the flying capacitors at large N makes the FCC impractical for $N > 10$ and this method cannot be used. The method used here uses the symmetric, skew-symmetric sum decomposition of $\mathbf{\Lambda}$ to estimate a minimum bound on the real part of the eigenvalues.

The flying capacitor converter finds typical application in high voltage drives [68]. When the converter is used as a drive, the load at the switching frequency and higher can be modelled as a pure inductance with ESR [37], when the high frequency effects such as the skin effect [69; 70] are ignored. In stand-alone inverter and DC source applications the converter output will be similar to the circuit of Fig. 4.19. The output filter capacitance will in most applications be fairly large, in other words large enough so that at the switching frequency

$$\frac{1}{\omega_c C_f} \ll R. \tag{4.7.69}$$

If the filter capacitor is large enough, the load at the switching frequency and above can be approximated as

$$Z(\omega) \approx r + j\omega L. \tag{4.7.70}$$

Using another approximation that $\omega L \gg r$ at the switching frequency and higher, it is true that

$$|Z(n\omega_s)| \approx n\omega_s L \tag{4.7.71}$$

$$Re\{Z(n\omega_s)\} \approx r. \tag{4.7.72}$$

A more accurate description of $Re\{Z(n\omega_c)\}$ would include the ESR of the output filter capacitor. However, this equivalent resistance is small in most capacitors and in most practical circuits it would be more than a magnitude of order smaller than the inductor ESR. For the remainder of this thesis, the influence of the filter capacitor ESR will be ignored.

Consider (4.7.19)-(4.7.21), repeated for convenience as

$$\mathbf{\Lambda_s} = \sum_{n=1}^{\infty} \mathbf{\Lambda_{s(n)}}$$

where

$$\mathbf{\Lambda_{s(n)}} = \alpha(n) \begin{bmatrix} 1 & \cos(2\pi n \frac{1}{N}) & \cos(2\pi n \frac{2}{N}) & \cdots & \cos(2\pi n \frac{2}{N}) \\ \cos(2\pi n \frac{1}{N}) & 1 & \cos(2\pi n \frac{1}{N}) & \cdots & \cos(2\pi n \frac{3}{N}) \\ \cos(2\pi n \frac{2}{N}) & \cos(2\pi n \frac{1}{N}) & 1 & \cdots & \cos(2\pi n \frac{4}{N}) \\ \vdots & \vdots & \vdots & \ddots & \vdots \\ \cos(2\pi n \frac{2}{N}) & \cos(2\pi n \frac{3}{N}) & \cos(2\pi n \frac{4}{N}) & \cdots & 1 \end{bmatrix}$$

and

$$\alpha(n) = \frac{|\Psi(n)|^2}{|Z(n\omega_s)|^2} \left(1 - Re\left\{\zeta_n\right\}\right) Re\left\{Z(n\omega_s)\right\}.$$

Using the approximated values for the load impedance at the switching frequency and higher $\mathbf{\Lambda_s}$ can be rewritten as

$$\mathbf{\Lambda_s} \approx \frac{r}{L^2 f_s^2} \mathbf{\Lambda_r}, \tag{4.7.73}$$

where

$$\mathbf{\Lambda_r} = \sum_{n=1}^{\infty} \mathbf{\Lambda_{r(n)}} \tag{4.7.74}$$

$$\mathbf{\Lambda_{r(n)}} = \beta(n) \begin{bmatrix} 1 & \cos(2\pi n \frac{1}{N}) & \cos(2\pi n \frac{2}{N}) & \cdots & \cos(2\pi n \frac{2}{N}) \\ \cos(2\pi n \frac{1}{N}) & 1 & \cos(2\pi n \frac{1}{N}) & \cdots & \cos(2\pi n \frac{3}{N}) \\ \cos(2\pi n \frac{2}{N}) & \cos(2\pi n \frac{1}{N}) & 1 & \cdots & \cos(2\pi n \frac{4}{N}) \\ \vdots & \vdots & \vdots & \ddots & \vdots \\ \cos(2\pi n \frac{2}{N}) & \cos(2\pi n \frac{3}{N}) & \cos(2\pi n \frac{4}{N}) & \cdots & 1 \end{bmatrix} \tag{4.7.75}$$

$$\begin{aligned} \beta(n) &= \frac{1}{4\pi^2 n^2} |\Psi(n)|^2 \Big(1 - \cos\Big(2\pi \frac{n}{N}\Big)\Big) \\ &= \frac{\sin^2(n\pi d)}{\pi^4 n^4} \Big(1 - \cos\Big(2\pi \frac{n}{N}\Big)\Big). \end{aligned} \tag{4.7.76}$$

Therefore the eigenvalues of $\mathbf{\Lambda_s}$ can be approximated by the eigenvalues of $\mathbf{\Lambda_r}$ as

$$\sigma_n(\mathbf{\Lambda_s}) \approx \frac{r}{L^2 f_s^2} \sigma_n(\mathbf{\Lambda_r}). \tag{4.7.77}$$

Expressing $\mathbf{\Lambda_s}$ in terms of $\mathbf{\Lambda_r}$ is beneficial, since $\mathbf{\Lambda_r}$ is invariant to the connected load.

4.7.6 Eigenvalues of the Rebalancing Matrix

When $\mathbf{\Lambda}$ is non-singular the solution to the balancing equation

$$C \frac{d}{dt} \mathbf{v_d} = -\mathbf{\Lambda} \mathbf{v_d},$$

is found by

$$\mathbf{v_d} = \sum_{n=1}^{N-1} A_n \mathbf{y_n} e^{-\varphi_n t / C}, \tag{4.7.78}$$

where φ_n and $\mathbf{y_n}$ denote the eigenvalues and eigenvectors of $\mathbf{\Lambda}$ respectively.

As shown in Section 4.7.2 it is possible to factorise $\mathbf{\Lambda}$ in such a manner that the balancing equation can be rewritten as

$$\frac{d}{dt}\mathbf{v_d} = \mathbf{\Lambda_s}\mathbf{v_d} + \mathbf{\Lambda_{sk}}\mathbf{v_d}.$$

Theorem 9. *For a matrix $\mathbf{A} \in \mathbb{R}^{m\times m}$ it is true that for all n [66, Fact 5.10.22,p 198]*

$$\sigma_{min}\left(\frac{\mathbf{A}+\mathbf{A^T}}{2}\right) \leq Re\left\{\sigma_n(\mathbf{A})\right\} \leq \sigma_{max}\left(\frac{\mathbf{A}+\mathbf{A^T}}{2}\right),$$
$$\sigma_{min}\left(\frac{\mathbf{A}-\mathbf{A^T}}{2j}\right) \leq Im\left\{\sigma_n(\mathbf{A})\right\} \leq \sigma_{max}\left(\frac{\mathbf{A}-\mathbf{A^T}}{j2}\right)$$

where $\sigma_{min}(\mathbf{A})$ and $\sigma_{max}(\mathbf{A})$ denotes the minimum and maximum eigenvalue in the spectrum of $\mathbf{A}$ respectively[3]. Also, $\sigma_n(\mathbf{A})$ denotes any eigenvalue in the spectrum of $\mathbf{A}$.

Using Theorem 9 and realising that, from Theorem 1,

$$\mathbf{\Lambda_s} = \frac{\mathbf{\Lambda}+\mathbf{\Lambda^T}}{2}$$
$$\mathbf{\Lambda_{sk}} = \frac{\mathbf{\Lambda}-\mathbf{\Lambda^T}}{2},$$

it is true that

$$\sigma_{min}(\mathbf{\Lambda_s}) \leq Re\left\{\sigma_n(\mathbf{\Lambda})\right\}. \tag{4.7.79}$$

Furthermore, the following statements can be made about the eigenvalues of $\mathbf{\Lambda}$, $\mathbf{\Lambda_s}$ and $\mathbf{\Lambda_{sk}}$:

1. $\sigma_n(\mathbf{\Lambda_s}) \subset \mathbb{R}$.
2. $\sigma_n(\mathbf{\Lambda_{sk}}) \subset j\mathbb{R}$.
3. However, it is not in general true that $Re\left\{\sigma_n(\mathbf{\Lambda})\right\} = \sigma_n(\mathbf{\Lambda_s})$ or $Im\left\{\sigma_n(\mathbf{\Lambda})\right\} = \sigma_n(\mathbf{\Lambda_{sk}})$.

Consider the voltage rebalancing following perturbation (at $t = 0$) as described by (4.7.78). The maximum rebalancing time constant is

$$\tau_{maxV} = \frac{C}{\min\limits_n(Re\left\{\sigma_n(\mathbf{\Lambda})\right\})}. \tag{4.7.80}$$

The response of any difference voltage will be bounded by

$$|v_{dn}(t)| \leq B_n e^{-t/\tau_{maxV}},\ t \geq 0, \tag{4.7.81}$$

where B_n is a constant that depends on the initial disturbance.

[3]It is true that the that spectrum of real symmetric matrices is real, and imaginary for real skew-symmetric matrices.

Let τ_{max} represent the time constant associated with the smallest eigenvalue of $\mathbf{\Lambda_s}$. It is possible to rewrite (4.7.79) as

$$\frac{C}{\sigma_{min}(\mathbf{\Lambda_s})} = \tau_{max} \geq \frac{C}{\min_n(Re\{\sigma_n(\mathbf{\Lambda})\})} = \tau_{maxV}, \tag{4.7.82}$$

and therefore

$$|v_{dn}(t)| \leq B_n e^{-t/\tau_{max}},\ t \geq 0. \tag{4.7.83}$$

Using the same approximation with regard to the nature of the load at the switching frequency and above as in Section 4.7.5 it is possible to approximate τ_{max}. Recall that according to (4.7.77), repeated for convenience as

$$\sigma_n(\mathbf{\Lambda_s}) \approx \frac{r}{L^2 f_s^2}\sigma_n(\mathbf{\Lambda_r}),$$

it is possible estimate the minimum eigenvalue of $\mathbf{\Lambda_s}$ using the minimum eigenvalue of $\mathbf{\Lambda_r}$. Let

$$\tau_{max} = \frac{-C}{\sigma_{min}(\mathbf{\Lambda_s})}. \tag{4.7.84}$$

The maximum time constant can be approximated with τ_{maxA} defined as

$$\tau_{maxA} = \frac{CL^2 f_s^2}{r}\tau_r, \tag{4.7.85}$$

where

$$\tau_r = \frac{1}{\sigma_{min}(\mathbf{\Lambda_r})}. \tag{4.7.86}$$

It is therefore true that

$$\tau_{maxV} \leq \tau_{max} \tag{4.7.87}$$

$$\tau_{max} \approx \tau_{maxA} \tag{4.7.88}$$

$$\tau_{maxA} = \frac{CL^2 f_s^2}{r}\tau_r. \tag{4.7.89}$$

The values of τ_r are tabulated in Tables E.1 - E.6 for various duty cycles for flying capacitor converters with 3-8 cells. A 8-cell converter was chosen as a maximum value since, due to the clamping capacitor requirements, FCCs with 5 cells or more are rarely used [72].

The ratio between τ_{max} and τ_{maxV} for are shown in Fig. 4.21 for a range of duty cycles. It is clear that τ_{max} gives a worst case approximation.

The ratio of the time constants in Fig. 4.21 does not contain information about the change in the maximum balancing time constant with duty cycle. In Fig. 4.22 the minimum eigenvalue of $\mathbf{\Lambda}$ and $\mathbf{\Lambda_s}$ are shown for 4-7 cell FCCs as a function of duty cycle.

A python script file is included in Appendix C.2.2. This file calculates both τ_{maxV} and τ_{max} for any FCC. Although the approximation using the reference tables in Appendix E can be used as a design guide, this file can be used if a more accurate value is required.

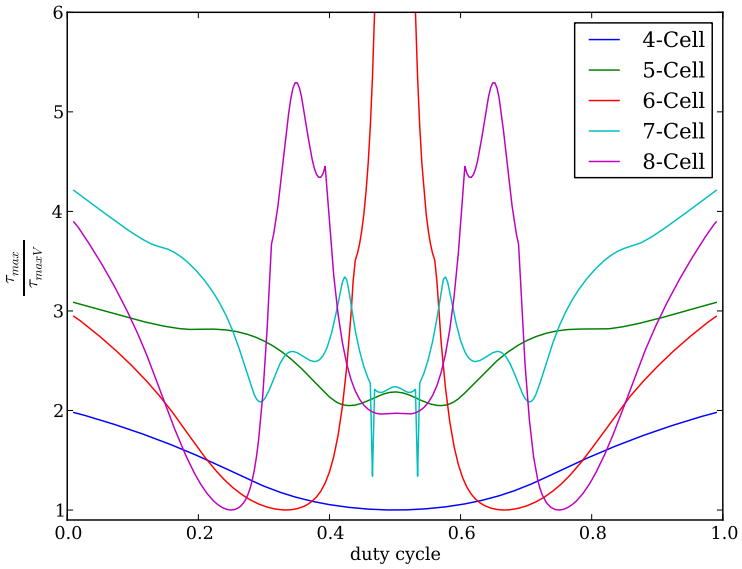

Figure 4.21: The ratio of τ_{max}/τ_{maxV}

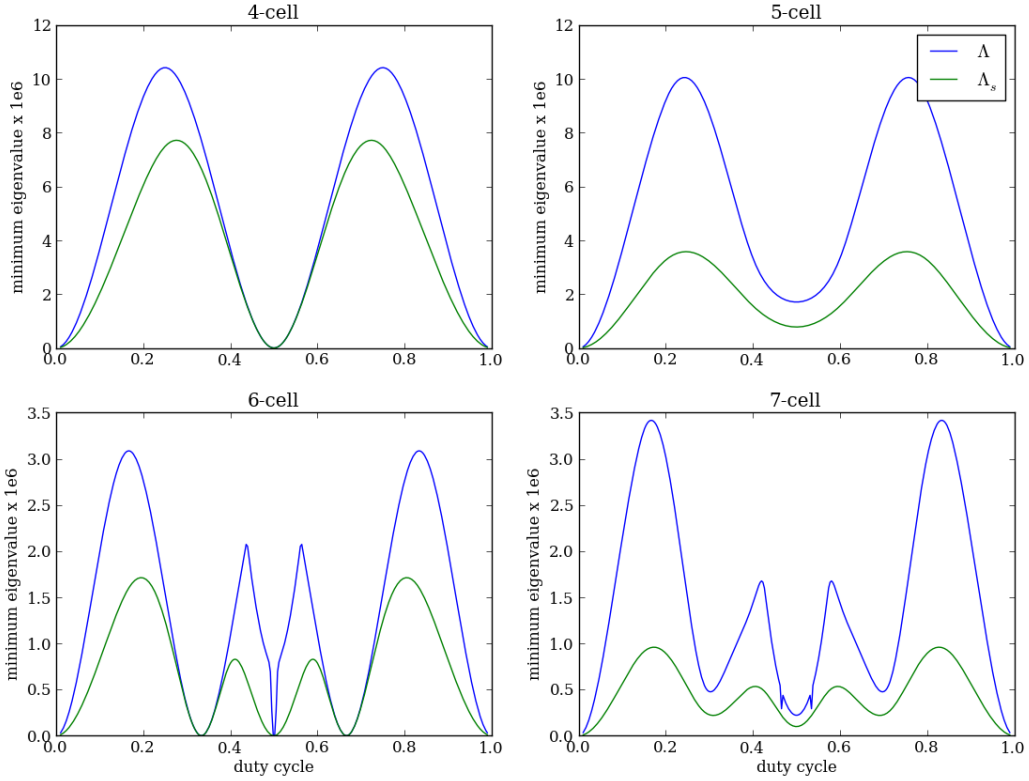

Figure 4.22: The minimum real part of the eigenvalues of $\mathbf{\Lambda}$ and $\mathbf{\Lambda_s}$ vs duty cycle for 4-7 cell FCC.

4.7.7 Duty Cycle Values where $\mathbf{\Lambda}$ is Singular

There are values of constant duty cycle where an eigenvalue with a real part equal to zero exists, or equivalently where $\mathbf{\Lambda}$ is singular. Under these conditions, the system will not rebalance. For an in-depth discussion, refer to [28]. These values are tabulated in Table 4.4.

Table 4.4: Values of constant duty cycle where $\mathbf{\Lambda}$ is singular

Number of Cells	Duty Cycles
2	0,1
3	0,1
4	$0,\frac{1}{2},1$
5	0,1
6	$0,\frac{1}{3},\frac{1}{2},\frac{2}{3},1$
7	0,1

4.8 Simulation Studies

4.8.1 4-Cell Example

A 4-cell FCC, with component values as tabulated in Table 4.1 on p. 62, was simulated under the following conditions:

1. At $t = 0\ s$ the system is assumed to be in voltage balance, i.e. $v_{d1} = v_{d2} = v_{d3} = 0$, with $i_o = v_o = 0$.
2. The FCC cells are operating at a constant duty cycle, with interleaved switching.
3. At $t = 20\ ms$ the value of v_{d3} is set to 20 V.

Using Table E.2 in Appendix E, the value of τ_r corresponding to a duty cycle of 0.28 is 518.58. Using (4.7.85) the worst case time constant is found as

$$\tau_{maxA} = 15.17 \text{ ms},$$

while the Python script listed in Appendix C.2.2 yields the more accurate values:

$$\tau_{maxV} = 10.7 \text{ ms}$$
$$\tau_{max} = 12.8 \text{ ms}$$

In Fig. 4.23 it is clear that there is an initial disturbance of the difference voltages. This initial disturbance is due to the transient response, as the load current and voltage rise to the steady state values.

It is clear that the voltages balance naturally after the introduction of the disturbance. Two traces are added to describe the theoretical approximations. The line describing the τ_{maxV} approximation is described by:

$$f = 20e^{-(t-0.02)/\tau_{maxV}}u(t-0.02)$$

At first glance, the approximated time constant seems conservative. However, the eigenvalues of $\mathbf{\Lambda}$ have large imaginary components, resulting in a high measure of energy exchange between the flying capacitors. It is clear that the initial unbalance energy in v_{d3} is quickly shared between v_{d3} and v_{d1}. In Fig. 4.24 the time constant approximation is changed to

$$f = 10e^{-(t-0.02)/\tau_{maxV}}u(t-0.02),$$

to compensate for this initial energy exchange. The predicted value of τ_{maxV} gives a very good indication of the system rebalancing time constant.

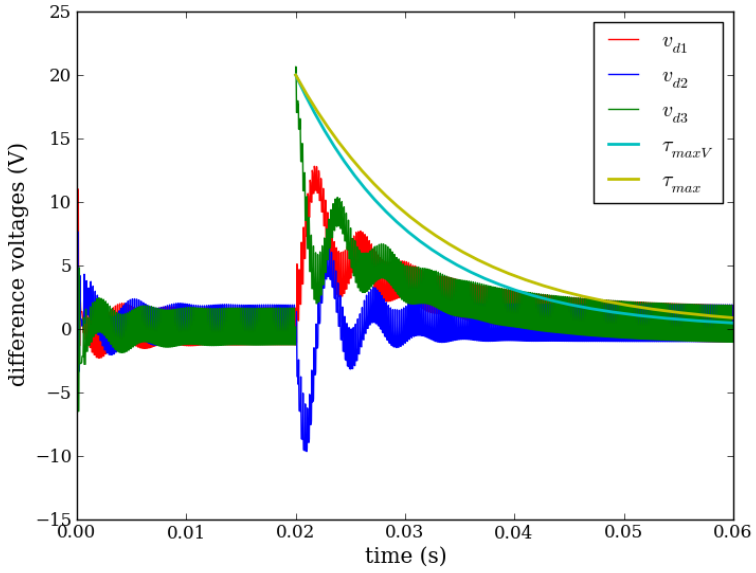

Figure 4.23: Simulation of 4-cell FCC, with $d = 28\%$

In Section 4.7.7, it was stated from [28] that the 4-cell FCC would not rebalance when operating at a constant duty cycle of 50 %. In Fig. 4.25 it can be seen that the FCC does not rebalance after unbalance in v_{d3} is introduced. However, the system rebalances when unbalance is introduced in v_{d2}, Fig. 4.26. For the 4-cell FCC there are 3 time constants, and although the largest is infinitely large at a constant duty-cycle of 50 %, the smallest is finite. The solution to the system: (4.7.78), repeated as

$$\mathbf{v_d} = \sum_{n=1}^{3} A_n \mathbf{y_n} e^{-\varphi_n t/C},$$

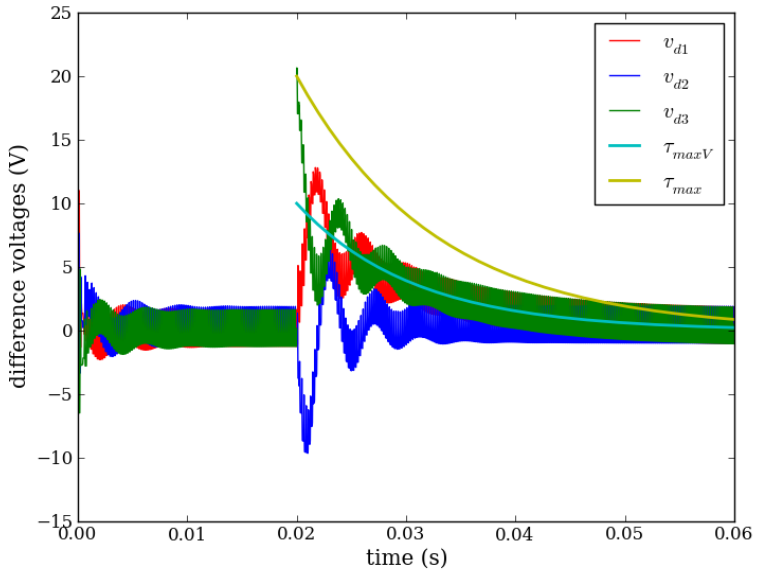

Figure 4.24: Simulation of 4-cell FCC, with $d = 28\%$, alternate representation of τ approximation

describes the rebalancing of the circuit after the introduction of a disturbance. The eigenvectors $\mathbf{y_n}$ and eigenvalues φ_n are invariant to the type of disturbance. However, the constants A_n vary according to the disturbance, and they are calculated from the initial conditions. When the disturbance is introduced in v_{d2}, the constant corresponding to the eigenvalue(s) with a real part of zero will be equal to zero, effectively removing the constant, that is the e^{0t}, term from the solution.

4.8.2 Limitations of the Approximation: 5-cell Examples

A 5-cell FCC was simulated using the same conditions and circuit component values as for the 4-cell case in the previous section. The converter is operating with a constant duty cycle, with $d = 70$ %. Using Table E.3 in Appendix E, the value of τ_r corresponding to a duty cycle of 0.7 is 1242.868. Using (4.7.85), the largest time constant is found as:

$$\tau_{maxA} = 36.368 \text{ ms}$$

while the Python script listed in Appendix C.2.2 yields the more accurate values:

$$\tau_{maxV} = 11.9 \text{ ms}$$
$$\tau_{max} = 32.13 \text{ ms}$$

The resulting difference voltages and an approximation of the form

$$f = 20e^{(t-0.02)/\tau}u(-t-0.02),$$

are shown in Fig 4.27. It is clear that the approximated time constant describes the system well.

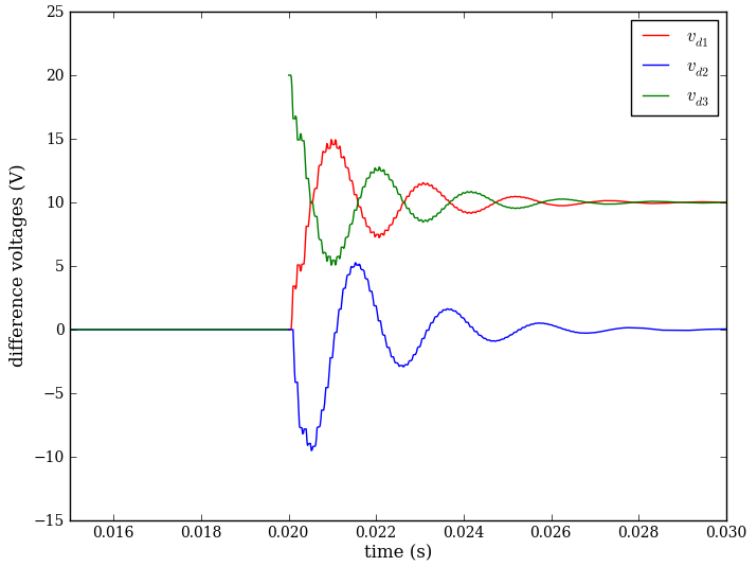

Figure 4.25: Simulation of 4-cell FCC, with $d = 50\%$, initial unbalance in v_{d3}

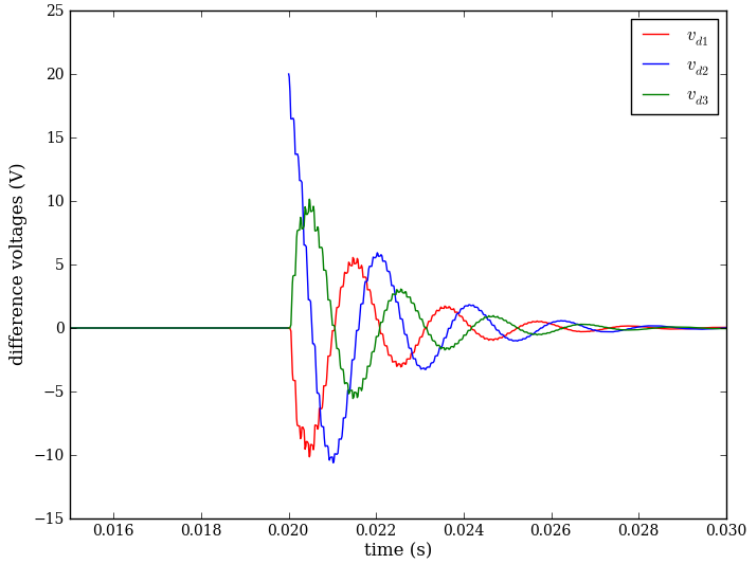

Figure 4.26: Simulation of 4-cell FCC, with $d = 50\%$, initial unbalance in v_{d2}

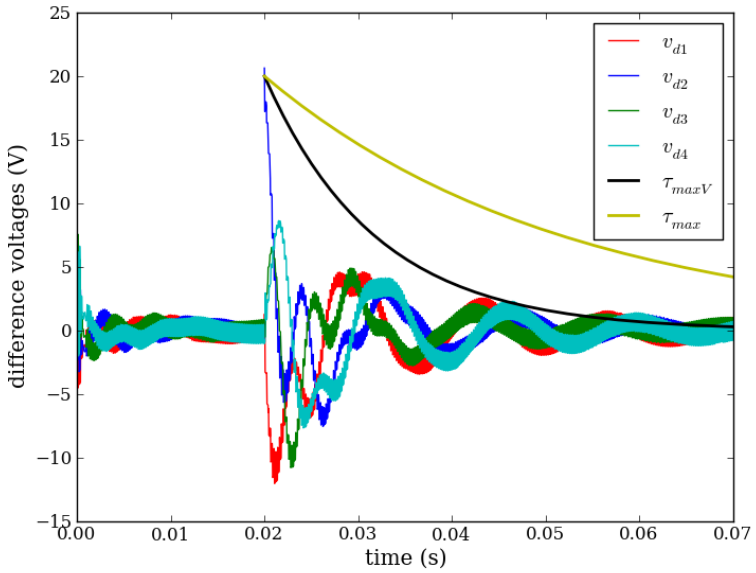

Figure 4.27: Simulation of 5-cell FCC, base-case with $d = 70\%$

The main assumptions in the approximation of τ_{max} with τ_{maxA} were that the filter inductor characteristics dominate the behaviour of $Z(\omega)$ at the switching frequency and above, and that $r \ll \omega L$, at the switching frequency. In Fig. 4.28, the filter inductor ESR is changed to 4.8 Ω, resulting in $r \approx \omega L$ at the switching frequency. The larger ESR alters the approximation time constant to $\tau_{maxA} = 6.06$ ms. The correct value of τ_{max} calculated with the Python script is 7.44 ms. It is clear from Fig. 4.28 that in this case the approximation still yields an acceptable result.

4.9 N-Cell FCC with Modulated Duty Cycle

In most applications of the FCC the output is sinusoidally modulated, for example, when the FCC is used as an electrical machine drive. The analysis of the FCC with modulated output requires the representation of modulated PWM signals in the frequency domain. Several methods of calculating the Fourier series coefficients exist:

1. The Fourier series expansion for a non-modulated signal can be used, with a time varying duty cycle. This method requires the manipulation of the resulting $\cos(\xi \cos(\theta))$ terms into Bessel function forms using the Jacobi-Anger expansions [5]. This method can be used for a sinusoidal reference modulated by a triangular carrier.

2. The double Fourier series method was first proposed by W.R. Bennet [73] for use in communication systems [5; 74]. It was later adapted for use in PWM power converters by Bowes and Bird [75]. This method had been used in previous studies concerning the natural balancing of the FCC [28; 25], three

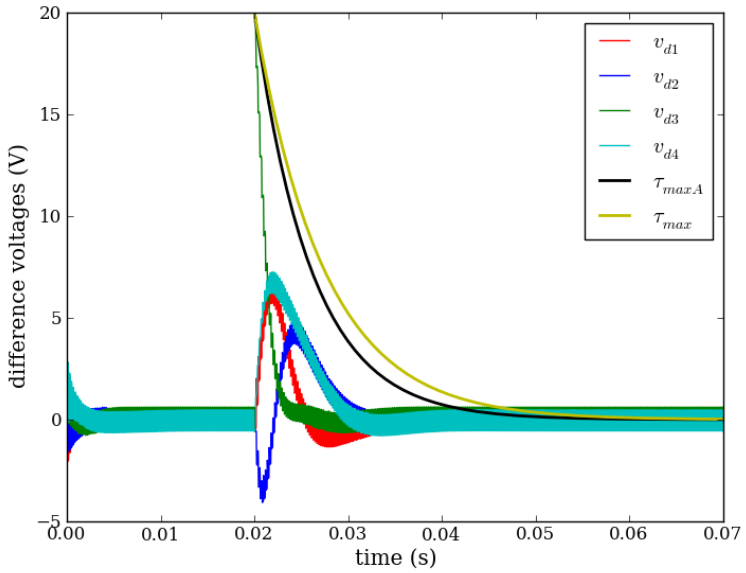

Figure 4.28: Simulation of 5-cell FCC, $d = 70\%$ with $r = 4.8\ \Omega$

phase diode clamped converters [29] and Series Stacked Power Conditioners [33], [32]. The use of the this method for various carriers are discussed in detail in [5] while [74] discusses the use of the method to express the double Fourier series in exponential form.

The double Fourier series method will be used in this study to derive the Fourier series coefficients. The exponential Fourier series, containing positive and negative frequencies, will be used, as the convolution operator is strictly only defined for the exponential Fourier series.

Let the switching PWM function of a single cell be created through comparison of a reference signal f_r and a triangular carrier signal, f_c, with frequency ω_s. A triangular carrier is used in lieu of a sawtooth carrier, since the triangular carrier results in lower harmonic distortion at the output voltage, especially in three phase inverters [5].

For the FCC the switching function has a value of either -1 or 1, and is derived in the following manner:

$$
\begin{aligned}
f_r &= m_a \sin(\omega_r t + \theta_r) \\
f_c &= \frac{2}{\pi} \arcsin(\sin(\omega_s + \theta_s)) \\
s(t) &= \begin{cases} 1, \text{ for } f_r \geq f_c(t) \\ -1, \text{ for } f_r < f_c(t) \end{cases}
\end{aligned}
$$

The process is illustrated in Fig.4.29.

The switching signal can be expressed in exponential Fourier series form, as shown in [74]. Defining $x(t) = \omega_L t + \theta_L$ and $y(t) = \omega_s t + \theta_s$, the switching function

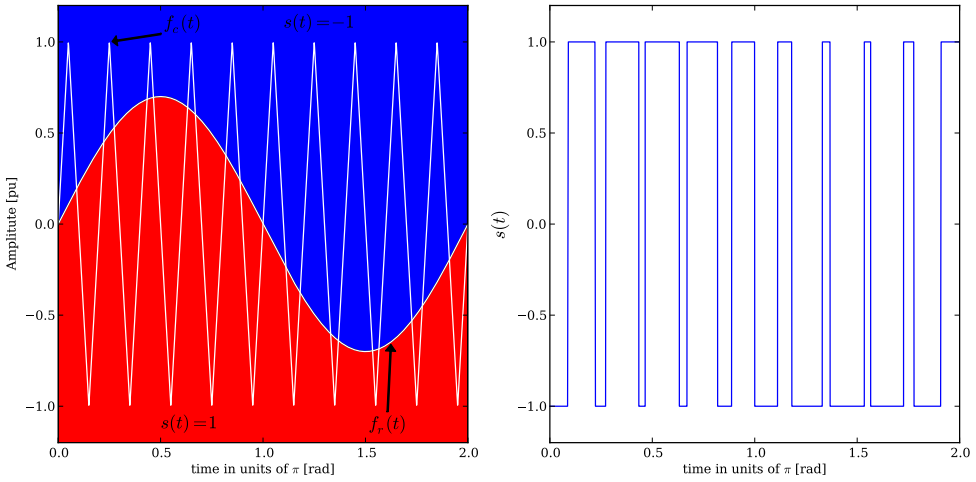

Figure 4.29: Generation of a modulated PWM signal

s is expressed as:

$$s(t) = \sum_{k=-\infty}^{\infty} \sum_{m=-\infty}^{\infty} \tilde{S}_{(k,m)} e^{j(kx+my)} \tag{4.9.1}$$

where

$$\tilde{S}_{(k,m)} = \frac{1}{4\pi^2} \int_0^{2\pi} \int_0^{2\pi} F(x,y) e^{-j(kx+my)} dxdy. \tag{4.9.2}$$

A unit cell of the background function $F(x,y)$ is indicated in Fig. 4.30. A complete discussion of the development of a general background function can be found in [5].

The double integral is evaluated over the area as indicated by Fig. 4.30. A complete derivation of the exponential Fourier series coefficients is included in Appendix A.6.4. For an N-cell FCC, the a^{th} modulated PWM switching signal can be expressed in Fourier series form as:

$$s_a(t) = \sum_{k=-\infty}^{\infty} \sum_{m=-\infty}^{\infty} \tilde{\Psi}(k,m) e^{jk\omega_r t} e^{jm\omega_s t} e^{jk\theta_r} \zeta_m^a \tag{4.9.3}$$

where

$$\tilde{\Psi}(k,m) = \begin{cases} \frac{-1}{j2} m_a & \text{when } m = 0, k = -1 \\ \frac{1}{j2} m_a & \text{when } m = 0, k = 1 \\ 0 & \text{when } m = 0, |k| \neq 1 \\ \frac{j}{\pi m} J_k(\frac{1}{2}\pi m m_a) \left((-1)^k e^{\frac{1}{2}j\pi m} - e^{-j\frac{1}{2}\pi m} \right) & \text{when } m \neq 0 \end{cases} \tag{4.9.4}$$

and

$$\zeta_m^a = e^{j2\pi a m/N}. \tag{4.9.5}$$

The $e^{jk\theta_r}$ term refers to the phase shift of the reference function f_r. For the remainder of this thesis it will be assumed that $\theta_r = 0$.

With reference to (4.9.4), it is important to note that:

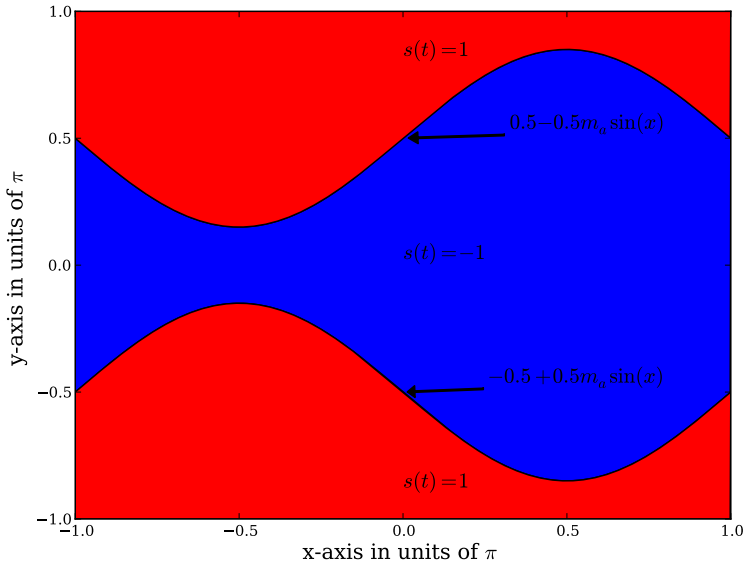

Figure 4.30: Background function unit cell, $F(x, y)$ used to calculate the boost switching function

1. The counter k denotes steps in the frequency domain with size ω_r.
2. Likewise m denotes steps with size ω_s.
3. $\tilde{\Psi}(k, 0)$ describe the low frequency harmonics of the switching function.
4. $\tilde{\Psi}(0, m)$ describes the carrier harmonics.
5. $\tilde{\Psi}(k, m)$ where $k, m \neq 0$ describes the sideband harmonics.
6. Harmonics decay as $|m|$ increase.
7. When $\omega_s \ggg \omega_L$ the groups of harmonics do not overlap [28; 33; 29].

4.9.1 Harmonic Content of Interleaved Modulated PWM Switching Signals

The following section discusses the harmonic content of a 3-cell FCC operating with modulated PWM and with interleaved switching. This section is included to aid the readability of this text.

The converter is operational with parameters as indicated in Table 4.5.

Table 4.5: Operating conditions of 3-cell FCC

f_r	50 Hz
f_s	2.5 kHz
m_a	0.7

When the switching signals are interleaved the carrier signals are phase shifted with respect to one another; choosing $s_0(t)$ as the reference signal, the three carriers are:

$$f_{c0} = \frac{2}{\pi}\arcsin(\sin(\omega_s))$$
$$f_{c1} = \frac{2}{\pi}\arcsin(\sin(\omega_s + \frac{2}{3}\pi))$$
$$f_{c2} = \frac{2}{\pi}\arcsin(\sin(\omega_s + \frac{4}{3}\pi))$$

The resulting switching signals s_0, s_1 and s_2 are shown in Fig. 4.31. The three derived signals s_t, s_{d1} and s_{d2} as defined by

$$s_t = \frac{1}{2}(s_0 + s_1 + s_2)$$
$$s_{d1} = \frac{1}{2}(s_1 - s_0)$$
$$s_{d2} = \frac{1}{2}(s_2 - s_1),$$

are also indicated in Fig. 4.31. The switching frequency in Fig. 4.31 is reduced from 2.5 kHz to 500 Hz for illustrative purposes.

The harmonic spectrum of the switching signal S_0 is indicated in Fig. 4.32. The following observations are highlighted:

1. The harmonics of S_0 appears in clusters around the multiples of the switching frequency. In this example the frequency modulation index, m_f defined as $m_f = \frac{f_c}{f_r}$ [40], is equal to 50 and relatively low for a medium power rating multi-level converter. Even at this lower switching frequency, it is clear that the harmonic clusters centred around the multiples of f_s do not overlap. This property of the harmonic spectrum was used extensively in [28; 33; 29] among others in describing the rebalancing process. This property facilitated the use of the concept of expressing the convolution of two signals by using of the "integrals over groups" concept, described in detail in [28].

2. The magnitude of the clusters of harmonics decreases as m increase. In [33] the following property of the harmonic spectrum was derived and discussed:

$$|\tilde{\Psi}(k,m)| \leq \min\left(\frac{2}{|m|\pi}, \frac{1}{|k|\pi}\int_0^{\frac{2\pi}{\omega_r}}\left|\frac{df_r(t)}{dt}\right|dt\right) \tag{4.9.6}$$

   Where $\int_0^{\frac{2\pi}{\omega_r}}\left|\frac{df_r(t)}{dt}\right|dt$ is a fixed number. The second part of the property describes the formation of the discussed clusters, in that the magnitude of the harmonics in the clusters decay with $|k|$; proving that when the frequency modulation index chosen is high enough the harmonic clusters will not overlap.

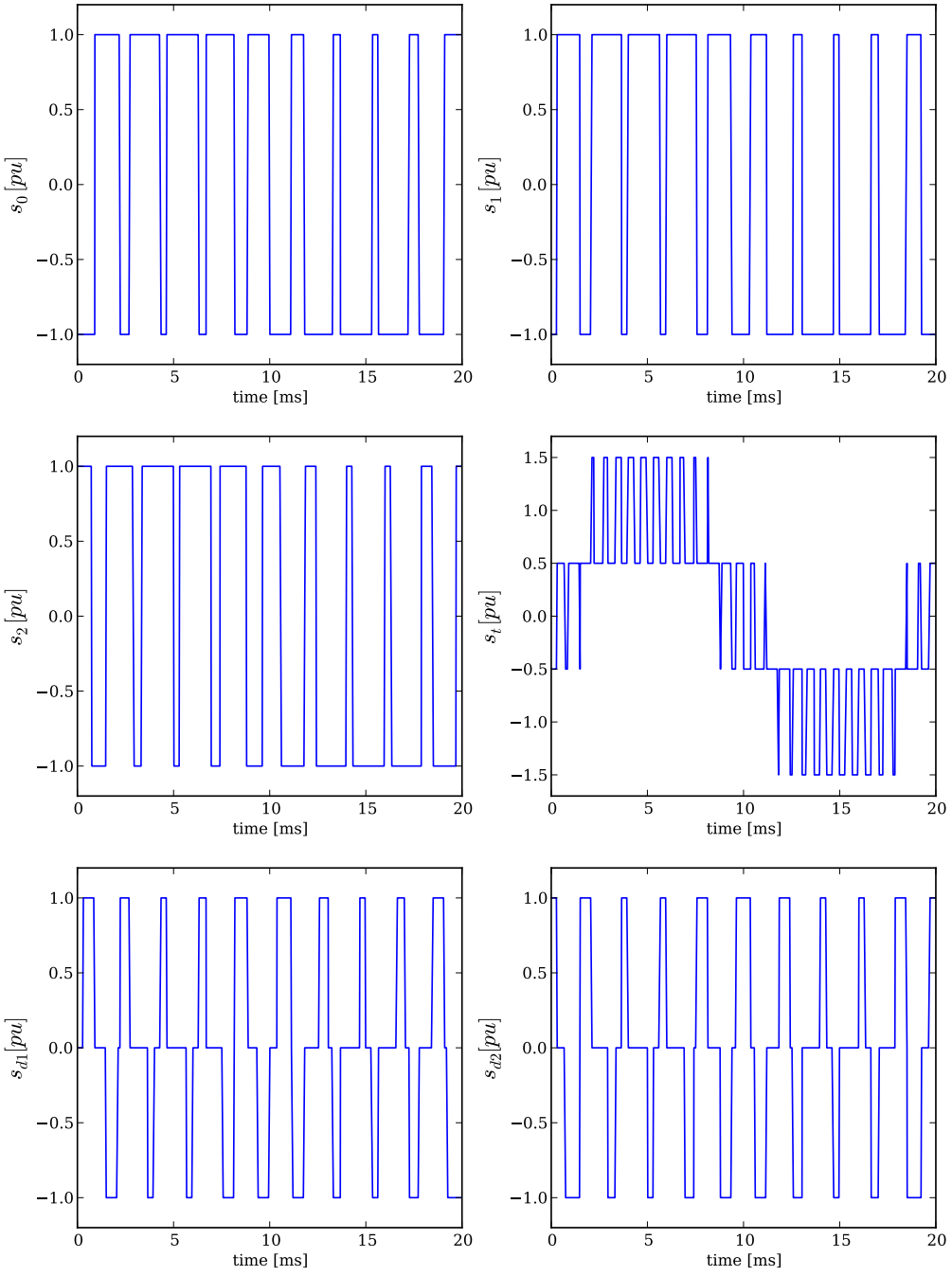

Figure 4.31: The switching signals of the 3-cell FCC

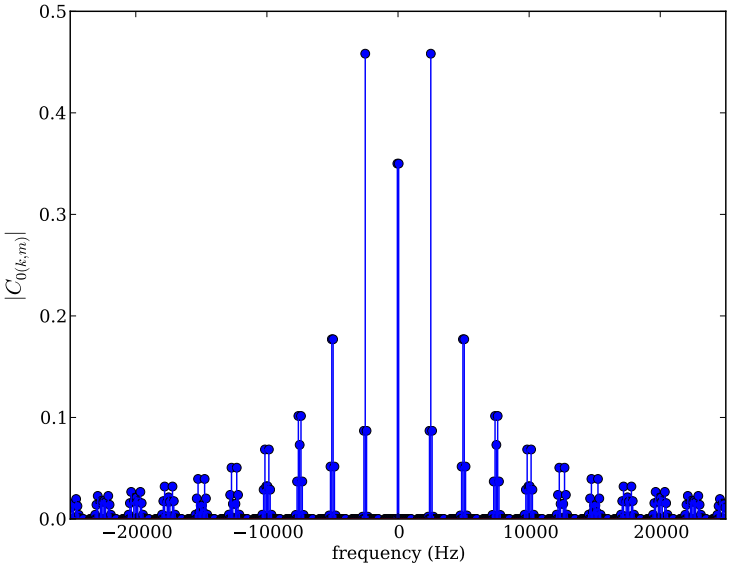

Figure 4.32: Harmonic content of example 3-cell FCC interleaved modulated switching, S_0.

The harmonic spectrum of the S_t switching function is shown in Fig. 4.33. Using the definition of the switching function, the Fourier series coefficients can be expressed as follows, using the result of Lemma 2:

$$\begin{aligned}\tilde{C}_{t(k,m)} &= \frac{1}{2}\left(\tilde{C}_{0(k,m)} + \tilde{C}_{1(k,m)} + \tilde{C}_{2(k,m)}\right) \\ &= \frac{1}{2}\tilde{\Psi}_{(k,m)}(\zeta_m^0 + \zeta_m^1 + \zeta_m^2) \\ &= \begin{cases} \frac{3}{2}\tilde{\Psi}_{(k,m)} & \text{when } m = \vartheta N \\ 0 & \text{otherwise} \end{cases}\end{aligned} \tag{4.9.7}$$

It is clear that, apart from the fundamental component, the first cluster of harmonics appears around the 3^{rd} harmonic of the switching frequency. This apparent multiplication of the switching frequency in interleaved multilevel converters is well known [3; 4]. This frequency multiplication increases the effective switching frequency at the converter output and allows for an output filter with a high cut-off frequency, often reducing the required filter inductor size.

Likewise, the harmonic spectrum of the $\tilde{C}_{d1(k,m)}$ switching function can be described using the definition of S_{d1}, and the result of Lemma 3 as:

$$\begin{aligned}\tilde{C}_{d1(k,m)} &= \frac{1}{2}\left(\tilde{C}_{1(k,m)} - \tilde{C}_{0(k,m)}\right) \\ &= \frac{1}{2}\tilde{\Psi}_{(k,m)}(\zeta_m^1 - \zeta_m^0) \\ &= \begin{cases} \tilde{\Psi}_{(k,m)} & \text{when } m \neq \vartheta N \\ 0 & \text{otherwise} \end{cases}\end{aligned} \tag{4.9.8}$$

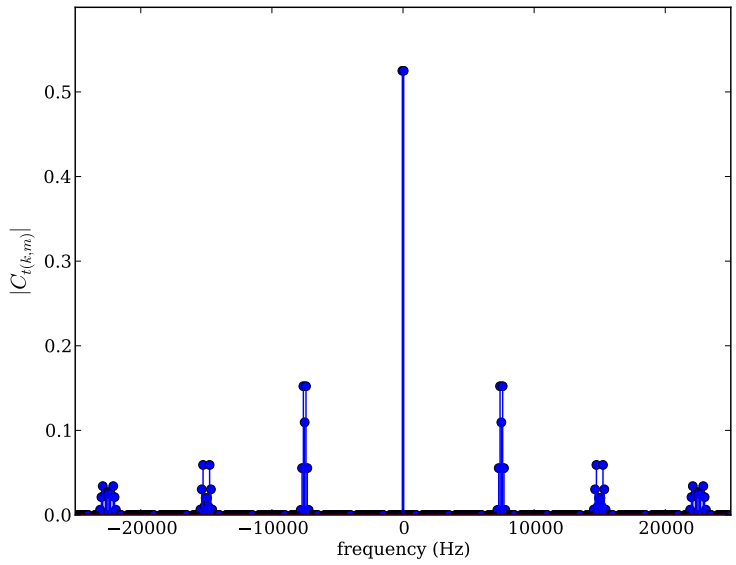

Figure 4.33: Harmonic content of example 3-cell FCC interleaved modulated switching, S_t.

It can be seen from Fig. 4.34, that the harmonics occur in clusters around the harmonics of the switching frequency that are not multiples of N. The harmonics of the $\tilde{S}_{d2}$ switching function are similar to that of $\tilde{S}_{d1}$, albeit phase shifted.

4.9.2 The Rebalancing Matrix

Using the same method as in section 4.7 An expression for the average current through the flying capacitor of cell a where $0 \leq a \leq N-1$ can be found as

$$i_{da} = \frac{V_t}{N} \frac{\tilde{S}_t(\omega)}{Z(\omega)} * \tilde{S}_{da}(\omega)\Big|_{\omega=0} + \sum_{n=1}^{N-1} V_{dn} \frac{\tilde{S}_{dn}(\omega)}{Z(\omega)} * \tilde{S}_{da}(\omega)\Big|_{\omega=0} \tag{4.9.9}$$

Using the results of (4.9.7) and (4.9.8) it can be seen that the harmonics of the $\tilde{S}_t$ and $\tilde{S}_{da}$ occur in clusters around different multiples of the switching frequency. When the frequency modulation index, m_f is high enough, the clusters associated with the $\tilde{S}_t$ and $\tilde{S}_{da}$ switching functions will not overlap. Under this condition the convolution of the modulated signals can be expressed as:

$$\frac{\tilde{S}_t(\omega)}{Z(\omega)} * \tilde{S}_{da}(\omega)\Big|_{\omega=0} = \sum_{\varrho=-\infty}^{\infty} \sum_{\xi=-\infty}^{\infty} \frac{\tilde{C}_{t(\varrho,\xi)}}{Z(\varrho\omega_r + \xi\omega_s)} \tilde{C}_{da(-\varrho,-\xi)} \tag{4.9.10}$$

Using this expression of the convolution sum, or equivalently the integrals over harmonic groups method as discussed in [28; 33; 29], it is shown in Lemma 11 that

$$\frac{V_t}{N} \frac{\tilde{S}_t(\omega)}{Z(\omega)} * \tilde{S}_{da}(\omega)\Big|_{\omega=0} = 0. \tag{4.9.11}$$

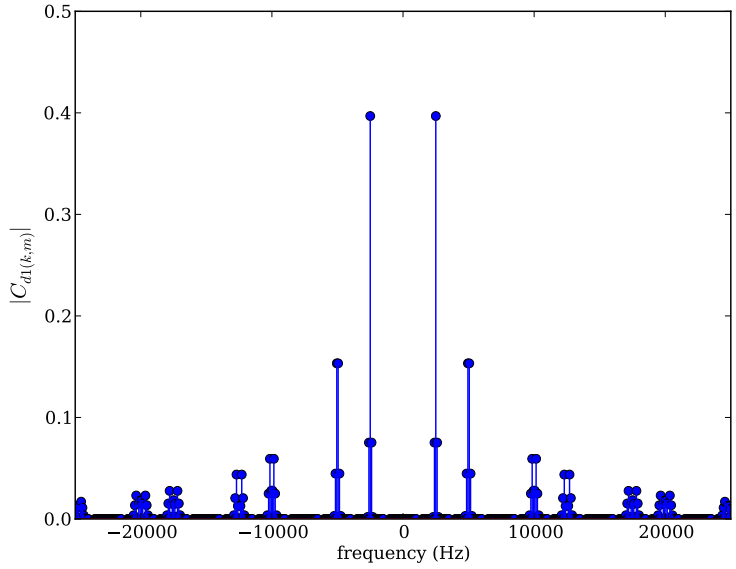

Figure 4.34: Harmonic content of example 3-cell FCC interleaved modulated switching, S_{d1}.

Rewriting in matrix form, the balancing equation can be expressed as:

$$C\dot{\mathbf{v}}_\mathbf{d} = -\tilde{\mathbf{\Lambda}}\mathbf{v}_\mathbf{d} \tag{4.9.12}$$

where

$$\tilde{\mathbf{\Lambda}} = \begin{bmatrix} \tilde{\lambda}_{11} & \tilde{\lambda}_{12} & \cdots & \tilde{\lambda}_{1(N-1)} \\ \tilde{\lambda}_{21} & \tilde{\lambda}_{22} & \cdots & \tilde{\lambda}_{2(N-1)} \\ \vdots & \vdots & \ddots & \vdots \\ \tilde{\lambda}_{(N-1)1} & \tilde{\lambda}_{(N-1)2} & \cdots & \tilde{\lambda}_{(N-1)(N-1)} \end{bmatrix}, \tag{4.9.13}$$

and

$$\tilde{\lambda}_{ab} = \frac{\tilde{S}_{db}(\omega)}{Z(\omega)} * \tilde{S}_{da}(\omega)\Big|_{\omega=0}. \tag{4.9.14}$$

Since the system is evaluated at $\omega = 0$ and the switching functions are real valued, the entries in $\tilde{\mathbf{\Lambda}}$ are all real. According to Theorem 1, it is possible to rewrite $\tilde{\mathbf{\Lambda}}$ as

$$\tilde{\mathbf{\Lambda}} = \tilde{\mathbf{\Lambda}}_\mathbf{s} + \tilde{\mathbf{\Lambda}}_\mathbf{sk} \tag{4.9.15}$$

where $\tilde{\mathbf{\Lambda}}_\mathbf{s}$ is symmetric and $\tilde{\mathbf{\Lambda}}_\mathbf{sk}$ is skew-symmetric.

In Section 4.7.6, it was shown that it is possible to define a maximum voltage rebalancing time constant. It is true that there exists a constant B_n such that

$$|v_{dn}(t)| \leq B_n e^{-t/\tilde{\tau}_{maxV}},\ t \geq 0, \tag{4.9.16}$$

where

$$\tilde{\tau}_{maxV} = \frac{-C}{\min_n(Re\left\{\sigma_n(\tilde{\mathbf{\Lambda}})\right\})}. \tag{4.9.17}$$

Furthermore, by using Theorem 9, a maximum rebalancing time constant can be found from the eigenvalues of $\tilde{\mathbf{\Lambda}}_\mathbf{s}$ such that the difference voltage will be bounded by

$$|v_{dn}(t)| \leq B_n e^{-t/\tilde{\tau}_{max}},\ t \geq 0, \tag{4.9.18}$$

where

$$\tilde{\tau}_{max} = \frac{-C}{\sigma_{min}(\tilde{\mathbf{\Lambda}}_\mathbf{s})}. \tag{4.9.19}$$

A Python script is included in Appendix C.2.3. This script generates $\tilde{\mathbf{\Lambda}}$ using (4.9.13) for any converter and a range of different passive loads with any component values. The values of $\tilde{\tau}_{max}$ and $\tilde{\tau}_{maxV}$ are calculated using (4.9.19) and (4.9.17). The matrix $\tilde{\mathbf{\Lambda}}_\mathbf{s}$ is numerically constructed by

$$\tilde{\mathbf{\Lambda}}_\mathbf{s} = \frac{1}{2}\left(\tilde{\mathbf{\Lambda}} + \tilde{\mathbf{\Lambda}}^\mathbf{T}\right). \tag{4.9.20}$$

4.9.3 Approximation of the Worst Case Voltage Rebalancing Time Constant

In Section 4.7.5 it was shown that under certain conditions it is possible to estimate τ_{max} using tabulated values for unmodulated systems. This section introduces a method that provides the same approximation for the modulated duty cycle case.

Using asymptotic analysis by assuming that $f_s \gg f_r$ the duty cycle can be rewritten as

$$d(t) = \frac{1}{2} + \frac{1}{2} m_a \sin(\omega_r t), \tag{4.9.21}$$

and from (4.2.7)

$$|\Psi(n)|^2 = 2\frac{1-\cos(2\pi n d)}{\pi^2 n^2}. \tag{4.9.22}$$

It is clear that the entries of $\mathbf{\Lambda}_\mathbf{s}$ are a function of the duty cycle.

Recall from (4.7.25) that $\mathbf{\Lambda}_\mathbf{s}$ can be rewritten, including the variable duty cycle term, as

$$\mathbf{\Lambda}_\mathbf{s}(d) = \sum_{n=1}^{\infty} \mathbf{\Lambda}_{\mathbf{s(n)}}(d) \tag{4.9.23}$$

$$\mathbf{\Lambda}_{\mathbf{s(n)}}(d) = \alpha(d,n)\mathbf{R}_{(\mathbf{n})} \tag{4.9.24}$$

$$\mathbf{R}_{(\mathbf{n})} = \begin{bmatrix} 1 & \cos(2\pi n\frac{1}{N}) & \cos(2\pi n\frac{2}{N}) & \cdots & \cos(2\pi n\frac{2}{N}) \\ \cos(2\pi n\frac{1}{N}) & 1 & \cos(2\pi n\frac{1}{N}) & \cdots & \cos(2\pi n\frac{3}{N}) \\ \cos(2\pi n\frac{2}{N}) & \cos(2\pi n\frac{1}{N}) & 1 & \cdots & \cos(2\pi n\frac{4}{N}) \\ \vdots & \vdots & \vdots & \ddots & \vdots \\ \cos(2\pi n\frac{2}{N}) & \cos(2\pi n\frac{3}{N}) & \cos(2\pi n\frac{4}{N}) & \cdots & 1 \end{bmatrix} \tag{4.9.25}$$

$$\alpha(d,n) = \frac{|\Psi(n)|^2}{|Z(n\omega_s)|^2}\left(1 - Re\left\{\zeta_n\right\}\right) Re\left\{Z(n\omega_s)\right\} \tag{4.9.26}$$

$$= \frac{2(1-\cos(2\pi n d))}{\pi^2 n^2 |Z(n\omega_s)|^2}\left(1 - Re\left\{\zeta_n\right\}\right) Re\left\{Z(n\omega_s)\right\}. \tag{4.9.27}$$

The following observations can be made:

1. According to (4.7.10) and (4.7.16) $\mathbf{A_s v_d}$ maps to a vector whose entries are a contribution to the flying capacitor currents, i_{dk} in Fig. 4.20. Let

$$\mathbf{i_s} = \mathbf{\Lambda_s v_d}. \tag{4.9.28}$$

2. Using (4.7.19) $\mathbf{i_s}$ can be calculated by investigating the contribution of the interactions of the switching functions at every harmonic,

$$\mathbf{i_s} = \sum_{n=1}^{\infty} \mathbf{i_{s(n)}} \tag{4.9.29}$$

$$\mathbf{i_{s(n)}} = \mathbf{\Lambda_{s(n)} v_d} \tag{4.9.30}$$

This approach of describing the contribution of each switching harmonic separately had been used in [37].

3. The term $|\Psi(n)|^2$ is symmetric around $d = \frac{1}{2}$ for all n.

4. Substituting (4.9.22) and (4.9.21) into (4.7.10) and expanding yields a linear periodic time variant system

$$\begin{aligned} \dot{\mathbf{v}}_\mathbf{d} &= \mathbf{\Lambda}(t)\mathbf{v_d} \\ &= \mathbf{\Lambda_s}(t)\mathbf{v_d} + \mathbf{\Lambda_{sk}}(t)\mathbf{v_d}. \end{aligned} \tag{4.9.31}$$

Since $d(t)$ is periodic and symmetric around $d = \frac{1}{2}$ an average of the current due to $\mathbf{v_d}$ generated by the interactions at harmonic n can be found. The average value of $|\Psi(n)|^2$ over a modulation period is, using a variable change $\xi = \omega_r t$,

$$\begin{aligned} |\Psi(n)|^2_{ave} &= \frac{1}{\pi}\int_0^\pi \frac{2(1-\cos(2\pi n(\frac{1}{2}+\frac{1}{2}m_s\sin(\xi)))}{\pi^2 n^2} d\xi \\ &= \frac{2}{\pi^2 n^2}\frac{1}{\pi}\int_0^\pi 1-\cos(\pi n + \pi n m_a \sin(\xi))d\xi \\ &= \frac{2}{\pi^2 n^2}\left(1-(-1)^n\frac{1}{\pi}\int_0^\pi \cos(\pi n m_a \sin(\xi))d\xi\right) \\ &= \frac{2}{\pi^2 n^2}\Big(1-(-1)^n J_0(\pi n m_a)\Big). \end{aligned} \tag{4.9.32}$$

As in Section 3.6 let $\hat{x}$ denote the averaged value of variable x, however in this discussion it is an average over a modulation cycle and not a switching cycle. The averaged current generated at harmonic n is therefore

$$\hat{\mathbf{i}}_{\mathbf{s(n)}} = \hat{\mathbf{\Lambda}}_{\mathbf{s(n)}}\mathbf{v_d} \tag{4.9.33}$$

$$\hat{\mathbf{\Lambda}}_{\mathbf{s(n)}} = \frac{2\Big(1-(-1)^n J_0(\pi n m_a)\Big)}{\pi^2 n^2 |Z(n\omega_s)|^2}\left(1 - Re\left\{\zeta_n\right\}\right) Re\left\{Z(n\omega_s)\right\}\mathbf{R_{(n)}}. \tag{4.9.34}$$

And the total averaged current attributable to the action of $\mathbf{\Lambda_s}$ is

$$\hat{\mathbf{i}}_\mathbf{s} = \sum_{n=1}^{\infty}\hat{\mathbf{\Lambda}}_{\mathbf{s(n)}}\mathbf{v_d}. \tag{4.9.35}$$

However, the same current must be found through

$$\mathbf{i_s} = \tilde{\mathbf{\Lambda}}_\mathbf{s} \mathbf{v_d}. \tag{4.9.36}$$

Therefore $\tilde{\mathbf{\Lambda}}_\mathbf{s}$ can be asymptotically approximated as

$$\tilde{\mathbf{\Lambda}}_\mathbf{s} \approx \sum_{n=1}^{\infty} \hat{\mathbf{\Lambda}}_{\mathbf{s(n)}}. \tag{4.9.37}$$

The following is highlighted:

1. The averaging of the current $\mathbf{i_d}$ will only yield an accurate answer if $\mathbf{v_d}$ remains constant over the averaging period.
2. Due to the even symmetry around $d = \frac{1}{2}$ the averaging period is one half of the modulation period.
3. The requirement that the vector $\mathbf{v_d}$ remains constant over an averaging period is satisfied when the averaging period is much faster than the fastest balancing time constant in the system.
4. When the modulation frequency is low, say 3 Hz, the effective duty cycle at the moment of perturbation will determine the balancing time constant. In this case the balancing occurs much quicker than the change in effective duty cycle due to the modulation.
5. This method yields the same result as generating $\tilde{\mathbf{\Lambda}}$ using the double Fourier series.
6. The time domain method uses the same approach to determine the time constants for modulated duty cycle, as discussed in Section 2.2.2.

Using the assumption that the filter inductor dominates the behaviour of the load at the switching frequency and above and that $\omega_c L \gg r$, it is possible to write

$$\tilde{\mathbf{\Lambda}}_\mathbf{s} \approx \hat{\mathbf{\Lambda}}_\mathbf{s} \approx \frac{r}{L^2 f_s^2} \tilde{\mathbf{\Lambda}}_\mathbf{r} \tag{4.9.38}$$

where

$$\tilde{\mathbf{\Lambda}}_\mathbf{r} \approx \sum_{n=1}^{\infty} \tilde{\mathbf{\Lambda}}_{\mathbf{r(n)}} \tag{4.9.39}$$

$$\tilde{\mathbf{\Lambda}}_{\mathbf{r(n)}} = \beta(n) \begin{bmatrix} 1 & \cos(2\pi n \frac{1}{N}) & \cos(2\pi n \frac{2}{N}) & \cdots & \cos(2\pi n \frac{2}{N}) \\ \cos(2\pi n \frac{1}{N}) & 1 & \cos(2\pi n \frac{1}{N}) & \cdots & \cos(2\pi n \frac{3}{N}) \\ \cos(2\pi n \frac{2}{N}) & \cos(2\pi n \frac{1}{N}) & 1 & \cdots & \cos(2\pi n \frac{4}{N}) \\ \vdots & \vdots & \vdots & \ddots & \vdots \\ \cos(2\pi n \frac{2}{N}) & \cos(2\pi n \frac{3}{N}) & \cos(2\pi n \frac{4}{N}) & \cdots & 1 \end{bmatrix} \tag{4.9.40}$$

$$\beta(n) = \frac{1 - (-1)^n J_0(\pi n m_a)}{2\pi^4 n^4} \left(1 - Re\left\{\zeta_n\right\}\right). \tag{4.9.41}$$

Therefore, the eigenvalues of $\tilde{\mathbf{\Lambda}}_\mathbf{s}$ can be approximated by the eigenvalues of $\tilde{\mathbf{\Lambda}}_\mathbf{r}$ as

$$\sigma(\tilde{\mathbf{\Lambda}}_\mathbf{s}) \approx \frac{r}{L^2 f_s^2}\sigma(\tilde{\mathbf{\Lambda}}_\mathbf{r}). \tag{4.9.42}$$

Expressing $\tilde{\mathbf{\Lambda}}_\mathbf{s}$ in terms of $\tilde{\mathbf{\Lambda}}_\mathbf{r}$ is beneficial, since $\tilde{\mathbf{\Lambda}}_\mathbf{r}$ is invariant of the connected load. A good approximation of the maximum rebalancing time constant can be found as

$$\tilde{\tau}_{maxA} = \frac{CL^2 f_s^2}{r}\tilde{\tau}_r, \tag{4.9.43}$$

where the values of $\tilde{\tau}_r$ are tabulated in Tables E.7-E.13 for a range of modulation indexes for converters with 2-8 cells. Again, the following are the relationships between the discussed time constants:

$$\begin{aligned}\tilde{\tau}_{max} &\approx \tilde{\tau}_{maxA} \\ &\geq \tilde{\tau}_{maxV}\end{aligned}$$

It should be noted that the accuracy of the approximation again hinges on the assumptions made when writing $Z(n\omega_s) \approx r + jn\omega_s L$ at the switching frequency and higher, as discussed throughout this Chapter.

4.9.4 Modulated Duty Cycle Simulation Studies

In this section, the presented theory is validated through comparison with time domain simulations. The parameters for two FCC converters are shown in Table 4.6. The equivalent induction motor parameters are adapted from from [37] and are derived from a 7 kW motor.

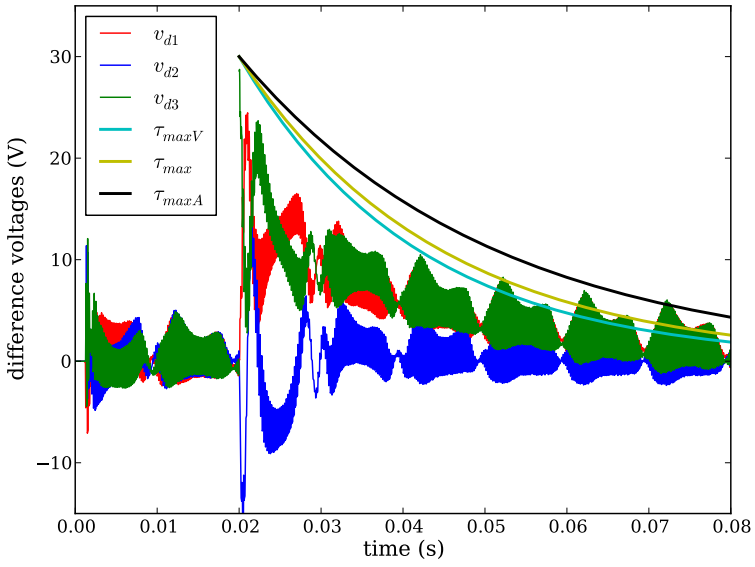

Figure 4.35: 4-Cell FCC rebalancing with modulated duty cycle: Case 1

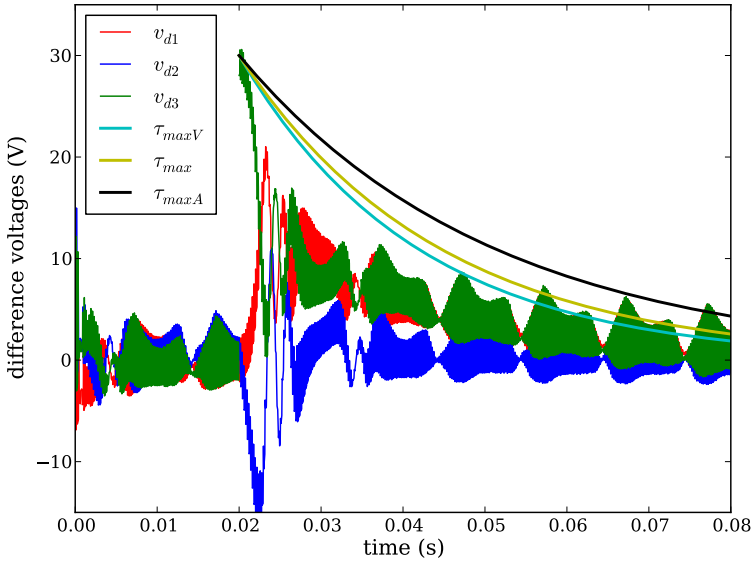

Figure 4.36: 4-Cell FCC rebalancing with modulated duty cycle: Case 2

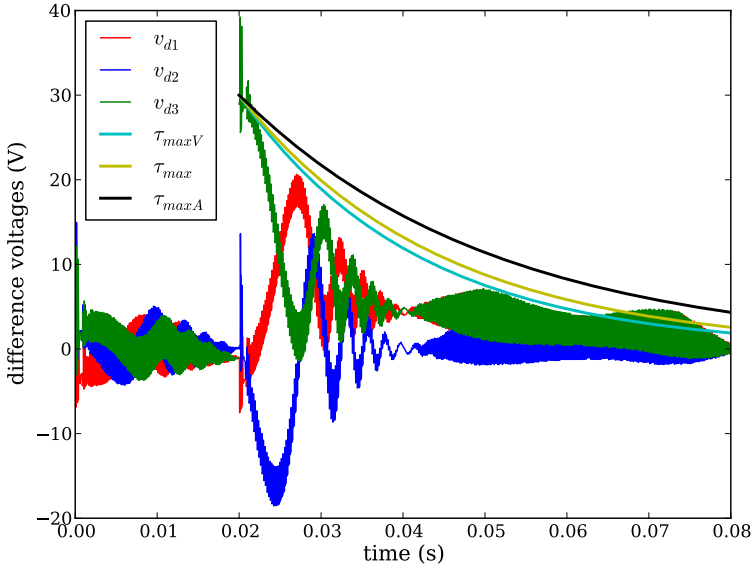

Figure 4.37: 4-Cell FCC rebalancing with modulated duty cycle: Case 3

Table 4.6: Component values for a typical FCC, modulated duty cycle case

Stand Alone Inverter Application			
V_t	100 V	C	20 μF
L	250 μH	C_f	75 μF
r_{dc}	0.8 Ω	f_s	5 kHz
R	10 Ω	m_a	0.8
Induction Drive Application			
V_t	100 V	C	20 μF
L	27.9 mH	r	4.9 Ω
f_s	5 kHz	m_a	0.8
C_b	4.7 μF	L_b	250 mH
r_b	2 Ω		

During the following simulations the flying capacitor voltages are initially balanced. The system is simulated for 20 ms until all parameters reach steady state. An unbalance is introduced at 20 ms.

A 4-cell FCC with LC filter is simulated in Figures 4.35-4.37. The different time constants derived in this study approximate the rebalancing well. In Fig. 4.35, the reference function was $f_r(t) = 0.8\sin(2\pi 50t)$, while in Fig. 4.36 $f_r(t) = 0.8\cos(2\pi 50t)$ was used. It can be seen that the instantaneous value of the reference function when the unbalance occurs has an influence on the rebalancing dynamics. However, the theory presented yields an averaged time constant. Similarly, the reference function frequency change in Fig. 4.37 where $f_r(t) = 0.8\cos(2\pi 12t)$ changes the balancing dynamics, but the averaged time constants still describe the system well.

A discussion of the natural balancing properties of a FCC, which is used as an induction machine drive, is found in [37]. It is shown that, since the balancing harmonics are much higher than the fundamental, the motor slip can be ignored for balancing study purposes. Therefore, the balancing dynamics are independent of mechanical load. It is true that the motor winding resistance has a strong dependence on frequency due to skin- and proximity effects [69; 70]. However, in the following analysis, this dependence will be ignored and the assumption is made that the leakage inductance is much lower than the magnetising inductance. The induction machine is modelled as a pure inductance in series with an equivalent resistance. Should a more representative model be required it is best to consult [37].

It is true for electrical machines that at the switching frequency the leakage inductance reactance is much larger than the winding ESR. This results in a very large natural balancing time constant. If the FCC is used in a drive application, it is imperative to use a balance booster. A 5-cell FCC was simulated as a drive with the indicated parameters, Fig. 4.38. The time constants were calculated using the Python script in Appendix C.2.3.

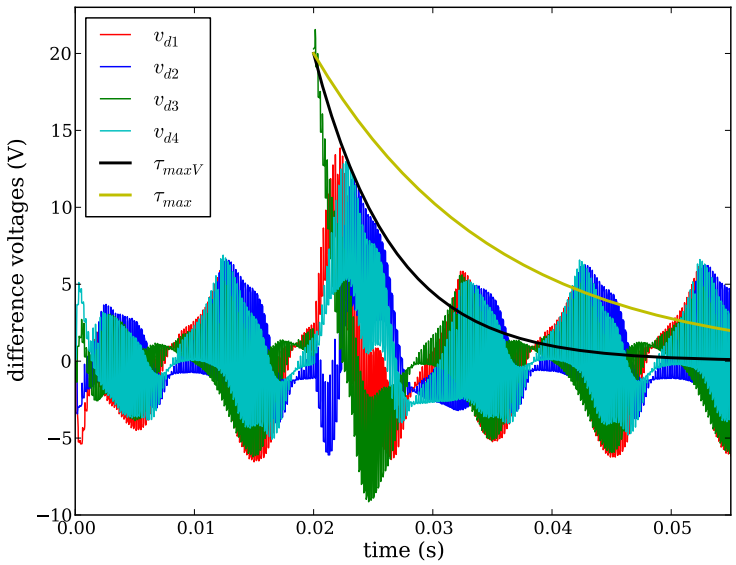

Figure 4.38: 5-Cell FCC rebalancing: drive application with balance booster

4.10 Practical Measurements

The presented theory was verified using practical measurements of the system described in Table 4.7.

In the presented theory it was shown that the balancing time constant depends on the ratio $Re\{Z(\omega)\}/|Z(\omega)|^2$ at the multiples of the switching frequency. Furthermore, it is true that, the real part of the load at the switching frequency multiples is mostly determined by the inductor ESR. The filter inductor was manufactured with a 150 turns. Litz wire with 5 strands at 0.2 mm diameter was used to minimise the effect of the skin effect and the proximity effect. However, the effects still had a significant influence on the ESR. With the equipment available it was possible to accurately measure the ESR at DC and at 75 kHz. Unfortunately it was not possible to measure the ESR with an acceptable accuracy at the frequencies in between.

Due to the uncertainty regarding the correct value of the ESR at the switching frequency multiples the following was decided:

1. The first N-1 switching harmonics (in a N-cell FCC) have the biggest influence on the rebalancing time constant.

2. It is true that the ESR will differ at these frequencies. However, it is assumed (in keeping with the assumption used in the theory development) that the ESR remains nearly constant over this frequency range.

3. The effective ESR was estimated by fitting the balancing time constant of a K-cell configuration at a specific duty cycle.

4. If the presented theory is accurate the predicted balancing time constants for the K-cell FCC will be accurate at all other values of duty cycle or modulation index.

5. Due to the fact that the first N-1 harmonics in a N-cell FCC have a large influence on the time constant the ESR estimation for the K-cell can not be used for the M-cell FCC.

Table 4.7: Practical FCC Setup

V_t for $t < 0$	49 V	V_t for $t \geq 0$	65 V
C	94 μF	C_f	50 μF
L	2.2 mH	f_s	3 kHz
r_{dc}	0.75 Ω	r_{75kHz}	8 Ω
R_{large}	8 Ω	R_{small}	32 Ω

4.10.1 3-Cell FCC

The balancing of the 3-cell FCC after the introduction of a step change in the input voltage is shown in Fig. 4.39. In Fig. 4.40 the same results are shown in terms of difference voltages. This measurement was used to estimate the inductor ESR as 3.5 Ω. The fitted time constant is shown in the figure.

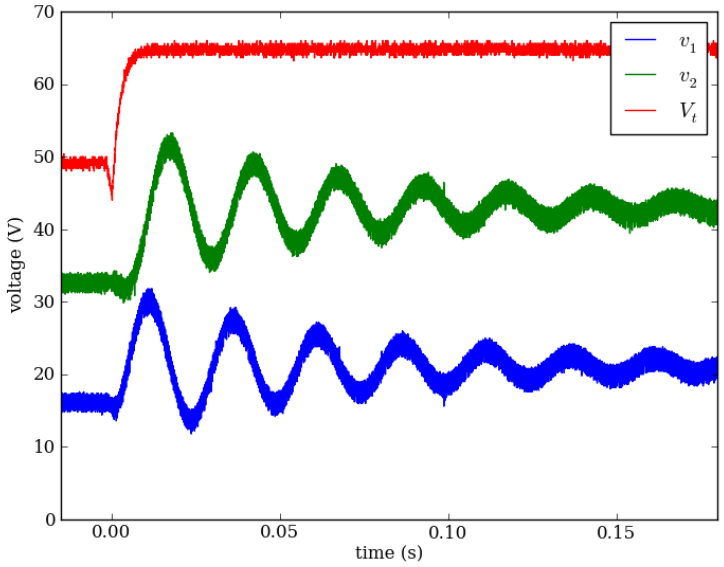

Figure 4.39: Measurement of the 3-Cell FCC rebalancing: $d = 63\%$

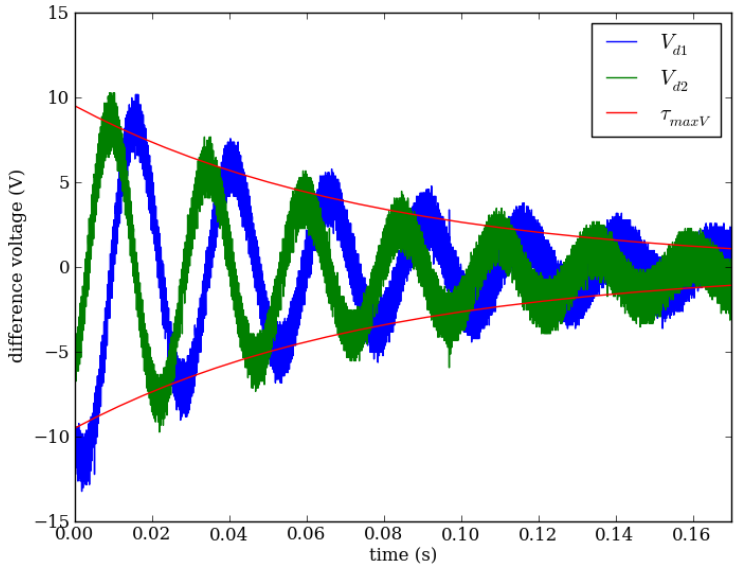

Figure 4.40: Measurement of the 3-Cell FCC rebalancing: ESR estimation, $d = 63$ %

The same ESR value was used to determine the time constants for the 3-cell FCC operating with a duty cycles of either 25 % or 82 %. The reference tables in Appendix E was used in conjunction with (4.7.85) to determine τ_{maxA}. The Python program listed in Appendix C was used to determine τ_{max} and τ_{maxV}. The resulting waveforms are shown in Fig. 4.41. It is clear that the presented theory approximates the measured results well.

The measured results of the 3-cell FCC with modulated duty cycle is shown in Fig. 4.42. The modulation index is $m_a = 0.75$ and the modulation frequency is 50 Hz. The balancing in terms of difference voltages are shown in Fig. 4.43. The same ESR as with the constant duty cycle 3-cell FCC was used to calculate the different time constants. Again, the presented theory describes the measured results well.

4.10.2 4-Cell FCC

The same tests were repeated for the 4-cell FCC. Using the balancing measurement for the FCC operating with $d = 13$ % the ESR was estimated as $r = 4.5\ \Omega$. The resulting waveforms are shown in Fig. 4.44.

Unlike the previous 3-cell example where there was two complex eigenvalues of $\mathbf{\Lambda}$, and therefore one time constant, the 4-cell FCC has two time constants. Due to imperfections in the practical system a steady state error was observed. In Fig. 4.44 the time constant was fitted to the non-oscillatory part of the V_{d3} waveform.

The estimated ESR was used to predict the time constants for the 4-cell FCC operating with $d = 82$ %, see Fig. 4.45. It is clear that a balancing error exists in the steady state. However, an error of around 2 V with an input of around 66 V is deemed to be acceptable. The existence of this error can be attributed to imperfections in the circuit. Any timing errors in the switching circuits (either due to

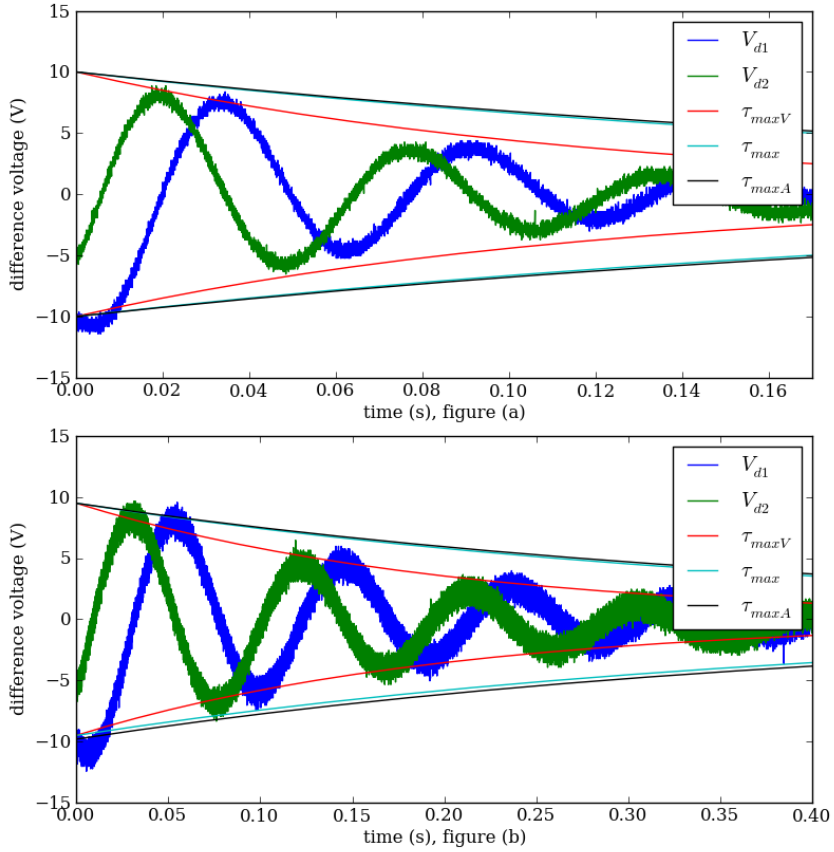

Figure 4.41: Measurement of the 3-Cell FCC rebalancing: (a) $d = 25$ % and (b) $d = 82\%$

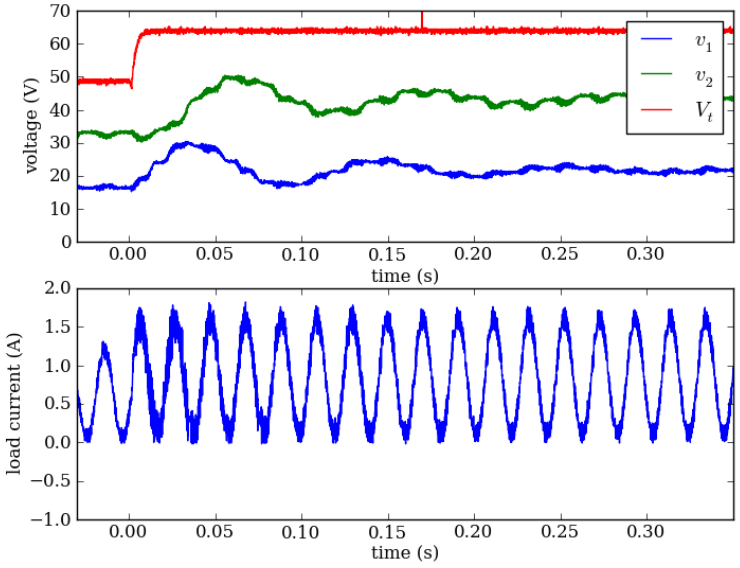

Figure 4.42: Measurement of the 3-Cell FCC rebalancing: modulated duty cycle $m_a = 0.75$

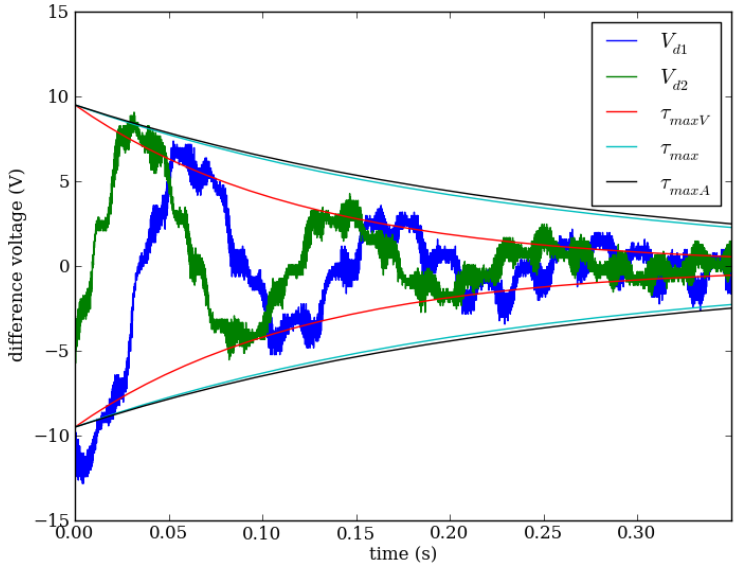

Figure 4.43: Measurement of the 3-Cell FCC rebalancing: modulated duty cycle $m_a = 0.75$, fitted time constants

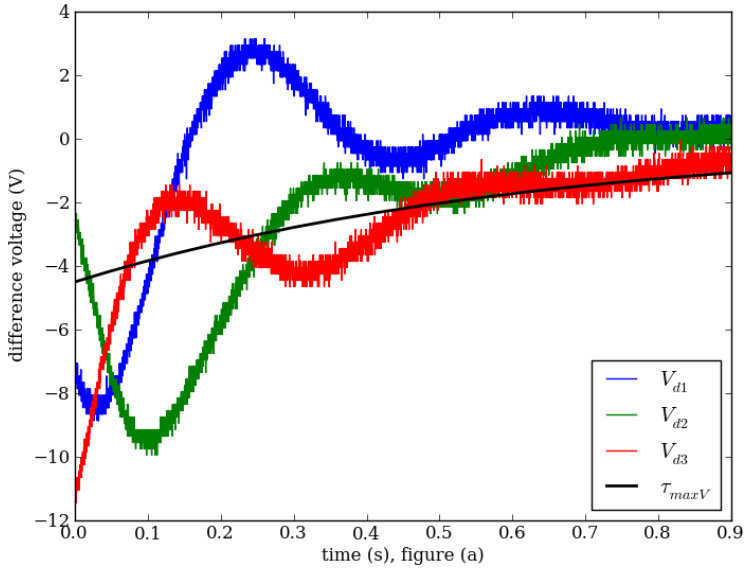

Figure 4.44: Measurement of the 4-Cell FCC rebalancing: ESR estimation, $d = 13$ %

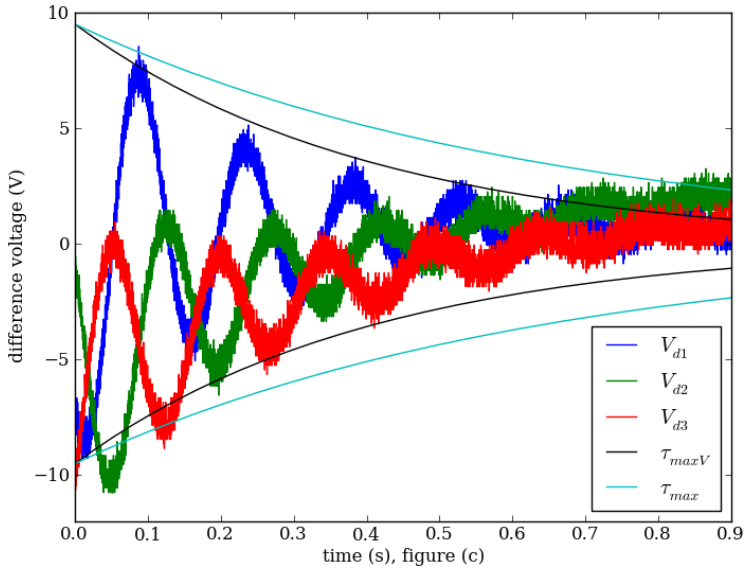

Figure 4.45: Measurement of the 4-Cell FCC rebalancing: $d = 82$ %

variations in the PWM generation process or variances in the switching behaviour of the switching elements) will result in faulty interleaving. The result, as described in Lemma 10, that the convolution of a difference and a total switching function results in a zero DC component strictly only holds for the case where there are no interleaving errors present. It is also worthwhile to note that when the circuit was measured with a balance booster, therefore with much improved balancing properties, the steady state error was eliminated.

Since the load did not change from the 3-cell example, the approximated time constant τ_{maxA} is not indicated in Fig. 4.45.

4.11 Conclusion

A model for the weak natural balancing process FCC was created in the frequency domain. The balancing process was investigated by means of a systematic increase in the complexity of the investigated system, starting with the 2-cell constant duty cycle case and concluding with the N-cell modulated duty cycle FCC. Accurate expressions for the worst case voltage and energy balancing time constants were found. Under many conditions, it was possible to find a simple, yet accurate, expression for the worst case time constant that could be calculated using a pocket calculator and reference table.

The theory presented is simple enough to yield insight into the natural balancing process. It was shown that the balancing occurs through the dissipation of the unbalance energy that was initially stored in the flying capacitor in the real part of the load at harmonics of the switching frequency. This provides clear insight into the operation of the balance booster as well as into why the ESR of an inductor will

influence the balancing time constant, especially when the effect of the skin- and proximity-effects are not negligible.

Several Python script files that can be used to investigate the balancing process and to accurately determine the discussed matrices and time constants are included in AppendixC.

In summary, it was found that:

1. The rebalancing time constant is dependent on the ratio of $\frac{Re\{Z(\omega)\}}{|Z(\omega)|^2}$ at the switching frequency harmonics.

2. The inclusion of a balance booster alters this ratio, thereby improving the natural balancing.

3. The system will be stable and dissipate any unbalance voltages when $\mathbf{\Lambda_s}$ is positive definite.

4. It was shown that for practical load configurations $-\mathbf{\Lambda_s}$ is be negative definite and the system therefore Lyapunov stable.

5. It was shown that a time constant can be found that forms a upper bound for the maximum voltage balancing time constant.

6. With most load configurations, it is possible to approximate the maximum time constant as:

$$\begin{aligned}\tau_{max} &\approx \tau_{maxE} \geq \tau_{maxV} \\ &= \frac{CL^2 f_s^2}{r}\tau_r\end{aligned}$$

The values for τ_r are tabulated in Appendix E for FCC converters operating with either constant or modulated duty cycle.

Chapter 5

The Loss Based Balancing Mechanism: Input-Series-Output-Series Converter

5.1 Introduction

In this chapter it will be shown that the converter losses play a role in the natural balancing of converters. The ISOS converter will be used as example.

In the literature, active balancing methods are typically proposed for the ISOS [76; 77]. However, these methods not only require additional measurement circuits and complicated control circuits, but they also limit the ability to isolate any faulty cell without hampering circuit operation.

Studies of common-duty ratio control of modular DC-DC converters and their natural balancing properties can be found in the literature [31; 78]. However, these studies indicated that the ISOS will be unstable under such a control scheme and that an active balancing method is a necessity. Although investigation of the circuit operation with traditional averaging techniques would support this hypothesis, this study in fact shows that the ISOS converter has natural balancing abilities.

Investigation of the ideal ISOS converter reveals a weak rebalancing mechanism similar to that found in the FCC, as discussed in Chapter 4. In other words that any voltage unbalance among the cells would be counteracted by the inherent circuit operation as long as the different cells are operating with interleaved switching signals. This weak rebalancing is identified in the ISOS, and quantified by analysing the circuit in the frequency domain. A time constant that describes the rebalancing is presented. The existence of the weak balancing mechanism is verified through time domain simulations.

When the switching losses and the isolation transformer magnetic losses, which are both dependent on the cell bus voltage, are included another rebalancing mechanism is identified. This mechanism is termed strong, as it does not depend on the interleaving of the cell switching signals.

Lastly, measurements from a practical converter are presented. From the pre-

sented theory and the measurements, it is shown that the ISOS will balance naturally. The strong rebalancing mechanism has a strong influence on the rebalancing time constant. However, the weak rebalancing mechanism plays an important role in limiting the voltage balancing deviation when cells that are not exactly the same are used.

5.2 Equivalent Balancing Circuit of the ISOS

A circuit of a 2-cell modular ISOS DC-DC converter is shown in Fig. 5.1. The following assumptions are made:

1. The switches and diodes are assumed to be ideal.
2. The source and other interconnection resistances are lumped together as r_s. The inductance of the interconnection is modelled as L_s. Both parameters are deemed to be small.
3. The ESR of the filter inductor L is lumped as r.
4. The output capacitor ESR is ignored.
5. The bus capacitance of the two cells are equal.
6. The isolation transformers are ideal, with negligible leakage inductance and a very large magnetising inductance.
7. The turns ratios of the two transformers are equal. For the sake of simplicity the turns ratio is assumed as $a = 1$.

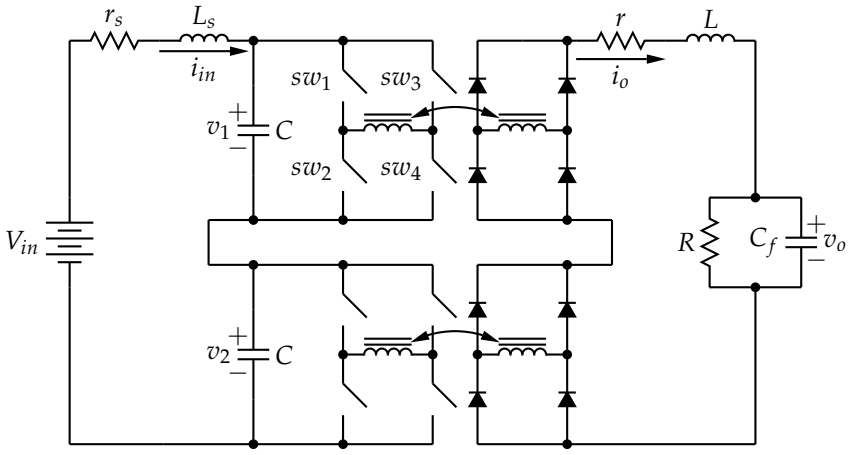

Figure 5.1: 2-Cell ISOS converter circuit

The full bridge converter and secondary rectifier can be modelled, in the continuous conduction mode, as a perfect transformer with a time varying turns ratio. Referring to Fig. 5.1 the states of switches 1-4 can be mapped to $s(t)$ as shown in Table 5.1.

Table 5.1: Mapping of the switch states to $s(t)$

Switches on	$s(t)$	Switches on	$s(t)$
sw_1,sw_4	1	sw_2,sw_3	1
sw_1,sw_3	0	sw_2,sw_4	0

The circuit operation can be described by the following system of differential equations:

$$\frac{d}{dt}\begin{bmatrix} L_s \cdot i_{in} \\ C \cdot v_1 \\ C \cdot v_2 \\ L \cdot i_o \\ C_f \cdot v_o \end{bmatrix} = \begin{bmatrix} -r_s & -1 & -1 & 0 & 0 \\ 1 & 0 & 0 & -s_1 & 0 \\ 1 & 0 & 0 & -s_2 & 0 \\ 0 & s_1 & s_2 & -r & -1 \\ 0 & 0 & 0 & 1 & \frac{-1}{R} \end{bmatrix} \begin{bmatrix} i_{in} \\ v_1 \\ v_2 \\ i_o \\ v_o \end{bmatrix} + \begin{bmatrix} V_{in} \\ 0 \\ 0 \\ 0 \\ 0 \end{bmatrix} \tag{5.2.1}$$

To study the unbalance in the circuit the following variables are defined:

$$s_t = \frac{1}{2}(s_1 + s_2) \qquad s_d = \frac{1}{2}(s_2 - s_1)$$
$$v_t = v_1 + v_2 \qquad v_d = v_1 - v_2$$

Where v_d now describes the unbalance voltage. Using these variables, the system of equations (5.2.1) can be rewritten as:

$$\frac{d}{dt}\begin{bmatrix} L_s \cdot i_{in} \\ C \cdot v_t \\ C \cdot v_d \\ L \cdot i_o \\ C_f \cdot v_o \end{bmatrix} = \begin{bmatrix} -r_s & -1 & 0 & 0 & 0 \\ 2 & 0 & 0 & -2s_t & 0 \\ 0 & 0 & 0 & -2s_d & 0 \\ 0 & s_t & s_d & -r & -1 \\ 0 & 0 & 0 & 1 & \frac{-1}{R} \end{bmatrix} \begin{bmatrix} i_{in} \\ v_t \\ v_d \\ i_o \\ v_o \end{bmatrix} + \begin{bmatrix} V_{in} \\ 0 \\ 0 \\ 0 \\ 0 \end{bmatrix} \tag{5.2.2}$$

The equivalent circuit of Fig. 5.1 can be redrawn in terms of the balancing parameters as shown in Fig 5.2. The transformers used to model the converters are ideal with a time varying turns ratio. It is important to note that the turns ratio is not a time averaged value of the switching functions.

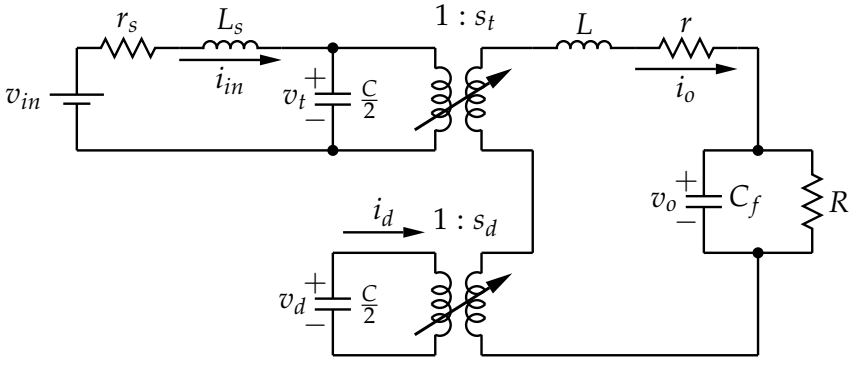

Figure 5.2: 2-Level ISOS converter circuit in terms of d and t parameters

5.3 Frequency Domain Analysis

Using the equivalent circuit, Fig 5.2, it can be seen that the current i_d can be given as

$$i_d(t) = i_o(t) \cdot s_d(t). \tag{5.3.1}$$

However, solving the problem in the time domain presents several obstacles, most of which can be circumvented by moving to the frequency domain. It is assumed that both converters operate with equal duty cycle at a constant and equal switching frequency. The function $s(t)$ can be expressed where $\Psi(n)$ is the exponential Fourier coefficients and d denotes the duty-cycle, as

$$s_1(t) = \sum_{n=-\infty}^{\infty} S_{1(n)} e^{jn\omega_s t} \tag{5.3.2}$$

$$S_{1(n)} = \Psi(n) \tag{5.3.3}$$

$$S_{2(n)} = (-1)^n \Psi(n) \tag{5.3.4}$$

$$\Psi(n) = \begin{cases} \frac{j}{2\pi n}\left(e^{-j2\pi nd} - 1\right) & \text{for } n \neq 0 \\ d & \text{for } n = 0 \end{cases} \tag{5.3.5}$$

when the two converters are operating with interleaved switching. When the two converters are operational with ordinary switching (that is switching the corresponding switches of the two converters at the same time), it follows logically that $S_{1(n)} = S_{2(n)} = \Psi(n)$. The frequency f_s is the effective output switching frequency as observed at the rectifier terminals, and it is typically twice the device switching frequency. Let $\omega_s = 2\pi f_s$.

In general the parameters r_s and L_s are small while the bus capacitor C is large. Under these conditions L_s and r_s will have little influence on the steady state operating points of the circuit. For the remainder of this discussion, the circuit will be investigated in the steady state and it will be assumed that $v_t = V_{in}$.

5.3.1 The Balancing Equation

It is assumed that C is sufficiently large that the switching frequency voltage ripple on v_1 and v_2 is small enough to be ignored. It is furthermore assumed that, due to the large cell bus capacitance, even when the cell bus voltages change in time, the rest of the converter is in the steady state. In the frequency domain the DC component of (5.3.1) can be found as

$$I_d(\omega)|_{\omega=0} = V_t \left.\frac{S_t(\omega)}{Z(\omega)} * S_d(\omega)\right|_{\omega=0} + V_d \left.\frac{S_d(\omega)}{Z(\omega)} * S_d(\omega)\right|_{\omega=0}, \tag{5.3.6}$$

where

$$Z(\omega) = j\omega L + r + \left(\frac{1}{R} + j\omega C_0\right)^{-1}. \tag{5.3.7}$$

As proven in Lemma 15 on p. 172 and discussed in Section 3.2.1 on p. 34 it is true that,

$$\left.\frac{S_t(\omega)}{Z(\omega)} * S_d(\omega)\right|_{\omega=0} = 0. \tag{5.3.8}$$

When the converter operates with interleaved switching, it is true that

$$\frac{S_d(\omega)}{Z(\omega)} * S_d(\omega)\bigg|_{\omega=0} = 2 \sum_{\xi=1,3,5}^{\infty} \frac{|\Psi(\xi)|^2}{|Z(\xi\omega_s)|^2} \mathrm{Re}\{Z(\xi\omega_s)\}, \tag{5.3.9}$$

as proven in Lemma 16 on p. 173 and also discussed in Section 3.2.1 on p. 34. When ordinary switching is used, it follows from the definition of $s_d(t)$ that $s_d(t) = 0$ for all t since $s_1(t) = s_2(t)$ for all t. In this case

$$\frac{S_d(\omega)}{Z(\omega)} * S_d(\omega)\bigg|_{\omega=0} = 0. \tag{5.3.10}$$

Substitution of (5.3.8) into (5.3.6), and assuming that interleaved switching is used, yields:

$$I_d(\omega)|_{\omega=0} = V_d \left.\frac{S_d(\omega)}{Z(\omega)} * S_d(\omega)\right|_{\omega=0} \tag{5.3.11}$$

From (5.3.9) it is clear that the convolution sum will always yield a positive value and hence the pole of

$$C\frac{dv_d}{dt} = -2\, I_d(\omega)|_{\omega=0} = -2v_d \left.\frac{S_d(\omega)}{Z(\omega)} * S_d(\omega)\right|_{\omega=0} \tag{5.3.12}$$

will always be in the left-hand half of the complex plane, implying that the voltage unbalance will decay towards $v_d = 0$ in the steady state.

The same assumption discussed in Chapter 4, namely that the characteristics of the inductor and inductor ESR dominate the behaviour of $Z(\omega)$ at the switching frequency and higher, will be used in the discussion below. Recall that this assumption is especially true for large values of C_o. Using this assumption (5.3.9) can be rewritten, with substitution of (5.3.5) and assuming that $r \ll \omega L$, as:

$$\begin{aligned}
&\frac{S_d(\omega)}{Z(\omega)} * S_d(\omega)\bigg|_{\omega=0} \\
&= \sum_{\xi=1,3,5}^{\infty} \frac{\frac{1}{\pi^2\xi^2}\left(\left(\cos(2\pi\xi d) - 1\right)^2 + \sin^2(2\pi\xi d)\right)}{4\xi^2\pi^2 f_s^2 L^2} r \\
&= \sum_{\xi=1,3,5}^{\infty} \frac{1 - \cos(2\pi\xi d)}{2\xi^4\pi^4 f_s^2 L^2} r
\end{aligned} \tag{5.3.13}$$

This result is similar to the result for the 2-cell FCC as discussed in Section 4.2 on p. 61. This follows logically, since the equivalent difference and total parameter circuits of the 2-cell ISOS and the 2-cell FCC are similar (see Fig. 5.2 and Fig. 4.2 on p. 60). Following the discussion of the 2-cell FCC, in Section 4.2, the convolution can be approximated by

$$\frac{S_d(\omega)}{Z(\omega)} * S_d(\omega)\bigg|_{\omega=0} \approx \frac{1 - \cos(2\pi d)}{2\pi^4 f_s^2 L^2} r \tag{5.3.14}$$

Using this approximation (5.3.12) can be rewritten as:

$$C\frac{dv_d}{dt} = -v_d \frac{1 - \cos(2\pi d)}{2\pi^4 f_s^2 L^2} r \tag{5.3.15}$$

with solution, for a given initial condition $v_d(0)$:

$$v_d(t) = v_d(0)e^{\frac{-t}{\tau}} \tag{5.3.16}$$

$$\tau = \frac{2C\pi^4 f_s^2 L^2}{r\left(1-\cos(2\pi d)\right)} \tag{5.3.17}$$

It should be noted that the rebalancing of the system depends on the convolution of S_d with itself. As noted earlier, when ordinary switching is used, it follows that $S_d = 0$ and no rebalancing is possible. Analysis of the converter operation using time domain averaging techniques cannot account for the effects of interleaving, thus resulting in the erroneous assumption that natural balancing is not possible for the ISOS converter.

The accuracy of the approximation of the time constant (5.3.17) (as with the approximated time constants for the FCC in Chapter 4) is conditional on the assumptions made when rewriting (5.3.9) as (5.3.13):

1. It is assumed that the characteristics of the filter inductor (including ESR) dominates the characteristics of the load at the switching frequency and higher.
2. This assumption hinges on the size of the filter capacitor, C_f. When C_f is large, it is true that at the switching frequency and higher $\frac{1}{j\omega C_f} \approx 0$. When this is true, the characteristics of the inductor dominates $Z(\omega)$ at the switching frequency and higher.
3. That $\omega L \gg r$ at the switching frequency and higher.

In circuits where this is not true, a more accurate expression for the time constant can be found through

$$\tau = \frac{C}{2\sum\limits_{\xi=1,3,5}^{\infty} \frac{|\Psi(\xi)|^2}{|Z(\xi\omega_s)|^2}\mathrm{Re}\{Z(\xi\omega_s)\}}. \tag{5.3.18}$$

The presented theory was verified with a time domain simulation where all elements are ideal and no losses are included apart from the inductor ESR losses. The circuit parameters of the simulated ISOS are tabulated in Table 5.2.

Table 5.2: Circuit values for the simulated ISOS converter

L	153 μH	r	1.2 Ω
R	50 Ω	C_f	470 μF
V_t	200 V	f_s	10 kHz

The rebalancing of the converter was simulated by introducing a difference voltage disturbance of -40 V after the circuit is operational in the steady state. The resulting rebalancing is shown in Fig. 5.3. It is clear that the system rebalances naturally. The simulated results correspond well with the time constant predicted by the presented theory. The simulation was repeated with ordinary switching but, as expected no, rebalancing of the voltages occurred.

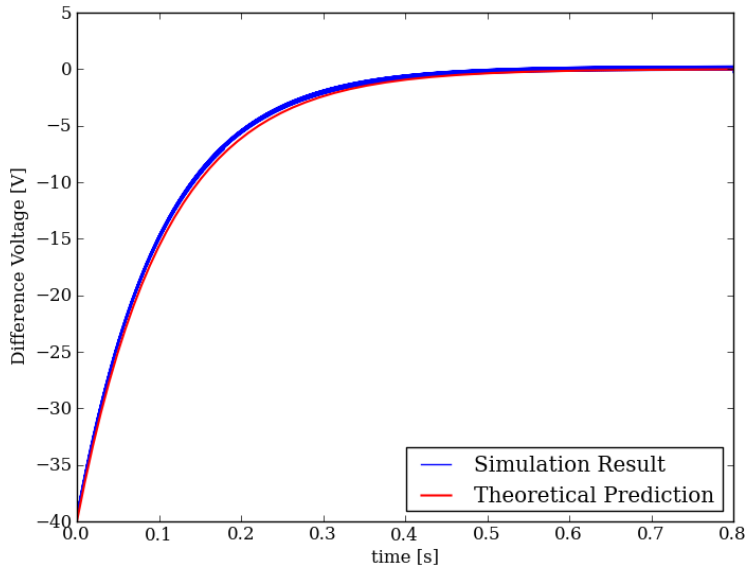

Figure 5.3: Simulation result of rebalancing with theoretical approximations

5.4 Voltage Dependent Losses

No practical converter is 100% efficient. In broad terms, the losses, associated with a cell as shown in Fig. 5.1, can be divided into conduction, switching and magnetic losses. In general it can be assumed that the conducted current in an ISOS converter will be equal for both cells, implying equal conduction losses. However, both the switching losses and transformer magnetic losses are dependent on the voltage.

5.4.1 Switching Losses

Let i'_o denote the output current referred to the primary of the isolation transformer. This current can be used as a good approximation of the current conducted by any switch in the on-state. For cell 1 the switching losses can be modelled as [40],

$$P_{sw(1)}(i'_o, v_1) = \frac{1}{2} v_1 i'_o f_s (t_{c(on)} + t_{c(off)}), \tag{5.4.1}$$

where $t_{c(on)}$ and $t_{c(off)}$ denote the switching turn-on and turn-off times inclusive of rising and falling times.

It is clear that the losses are a function of the cell bus voltages. Assuming that the referred current i'_o is equal for both cells, the difference in switching losses between the two cells can be expressed in terms of the difference voltage v_d as

$$P_{sw(d)}(i'_o, v_d) = \frac{1}{2} v_d i'_o f_s (t_{c(on)} + t_{c(off)}). \tag{5.4.2}$$

5.4.2 Magnetic Losses

The isolation transformer losses can be divided into conduction and core losses. The core losses per volume can be approximated as [40]

$$P_{core} \approx K_{fe} f^{\alpha} (\frac{1}{2}\Delta B)^{\beta}, \tag{5.4.3}$$

where K_{fe}, α and β are constants associated with the core material. Here, the term ΔB denotes the flux excursion, and it is assumed that there is no DC flux. Typically for ferrite material $1 \leq \alpha \leq 2$ and $2 \leq \beta \leq 3$, [79]. The maximum flux excursion, ΔB can be found, for the transformer of cell 1 with N_1 primary turns, as

$$\Delta B = \frac{d}{2 f_s N_1 A_e} v_1, \tag{5.4.4}$$

where A_e is the effective magnetic area of the core. Using the assumption of a constant duty cycle and switching frequency, the core loss for cell 1 can be expressed as follows, using a generalised constant K_c,

$$P_{core(1)}(v_1) \approx K_c v_1^{\beta}. \tag{5.4.5}$$

The difference in the core losses between the two cells can be expressed as

$$P_{core(d)}(v_1, v_2) \approx K_c (v_1^{\beta} - v_2^{\beta}), \tag{5.4.6}$$

or with $\beta = 2$

$$P_{core(d)}(v_t, v_d) \approx K_c v_t v_d. \tag{5.4.7}$$

5.5 Balancing of Non-Ideal Cells

In Section 5.3 the rebalancing effects of interleaved switching were identified. According to the presented theory the cells will rebalance naturally if the switching signals are interleaved but, no rebalancing will occur when ordinary switching is used. However, in practical systems it was found that the voltages rebalances naturally regardless of whether interleaved or ordinary switching is used.

The components of the losses that are dependent on the cell voltage present another rebalancing mechanism. If two perfectly similar cells are used, the cell with the higher voltage will have higher switching and transformer core losses. Let $i_{loss(1)}(t)$ be the current associated with the losses of cell 1; $i_{loss(1)} = P_{loss(1)}/v_1$. Using this definition the differential equations for the bus voltages in (5.2.1) can be rewritten as:

$$C\frac{dv_1}{dt} = i_{in} - i_{loss(1)} - s_1 i_o \tag{5.5.1}$$

$$C\frac{dv_2}{dt} = i_{in} - i_{loss(2)} - s_2 i_o \tag{5.5.2}$$

Using time averaged values of the currents, it is true that if the cells are operating at the same duty cycle then $s_1 i_o = s_2 i_o$. It follows that the bus voltage of the cell with the higher switching losses will decrease until $i_{loss(1)} = i_{loss(2)}$.

5.5.1 Steady State Value of V_d

When the cells are similar in every respect they will share the input voltage equally. However, small variations in effective duty cycle, switching behaviour (i.e. effective switching losses) and faulty interleaving will influence the steady state value of v_d. The voltages will balance at a point where the rebalancing currents due to the effect of interleaving and losses counteract the effect of any variations between the cells.

Since both rebalancing currents (weak and strong) are dependent on the difference voltage, they serve to limit the steady state unbalance. It follows therefore that the steady state unbalance of two cells will be smaller when interleaving is used when it is not. Likewise, since the switching losses increase with the output current, the steady state unbalance will decrease with an increase in output current.

5.5.2 Practical Setup

Table 5.3: Circuit values for the practical system

L	153 μH	r	2.2 Ω
C_f	470 μF	V_t	200 V
f_s	35 kHz	R_{ub}	20 kΩ

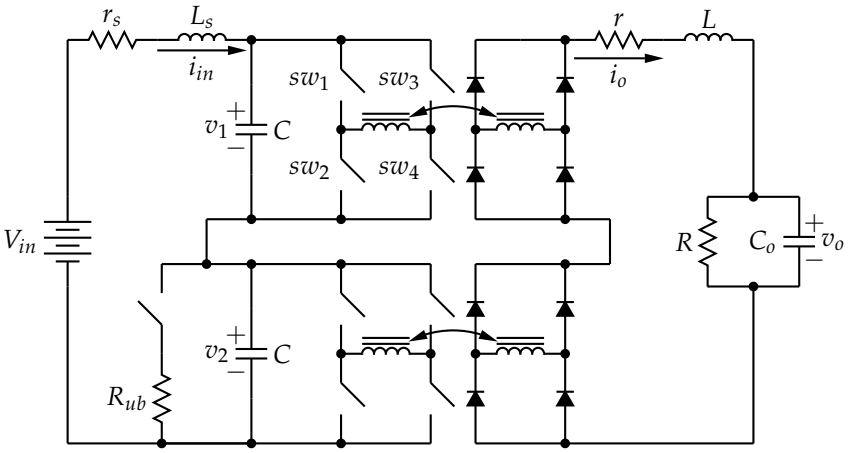

Figure 5.4: Practical setup with unbalancing resistor

Two separate cells with component values tabulated in Table 5.3 were used and connected as shown in Fig. 5.4. Each cell has a controller, implemented by means of a FPGA, which generates the switching signals for each cell. One of the controllers acts as a master and generates triangular carriers that are compared to a constant reference value to generate the switching signals of the four switches. The triangular carrier is also compared to another constant reference value, called the interleaving reference, to send a synchronisation signal to the slave controller via a

fibre optic link. The slave controller uses the synchronisation signal to synchronise its triangular carriers, which are used to generate switching signals for the switches of cell 2. By varying the interleaving reference, it is possible to either operate the two cells with interleaved switching or with ordinary switching. The control system is discussed further in [19] available in Appendix B.

The cells are forced into unbalance by connecting an unbalancing resistor, R_{ub} across the bus of cell 2. The bus voltages during rebalancing are measured and analysed using Matplotlib and Python. The test is repeated for 5 different load values, that is $R = 420, 300, 200, 100$ and $50\ \Omega$ and 4 different switching conditions, with a dead time of either 1.2 μs or 600 ns and with either interleaved switching or ordinary switching, giving rise to a total of 20 different measurements.

Using the measurements, the steady state unbalance V_d and the perturbation deviation ΔV_d are determined. Using these values, a time constant describing the measured rebalancing to the steady state values is fitted to the measured values. The fitted rebalancing estimation is described by, let the unbalancing resistor be removed at time $t = 0$,

$$v_d(t) = V_d + \Delta V_d e^{-t/\tau} u(t). \tag{5.5.3}$$

To indicate the measured characteristics of the rebalancing waveform, the measured bus voltages and the difference voltage with the fitted estimation of the rebalancing are shown in Fig 5.5. A system operational with non-interleaved switching, $1.2\mu s$ dead time and a load of $R = 300\ \Omega$ was used for this example. The different values were measured as: $V_d = -38.75$ V, $\Delta V_d = 90.94$ V and $\tau = 1.15$ s. In this instance a large steady state error can be observed. This measurement was specifically chosen for illustrative purposes, a similar measurement using interleaved switching is shown in Fig. 5.6. It is clear that in this instance the voltages balance in the steady state.

5.6 Results

The cells were operational with the phase shifted ZVS (zero voltage switched) PWM resonant switching scheme. This scheme is discussed in detail in [80], among others. The system design is such that the switch-on transitions in the converter switches will be soft when the dead time is 600 ns. However, when the dead time is increased to 1.2 μs, the switch-on transitions will be hard. For illustrative purposes, two measurements taken from [80] are presented in Fig. 5.7 and Fig. 5.8. The measurements were taken under light load where the ZVS transition is incomplete due to insufficient energy storage in the transformer leakage inductance. In Fig. 5.7 the dead time is set to correspond with a quarter period of the resonant LC circuit, consisting of the transformer leakage inductance and the combination of the switch parasitic capacitance and the transformer inter winding capacitance. Under higher load conditions, the switch-on transition will be soft. In Fig. 5.8 the dead time is increased to more than half of the LC circuit resonant period. It is seen that the switch-on transitions in this case is hard. The underdamped ring on the rising edge of the transition is mainly due to the hard switched nature of the transition. Since the converter was designed to operate with soft switching, no remedial actions was

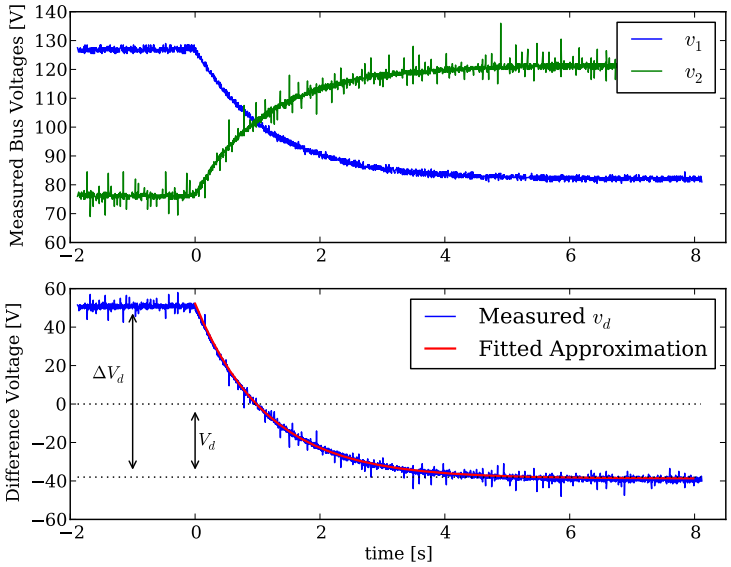

Figure 5.5: Measured rebalancing and a fitted approximation: ordinary switching

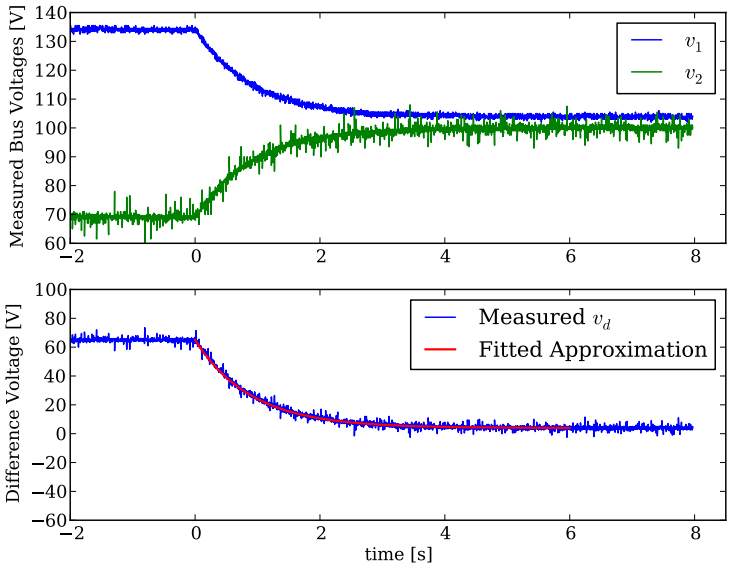

Figure 5.6: Measured rebalancing and a fitted approximation: interleaved switching

taken to mitigate this effect. It is furthermore believed that this phenomena will not have a noticeable influence on the results of this study.

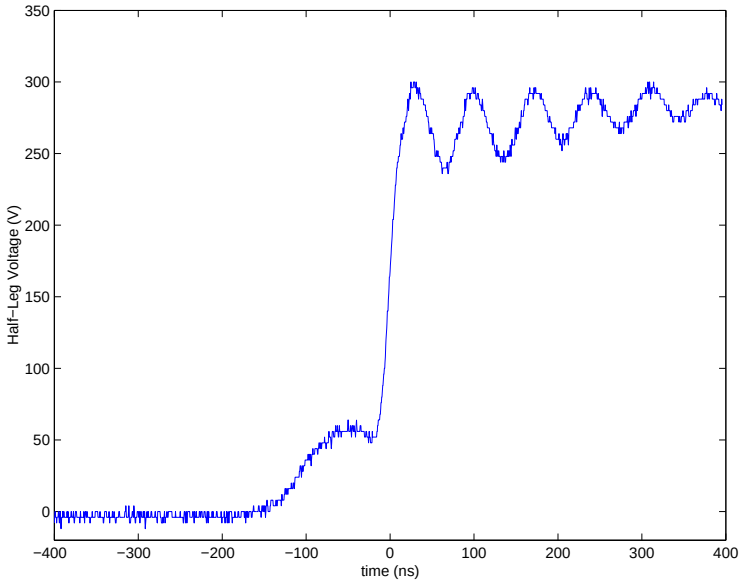

Figure 5.7: Switch voltage under phase shift ZVS: optimal dead time choice

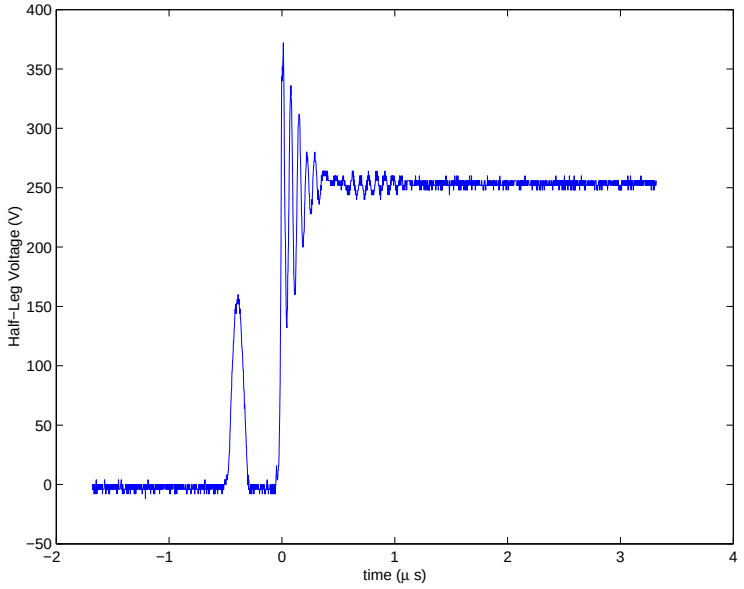

Figure 5.8: Switch voltage under phase shift ZVS: dead time too large

The dead time was manipulated in the experiment in an effort to increase the switching losses. The switching losses of the system with a dead time of 1.2 μs should theoretically be higher than a system with a dead time of 600 ns. However,

it was found that the effective duty cycle increases as dead time decreases and that the output voltage is therefore higher when the dead time is small. The output voltage is also slightly higher when interleaved switching is used, as can be seen in Fig. 5.9. A higher output voltage implies a higher output current and hence higher switching losses. It should be noted that all 20 measurements are used in the analysis.

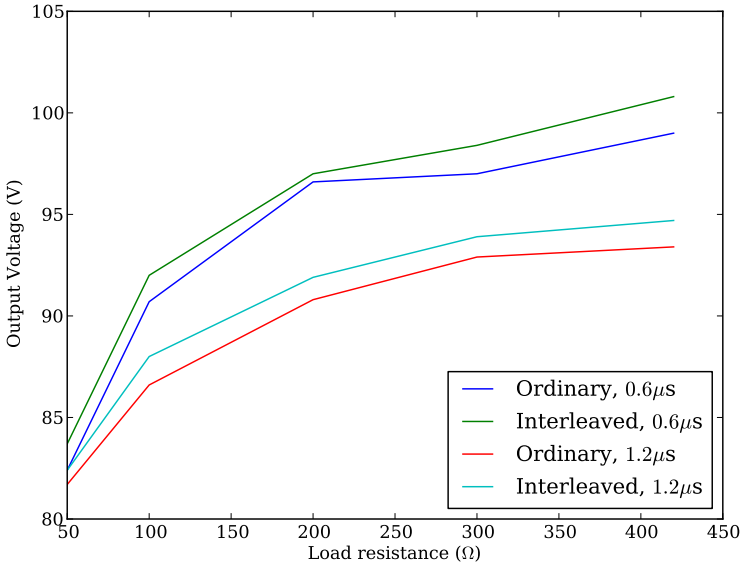

Figure 5.9: Measured output voltage

The increased current, when a smaller dead time is used, increases the switching losses and counteracts the purpose behind the manipulation of the dead time. In an effort to decouple this interaction the remainder of this analysis was done by comparing the systems at the same output current rather than at operational points having the same load resistance.

According to the presented theory, the system should rebalance faster when interleaved switching is used than when it is not. Likewise, the rebalancing should be faster as the output current and hence the switching losses increase. The fitted time constants are shown in Fig 5.10. The measured values support the theoretical findings in that the time constants decrease with an increase in output current. However, the time constant associated with hard switching is slower than that of soft switching. This result is contrary to the expectation that the increased dead time will result in higher switching losses due to the effect of hard switching.

It is true that the switching losses associated with the longer dead time are slightly larger than the switching losses associated with the shorter dead time. This difference between the switching losses increases with an increase in output current, due to the increased energy that is stored in the leakage inductance to facilitate the resonant transition. However, a difference of 600 ns in the switching waveforms is large, and at 35 kHz it represents a change in duty cycle of approximately 5 %. In

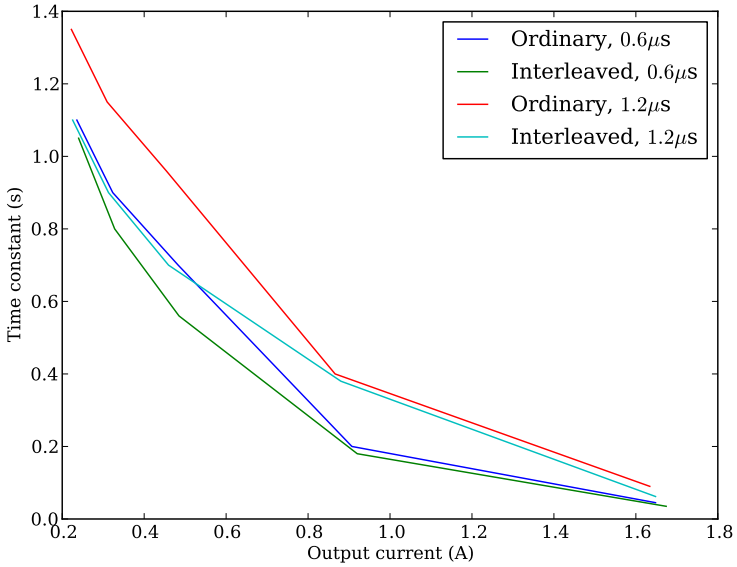

Figure 5.10: Fitted time constants

fact, when the output voltages of the different operating conditions are compared, as shown in Fig. 5.9, it emerges that the effective duty cycle is changed by a factor of about 1,05. Although this seems small, the peak induction of the transformer core will also increase due to this increased duty cycle. Due to the β exponent in the core loss calculation, this increase represents an increase of between 5 % and 8 % (depending on the value of β) in the transformer core loss. Therefore, although the switching loss is less with the shorter dead time, the increased core loss is such that the total system losses are higher.

The weak balancing mechanism has a small influence on the rebalancing time constant, as seen in Fig. 5.10. However, the weak balancing mechanism plays a major role in limiting the steady state error, as shown in Fig. 5.11. Here, the weighted error of the steady state difference voltage is defined as

$$error = \frac{|V_d|}{V_t} \times 100\ \%. \tag{5.6.1}$$

As discussed in Section 5.5, any difference in the characteristics of the cells will result in unbalance. The differences can be attributed to timing errors (both faulty interleaving and small variations in duty cycle due to varying switching characteristics) and variations in the losses. It is expected that no two cells can be perfectly similar. When ordinary switching is used, the only balancing mechanism is the loss-based mechanism. This mechanism will inherently reflect any unequal losses in the steady state voltage balancing error.

This steady state balancing error due to unequal losses is a function of temperature. There is a well-defined relationship between temperature and losses. When two transformers experience different core losses, the steady state temperature of the transformer with the higher loss will be higher than that of the transformer with

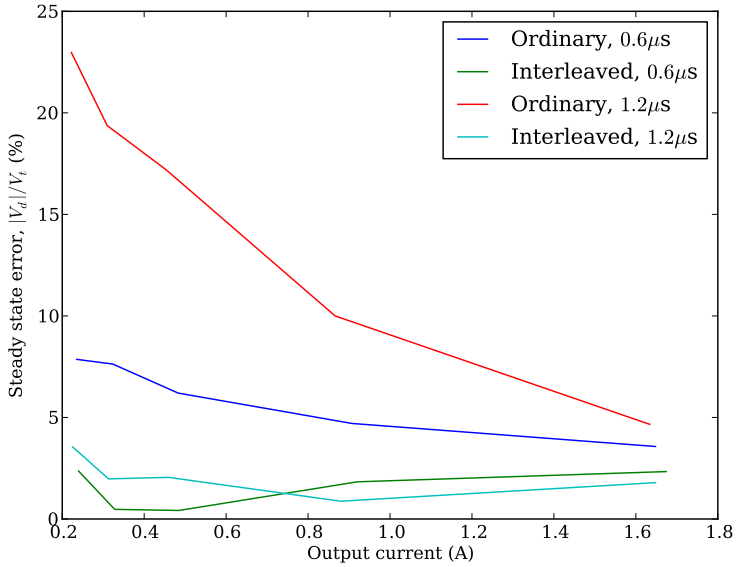

Figure 5.11: Weighted steady state balancing error

lower losses. The same argument holds for variations in switching losses and the switch junction temperature. However, both core losses and switching losses increase with an increase in temperature. The interaction between voltage balancing and temperature can be explained as follows:

1. Two similar cells, with no timing variations and equal switching losses are used in an ISOS converter. Let every component in both cells be at room temperature. Assume that the two transformers are such that the transformer of cell 1 has higher core losses that that of cell 2. Ordinary switching is used, and no weak rebalancing is therefore possible. Assume that IGBTs are used as switch elements.

2. When the converter starts up, the higher losses in cell 1 will result in a lower bus voltage in cell 1, and hence a higher bus voltage in cell 2. The cells will balance at a point where the losses in the transformer cores are equal.

3. However, since the voltage of cell 2 is slightly higher, the switching losses in cell 2 will be higher than in cell 1. This higher switching loss will increase the junction temperature of the IGBTs and result in an increase in switching losses.

4. The steady state voltage error will change to reflect the inequality in the switching losses. However, since the bus voltage of cell 1 rises, due to the increase in switching losses of cell 2, the core losses of cell 1 will be higher than the core losses of cell 2.

5. Again, due to the higher losses in the transformer core of cell 1, the temperature of the core will rise and likewise the core losses.

6. This increase in core losses will again change the steady state voltage balancing and the cycle starts again at point 3.

7. Although the variations in bus voltages do not occur in such a discrete stepped fashion as described here, it is true that temperature variations do have an influence on the steady state voltage balancing.

8. The system will eventually reach a thermal steady state. In this temperature equilibrium, the transformer of cell 1 will be hotter than the transformer of cell 2. Likewise, the IGBTs of cell 2 will be hotter than the IGBTs of cell 1.

9. The losses in the transformer core and the switching losses do not have the same temperature dependence coefficients. The balancing error will therefore be a function of ambient temperature due to the variation of the different losses.

In a separate experiment, the effect of temperature on the steady state balancing error was investigated. The converter was switched off for a long period of time to ensure that all the components were at, or near to, ambient temperature. The converter input voltage, bus voltages, output voltage and output current were measured at 10 minute intervals. As expected the steady state balancing error changed with time. After approximately 30 minutes, the parameters remained constant and the converter was assumed to be in a thermal steady state. The results are summarised in Table 5.4. It is clear that there is a drift in the balancing error with temperature. Under different load conditions, the switch elements and the transformer will have different losses and hence different steady state temperatures. The steady state balancing error will therefore be a function of load.

In the experimental setup, as shown in Fig. 5.4, the unbalancing resistor increased the bus voltage of cell 1. When the unbalancing resistor was connected, both the switching losses and core losses in cell 1 increased. Since the test was repeated often, these unbalance induced losses resulted in higher temperatures in cell 1 than would have been the case had unbalance not been forced through the unbalance resistor. In the unperturbed state, the higher losses in cell 1 resulted in faulty balancing that can be ascribed to the test procedure. However, as seen in Fig. 5.11, the weak balancing mechanism plays a major role in correcting this error.

It is also interesting to note that the weak balancing mechanism has a limiting effect on the excursion of v_d from the steady state in the presence of a disturbance, as shown in Fig. 5.12.

5.7 Conclusion

The modular ISOS DC-DC converter exhibits natural balancing characteristics. When the ISOS is analysed using ideal components, a weak balancing mechanism similar to that of the FCC is identified. This weak balancing mechanism depends on the interleaving of the switching functions of the different cells. Through analysis of the circuit operation in the frequency domain, an expression for the weak rebalancing time-constant was found.

Table 5.4: Relationship between temperature and voltage balancing

Ordinary switching		
Parameter	Value at start	Value after 30 min.
Ambient temp.	22.3°C	23.3°C
Cell 1 IGBT temp.	24.5°C	30.7°C
Cell 1 core temp.	24°C	27.4°C
Cell 2 IGBT temp.	24.5°C	29.9°C
Cell 2 core temp.	24°C	25°C
Input voltage	201 V	200.6 V
Cell 1 bus voltage	107.3 V	113.5 V
Cell 2 bus voltage	93.4 V	87.5 V
Output voltage	139.1 V	139.4 V
Output current	1.66 A	1.67 A
Balancing error	6.92%	12.71%
Interleaved switching		
Parameter	Value at start	Value after 30 min.
Ambient temp.	22.2°C	23.4°C
Cell 1 IGBT temp.	22.5°C	30.3°C
Cell 1 core temp.	23.2°C	27.4°C
Cell 2 IGBT temp.	22.4°C	29.7°C
Cell 2 core temp.	23.1°C	25.9°C
Input voltage	201 V	201.2 V
Cell 1 bus voltage	103.5 V	110.6 V
Cell 2 bus voltage	96.5 V	90.2 V
Output voltage	138.8 V	139.1 V
Output current	1.65 A	1.67 A
Balancing error	3.48%	10.14%

In practical ISOS circuits the voltage dependent losses of the cell converters, notably switching and isolation transformer magnetic losses, form another rebalancing mechanism. This strong balancing mechanism does not depend on the interleaving of the switching signals of the different cells.

However, it is shown that the different losses vary with temperature. This variation will result in a variation of the balanced voltages, both with ambient temperature and with load. Therefore, although the loss based balancing mechanism exists, it is not robust enough to be used in practical converters.

The theory presented was verified through measurements. It is shown that the strong balancing mechanism has a significant influence on the rebalancing time constant. However, the weak balancing mechanism plays a significant role in the steady state value of the bus voltages when the cells are not exactly similar or when an external disturbance is present. The weak balancing mechanism also provides the only rebalancing under no load conditions.

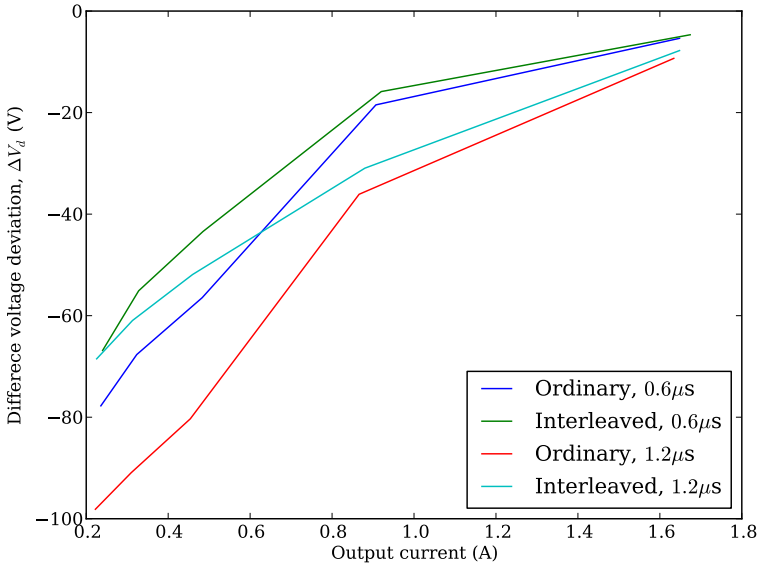

Figure 5.12: Excursion of V_d from the steady state value in the presence of a disturbance, ΔV_d

Chapter 6

Conclusion

6.1 Conclusion

Three natural balancing mechanisms were identified and discussed in this dissertation.

Firstly, it was shown, using an ISOP converter as example, that a strong balancing mechanism exists and that this relies on the direct exchange of unbalance energy. This mechanism occurs whether interleaved switching is used or not. It was shown that the ISOP converter would be balanced in the steady state. Furthermore, balancing models were proposed to describe the rebalancing of the converter after a perturbation. The first two models describe the rebalancing of the converter operating with active rectification, both when similar cells and non-similar cells are used. A third model describes the rebalancing of a converter with passive rectifiers.

The weak balancing mechanism was introduced by analysing the FCC. It was shown that the balancing time constant depends on the characteristics of the load, specifically the ratio $Re\{Z(\omega)\}/|Z(\omega)|^2$ at the multiples of switching frequency. It was also shown that the expressions describing the convolution of two frequency domain signals could be simplified by using the characteristics of the switching functions. The resulting expressions were simplified further by using certain assumptions with regard to the nature of the load at the switching frequency multiples. Using the simplified expressions, a closed form expression for the rebalancing time constant for the 2-cell FCC was found. This expression is similar to the expression found by time domain studies. Furthermore, it was shown that the characteristic matrix of the system of differential equations decomposes naturally into the sum of a symmetric matrix and a skew-symmetric matrix. Using the symmetric part and Lyapunov's theorem, proof was provided for the statement that the FCC is Lyapunov stable. This stability theorem had been inferred in previous studies. The symmetric part of the characteristic matrix decomposition can be used to calculate a maximum bound on the rebalancing time constant. It was shown that the symmetric matrix could be factorised if certain assumptions regarding the characteristics of the load were made. Using these assumptions, a closed form expression, using a look-up table, for the absolute maximum rebalancing time constant was provided. Again, this expression mimics the results of time domain studies. Finally, the results of the constant duty cycle case were extended to the modulated

FCC by means of an averaging technique.

It was shown that the voltage dependent losses also act as a balancing mechanism. Theoretical analysis of the ISOS DC-DC converter, and assuming the system to be loss less, showed that the converter should only balance when interleaved switching is used. This result was verified through simulation studies that ignored the system losses. However, in practical systems it was found that the converter balances irrespective of the switching scheme used. It was sound that this rebalancing could be ascribed to the voltage dependence of the switching losses as well as the transformer magnetic losses.

6.2 Recommendations for Future Research

1. It was shown in Chapter 5 that the switching losses play a role in the natural balancing. It is true that in converters where the strong direct method is observable, the loss-based mechanism will, be negligible in comparison to the direct method. However, in converters that exhibit only the weak balancing mechanism, such as the FCC, this effect might indeed be measurable.

2. The effect of skin and proximity effects on the inductor ESR at the frequencies of interest was ignored in this study. It might be possible to adapt the closed form expressions for the weak balancing time constant to allow for this variation of ESR with frequency.

3. In Chapter 4 the minimum eigenvalue of $\mathbf{\Lambda_s}$ was determined numerically and tabulated. It might be possible to determine a closed form expression for this eigenvalue.

4. The presented theory can be used to find a closed form expression for the maximum time constant for the rebalancing of systems where a balance booster is used.

5. Timing errors play a significant role in the steady state errors, especially in a system where the weak balancing mechanism dominates. The method used to simplify the convolution expression makes allowance for the inclusion of timing errors into the analysis. When timing errors are present, it is no longer true that
$$\left.\frac{S_d(\omega)}{Z(\omega)} * S_t(\omega)\right|_{\omega=0} = 0.$$

6. The method of determining a maximum time constant could be extended to three-phase systems.

Bibliography

[1] van der Merwe, W. and Mouton, T.: Natural balancing of the two-cell back-to-back multilevel converter with specific application to the solid-state transformer concept. In: *Industrial Electronics and Applications, 2009. ICIEA 2009. 4th IEEE Conference on*, pp. 2955–2960. May 2009.

[2] van der Merwe, J. and du T. Mouton, H.: An investigation of the natural balancing mechanisms of cascaded active-rectifiers. In: *Power Electronics and Motion Control Conference (EPE/PEMC), 2010 14th International*, pp. T2–22 –T2–28. sept 2010.

[3] Rodríguez, J., Lai, J. and Peng, F.: Multilevel inverters: A survey of topologies, controls and applications. *IEEE Transactions on Industrial Electronics*, vol. 49, no. 4, pp. 724–738, aug 2002.

[4] Lai, J.-S. and Peng, F.Z.: Multilevel converters-a new breed of power converters. *IEEE Transactions on Industry Applications*, vol. 32, pp. 509–517, May / June 1996.

[5] Holmes, D. and Lipo, T.: *Pulse Width Modulation For Power Converters, Principles and Practice*. IEEE Press, 2003.

[6] Tolbert, L., Peng, F.Z., Cunnyngham, T. and Chiasson, J.: Charge balance control schemes for cascade multilevel converter in hybrid electric vehicles. *Industrial Electronics, IEEE Transactions on*, vol. 49, no. 5, pp. 1058 – 1064, oct 2002. ISSN 0278-0046.

[7] Tolbert, L., Peng, F.Z. and Habetler, T.: Multilevel converters for large electric drives. *Industry Applications, IEEE Transactions on*, vol. 35, no. 1, pp. 36 –44, jan 1999. ISSN 0093-9994.

[8] Wu, B. and Song, P.G.: Current status of multi-megawatt ac drives. In: *Industrial Technology, 2004. IEEE ICIT '04. 2004 IEEE International Conference on*, vol. 1, pp. 438 – 443 Vol. 1. dec 2004.

[9] Forest, F., Laboure, E., Meynard, T. and Huselstein, J.-J.: Multicell interleaved flyback using intercell transformers. *IEEE Transactions on Power Electronics*, vol. 22, no. 5, pp. 1662 –1671, sep 2007. ISSN 0885-8993.

[10] Steimer, P.: PEBB-based high pulsed power demonstrator. In: *IEEE International Symposium on Industrial Electronics, 2010. ISIE*. Bari, Italy, July 2010.

[11] Winkelnkemper, M., Korn, A. and Steimer, P.: A modular direct converter for transformerless rail interties. In: *IEEE International Symposium on Industrial Electronics, 2010. ISIE*. Bari, Italy, July 2010.

[12] Steiner, M. and Reinold, H.: Medium frequency topology in railway applications. In: *European Conference on Power Electronics and Applications, 2007*, pp. 1–10. Sept 2007.

[13] Henning, P., Fuchs, H., le Roux, A. and du T. Mouton, H.: A 1.5-mw seven-cell series-stacked converter as an active power filter and regeneration converter for a dc traction substation. *Power Electronics, IEEE Transactions on*, vol. 23, no. 5, pp. 2230 –2236, sep 2008. ISSN 0885-8993.

[14] Retzmann, D. and Gambach, H.: PEBB concepts - from medium voltage drives to high voltage applications. In: *IEEE International Symposium on Industrial Electronics, 2010. ISIE*. Bari, Italy, July 2010.

[15] Lezana, P., Rodriguez, J. and Oyarzun, D.: Cascaded multilevel inverter with regeneration capability and reduced number of switches. *Industrial Electronics, IEEE Transactions on*, vol. 55, no. 3, pp. 1059–1066, March 2008. ISSN 0278-0046.

[16] Lai, J.-S., Maitra, A., Mansoor, A. and Goodman, F.: Multilevel intelligent universal transformer for medium voltage applications. In: *Conference Record of the 2005 Industry Applications Conference, Fourtieth IAS Annual Meeting.*, vol. 3, pp. 1893–1899 Vol. 3. Oct 2005. ISSN 0197-2618.

[17] Lai, J.-S., Maitra, A. and Goodman, F.: Performance of a distribution intelligent universal transformer under source and load disturbances. vol. 2, pp. 719–725. Oct 2006. ISSN 0197-2618.

[18] van der Merwe, W. and Mouton, T.: Solid-state transformer topology selection. In: *IEEE International Conference on Industrial Technology, 2009. ICIT 2009.*, pp. 1–6. Feb 2009.

[19] Breet, C., du T. Mouton, H. and van der Merwe, J.W.: Modular cell controller and measurement system design for implementation in a solid-state transformer. In: *Proceedings of the 19th South African Power Engineering Conference*. Johannesburg, South Africa, Jan 2010.

[20] Schietekat, L., du T. Mouton, H. and van der Merwe, J.W.: Design of a cascaded rectifier control strategy, implemented in the main controller of a solid-state transformer. In: *Proceedings of the 19th South African Power Engineering Conference*. Johannesburg, Jan 2010.

[21] Ronan, E., Sudhoff, S., Glover, S. and Galloway, D.: A power electronic-based distribution transformer. *IEEE Transactions on Power Delivery*, vol. 17, no. 2, pp. 537–543, Apr 2002. ISSN 0885-8977.

[22] Heinemann, L.: Analysis and design of a modular, high power converter with high efficiency for electrical power distribution systems. *Power Electronics Specialists Conference, 2002. pesc 02. 2002 IEEE 33rd Annual*, vol. 2, pp. 713–718 vol.2, 2002.

[23] Iov, F., Blaabjerg, F., Clare, J., Wheeler, P., Rufer, A. and Hyde, A.: UNI-FLEXâPM â a key-enabling technology for future european electricity networks. *European Power Electronics and Drives Journal (EPE)*, vol. 19, no. 4, 2009.

[24] van der Merwe, W. and Mouton, T.: The solid-state transformer concept: A new era in power distribution. In: *Conference Record of the 9th IEEE AFRICON*. September 2009.

[25] McGrath, B. and Holmes, D.: Analytical modelling of voltage balance dynamics for a flying capacitor multilevel converter. *Power Electronics, IEEE Transactions on*, vol. 23, no. 2, pp. 543 –550, march 2008. ISSN 0885-8993.

[26] Wilkinson, R., Meynard, T. and du T. Mouton, H.: Natural balance of multicell converters: The general case. *IEEE Transactions on Power Electronics*, vol. 21, no. 6, pp. 1658–1666, Nov 2006. ISSN 0885-8993.

[27] Ruderman, A., Reznikov, B. and Margaliot, M.: Simple analysis of a flying capacitor converter voltage balance dynamics for dc modulation. In: *Power Electronics and Motion Control Conference, 2008. EPE-PEMC 2008. 13th*, pp. 260 –267. 1-3 2008.

[28] Wilkinson, R.: *Natural Balancing of Multicell Converters*. Ph.D. thesis, University of Stellenbosch, December 2003.

[29] Salagae, I.M.: *Natural Balancing of the Three-phase 2-cell and 3-cell Multicell Converters*. Ph.D. thesis, University of Stellenbosch, 2009.

[30] du Toit Mouton, H.: Natural balancing of three-level neutral-point-clamped pwm inverters. *Industrial Electronics, IEEE Transactions on*, vol. 49, no. 5, pp. 1017 – 1025, October 2002. ISSN 0278-0046.

[31] Giri, R., Choudhary, V., Ayyanar, R. and Mohan, N.: Common-duty-ratio control of input-series connected modular DC-DC converters with active input voltage and load-current sharing. *IEEE Transactions on Industry Applications*, vol. 42, no. 4, pp. 1101–1111, Jule/August 2006.

[32] Mouton, H.d.T., Enslin, J. and Akagi, H.: Natural balancing of series-stacked power quality conditioners. *IEEE Transactions on Power Electronics*, vol. 18, no. 1, pp. 198–207, jan 2003.

[33] Mouton, H.d.T.: *Analysis and Synthesis of a 2 MVA Series-stacked Power-Quality Conditioner*. Ph.D. thesis, University of Stellenbosch, 1999.

[34] Meynard, T., Fadel, M. and Aouda, N.: Modeling of multilevel converters. *Industrial Electronics, IEEE Transactions on*, vol. 44, no. 3, pp. 356–364, Jun 1997. ISSN 0278-0046.

[35] Gateau, G., Fadel, M., Maussion, P., Bensaid, R. and Meynard, T.: Multicell converters: active control and observation of flying-capacitor voltages. *Industrial Electronics, IEEE Transactions on*, vol. 49, no. 5, pp. 998 – 1008, oct 2002. ISSN 0278-0046.

[36] Wilkinson, R., Meynard, T. and du Toit Mouton, H.: Natural balance of multicell converters: The two-cell case. *Power Electronics, IEEE Transactions on*, vol. 21, no. 6, pp. 1649–1657, Nov 2006. ISSN 0885-8993.

[37] McGrath, B. and Holmes, D.: Natural capacitor voltage balancing for a flying capacitor converter induction motor drive. *Power Electronics, IEEE Transactions on*, vol. 24, no. 6, pp. 1554 –1561, june 2009. ISSN 0885-8993.

[38] McGrath, B., Meynard, T., Gateau, G. and Holmes, D.: Optimal modulation of flying capacitor and stacked multicell converters using a state machine decoder. *Power Electronics, IEEE Transactions on*, vol. 22, no. 2, pp. 508–516, March 2007. ISSN 0885-8993.

[39] Liberzon, D.: *Switching in systems and control*. Birkhaüser, 2003.

[40] Mohan, N., Undeland, T. and Robbins, W.: *Power electronics: converters, applications, and design*. Wiley New York, 2007.

[41] Ruderman, A., Reznikov, B. and Margaliot, M.: Analysis of a Flying Capacitor Converter: A Switched Systems Approach, Feb 2009.
Available at: `http://picasso.eng.tau.ac.il/ michaelm/alex.pdf`

[42] Jacobson, N.: *Basic Algebra I*. Dover Publications, 2009.

[43] Thielemans, S., Ruderman, A. and Melkebeek, J.: Flying-capacitor multilevel converter voltage balance dynamics for pure resistive load. In: *Advanced Electromechanical Motion Systems Electric Drives Joint Symposium, 2009. ELECTROMOTION 2009. 8th International Symposium on*, pp. 1 –6. 2009.

[44] Ruderman, A. and Reznikov, B.: Five-level single-leg flying capacitor converter voltage balance dynamics analysis. In: *Industrial Electronics, 2009. IECON '09. 35th Annual Conference of IEEE*, pp. 486 –491. nov 2009. ISSN 1553-572X.

[45] Ruderman, A., Reznikov, B. and Thielemans, S.: Four-level h-bridge flying capacitor converter voltage balance dynamics analysis. In: *Industrial Electronics, 2009. IECON '09. 35th Annual Conference of IEEE*, pp. 498 –503. 2009. ISSN 1553-572X.

[46] Thielemans, S., Ruderman, A. and Reznikov, B.: Five-level h-bridge flying capacitor converter voltage balance dynamics analysis. In: *IEEE International Symposium on Industrial Electronics, 2010. ISIE*. Bari, Italy, July 2010.

[47] Erickson, R. and Maksimović, D.: *Fundamentals of power electronics*. Kluwer Academic Pub, 2001.

[48] Nilsson, J. and Riedel, S.: *Electric Circuits*. 7th edn. Pearson Prentice Hall, 2005.

[49] Stuart, R.: *An introduction to Fourier analysis*. Methuen & Co LTD and Science Paperbacks, London, 1966.

[50] Proakis, J.G. and Manolakis, D.G.: *Digital Signal Processing: Principles, Algorithms and Applications*. 3rd edn. Prentice Hall International Editions, Upper Sadle River, New Jersey, 1996.

[51] Ivić, A.: *The Riemann zeta-function: theory and applications*. 1st edn. Dover Publications, Mineola, New York, 2003.

[52] Hindmarsh, A.: LSODE and LSODI, two new initial value ordinary differnetial equation solvers. *ACM Signum Newsletter*, vol. 15, no. 4, p. 11, 1980.

[53] Yuang, X., Stemmler, H. and Barbi, I.: Self-balancing of the clamping-capacitor-voltages in the multilevel capacitor-clamping-inverter under subharmonic pwm modulation. *Power Electronics, IEEE Transactions on*, vol. 16, no. 2, pp. 256 –263, mar 2001. ISSN 0885-8993.

[54] Reznikov, B. and Ruderman, A.: Four-level single-leg flying capacitor converter voltage balance dynamics analysis. In: *Power Electronics and Applications, 2009. EPE '09. 13th European Conference on*, pp. 1 –10. 8-10 2009.

[55] Ruderman, A. and Reznikov, B.: Three-level h-bridge flying capacitor converter voltage balance dynamics analysis. In: *Power Electronics and Applications, 2009. EPE '09. 13th European Conference on*, pp. 1 –10. 8-10 2009.

[56] Thielemans, S., Ruderman, A. and Melkebeek, J.: Self-precharge in single-leg flying capacitor converters. In: *Industrial Electronics, 2009. IECON '09. 35th Annual Conference of IEEE*, pp. 812 –817. 3-5 2009. ISSN 1553-572X.

[57] Swift, R.J. and Wirkus, S.A.: *A Course in ordinary differential equations*. Chapman & Hall / CRC, Boca Raton, FL, 2007.

[58] Bellman, R.: *Introduction to Matrix Analysis*. McGraw-Hill, London, 1960.

[59] Lay, D.C.: *Linear Algebra and its Applications*. 2nd edn. Addison Wesley, 1997.

[60] Gray, R.M.: *Toeplitz and Circulant Matrices: A Review*. Now Publishers, Norwell, Massachusetts, December 2005. ISBN 1-933019-23-9 84.

[61] Beardon, A.F.: *Algebra and Geometry*. Cambridge University Press, 2005.

[62] Debnath, L.: *The Legacy of Leonard Euler: A Tricentennial Tribute*. Imperial College Press, London, 2010.

[63] Lerner, D.: Lecture notes on linear algebra - math 290/291, chapter 21. Kansas University.
Available at: `http://www.math.ku.edu/ lerner/LAnotes/ chapter 21`

[64] Diwekar, A. and Yedavalli, R.: Stability of matrix second-order systems: new conditions and perspectives. *Automatic Control, IEEE Transactions on*, vol. 44, no. 9, pp. 1773 –1777, sep 1999. ISSN 0018-9286.

[65] Tu, P.N.: *Dynamical Systems*. 1st edn. Springer-Verlag, Berlin, Germany, 1992.

[66] Bernstein, D.S.: *Matrix Mathematics: Theory, Facts, and Formulas with Application to Linear Systems Theory*. Princeton University Press, Princeton, 2005.

[67] Horn, R.A. and Johnson, C.R.: *Matrix analysis*. 1st edn. Cambridge University Press, Cambridge, 1985.

[68] Meynard, T., Foch, H., Thomas, P., Courault, J., Jakob, R. and Nahrstaedt, M.: Multicell converters: basic concepts and industry applications. *Industrial Electronics, IEEE Transactions on*, vol. 49, no. 5, pp. 955 – 964, oct 2002. ISSN 0278-0046.

[69] Gorter, R., Veltman, A. and van den Bosch, P.: Skin effect impact on induction motor parameters estimation using an output-error identification method. In: *Power Electronics Specialists Conference, PESC '94 Record., 25th Annual IEEE*, pp. 763 –768 vol.1. 20-25 1994.

[70] Boglietti, A., Cavagnino, A. and Lazzari, M.: Experimental high-frequency parameter identification of ac electrical motors. *Industry Applications, IEEE Transactions on*, vol. 43, no. 1, pp. 23 –29, jan-feb 2007. ISSN 0093-9994.

[71] Chen, B., Lin, Z. and Shamash, Y.: *Linear systems theory: a structural decomposition approach*. Birkhaüser, Boston, 2004.

[72] Meynard, T., Lienhardt, A., Gateau, G., Haederli, C. and Barbosa, P.: Flying capacitor multicell converters with reduced stored energy. In: *Industrial Electronics, 2006 IEEE International Symposium on*, vol. 2, pp. 914 –918. jul 2006.

[73] Bennet, W.: New results in the calculation of modulation products. *Bell Systems Technical Journal*, vol. 12, pp. 228–243, 1933.

[74] Black, H.S.: *Modulation Theory*. 1st edn. D. van Nostrand Company Inc., Princeton, New Jersey, 1953.

[75] Bowes, S. and Bird, B.: Novel approach to the analysis and synthesis of modulation processes in power converters. *Proceedings of the IEE*, vol. 122, no. 11, pp. 1279–1285, Nov 1975.

[76] Giri, R., Ayyanar, R. and Ledezma, E.: Input-series and output-series connected modular dc-dc converters with active input voltage and output voltage sharing. In: *Applied Power Electronics Conference and Exposition, 2004. APEC '04. Nineteenth Annual IEEE*, vol. 3, pp. 1751–1756 Vol.3. 2004.

[77] Fang, T., Ruan, X. and Tse, C.: Control strategy of achieving input voltage sharing and output voltage sharing for input-series-output-series inverters system. In: *Energy Conversion Congress and Exposition, 2009. ECCE. IEEE*, pp. 908–915. Sept 2009.

[78] Chen, W., Ruan, X., Yan, H. and Tse, C.: Dc/dc conversion systems consisting of multiple converter modules: Stability, control, and experimental verifications. *Power Electronics, IEEE Transactions on*, vol. 24, no. 6, pp. 1463–1474, June 2009. ISSN 0885-8993.

[79] EPCOS AG: Ferrites and accessories. Application Notes, Sep 2006.

[80] van der Merwe, W.: *PWM Converter for a Highly Non-Linear Plasma Load*. Master's thesis, University of Stellenbosch, 2006.

Appendix A

Mathematical Derivations

A.1 The Invertible Matrix Theorem

Let $\mathbf{A}$ be a $n \times n$ matrix. Then the following statements are equivalent [59].

1. $\mathbf{A}$ is an invertible matrix.
2. $\mathbf{A}$ is row equivalent to the $n \times n$ identity matrix.
3. $\mathbf{A}$ has n pivot positions.
4. The equation $\mathbf{A}x = 0$ has only the trivial solution.
5. The columns of $\mathbf{A}$ form a linearly independent set.
6. The linear transformation $x \mapsto \mathbf{A}x$ is one-to-one.
7. The equation $\mathbf{A}x = b$ has at least one solution for each $b \in \mathbb{R}^n$.
8. The columns of $\mathbf{A}$ span $\mathbb{R}^n$.
9. The linear transformation $x \mapsto \mathbf{A}x$ maps $\mathbb{R}^n$ onto $\mathbb{R}^n$.
10. There is an $n \times n$ matrix $\mathbf{C}$ such that $\mathbf{CA} = \mathbf{I}$.
11. There is an $n \times n$ matrix $\mathbf{D}$ such that $\mathbf{AD} = \mathbf{I}$.
12. $\mathbf{A}^T$ is an invertible matrix.
13. The columns of $\mathbf{A}$ forms a basis of $\mathbb{R}^n$.
14. Col $\mathbf{A}$ = $\mathbb{R}^n$.
15. dim Col $\mathbf{A} = \ n$.
16. rank $\mathbf{A} = \ n$.
17. Null $\mathbf{A} = 0$.
18. dim Null $\mathbf{A} = \ 0$.
19. The number 0 is not an eigenvalue of $\mathbf{A}$.

A.2 Characteristics of Selected Matrix Types

In this study reference is made to the following types of matrices.

Toeplitz A Toeplitz matrix, $\mathbf{T}$ is a $n \times n$ constant diagonal matrix where $\mathbf{T}_{(\mathbf{i},\mathbf{j})} = \mathbf{T}_{(\mathbf{i}-\mathbf{1},\mathbf{j}-\mathbf{1})}$ [60, p. 1] . A Toeplitz matrix has the form

$$\mathbf{T} = \begin{bmatrix} z_0 & z_1 & z_2 & \cdots & z_{n-1} \\ z_{-1} & z_0 & z_1 & \cdots & z_{n-2} \\ z_{-2} & z_{-1} & z_0 & \cdots & z_{n-3} \\ \vdots & \vdots & \vdots & \ddots & \vdots \\ z_{n-1} & z_{n-2} & z_{n-3} & \cdots & z_0 \end{bmatrix}.$$

Symmetric A symmetric matrix, $\mathbf{A_s}$, is a square matrix that is equal to its transpose, or

$$\mathbf{A_s} = \mathbf{A_s^T}.$$

Furthermore for any square matrix $\mathbf{A}$ the sum

$$\frac{\mathbf{A} + \mathbf{A^T}}{2},$$

yields a symmetric matrix. Finally it is true that

$$\sigma_n(\mathbf{A_s}) \in \mathbb{R}.$$

Skew-Symmetric A skew-symmetric matrix, $\mathbf{A_{sk}}$, is a square matrix whose negative is also its transpose, or

$$\mathbf{A_{sk}} = -\mathbf{A_{sk}^T}.$$

Furthermore for any square matrix $\mathbf{A}$ the sum

$$\frac{\mathbf{A} - \mathbf{A^T}}{2},$$

yields a skew-symmetric matrix. Furthermore it is true that

$$\sigma_n(\mathbf{A_{sk}}) \in j\mathbb{R}.$$

Positive Definite A positive definite matrix is either a Hermitian or a real symmetric matrix where (for a real square matrix) and for any non-zero vector $\mathbf{x} \in \mathbb{R}^n$

$$\mathbf{x^T A x} > 0,$$

Furthermore, since $\sigma(\mathbf{A}) \subset \mathbb{R}$, it is true that

$$\mathbf{x^T A x} > 0 \Longleftrightarrow \sigma(\mathbf{A}) > 0.$$

Positive Semidefinite A positive definite matrix is either a Hermitian or a real symmetric matrix where (for a real square matrix) and for any non-zero vector $\mathbf{x} \in \mathbb{R}^n$

$$\mathbf{x^T A x} \geq 0,$$

Furthermore, since $\sigma(\mathbf{A}) \subset \mathbb{R}$, it is true that

$$\mathbf{x^T A x} \geq 0 \Longleftrightarrow \sigma(\mathbf{A}) \geq 0.$$

A.3 Complex Number Identities

The following identities are for any $A, B \in \mathbb{C}$ where $A = x + jy$ and $a, b, x, y \in \mathbb{R}$.

$$Re\{A \pm B\} = Re\{A\} \pm Re\{B\} \tag{A.3.1}$$
$$Im\{A \pm B\} = Im\{A\} \pm Im\{B\} \tag{A.3.2}$$
$$Re\{xA \pm yB\} = xRe\{A\} \pm yRe\{B\} \tag{A.3.3}$$
$$Im\{xA \pm yB\} = xIm\{A\} \pm yIm\{B\} \tag{A.3.4}$$
$$(xA + yB)^* = xA^* + yB^* \tag{A.3.5}$$
$$|A^* + B^*| = |A - B| \tag{A.3.6}$$
$$\frac{A}{B} = \frac{AB^*}{|B|^2} \tag{A.3.7}$$
$$Re\{AB\} = Re\{A\}\,Re\{B\} - Im\{A\}\,Im\{B\} \tag{A.3.8}$$
$$Im\{AB\} = Re\{A\}\,Im\{B\} + Im\{A\}\,Re\{B\} \tag{A.3.9}$$
$$(AB)^* = A^*B^* \tag{A.3.10}$$
$$Re\{A\} = \frac{A + A^*}{2} \tag{A.3.11}$$
$$Im\{A\} = \frac{A - A^*}{2j} \tag{A.3.12}$$
$$Im\{AB^*\} = -Im\{A^*B\} \tag{A.3.13}$$

A.4 List of Lemmas

A.4.1 General Proofs

Lemma 1. *Let $f_1(t)$ and $f_2(t)$ be two periodic functions with period 2π. Furthermore the exponential Fourier series coefficients of $f_1(t)$ and $f_2(t)$ are $C_{1(n)}$ and $C_{2(n)}$. Then the average value of the product $f_1(t)f_2(t)$ can be found as [49, p. 23]:*

$$\frac{1}{2\pi}\int_{\pi}^{\pi} f_1(t)f_2(t)dt = \sum_{n=-\infty}^{\infty} C_{1(n)}C_{2(-n)}$$

Proof. The relationship between $f_1(t)$ and $C_{1(n)}$ is

$$f_1(t) = \sum_{n=-\infty}^{\infty} C_{1(n)}e^{jnt}$$
$$C_{1(n)} = \frac{1}{2\pi}\int_{-\pi}^{\pi} f_1(t)e^{-jnt}dt,$$

and likewise for $f_2(t)$ and $C_{2(n)}$. The average value of the product $f_1(t)f_2(t)$ over a

complete period is found as:

$$\begin{aligned}\frac{1}{2\pi}\int_{\pi}^{\pi} f_1(t)f_2(t)dt &= \frac{1}{2\pi}\int_{-\pi}^{\pi}\left(\sum_{n=-\infty}^{\infty} C_{1(n)}e^{jnt}\right)f_2(t)dt \\ &= \sum_{n=-\infty}^{\infty} C_{1(n)}\left(\frac{1}{2\pi}\int_{-\pi}^{\pi} f_2(t)e^{jnt}dt\right) \\ &= \sum_{n=-\infty}^{\infty} C_{1(n)}C_{2(-n)}\end{aligned}$$

□

A.4.2 Harmonic Content of Signals

The following symbols are defined:

$\Psi(n)$ The exponential Fourier series coefficients.

ζ_n^a The indexed N roots of unity, $\zeta_n^a = e^{-j2\pi n\frac{a}{N}}$.

$C_{a(n)}$ Exponential Fourier coefficients of switching function $s_a(t)$.

N Number of cells.

For an exhaustive definition list refer to the nomenclature included before Chapter 1.

Lemma 2. *For all $\xi \neq \vartheta N$ and $\vartheta \in \mathbb{Z}$ it is true that:*

$$\sum_{n=0}^{N-1} \zeta_\xi^n = 0$$

Proof. Although it is possible to prove the statement using elementary symmetric polynomials and algebraic theory the DFT (Discrete Fourier Transform) yields an elegant proof. Define $\beta(\xi)$ as:

$$\begin{aligned}\beta(\xi) &= \sum_{n=0}^{N-1} \zeta_\xi^n \\ &= \sum_{n=0}^{N-1} e^{-j2\pi n\frac{\xi}{N}}\end{aligned}$$

Create a N-periodic signal $b_{(\xi)}$ such that:

$$b_\xi = \begin{cases} 1 & \text{if } \xi = \vartheta N \text{ where } \vartheta \in \mathbb{Z} \\ 0 & \text{otherwise} \end{cases}$$

The DFT of $b_{(\xi)}$ is found as:

$$B_n = \sum_{\xi=0}^{N-1} b_\xi \cdot e^{-j2\pi n\frac{\xi}{N}} \text{ for } n = 0, 1, \ldots, N-1$$

Using the definition of $b_{(\xi)}$ the values of B_n are found as:

$$B_n = 1 \text{ for } n = 0, 1, \ldots, N-1$$

Using the inverse DFT the signal $b_{(\xi)}$ can be reconstructed from B_n through,

$$b_{(\xi)} = \frac{1}{N} \sum_{n=0}^{N-1} B_n \cdot e^{j2\pi\xi \frac{n}{N}}.$$

Substituting the values for B_n yields,

$$\begin{aligned} b_{(\xi)} &= \frac{1}{N} \sum_{n=0}^{N-1} e^{j2\pi\xi \frac{n}{N}} \\ &= \frac{1}{N}\beta(-\xi). \end{aligned}$$

From the definition of $b_{(\xi)}$ it follows that for all $\xi \neq \vartheta N$ and $\vartheta \in \mathbb{Z}$:

$$b_\xi = 0 \Rightarrow \beta(\xi) = 0$$

□

Lemma 3. *For all $\xi = \vartheta N$ and $\vartheta \in \mathbb{Z}$ it is true that:*

$$\zeta_\xi^a - \zeta_\xi^b = 0$$

Proof. Define $\beta(\xi)$ as:

$$\begin{aligned} \beta(\xi) &= \zeta_\xi^a - \zeta_\xi^b \\ &= e^{-j2\pi a \frac{\xi}{N}} - e^{-j2\pi b \frac{\xi}{N}} \end{aligned}$$

When $\xi = \vartheta N$:

$$\begin{aligned} \beta(\xi) &= e^{-j2\pi a\vartheta} - e^{-j2\pi b\vartheta} \\ &= 1 - 1 \\ &= 0 \end{aligned}$$

□

Lemma 4. *For any two real valued switching functions, s_1 and s_2 with Fourier coefficients $C_{1(n)}$ and $C_{2(n)}$:*

$$\sum_{\xi=-\infty}^{\infty} \frac{C_{1(-\xi)}C_{2(\xi)} - C_{1(\xi)}C_{2(-\xi)}}{4Z(\xi\omega_s)} = \sum_{\xi=1}^{\infty} \frac{Im\left\{C_{1(\xi)}^* C_{2(\xi)}\right\} Im\left\{Z(\xi\omega_s)\right\}}{|Z(\xi\omega_s)|^2}$$

Proof.

$$\begin{aligned}
&\sum_{\xi=-\infty}^{\infty} \frac{C_{1(-\xi)}C_{2(\xi)} - C_{1(\xi)}C_{2(-\xi)}}{4Z(\xi\omega_s)} \\
&= \sum_{\xi=-\infty}^{\infty} \frac{C^*_{1(\xi)}C_{2(\xi)} - C_{1(\xi)}C^*_{2(\xi)}}{4Z(\xi\omega_s)} \\
&= \sum_{\xi=-\infty}^{\infty} \frac{2jIm\left\{C^*_{1(\xi)}C_{2(\xi)}\right\}}{4Z(\xi\omega_s)} \\
&= \sum_{\xi=-\infty}^{-1} \frac{2jIm\left\{C^*_{1(\xi)}C_{2(\xi)}\right\}}{4Z(\xi\omega_s)} + \frac{2jIm\left\{C_{1(0)}C_{2(0)}\right\}}{4Z(0)} + \sum_{\xi=1}^{\infty} \frac{2jIm\left\{C^*_{1(\xi)}C_{2(\xi)}\right\}}{4Z(\xi\omega_s)}
\end{aligned}$$

since the switching functions are real-valued $Im\left\{C_{1(0)}\right\} = Im\left\{C_{2(0)}\right\} = 0$, therefore:

$$\begin{aligned}
&= \sum_{\xi=1}^{\infty} \frac{2jIm\left\{C^*_{1(\xi)}C_{2(\xi)}\right\}}{4Z(\xi\omega_s)} - \frac{2jIm\left\{C^*_{1(\xi)}C_{2(\xi)}\right\}}{4Z(-\xi\omega_s)} \\
&= \sum_{\xi=1}^{\infty} 2jIm\left\{C^*_{1(\xi)}C_{2(\xi)}\right\} \frac{Z(\xi\omega_s)^* - Z(\xi\omega_s)}{4|Z(\xi\omega_s)|^2} \\
&= \sum_{\xi=1}^{\infty} 2jIm\left\{C^*_{1(\xi)}C_{2(\xi)}\right\} \frac{-2jIm\left\{Z(\xi\omega_s)\right\}}{4|Z(\xi\omega_s)|^2} \\
&= \sum_{\xi=1}^{\infty} \frac{Im\left\{C^*_{1(\xi)}C_{2(\xi)}\right\} Im\left\{Z(\xi\omega_s)\right\}}{|Z(\xi\omega_s)|^2}
\end{aligned}$$

□

Lemma 5. *For any two real valued switching functions, s_1 and s_2 with Fourier coefficients $C_{1(n)}$ and $C_{2(n)}$:*

$$\sum_{\xi=-\infty}^{\infty} \frac{C_{1(-\xi)}C_{2(\xi)} + C_{1(\xi)}C_{2(-\xi)}}{4Z(\xi\omega_s)} = \sum_{\xi=1}^{\infty} \frac{Re\left\{C^*_{1(\xi)}C_{2(\xi)}\right\} Re\left\{Z(\xi\omega_s)\right\}}{|Z(\xi\omega_s)|^2} + \frac{C_{1(0)}C_{2(0)}}{2Z(0)}$$

Proof.

$$\sum_{\xi=-\infty}^{\infty} \frac{C_{1(-\xi)}C_{2(\xi)} + C_{1(\xi)}C_{2(-\xi)}}{4Z(\xi\omega_s)}$$
$$= \sum_{\xi=-\infty}^{\infty} \frac{C^*_{1(\xi)}C_{2(\xi)} + C_{1(\xi)}C^*_{2(\xi)}}{4Z(\xi\omega_s)}$$
$$= \sum_{\xi=-\infty}^{\infty} \frac{2Re\left\{C^*_{1(\xi)}C_{2(\xi)}\right\}}{4Z(\xi\omega_s)}$$
$$= \sum_{\xi=-\infty}^{-1} \frac{2Re\left\{C^*_{1(\xi)}C_{2(\xi)}\right\}}{4Z(\xi\omega_s)} + \frac{2C_{1(0)}C_{2(0)}}{4Z(0)} + \sum_{\xi=1}^{\infty} \frac{2Re\left\{C^*_{1(\xi)}C_{2(\xi)}\right\}}{4Z(\xi\omega_s)}$$

since the switching functions are real-valued $Re\left\{C^*_{1(\xi)}C_{2(\xi)}\right\} = Re\left\{C_{1(\xi)}C^*_{2(\xi)}\right\}$,

$$\therefore \sum_{\xi=-\infty}^{-1} \frac{2Re\left\{C^*_{1(\xi)}C_{2(\xi)}\right\}}{4Z(\xi\omega_s)} + \frac{2C_{1(0)}C_{2(0)}}{4Z(0)} + \sum_{\xi=1}^{\infty} \frac{2Re\left\{C^*_{1(\xi)}C_{2(\xi)}\right\}}{4Z(\xi\omega_s)}$$
$$= \sum_{\xi=1}^{\infty} \frac{2Re\left\{C^*_{1(\xi)}C_{2(\xi)}\right\}}{4Z(\xi\omega_s)} + \frac{2Re\left\{C^*_{1(\xi)}C_{2(\xi)}\right\}}{4Z(-\xi\omega_s)} + \frac{2C_{1(0)}C_{2(0)}}{4Z(0)}$$
$$= \sum_{\xi=1}^{\infty} 2Re\left\{C^*_{1(\xi)}C_{2(\xi)}\right\} \frac{Z(\xi\omega_s)^* + Z(\xi\omega_s)}{4|Z(\xi\omega_s)|^2} + \frac{2C_{1(0)}C_{2(0)}}{4Z(0)}$$
$$= \sum_{\xi=1}^{\infty} 2Re\left\{C^*_{1(\xi)}C_{2(\xi)}\right\} \frac{2Re\left\{Z(\xi\omega_s)\right\}}{4|Z(\xi\omega_s)|^2} + \frac{2C_{1(0)}C_{2(0)}}{4Z(0)}$$
$$= \sum_{\xi=1}^{\infty} \frac{Re\left\{C^*_{1(\xi)}C_{2(\xi)}\right\} Re\left\{Z(\xi\omega_s)\right\}}{|Z(\xi\omega_s)|^2} + \frac{C_{1(0)}C_{2(0)}}{2Z(0)}$$

□

Lemma 6. *For any two real valued switching functions, s_1 and s_2 with Fourier coefficients $C_{1(n)}$ and $C_{2(n)}$:*

$$\sum_{\xi=-\infty}^{\infty} \frac{|C_{1(\xi)}|^2 - |C_{2(\xi)}|^2}{4Z(\xi\omega_s)} = \frac{|C_{1(0)}|^2 - |C_{2(0)}|^2}{4Z(0)} + \sum_{\xi=1}^{\infty} \frac{\left(|C_{1(\xi)}|^2 - |C_{2(\xi)}|^2\right) Re\left\{Z(\xi\omega_s)\right\}}{2|Z(\xi\omega_s)|^2}$$

Proof.

$$\begin{aligned}
&\sum_{\xi=-\infty}^{\infty} \frac{|C_{1(\xi)}|^2 - |C_{2(\xi)}|^2}{4Z(\xi\omega_s)} \\
&= \sum_{\xi=-\infty}^{-1} \frac{|C_{1(\xi)}|^2 - |C_{2(\xi)}|^2}{4Z(\xi\omega_s)} + \frac{|C_{1(0)}|^2 - |C_{2(0)}|^2}{4Z(0)} + \sum_{\xi=1}^{\infty} \frac{|C_{1(\xi)}|^2 - |C_{2(\xi)}|^2}{4Z(\xi\omega_s)} \\
&= \sum_{\xi=1}^{\infty} \frac{|C_{1(\xi)}|^2 - |C_{2(\xi)}|^2}{4Z(\xi\omega_s)^*} + \frac{|C_{1(0)}|^2 - |C_{2(0)}|^2}{4Z(0)} + \sum_{\xi=1}^{\infty} \frac{|C_{1(\xi)}|^2 - |C_{2(\xi)}|^2}{4Z(\xi\omega_s)} \\
&= \frac{|C_{1(0)}|^2 - |C_{2(0)}|^2}{4Z(0)} + \delta
\end{aligned}$$

The two summation terms, δ, can be combined:

$$\begin{aligned}
\delta &= \sum_{\xi=1}^{\infty} \frac{|C_{1(\xi)}|^2 - |C_{2(\xi)}|^2}{4Z(\xi\omega_s)^*} + \sum_{\xi=1}^{\infty} \frac{|C_{1(\xi)}|^2 - |C_{2(\xi)}|^2}{4Z(\xi\omega_s)} \\
&= \sum_{\xi=1}^{\infty} \frac{\left(|C_{1(\xi)}|^2 - |C_{2(\xi)}|^2\right) Z(\xi\omega_s) + \left(|C_{1(\xi)}|^2 - |C_{2(\xi)}|^2\right) Z(\xi\omega_s)^*}{4|Z(\xi\omega_s)|^2} \\
&= \sum_{\xi=1}^{\infty} \frac{\left(|C_{1(\xi)}|^2 - |C_{2(\xi)}|^2\right) \left(Z(\xi\omega_s) + Z(\xi\omega_s)^*\right)}{4|Z(\xi\omega_s)|^2} \\
&= \sum_{\xi=1}^{\infty} \frac{\left(|C_{1(\xi)}|^2 - |C_{2(\xi)}|^2\right) 2Re\left\{Z(\xi\omega_s)\right\}}{4|Z(\xi\omega_s)|^2}
\end{aligned}$$

Combining yields:

$$\sum_{\xi=-\infty}^{\infty} \frac{|C_{1(\xi)}|^2 - |C_{2(\xi)}|^2}{4Z(\xi\omega_s)} = \frac{|C_{1(0)}|^2 - |C_{2(0)}|^2}{4Z(0)} + \sum_{\xi=1}^{\infty} \frac{\left(|C_{1(\xi)}|^2 - |C_{2(\xi)}|^2\right) Re\left\{Z(\xi\omega_s)\right\}}{2|Z(\xi\omega_s)|^2}$$

□

Lemma 7. *For any two real valued switching functions, s_1 and s_2 with Fourier coefficients $C_{1(n)}$ and $C_{2(n)}$:*

$$\sum_{\xi=-\infty}^{\infty} \frac{|C_{1(\xi)}|^2 + |C_{2(\xi)}|^2}{4Z(\xi\omega_s)} = \frac{|C_{1(0)}|^2 + |C_{2(0)}|^2}{4Z(0)} + \sum_{\xi=1}^{\infty} \frac{\left(|C_{1(\xi)}|^2 + |C_{2(\xi)}|^2\right) Re\left\{Z(\xi\omega_s)\right\}}{2|Z(\xi\omega_s)|^2}$$

Proof.

$$
\begin{aligned}
&\sum_{\xi=-\infty}^{\infty} \frac{|C_{1(\xi)}|^2 + |C_{2(\xi)}|^2}{4Z(\xi\omega_s)} \\
&= \sum_{\xi=-\infty}^{-1} \frac{|C_{1(\xi)}|^2 + |C_{2(\xi)}|^2}{4Z(\xi\omega_s)} + \frac{|C_{1(0)}|^2 + |C_{2(0)}|^2}{4Z(0)} + \sum_{\xi=1}^{\infty} \frac{|C_{1(\xi)}|^2 + |C_{2(\xi)}|^2}{4Z(\xi\omega_s)} \\
&= \sum_{\xi=1}^{\infty} \frac{|C_{1(\xi)}|^2 - |C_{2(\xi)}|^2}{4Z(\xi\omega_s)^*} + \frac{|C_{1(0)}|^2 + |C_{2(0)}|^2}{4Z(0)} + \sum_{\xi=1}^{\infty} \frac{|C_{1(\xi)}|^2 - |C_{2(\xi)}|^2}{4Z(\xi\omega_s)} \\
&= \sum_{\xi=1}^{\infty} \left(|C_{1(\xi)}|^2 + |C_{2(\xi)}|^2\right) \frac{Z(\xi\omega_s) + Z(\xi\omega_s)}{4|Z(\xi\omega_s)|^2} + \frac{|C_{1(0)}|^2 + |C_{2(0)}|^2}{4Z(0)} \\
&= \sum_{\xi=1}^{\infty} \frac{\left(|C_{1(\xi)}|^2 + |C_{2(\xi)}|^2\right) 2Re\left\{Z(\xi\omega_s)\right\}}{4|Z(\xi\omega_s)|^2} + \frac{|C_{1(0)}|^2 + |C_{2(0)}|^2}{4Z(0)} \\
&= \sum_{\xi=1}^{\infty} \frac{\left(|C_{1(\xi)}|^2 + |C_{2(\xi)}|^2\right) Re\left\{Z(\xi\omega_s)\right\}}{2|Z(\xi\omega_s)|^2} + \frac{|C_{1(0)}|^2 + |C_{2(0)}|^2}{4Z(0)}
\end{aligned}
$$

□

Lemma 8. *For any three real valued switching functions, s_1, s_2 and s_3 with Fourier coefficients $C_{1(n)}$, $C_{2(n)}$ and $C_{3(n)}$ and $Z(\omega) = r + jL\omega$:*

$$
\sum_{\xi=-\infty}^{\infty} \frac{C_{3(\xi)}(C_{2(-\xi)} - C_{1(-\xi)})}{4Z(\xi\omega_s)} = \sum_{\xi=1}^{\infty} \frac{Re\left\{Z(\xi\omega_2)C_{3(\xi)}^*(C_{2(\xi)} - C_{1(\xi)})\right\}}{2|Z(\xi\omega_s)|^2} + \frac{C_{3(0)}(C_{2(0)} - C_{1(0)})}{4r}
$$

Proof.

$$
\begin{aligned}
&\sum_{\xi=-\infty}^{\infty} \frac{C_{3(\xi)}(C_{2(-\xi)} - C_{1(-\xi)})}{4Z(\xi\omega_s)} \\
&= \sum_{\xi=-\infty}^{-1} \frac{C_{3(\xi)}(C_{2(\xi)}^* - C_{1(\xi)}^*)}{4Z(\xi\omega_s)} + \sum_{\xi=1}^{\infty} \frac{C_{3(\xi)}(C_{2(\xi)}^* - C_{1(\xi)}^*)}{4Z(\xi\omega_s)} + \frac{C_{3(0)}(C_{2(0)} - C_{1(0)})}{4r} \\
&= \sum_{\xi=1}^{\infty} \frac{C_{3(\xi)}^*(C_{2(\xi)} - C_{1(\xi)})}{4Z(\xi\omega_s)^*} + \sum_{\xi=1}^{\infty} \frac{C_{3(\xi)}(C_{2(\xi)}^* - C_{1(\xi)}^*)}{4Z(\xi\omega_s)} + \frac{C_{3(0)}(C_{2(0)} - C_{1(0)})}{4r} \\
&= \sum_{\xi=1}^{\infty} \frac{C_{3(\xi)}^*(C_{2(\xi)} - C_{1(\xi)})Z(\xi\omega_s) + C_{3(\xi)}(C_{2(\xi)}^* - C_{1(\xi)}^*)Z(\xi\omega_s)^*}{4|Z(\xi\omega_s)|^2} + \frac{C_{3(0)}(C_{2(0)} - C_{1(0)})}{4r} \\
&= \sum_{\xi=1}^{\infty} \frac{Re\left\{Z(\xi\omega_s)C_{3(\xi)}^*(C_{2(\xi)} - C_{1(\xi)})\right\}}{2|Z(\xi\omega_s)|^2} + \frac{C_{3(0)}(C_{2(0)} - C_{1(0)})}{4r}
\end{aligned}
$$

□

Lemma 9. *For the two cell case*

$$\left.\frac{S_t(\omega)}{Z(\omega)} * S_d(\omega)\right|_{\omega=0} = \frac{|C_{1(0)}|^2 - |C_{2(0)}|^2}{4r} + \sum_{\xi=1}^{\infty} \frac{\frac{r}{2}|C_{1(\xi)}|^2 - \frac{r}{2}|C_{2(\xi)}|^2 + Im\left\{C_{1(-\xi)}C_{2(\xi)}\right\} L\xi\omega_s}{|Z(\xi\omega_s)|^2}$$

Proof.

$$\begin{aligned}
\left.\frac{S_t(\omega)}{Z(\omega)} * S_d(\omega)\right|_{\omega=0} &= \sum_{\xi=-\infty}^{\infty} \frac{\frac{1}{2}\left(C_{1(\xi)} + C_{1(\xi)}\right)\frac{1}{2}\left(C_{1(-\xi)} - C_{2(-\xi)}\right)}{Z(\xi\omega_s)} \\
&= \sum_{\xi=-\infty}^{\infty} \frac{C_{1(\xi)}C_{1(-\xi)} - C_{1(\xi)}C_{2(-\xi)} + C_{2(\xi)}C_{1(-\xi)} - C_{2(\xi)}C_{2(-\xi)}}{4Z(\xi\omega_s)} \\
&= \sum_{\xi=-\infty}^{\infty} \frac{C_{1(\xi)}C_{1(-\xi)} - C_{2(\xi)}C_{2(-\xi)}}{4Z(\xi\omega_s)} + \sum_{\xi=-\infty}^{\infty} \frac{C_{2(\xi)}C_{1(-\xi)} - C_{1(\xi)}C_{2(-\xi)}}{4Z(\xi\omega_s)} \\
&= \alpha + \beta
\end{aligned}$$

From Lemma 6 it follows that:

$$\alpha = \frac{|C_{1(0)}|^2 - |C_{2(0)}|^2}{4r} + \sum_{\xi=1}^{\infty} \frac{r|C_{1(\xi)}|^2 - r|C_{2(\xi)}|^2}{2|Z(\xi\omega_s)|^2}$$

likewise, from Lemma 4:

$$\beta = \sum_{\xi=1}^{\infty} \frac{Im\left\{C^*_{1(\xi)}C_{2(\xi)}\right\} L\xi\omega_s}{|Z(\xi\omega_s)|^2}$$

Combining:

$$\alpha + \beta = \frac{|C_{1(0)}|^2 - |C_{2(0)}|^2}{4r} + \sum_{\xi=1}^{\infty} \frac{\frac{r}{2}|C_{1(\xi)}|^2 - \frac{r}{2}|C_{2(\xi)}|^2 + Im\left\{C^*_{1(\xi)}C_{2(\xi)}\right\} L\xi\omega_s}{|Z(\xi\omega_s)|^2}$$

□

Lemma 10. *Using the definitions of S_t and S_{da} for all converters presented, it is true that*

$$\left.\frac{S_t(\omega)}{Z(\omega)} * S_{dc}(\omega)\right|_{\omega=0} = 0,$$

when:

1. *The different cells operate with the same duty cycle.*

2. *The different cells are interleaved.*

3. *The statement is true for any number of cells.*

Proof. Although the definition of S_{dc} differs between the presented converters, for example for the ISOP $s_{dc} = \frac{1}{N}(s_0 - s_c)$ while for the FCC $s_{dc} = \frac{1}{2}(s_c - s_{c-1})$ in general the definition can be rewritten as:

$$s_{dc} = \frac{1}{x}(s_a - s_b)$$

The definition of s_t differs also slightly between the different topologies but can be generalised as:

$$s_t = \frac{1}{y}\sum_{n=0}^{N-1} s_n$$

When the cells are interleaved and operating with the same duty cycle the switching function Fourier series coefficients can be rewritten as:

$$C_{a(\xi)} = \Psi(\xi)\zeta_\xi^a$$

Using the generalised definitions the convolution can be expressed as:

$$\begin{aligned}\frac{S_t(\omega)}{xyZ(\omega)} * S_{dc}(\omega)\Big|_{\omega=0} &= \sum_{\xi=-\infty}^{\infty} \frac{\sum_{n=0}^{N-1}\Psi(\xi)\zeta_\xi^n}{xyZ(\xi\omega_s)}\left(\Psi(-\xi)\zeta_{-\xi}^a - \Psi(-\xi)\zeta_{-\xi}^b\right)\\ &= \sum_{\xi=-\infty}^{\infty} \frac{|\Psi(\xi)|^2}{xyZ(\xi\omega_s)}\left(\zeta_{-\xi}^a - \zeta_{-\xi}^b\right)\sum_{n=0}^{N-1}\zeta_\xi^n\\ &= \sum_{\xi=-\infty}^{\infty} \frac{|\Psi(\xi)|^2}{xyZ(\xi\omega_s)}\alpha\beta\end{aligned}$$

From Lemma 3, when $\xi = \vartheta N$:

$$\alpha = \zeta_{-\xi}^a - \zeta_{-\xi}^b = 0$$

Likewise from Lemma 2, when $\xi \neq \vartheta N$:

$$\begin{aligned}\beta &= \sum_{n=0}^{N-1}\zeta_\xi^n = 0\\ \therefore \forall\, \xi &: \alpha\beta = 0\end{aligned}$$

□

Lemma 11. *Using the definitions of S_t and S_{da} for all converters presented, it is true that, for the modulated duty cycle case*

$$\frac{\tilde{S}_t(\omega)}{Z(\omega)} * \tilde{S}_{dn}(\omega)\Big|_{\omega=0} = 0,$$

when:

1. *The different cells operate with the same duty cycle in that the same reference function is used to determine the switching functions.*
2. *The different cells are interleaved.*
3. *The switching frequency is significantly higher than the modulation frequency. This implies that the harmonic content of the switching signals, occurring in clusters around the multiples of the switching frequency will be spaced far enough from each other that they will not overlap [28; 33; 29].*
4. *The statement is true for any number of cells.*

Proof. Using the same general definition of both s_t and s_{da} as in Lemma 10, the functions can be described as:

$$\tilde{S}_{dc} = \frac{1}{x}(\tilde{S}_a - \tilde{S}_b)$$
$$\tilde{S}_t = \frac{1}{y}\sum_{n=0}^{N-1}\tilde{S}_n$$

When the cells are interleaved and operating with the same duty cycle the switching function Fourier series coefficients can be rewritten as:

$$\tilde{C}_{a(k,m)} = \tilde{\Psi}_{(k,m)}\zeta_m^a$$

When the switching frequency is high enough that the harmonic clusters does not overlap the convolution can be expressed as:

$$\begin{aligned}
\frac{\tilde{S}_t(\omega)}{Z(\omega)} * \tilde{S}_{da}(\omega)\Big|_{\omega=0} &= \sum_{\varrho=-\infty}^{\infty}\sum_{\xi=-\infty}^{\infty}\frac{\tilde{C}_{t(\varrho,\xi)}}{Z(\varrho\omega_r+\xi\omega_s)}\tilde{C}_{da(-\varrho,-\xi)} \\
&= \sum_{\varrho=-\infty}^{\infty}\sum_{\xi=-\infty}^{\infty}\frac{\tilde{\Psi}_{(\varrho,\xi)}\sum_{n=0}^{N-1}\zeta_\xi^n}{Z(\varrho\omega_r+\xi\omega_s)}\tilde{\Psi}_{(-\varrho,-\xi)}(\zeta_{-\xi}^a-\zeta_{-\xi}^b) \\
&= \sum_{\varrho=-\infty}^{\infty}\sum_{\xi=-\infty}^{\infty}\frac{|\tilde{\Psi}_{(\varrho,\xi)}|^2}{Z(\varrho\omega_r+\xi\omega_s)}(\zeta_{-\xi}^a-\zeta_{-\xi}^b)\sum_{n=0}^{N-1}\zeta_\xi^n \\
&= \sum_{\varrho=-\infty}^{\infty}\sum_{\xi=-\infty}^{\infty}\frac{|\tilde{\Psi}_{(\varrho,\xi)}|^2}{Z(\varrho\omega_r+\xi\omega_s)}\alpha\beta
\end{aligned}$$

From Lemma 3, when $\xi = \vartheta N$:

$$\alpha = \zeta_{-\xi}^a - \zeta_{-\xi}^b = 0$$

Likewise from Lemma 2, when $\xi \neq \vartheta N$:

$$\beta = \sum_{n=0}^{N-1}\zeta_\xi^n = 0$$
$$\therefore \forall\,\xi : \alpha\beta = 0$$

□

$$\frac{\tilde{S}_t(\omega)}{Z(\omega)} * \tilde{S}_{dn}(\omega)\Big|_{\omega=0} = \sum_{\varrho=-\infty}^{\infty}\sum_{\xi=-\infty}^{\infty} \frac{\tilde{C}_{t(\varrho,\xi)}}{Z(\varrho\omega_r + \xi\omega_s)}\tilde{C}_{da(\varrho,\xi)} \tag{A.4.1}$$

Lemma 12. *For the N-cell FCC the entries λ_{ab} $1 \leq a, b \leq N-1$, or the convolution of the impedance modified S_{db} function with S_{da} can be expressed as:*

$$\lambda_{ab} = \sum_{\xi=-\infty}^{\infty} \frac{S_{db(\xi)}}{Z(\xi\omega_s)} S_{da(-\xi)} = \sum_{\xi=-\infty}^{\infty} \frac{|\Psi(\xi)|^2}{2Z(\xi\omega_s)} \left(1 - Re\left\{\zeta_\xi\right\}\right) \zeta_\xi^{b-a}$$

When the cells are interleaved and the duty cycle is equal across all cells.

Proof. Using $\zeta_{-n}^{x} = \zeta_n^{-x}$:

$$\begin{aligned}
\lambda_{ab} &= \sum_{\xi=-\infty}^{\infty} \frac{S_{db(\xi)}}{Z(\xi\omega_s)} S_{da(\xi)} \\
&= \sum_{\xi=-\infty}^{\infty} \frac{C_{b(\xi)} - C_{(b-1)(\xi)}}{4Z(\xi\omega_s)} \left(C_{a(-\xi)} - C_{(a-1)(-\xi)}\right) \\
&= \sum_{\xi=-\infty}^{\infty} \frac{\Psi(\xi)\left(\zeta_\xi^b - \zeta_\xi^{b-1}\right)}{4Z(\xi\omega_s)} \Psi^*(\xi) \left(\zeta_{-\xi}^a - \zeta_{-\xi}^{a-1}\right) \\
&= \sum_{\xi=-\infty}^{\infty} \frac{|\Psi(\xi)|^2}{4Z(\xi\omega_s)} \left(\zeta_\xi^b - \zeta_\xi^{b-1}\right) \left(\zeta_{-\xi}^a - \zeta_{-\xi}^{a-1}\right) \\
&= \sum_{\xi=-\infty}^{\infty} \frac{|\Psi(\xi)|^2}{4Z(\xi\omega_s)} \left(\zeta_\xi^{b-a} - \zeta_\xi^{b-a-1} - \zeta_\xi^{b-a+1} + \zeta_\xi^{b-a}\right) \\
&= \sum_{\xi=-\infty}^{\infty} \frac{|\Psi(\xi)|^2}{4Z(\xi\omega_s)} \left(-\zeta_\xi^{b-a-1} + 2\zeta_\xi^{b-a} - \zeta_\xi^{b-a+1}\right) \\
&= \sum_{\xi=-\infty}^{\infty} \frac{|\Psi(\xi)|^2}{4Z(\xi\omega_s)} \zeta_\xi^{b-a} \left(2 - \zeta_\xi - \zeta_\xi^*\right) \\
&= \sum_{\xi=-\infty}^{\infty} \frac{|\Psi(\xi)|^2}{2Z(\xi\omega_s)} \left(1 - Re\left\{\zeta_\xi\right\}\right) \zeta_\xi^{b-a}
\end{aligned} \tag{A.4.2}$$

□

Lemma 13. *For the N-cell FCC operating with modulated duty cycle the entries $\tilde{\lambda}_{ab}$ $1 \leq a, b \leq N-1$, or the convolution of the impedance modified $\tilde{S}_{db}$ function with $\tilde{S}_{da}$ can be expressed as:*

$$\begin{aligned}
\tilde{\lambda}_{ab} &= \sum_{\varrho=-\infty}^{\infty}\sum_{\xi=-\infty}^{\infty} \frac{\tilde{C}_{db(\varrho,\xi)}}{Z(\varrho\omega_r + \xi\omega_s)} \tilde{C}_{da(-\varrho,-\xi)} \\
&= \sum_{\varrho=-\infty}^{\infty}\sum_{\xi=-\infty}^{\infty} \frac{|\tilde{\Psi}_{(\varrho,\xi)}|^2}{2Z(\varrho\omega_r + \xi\omega_s)} \left(1 - Re\left\{\zeta_\xi\right\}\right) \zeta_\xi^{b-a}
\end{aligned}$$

When:

1. *The different cells operate with the same duty cycle in that the same reference function is used to determine the switching functions.*
2. *The different cells are interleaved.*
3. *The switching frequency is significantly higher than the modulation frequency. This implies that the harmonic content of the switching signals, occurring in clusters around the multiples of the switching frequency will be spaced far enough from each other that they will not overlap [28; 33; 29].*

Proof. Using $\zeta_{-n}^{x} = \zeta_{n}^{-x}$:

$$\begin{aligned}
\lambda_{ab} &= \sum_{\varrho=-\infty}^{\infty}\sum_{\xi=-\infty}^{\infty} \frac{\tilde{C}_{db(\varrho,\xi)}}{Z(\varrho\omega_r+\xi\omega_s)}\tilde{C}_{da(-\varrho,-\xi)} \\
&= \sum_{\varrho=-\infty}^{\infty}\sum_{\xi=-\infty}^{\infty} \frac{\tilde{C}_{b(\varrho,\xi)}-\tilde{C}_{(b-1)(\varrho,\xi)}}{4Z(\varrho\omega_r+\xi\omega_s)}\left(\tilde{C}_{a(-\varrho,-\xi)}-\tilde{C}_{(a-1)(-\varrho,-\xi)}\right) \\
&= \sum_{\varrho=-\infty}^{\infty}\sum_{\xi=-\infty}^{\infty} \frac{\tilde{\Psi}_{(\varrho,\xi)}\left(\zeta_{\xi}^{b}-\zeta_{\xi}^{b-1}\right)}{4Z(\varrho\omega_r+\xi\omega_s)}\tilde{\Psi}_{(-\varrho,-\xi)}\left(\zeta_{-\xi}^{a}-\zeta_{-\xi}^{a-1}\right) \\
&= \sum_{\varrho=-\infty}^{\infty}\sum_{\xi=-\infty}^{\infty} \frac{|\tilde{\Psi}_{(\varrho,\xi)}|^2}{4Z(\varrho\omega_r+\xi\omega_s)}\left(\zeta_{\xi}^{b}-\zeta_{\xi}^{b-1}\right)\left(\zeta_{-\xi}^{a}-\zeta_{-\xi}^{a-1}\right) \\
&= \sum_{\varrho=-\infty}^{\infty}\sum_{\xi=-\infty}^{\infty} \frac{|\tilde{\Psi}_{(\varrho,\xi)}|^2}{4Z(\varrho\omega_r+\xi\omega_s)}\left(\zeta_{\xi}^{b-a}-\zeta_{\xi}^{b-a-1}-\zeta_{\xi}^{b-a+1}+\zeta_{\xi}^{b-a}\right) \\
&= \sum_{\varrho=-\infty}^{\infty}\sum_{\xi=-\infty}^{\infty} \frac{|\tilde{\Psi}_{(\varrho,\xi)}|^2}{4Z(\varrho\omega_r+\xi\omega_s)}\left(-\zeta_{\xi}^{b-a-1}+2\zeta_{\xi}^{b-a}-\zeta_{\xi}^{b-a+1}\right) \\
&= \sum_{\varrho=-\infty}^{\infty}\sum_{\xi=-\infty}^{\infty} \frac{|\tilde{\Psi}_{(\varrho,\xi)}|^2}{4Z(\varrho\omega_r+\xi\omega_s)}\zeta_{\xi}^{b-a}\left(2-\zeta_{\xi}-\zeta_{\xi}^{*}\right) \\
&= \sum_{\varrho=-\infty}^{\infty}\sum_{\xi=-\infty}^{\infty} \frac{|\tilde{\Psi}_{(\varrho,\xi)}|^2}{2Z(\varrho\omega_r+\xi\omega_s)}\left(1-Re\left\{\zeta_{\xi}\right\}\right)\zeta_{\xi}^{b-a}
\end{aligned}$$

□

Lemma 14. *For the N-Cell FCC the entries λ_{ab} $1 \le a, b \le N-1$, or the convolution of the impedance modified S_{db} function with S_{da} can be rewritten as:*

$$\begin{aligned}
\lambda_{ab} = \sum_{\xi=1}^{\infty} \frac{|\Psi(\xi)|^2}{|Z(\xi\omega_s)|^2}\left(1-Re\left\{\zeta_{\xi}\right\}\right)\Big(&Re\left\{Z(\xi\omega_s)\right\}Re\left\{\zeta_{\xi}^{a-b}\right\} \\
&-Im\left\{Z(\xi\omega_s)\right\}Im\left\{\zeta_{\xi}^{a-b}\right\}\Big)
\end{aligned}$$

When the cells are interleaved and the duty cycle is equal across all cells.

Proof. From Lemma 12

$$\lambda_{ab} = \sum_{\xi=-\infty}^{\infty} \frac{|\Psi(\xi)|^2}{2Z(\xi\omega_s)}\left(1-Re\left\{\zeta_{\xi}\right\}\right)\zeta_{\xi}^{b-a}$$

This expression for λ_{ab} can be rewritten by combining the sum for positive and negative values of ξ, and realising that $Re\left\{\zeta_{\xi}\right\} = 1$ when $\xi = 0$, as:

$$\begin{aligned}\lambda_{ab} &= \sum_{\xi=-\infty}^{\infty} \frac{|\Psi(\xi)|^2}{2Z(\xi\omega_s)} \left(1 - Re\left\{\zeta_{\xi}\right\}\right) \zeta_{\xi}^{b-a} \\ &= \sum_{\xi=1}^{\infty} \frac{|\Psi(\xi)|^2}{2Z(\xi\omega_s)} \left(1 - Re\left\{\zeta_{\xi}\right\}\right) \zeta_{\xi}^{b-a} + \sum_{\xi=1}^{\infty} \frac{|\Psi(\xi)|^2}{2Z(-\xi\omega_s)} \left(1 - Re\left\{\zeta_{-\xi}\right\}\right) \zeta_{-\xi}^{b-a}\end{aligned}$$

It is known that $Re\left\{\zeta_{\xi}\right\} = Re\left\{\zeta_{-\xi}\right\}$ and $\zeta_{-\xi}^{a} = \zeta_{\xi}^{-a}$ therefore:

$$\begin{aligned}\lambda_{ab} &= \sum_{\xi=1}^{\infty} |\Psi(\xi)|^2 \left(1 - Re\left\{\zeta_{\xi}\right\}\right) \left(\frac{\zeta_{\xi}^{b-a}}{2Z(\xi\omega_s)} + \frac{\zeta_{\xi}^{a-b}}{2Z(-\xi\omega_s)}\right) \\ &= \sum_{\xi=1}^{\infty} |\Psi(\xi)|^2 \left(1 - Re\left\{\zeta_{\xi}\right\}\right) \left(\frac{\zeta_{\xi}^{b-a} Z(-\xi\omega_s) + \zeta_{\xi}^{a-b} Z(\xi\omega_s)}{2|Z(\xi\omega_s)|^2}\right) \\ &= \sum_{\xi=1}^{\infty} \frac{|\Psi(\xi)|^2}{|Z(\xi\omega_s)|^2} \left(1 - Re\left\{\zeta_{\xi}\right\}\right) Re\left\{Z(\xi\omega_s)\zeta_{\xi}^{a-b}\right\} \\ &= \sum_{\xi=1}^{\infty} \frac{|\Psi(\xi)|^2}{|Z(\xi\omega_s)|^2} \left(1 - Re\left\{\zeta_{\xi}\right\}\right) \Big(Re\left\{Z(\xi\omega_s)\right\} Re\left\{\zeta_{\xi}^{a-b}\right\} \\ &\qquad - Im\left\{Z(\xi\omega_s)\right\} Im\left\{\zeta_{\xi}^{a-b}\right\}\Big)\end{aligned}$$

□

Lemma 15. *For the 2-cell case*

$$\left.\frac{S_t(\omega)}{Z(\omega)} * S_d(\omega)\right|_{\omega=0} = 0,$$

when the duty-cycles of the two cells are equal and the cells are interleaved.

Proof.

$$\begin{aligned}\left.\frac{S_t(\omega)}{Z(\omega)} * S_d(\omega)\right|_{\omega=0} &= \sum_{\xi=-\infty}^{\infty} \frac{S_{1(\xi)} + S_{2(\xi)}}{4Z(\xi\omega_s)} \left(S_{2(-\xi)} - S_{1(-\xi)}\right) \\ &= \sum_{\xi=-\infty}^{\infty} \frac{\Psi(\xi) + (-1)^{\xi}\Psi(\xi)}{4Z(\xi\omega_s)} \left((-1)^{-\xi}\Psi(-\xi) - \Psi(-\xi)\right) \\ &= \sum_{\xi=-\infty}^{\infty} \frac{\Psi(\xi)\left(1 + (-1)^{\xi}\right)}{4Z(\xi\omega_s)} \Psi(-\xi) \left((-1)^{-\xi} - 1\right) \\ &= \sum_{\xi=-\infty}^{\infty} \frac{|\Psi(\xi)|^2}{4Z(\xi\omega_s)} \left(1 + (-1)^{\xi}\right) \left((-1)^{-\xi} - 1\right) \\ &= \sum_{\xi=-\infty}^{\infty} \frac{|\Psi(\xi)|^2}{4Z(\xi\omega_s)} 0 = 0\end{aligned}$$

□

Lemma 16. *For the 2-cell case*

$$\frac{S_d(\omega)}{Z(\omega)} * S_d(\omega)\bigg|_{\omega=0} = 2\sum_{\xi=1,3}^{\infty} \frac{|\Psi(\xi)|^2}{|Z(\xi\omega_s)|^2}\mathrm{Re}\{Z(\xi\omega_s)\},$$

when the duty-cycles of the two cells are equal and the cells are interleaved.

Proof.

$$\begin{aligned}
\frac{S_d(\omega)}{Z(\omega)} * S_d(\omega)\bigg|_{\omega=0} &= \sum_{\xi=-\infty}^{\infty} \frac{S_{2(\xi)} - S_{1(\xi)}}{4Z(\xi\omega_s)} \left(S_{2(-\xi)} - S_{1(-\xi)}\right) \\
&= \sum_{\xi=-\infty}^{\infty} \frac{(-1)^{\xi}\Psi(\xi) - \Psi(\xi)}{4Z(\xi\omega_s)} \left((-1)^{-\xi}\Psi(-\xi) - \Psi(-\xi)\right) \\
&= \sum_{\xi=-\infty}^{\infty} \frac{\Psi(\xi)\left((-1)^{\xi} - 1\right)}{4Z(\xi\omega_s)}\Psi(-\xi)\left((-1)^{-\xi} - 1\right) \\
&= \sum_{\xi=-\infty}^{\infty} \frac{|\Psi(\xi)|^2}{4Z(\xi\omega_s)} \left((-1)^{\xi} - 1\right)\left((-1)^{-\xi} - 1\right) \\
&= \sum_{\xi=-\infty}^{\infty} \frac{|\Psi(\xi)|^2}{2Z(\xi\omega_s)} \left(1 - (-1)^{\xi}\right)
\end{aligned}$$

The sum can be simplified by adding the positive and negative parts of the sum together. With knowledge that $1 - (-1)^{\xi} = 0$ for equal numbers of ξ :

$$\begin{aligned}
\frac{S_d(\omega)}{Z(\omega)} * S_d(\omega)\bigg|_{\omega=0} &= \sum_{\xi=1,3}^{\infty} \frac{|\Psi(\xi)|^2}{Z(\xi\omega_s)} + \frac{|\Psi(-\xi)|^2}{Z(-\xi\omega_s)} \\
&= \sum_{\xi=1,3}^{\infty} \frac{|\Psi(\xi)|^2 Z(-\xi\omega_s) + |\Psi(\xi)|^2 Z(\xi\omega_s)}{|Z(\xi\omega_s)|^2} \\
&= 2\sum_{\xi=1,3}^{\infty} \frac{|\Psi(\xi)|^2}{|Z(\xi\omega_s)|^2}\mathrm{Re}\{Z(\xi\omega_s)\}
\end{aligned}$$

□

Lemma 17. *For the 2-cell case*

$$\frac{S_t(\omega)}{Z(\omega)} * S_t(\omega)\bigg|_{\omega=0} = \frac{d^2}{Z(0)} + 2\sum_{\xi=2,4,6}^{\infty} \frac{|\Psi(\xi)|^2}{|Z(\xi\omega_s)|^2}\mathrm{Re}\{Z(\xi\omega_s)\},$$

when the duty-cycles of the two cells are equal and the cells are interleaved.

Proof.

$$\begin{aligned}
\frac{S_t(\omega)}{Z(\omega)} * S_t(\omega)\Big|_{\omega=0} &= \sum_{\xi=-\infty}^{\infty} \frac{S_{1(\xi)} + S_{2(\xi)}}{4Z(\xi\omega_s)} \Big(S_{1(-\xi)} + S_{2(-\xi)}\Big) \\
&= \sum_{\xi=-\infty}^{\infty} \frac{\Psi(\xi) + (-1)^{\xi}\Psi(\xi)}{4Z(\xi\omega_s)} \Big(\Psi(-\xi) + (-1)^{\xi}\Psi(-\xi)\Big) \\
&= \sum_{\xi=-\infty}^{\infty} \frac{|\Psi(\xi)|^2}{4Z(\xi\omega_s)} \Big(1 + (-1)^{\xi}\Big)^2 \\
&= \sum_{\xi=-\infty}^{\infty} \frac{|\Psi(\xi)|^2}{2Z(\xi\omega_s)} \Big(1 + (-1)^{\xi}\Big) \\
&= \frac{\Psi(0)^2}{Z(0)} + \sum_{\xi=2,4,6}^{\infty} \frac{|\Psi(\xi)|^2}{Z(\xi\omega_s)} + \frac{|\Psi(-\xi)|^2}{Z(-\xi\omega_s)} \\
&= \frac{d^2}{Z(0)} + \sum_{\xi=2,4,6}^{\infty} \frac{|\Psi(\xi)|^2 Z(-\xi\omega_s) + |\Psi(\xi)|^2 Z(\xi\omega_s)}{|Z(\xi\omega_s)|^2} \\
&= \frac{d^2}{Z(0)} + 2\sum_{\xi=2,4,6}^{\infty} \frac{|\Psi(\xi)|^2}{|Z(\xi\omega_s)|^2} \mathrm{Re}\{Z(\xi\omega_s)\}
\end{aligned}$$

□

A.5 Calculating the Circuit Equations in Terms of d and t Parameters

A.5.1 Input-Series-Output-Parallel Converter

Equation (3.1.1) is repeated for convenience:

$$\frac{d}{dt}\begin{bmatrix} L_s \cdot i_{in} \\ C \cdot v_1 \\ C \cdot v_2 \\ L \cdot i_1 \\ L \cdot i_2 \\ C_o \cdot v_o \end{bmatrix} = \begin{bmatrix} -r_s & -1 & -1 & 0 & 0 & 0 \\ 1 & 0 & 0 & -s_1 & 0 & 0 \\ 1 & 0 & 0 & 0 & -s_2 & 0 \\ 0 & s_1 & 0 & -r & 0 & -1 \\ 0 & 0 & s_2 & 0 & -r & -1 \\ 0 & 0 & 0 & 1 & 1 & \frac{-1}{R} \end{bmatrix} \begin{bmatrix} i_{in} \\ v_1 \\ v_2 \\ i_1 \\ i_2 \\ v_o \end{bmatrix} + \begin{bmatrix} v_{in} \\ 0 \\ 0 \\ 0 \\ 0 \\ 0 \end{bmatrix}$$

The total and difference parameters are defined as:

$$\begin{aligned} s_d &= \frac{s_1 - s_2}{2} & s_t &= \frac{s_1 + s_2}{2} \\ v_d &= v_1 - v_2 & v_t &= v_1 + v_2 \\ i_d &= i_1 - i_2 & i_t &= i_1 + i_2 \end{aligned}$$

The equations for $\frac{di_{in}}{dt}$ can be rewritten as:

$$\begin{aligned} L_s \frac{di_{in}}{dt} &= -r_s i_{in} - (v_1 + v_2) + v_{in} \\ &= -r_s i_{in} - v_t + v_{in} \end{aligned}$$

Adding the equations for $\frac{dv_1}{dt}$ and $\frac{dv_2}{dt}$ together yields

$$\begin{aligned} C\frac{d}{dt}(v_1 + v_2) &= 2i_{in} - s_1 i_1 - s_2 i_2 \\ C\frac{dv_t}{dt} &= 2i_{in} - s_1 i_1 - s_2 i_2 \\ &= 2i_{in} - s_t i_t - s_d i_d, \end{aligned}$$

since

$$\begin{aligned} s_t i_t + s_d i_d &= \left(\frac{s_1 + s_2}{2}\right)(i_1 + i_2) + \left(\frac{s_1 - s_2}{2}\right)(i_1 - i_2) \\ &= \frac{s_1 i_1}{2} + \frac{s_2 i_1}{2} + \frac{s_1 i_2}{2} + \frac{s_2 i_2}{2} + \frac{s_1 i_1}{2} - \frac{s_2 i_1}{2} - \frac{s_1 i_2}{2} + \frac{s_2 i_2}{2} \\ &= s_1 i_1 + s_2 i_2. \end{aligned}$$

Subtracting the equations for $\frac{dv_1}{dt}$ and $\frac{dv_2}{dt}$ yields

$$\begin{aligned} C\frac{d}{dt}(v_1 - v_2) &= -s_1 i_1 + s_2 i_2 \\ C\frac{dv_d}{dt} &= -s_1 i_1 + s_2 i_2 \\ &= -s_d i_t - s_t i_d, \end{aligned}$$

since

$$\begin{aligned} s_d i_t + s_t i_d &= \left(\frac{s_1 - s_2}{2}\right)(i_1 + i_2) + \left(\frac{s_1 + s_2}{2}\right)(i_1 - i_2) \\ &= \frac{s_1 i_1}{2} - \frac{s_2 i_1}{2} + \frac{s_1 i_2}{2} - \frac{s_2 i_2}{2} + \frac{s_1 i_1}{2} + \frac{s_2 i_1}{2} - \frac{s_1 i_2}{2} - \frac{s_2 i_2}{2} \\ &= s_1 i_1 - s_2 i_2. \end{aligned}$$

Adding the equations for $\frac{di_1}{dt}$ and $\frac{di_2}{dt}$ together yields

$$\begin{aligned} L\frac{d}{dt}(i_1 + i_2) &= s_1 v_1 + s_2 v_2 - r(i_1 + i_2) - 2v_o \\ L\frac{di_t}{dt} &= s_1 v_1 + s_2 v_2 - r i_t - 2v_o \\ &= s_t v_t + s_d v_d - r i_t - 2v_o, \end{aligned}$$

since as shown above

$$s_t v_t + s_d v_d = s_1 v_1 + s_2 v_2.$$

Subtracting the equations for $\frac{di_1}{dt}$ and $\frac{di_2}{dt}$ yields

$$\begin{aligned} L\frac{d}{dt}(i_1 - i_2) &= s_1 v_1 - s_2 v_2 - r(i_1 - i_2) \\ L\frac{di_d}{dt} &= s_1 v_1 - s_2 v_2 - r i_d \\ &= s_d v_t + s_t v_d - r i_d, \end{aligned}$$

since as shown above

$$s_d v_t + s_t v_d = s_1 v_1 - s_2 v_2.$$

Rewriting the expression for $\frac{dv_o}{dt}$ yields:

$$\begin{aligned} C_o \frac{dv_o}{dt} &= i_1 + i_2 - \frac{v_o}{R} \\ &= i_t - \frac{v_o}{R} \end{aligned}$$

Combining yields (3.1.3), repeated below:

$$\frac{d}{dt}\begin{bmatrix} L_s \cdot i_{in} \\ C \cdot v_t \\ C \cdot v_d \\ L \cdot i_t \\ L \cdot i_d \\ C_o \cdot v_o \end{bmatrix} = \begin{bmatrix} -r_s & -1 & 0 & 0 & 0 & 0 \\ 2 & 0 & 0 & -s_t & -s_d & 0 \\ 0 & 0 & 0 & -s_d & -s_t & 0 \\ 0 & s_t & s_d & -r & 0 & -2 \\ 0 & s_d & s_t & 0 & -r & 0 \\ 0 & 0 & 0 & 1 & 0 & \frac{-1}{R} \end{bmatrix} \begin{bmatrix} i_{in} \\ v_t \\ v_d \\ i_t \\ i_d \\ v_o \end{bmatrix} + \begin{bmatrix} v_{in} \\ 0 \\ 0 \\ 0 \\ 0 \\ 0 \end{bmatrix}$$

A.5.2 Input-Series-Output-Series Converter

Equation (5.2.1) is repeated for convenience:

$$\frac{d}{dt}\begin{bmatrix} L_s \cdot i_{in} \\ C \cdot v_1 \\ C \cdot v_2 \\ L \cdot i_o \\ C_f \cdot v_o \end{bmatrix} = \begin{bmatrix} -r_s & -1 & -1 & 0 & 0 \\ 1 & 0 & 0 & -s_1 & 0 \\ 1 & 0 & 0 & -s_2 & 0 \\ 0 & s_1 & s_2 & -r & -1 \\ 0 & 0 & 0 & 1 & \frac{-1}{R} \end{bmatrix} \begin{bmatrix} i_{in} \\ v_1 \\ v_2 \\ i_o \\ v_o \end{bmatrix} + \begin{bmatrix} V_{in} \\ 0 \\ 0 \\ 0 \\ 0 \end{bmatrix}$$

The total and difference parameters are defined as:

$$\begin{aligned} s_d &= \frac{s_2 - s_1}{2} & s_t &= \frac{s_1 + s_2}{2} \\ v_d &= v_1 - v_2 & v_t &= v_1 + v_2 \end{aligned} \tag{A.5.1}$$

The equations for $\frac{di_{in}}{dt}$ can be rewritten as:

$$\begin{aligned} L_s \frac{di_{in}}{dt} &= -r_s i_{in} - (v_1 + v_2) + v_{in} \\ &= -r_s i_{in} - v_t + v_{in} \end{aligned}$$

Adding the equations for $\frac{dv_1}{dt}$ and $\frac{dv_2}{dt}$ together yields

$$\begin{aligned} C \frac{d}{dt}(v_1 + v_2) &= 2i_{in} - s_1 i_o - s_2 i_o \\ C \frac{dv_t}{dt} &= 2i_{in} - 2s_t i_o. \end{aligned}$$

Subtracting the equations for $\frac{dv_1}{dt}$ and $\frac{dv_2}{dt}$ yields

$$C\frac{d}{dt}(v_1 - v_2) = -s_1 i_o + s_2 i_o$$
$$C\frac{dv_d}{dt} = -s_d i_o - 2s_d i_d.$$

The expression for $\frac{di_o}{dt}$ can be rewritten (using a result from the ISOP d& t circuit development above) as

$$L\frac{di_o}{dt} = s_1 v_1 + s_2 v_2 - r i_o - v_o$$
$$= s_t v_t + s_d v_d - r i_o - v_o.$$

The expression for $\frac{dv_o}{dt}$ remains:

$$C_o\frac{dv_o}{dt} = i_o - \frac{v_o}{R}$$

Combining yields (5.2.2), repeated below:

$$\frac{d}{dt}\begin{bmatrix} L_s \cdot i_{in} \\ C \cdot v_t \\ C \cdot v_d \\ L \cdot i_o \\ C_f \cdot v_o \end{bmatrix} = \begin{bmatrix} -r_s & -1 & 0 & 0 & 0 \\ 2 & 0 & 0 & -2s_t & 0 \\ 0 & 0 & 0 & -2s_d & 0 \\ 0 & s_t & s_d & -r & -1 \\ 0 & 0 & 0 & 1 & \frac{-1}{R} \end{bmatrix} \begin{bmatrix} i_{in} \\ v_t \\ v_d \\ i_o \\ v_o \end{bmatrix} + \begin{bmatrix} v_{in} \\ 0 \\ 0 \\ 0 \\ 0 \end{bmatrix}$$

A.6 Fourier Series Calculations

A.6.1 Derivation of the Fourier Series Coefficients for the Interleaved Constant Duty Cycle Case

The exponential Fourier series expression of a function $f(t)$, periodic with f_s, is given by [48]:

$$f(t) = \sum_{n=-\infty}^{\infty} C_{(n)} e^{jn\omega_s t}$$
$$\text{where } C_{(n)} = \frac{1}{T_s}\int_{t_0}^{t_0+T_s} f(t) e^{-jn\omega_s t} dt$$

The Fourier series coefficients for a PWM switching function $s(t)$ can be calculated, with the following assumptions and definitions:

1. The switching frequency, f_s, is constant, with $\omega_s = 2\pi f_s$.
2. The switching period, T_s, is defined as $T_s = \frac{1}{f_s}$.
3. The switching function is generated through comparison of a PWM reference signal with a sawtooth carrier.

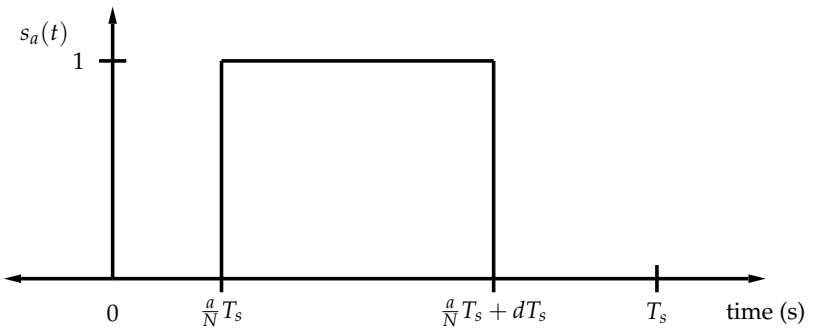

Figure A.1: Constant Duty Cycle Integration Interval

4. The duty cycle, d, is constant. d is also the average value of the switching function, where: $d = \frac{1}{T_s}\int_0^{T_s} s(t)dt$

5. The interleaving of switching functions are achieved through phase shifting of the sawtooth carriers.

6. The switching function evaluates to either 1 or 0, or equivalently $s(t) \in \{0, 1\}$.

Formally the PWM switching function for the reference cell is defined as:

$$f_c(t) = \frac{1}{\pi}\arctan(\tan(\frac{1}{2}\omega_s t)) + \frac{1}{2}$$
$$s(t) = \begin{cases} 1, \text{ for } d \geq f_c(t) \\ 0, \text{ for } d < f_c(t) \end{cases}$$

When the switching functions of a N-cell structure are interleaved the carrier is phase shifted with respect to the reference carrier. For the a^{th} switching function of a N-cell structure the PWM switching function is found by:

$$f_{ca}(t) = \frac{1}{\pi}\arctan(\tan(\frac{1}{2}\omega_s t + \frac{a}{N}\pi)) + \frac{1}{2}$$
$$s_a(t) = \begin{cases} 1, \text{ for } d \geq f_{ca}(t) \\ 0, \text{ for } d < f_{ca}(t) \end{cases}$$

The resulting function $s_a(t)$ is shown in Fig. A.1 for one switching period.

Using the integration interval as defined by Fig. A.1 the Fourier series coefficients can be found as:

$$\begin{aligned} C_{a(n)} &= \frac{1}{T_s}\int_{\frac{a}{N}T_s}^{\frac{a}{N}T_s + dT_s} e^{-jn\omega_s t}dt \\ &= \frac{j}{2\pi n}e^{-j2\pi n\frac{a}{N}}\left(e^{-j2\pi nd} - 1\right) \\ &= \Psi(n)e^{-j2\pi n\frac{a}{N}} \\ &= \Psi(n)\zeta_n^a \end{aligned}$$

The basic building block $\Psi(n)$ is defined as:

$$\Psi(n) = \begin{cases} \frac{j}{2\pi n}\left(e^{-j2\pi nd} - 1\right) & \text{for } n \neq 0 \\ d & \text{for } n = 0 \end{cases}$$

The function ζ_n^a is used to denote the sequence of de Moivre numbers or the N square roots of -1. Although the notation does not specifically make allowance for variations in N, the switching functions are typically calculated for a specific structure with the value of N implicit in the definition of ζ_n^a. Formally:

$$\zeta_n^a = e^{-j2\pi n\frac{a}{N}} \tag{A.6.1}$$

A.6.2 Derivation of the Fourier Series Coefficients for the Interleaved Constant Duty Cycle Case: Flying Capacitor Converter

Let the switching PWM function be created through comparison of the reference signal f_r and a triangle carrier signal with frequency ω_c. A triangular carrier is used in lieu of a sawtooth carrier since the triangular carrier results in lower harmonic distortion at the output voltage, especially in three phase inverters [5].

For the FCC the switching functions have a value of either -1 or 1 and are derived in the following manner:

$$\begin{aligned} f_r &= 2d - 1 \\ f_c &= \frac{2}{\pi}\arcsin(\sin(\omega_c + \theta_c)) \\ s(t) &= \begin{cases} 1, \text{ for } f_r \geq f_c(t) \\ -1, \text{ for } f_r < f_c(t) \end{cases} \end{aligned}$$

The reference switching signal, $s_0(t)$ will be considered. The other switching functions can be recreated through the use of the time shift theorem. The resulting function $s_0(t)$, with $\theta_c = \frac{\pi}{2}$ is shown in Fig. A.2 for one switching period.

The Fourier series coefficients for the PWM switching function $s_0(t)$ is calculated, with the following assumptions and definitions:

1. The switching frequency, f_s, is constant, with $\omega_s = 2\pi f_s$.
2. The switching period, T_s, is defined as $T_s = \frac{1}{f_s}$.
3. The switching function is generated through comparison of a PWM reference signal with a triangular carrier.
4. The duty cycle, d, is constant.
5. The interleaving of switching functions are achieved through phase shifting of the carriers.
6. The switching function evaluates to either 1 or -1, or equivalently $s(t) \in \{-1, 1\}$.

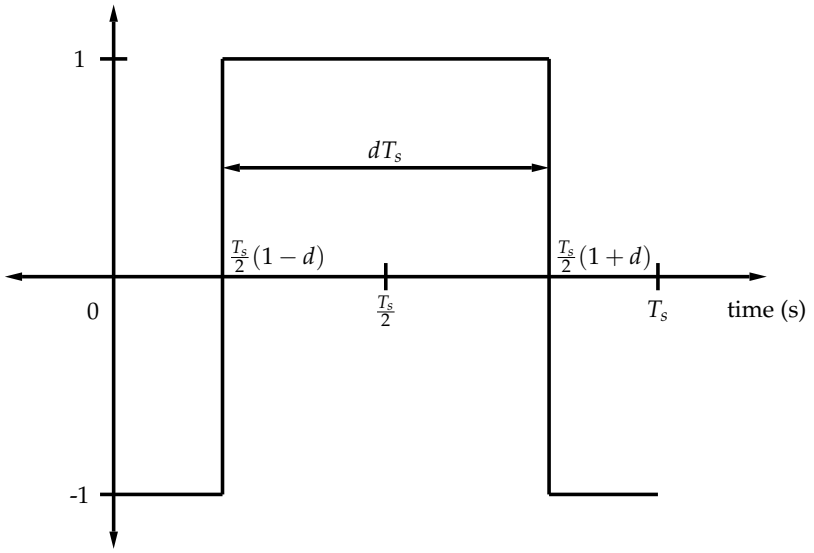

Figure A.2: Constant duty cycle integration interval, FCC

The exponential Fourier series expression of a periodic function $f(t)$is given by [48]:

$$f(t) = \sum_{n=-\infty}^{\infty} C_{(n)} e^{jn\omega_s t}$$
$$\text{where } C_{(n)} = \frac{1}{T_s} \int_{t_0}^{t_0+T_s} f(t) e^{-jn\omega_s t} dt$$

Using the integration interval as defined by Fig. A.2 the Fourier series coefficients can be found as, for $n \neq 0$:

$$\begin{aligned}
C_{0(n)} &= \frac{1}{T_s}\left(-\int_0^{\frac{T_s}{2}(1-d)} e^{-jn\omega_s t}dt + \int_{\frac{T_s}{2}(1-d)}^{\frac{T_s}{2}(1+d)} e^{-jn\omega_s t}dt - \int_{\frac{T_s}{2}(1+d)}^{T_s} e^{-jn\omega_s t}dt\right) \\
&= \frac{j}{2\pi n}\left(-e^{-j\pi n(1-d)} + 1 + e^{-j\pi n(1+d)} - e^{-j\pi n(1-d)} - e^{-j2\pi n} + e^{-j\pi n(1+d)}\right) \\
&= \frac{j}{\pi n} e^{-j\pi n}\left(e^{-j\pi nd} + e^{j\pi nd}\right) \\
&= \frac{2(-1)^n}{\pi n}\sin(\pi nd) \\
&= \Psi(n)
\end{aligned}$$

For simplicity the reference signal is shifted by 180° by choosing $\theta_s = -\frac{\pi}{2}$. With implementation of the time shift theorem the Fourier coefficients are multiplied by $(-1)^n$ and the Fourier coefficients, $\Psi(n)$, becomes:

$$\Psi(n) = \begin{cases} \frac{2}{\pi n}\sin(\pi nd) & \text{for } n \neq 0 \\ 2d - 1 & \text{for } n = 0 \end{cases}$$

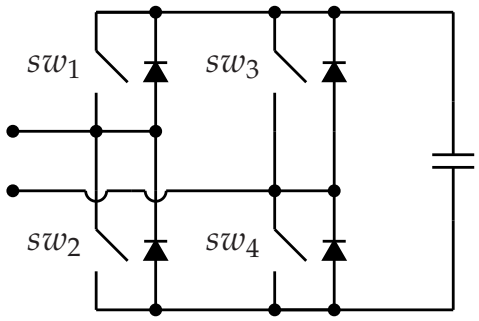

Figure A.3: General full bridge converter circuit

A.6.3 Derivation of the Fourier Series Coefficients for the Unipolar Switched Full-Bridge, Constant Duty Cycle Case

For unipolar switching the switching signals are created by comparing both the reference function f_r and its negative $-f_r$ to a triangular carrier, f_c. Let the carrier be given as:

$$f_c = \arcsin(\sin(2\pi f_s t - \frac{\pi}{2}))$$

With reference to the switch assignments indicated in Fig. A.3 the switches in each leg, consisting of sw_1 and sw_2 (leg 1) and sw_3 and sw_4 (leg 2) are switched as complimentary pairs. The mapping of the switching function $s(t)$ describing the circuit operation to the switch states are indicated in Table A.1. Let the switching function of each leg be equal to 1 when the top switch is on and 0 when the bottom switch is on. The carrier and reference function, switching function of both legs and $s(t)$ are shown in Fig. A.4 for f_r = 0.5.

Table A.1: Map of the Switch States to $s(t)$

Switches on	$s(t)$	Condition
sw_1, sw_3	0	$f_r > f_c$ and $-f_r > f_c$
sw_1, sw_4	1	$f_r > f_c$ and $-f_r < f_c$
sw_2, sw_3	-1	$f_r < f_c$ and $-f_r > f_c$
sw_2, sw_4	0	$f_r < f_c$ and $-f_r < f_c$

A.6.3.1 Fourier Coefficients of Leg 1

Using the definitions of Fig. A.4 the coefficients for leg 1 can be calculated as, for $n \neq 0$:

$$\begin{aligned} C_{leg1(n)} &= \frac{1}{T_s}\left(\int_0^{\frac{1+f_r}{4T_s}} e^{-jn\omega_s t}dt + \int_{\frac{3-f_r}{4T_s}}^{T_s} e^{-jn\omega_s t}dt\right) \\ &= \frac{j}{2\pi n}\left(e^{-j2\pi n\frac{1+f_r}{4}} - e^{-j2\pi n\frac{3-f_r}{4}}\right) \end{aligned}$$

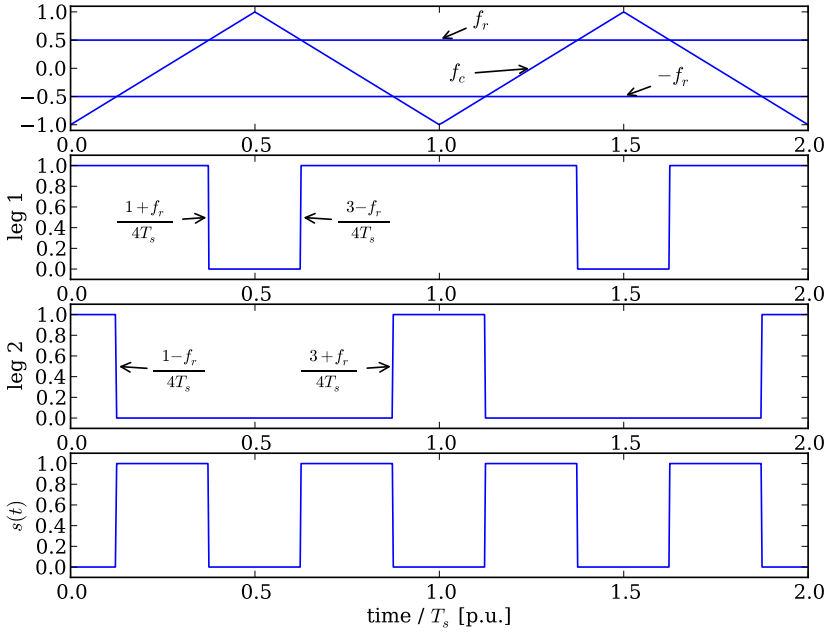

Figure A.4: Creation of the switching signals: unipolar switching

For $n = 0$:

$$C_{leg1(0)} = \frac{1}{T_s}\left(\int_0^{\frac{1+f_r}{4T_s}} 1dt + \int_{\frac{3-f_r}{4T_s}}^{T_s} 1dt\right)$$
$$= \frac{1+f_r}{2}$$

A.6.3.2 Fourier Coefficients of Leg 2

Again, using the definitions of Fig. A.4 the coefficients for leg 2 can be calculated as, for $n \neq 0$:

$$C_{leg2(n)} = \frac{1}{T_s}\left(\int_0^{\frac{1-f_r}{4T_s}} e^{-jn\omega_s t}dt + \int_{\frac{3+f_r}{4T_s}}^{T_s} e^{-jn\omega_s t}dt\right)$$
$$= \frac{j}{2\pi n}\left(e^{-j2\pi n\frac{1-f_r}{4}} - e^{-j2\pi n\frac{3+f_r}{4}}\right)$$

For $n = 0$:

$$C_{leg1(0)} = \frac{1}{T_s}\left(\int_0^{\frac{1-f_r}{4T_s}} 1dt + \int_{\frac{3+f_r}{4T_s}}^{T_s} 1dt\right)$$
$$= \frac{1-f_r}{2}$$

A.6.3.3 Fourier Coefficients of the Complete Converter

The switching function $s(t)$ can be found by:

$$s(t) = s_{leg1}(t) - s_{leg2}(t)$$

When $n \neq 0$:

$$\begin{aligned}
S_{(n)} &= \frac{j}{2\pi n}\left(e^{-j2\pi n\frac{1+f_r}{4}} - e^{-j2\pi n\frac{3-f_r}{4}} - e^{-j2\pi n\frac{1-f_r}{4}} + e^{-j2\pi n\frac{3+f_r}{4}}\right) \\
&= \frac{j}{2\pi n}\left(e^{-j\pi\frac{n}{2}}e^{-j\pi n\frac{f_r}{2}} - e^{-j\pi n\frac{3}{2}}e^{j\pi n\frac{f_r}{2}} - e^{-j\pi\frac{n}{2}}e^{j\pi n\frac{f_r}{2}} + e^{-j\pi n\frac{3}{2}}e^{-j\pi n\frac{f_r}{2}}\right) \\
&= \frac{j}{2\pi n}\left(e^{-j\pi n\frac{f_r}{2}}\left\{e^{-j\pi\frac{n}{2}} + e^{j\pi\frac{n}{2}}\right\} - e^{j\pi n\frac{f_r}{2}}\left\{e^{j\pi\frac{n}{2}} + e^{-j\pi\frac{n}{2}}\right\}\right) \\
&= \frac{j}{\pi n}Re\left\{j^n\right\}\left(e^{-j\pi n\frac{f_r}{2}} - e^{j\pi n\frac{f_r}{2}}\right) \\
&= \frac{2}{\pi n}Re\left\{j^n\right\}\sin(\pi n\frac{f_r}{2})
\end{aligned}$$

When $n = 0$:

$$\begin{aligned}
S_{(0)} &= \frac{1+f_r}{2} - \frac{1-f_r}{2} \\
&= f_r
\end{aligned}$$

Since $Re\left\{j^n\right\} = 0$ for all uneven values of n, the substitution $n = 2m$ can be made to yield the following expression for $s(t)$:

$$s(t) = \sum_{m=-\infty}^{\infty} S_{(m)}e^{j2m\omega_s t} \tag{A.6.2}$$

$$S_{(m)} = \Psi(m) \tag{A.6.3}$$

$$\Psi(m) = \begin{cases} \frac{1}{\pi m}\sin(m\pi f_r) & \text{for } m \neq 0 \\ f_r & \text{for } m = 0, \end{cases} \tag{A.6.4}$$

A.6.4 Derivation of the Fourier Series Coefficients for the Interleaved Modulated Duty Cycle Case, for the FCC

Let the switching PWM function be created through comparison of the reference signal f_r and a triangle carrier signal with frequency ω_c. A triangular carrier is used in lieu of a sawtooth carrier since the triangular carrier results in lower harmonic distortion at the output voltage, especially in three phase inverters [5].

For the FCC the switching functions have a value of either -1 or 1 and are derived in the following manner:

$$\begin{aligned}
f_r &= m_a\sin(\omega_r t + \theta_r) \\
f_c &= \frac{2}{\pi}\arcsin(\sin(\omega_c + \theta_c)) \\
s(t) &= \begin{cases} 1, \text{ for } f_r \geq f_c(t) \\ -1, \text{ for } f_r < f_c(t) \end{cases}
\end{aligned}$$

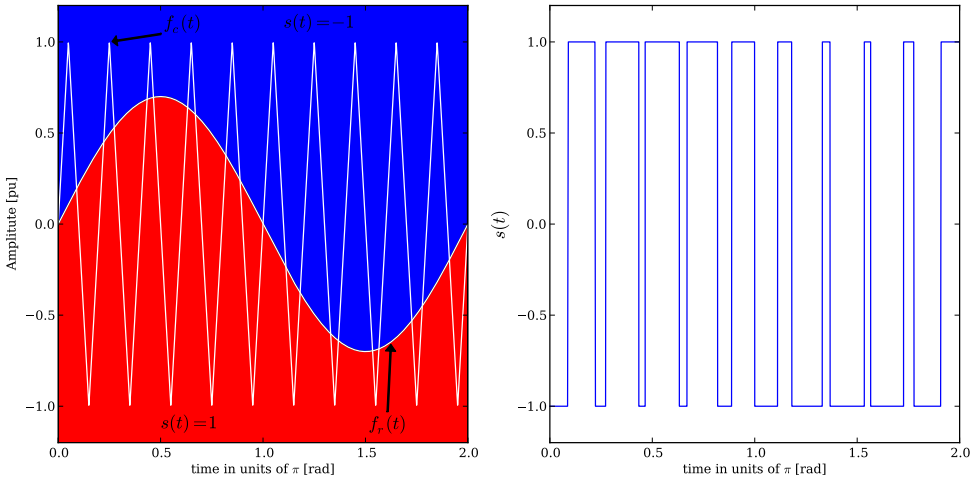

Figure A.5: Generation of a modulated PWM signal

The process is illustrated in Fig.A.5.

Using the double Fourier series expression, in exponential form, as described in more detail in [5], the switching function s_1 can be expressed as, with the following definitions; $x(t) = \omega_r t + \theta_r$ and $y(t) = \omega_c t + \theta_c$:

$$s(t) = \sum_{k=-\infty}^{\infty} \sum_{m=-\infty}^{\infty} \tilde{S}_{km} e^{j(kx+my)} \tag{A.6.5}$$

where

$$\tilde{S}_{km} = \frac{1}{4\pi^2} \int_{-\pi}^{\pi} \int_{-\pi}^{\pi} F(x,y) e^{-j(kx+my)} dxdy.$$

The unit-cell integration area can be created as discussed in detail in [5; 28; 33] among others, and is indicated in Fig. A.6. The coefficients must be calculated for two cases: viz. when $m = 0$ and $m \neq 0$.

- Case 1: $m = 0$

  When $m = 0$ the expression for $\tilde{S}_{km}$ can be rewritten as:

  $$\tilde{S}_{k0} = \frac{1}{4\pi^2} \int_{-\pi}^{\pi} \int_{-\pi}^{\pi} F(x,y) e^{-jkx} dydx$$

  Integrating over intervals, through the unit cell, yields:

  $$\tilde{S}_{k0} = \frac{1}{4\pi^2} \int_{-\pi}^{\pi} \left(\int_{-\pi}^{-\frac{\pi}{2}(1-m_a \sin(x))} e^{-jkx} dy - \int_{-\frac{\pi}{2}(1-m_a \sin(x))}^{\frac{\pi}{2}(1-m_a \sin(x))} e^{-jkx} dy + \int_{\frac{\pi}{2}(1-m_a \sin(x))}^{\pi} e^{-jkx} dy \right) dx$$

  or

  $$\tilde{S}_{k0} = \frac{1}{4\pi^2} \int_{-\pi}^{\pi} \alpha + \beta + \delta \, dx$$

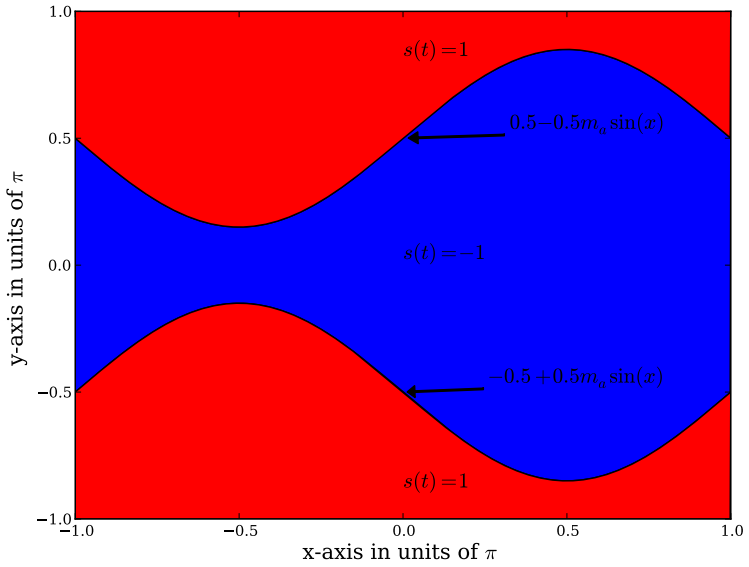

Figure A.6: Unit cell for modulated PWM

where

$$\begin{aligned}\alpha &= \int_{-\pi}^{-\frac{\pi}{2}(1-m_a\sin(x))} e^{-jkx}dy \\ &= e^{-jkx}\left(-\frac{\pi}{2}(1-m_a\sin(x))+\pi\right),\end{aligned}$$

$$\begin{aligned}\beta &= -\int_{-\frac{\pi}{2}(1-m_a\sin(x))}^{\frac{\pi}{2}(1-m_a\sin(x))} e^{-jkx}dy \\ &= -e^{-jkx}\left(\frac{\pi}{2}(1-m_a\sin(x))+\frac{\pi}{2}(1-m_a\sin(x))\right) \\ &= -e^{-jkx}\pi(1-m_a\sin(x))\end{aligned}$$

and

$$\begin{aligned}\delta &= \int_{\frac{\pi}{2}(1-m_a\sin(x))}^{\pi} e^{-jkx}dy \\ &= e^{-jkx}\left(\pi-\frac{\pi}{2}(1-m_a\sin(x))\right).\end{aligned}$$

Expanding;

$$\begin{aligned}\alpha+\beta+\delta &= e^{-jkx}\left(-\frac{\pi}{2}(1-m_a\sin(x))+\pi-\pi(1-m_a\sin(x))+\pi-\frac{\pi}{2}(1-m_a\sin(x))\right) \\ &= e^{-jkx}\left(-2\pi(1-m_a\sin(x))+2\pi\right) \\ &= 2\pi e^{-jkx}m_a\sin(x)\end{aligned}$$

and substituting into the expression for $\tilde{C}_{k0}$:

$$\begin{aligned}\tilde{S}_{k0} &= \frac{1}{4\pi^2}\int_{-\pi}^{\pi} \alpha + \beta + \delta \; dx \\ &= \frac{1}{2\pi}\int_{-\pi}^{\pi} e^{-jkx} m_a \sin(x) dx\end{aligned}$$

When $k = 0$:

$$\begin{aligned}\tilde{S}_{00} &= \frac{1}{2\pi}\int_{-\pi}^{\pi} m_a \sin(x) dx \\ &= 0\end{aligned}$$

When $k \neq 0$, and using Euler's identity:

$$\begin{aligned}\tilde{S}_{k0} &= \frac{1}{2\pi}\int_{-\pi}^{\pi} e^{-jkx}\frac{m_a}{2j}(e^{jx} - e^{-jx}) dx \\ &= \frac{m_a}{j4\pi}\int_{-\pi}^{\pi} e^{-jkx}(e^{jx} - e^{-jx}) dx \\ &= \frac{m_a}{j4\pi}\int_{-\pi}^{\pi} e^{-jx(k-1)} - e^{-jx(k+1)} dx\end{aligned}$$

Since $\int_{-\pi}^{\pi} e^{-j\alpha x} dx = 0$ for all nonzero values of α, only 2 cases remain, namely:

1. $k = -1$

$$\begin{aligned}\tilde{S}_{(-1)0} &= \frac{m_a}{j4\pi}\int_{-\pi}^{\pi} -1 dx \\ &= \frac{-1}{j2} m_a\end{aligned}$$

2. $k = 1$

$$\begin{aligned}\tilde{S}_{(1)0} &= \frac{m_a}{4j\pi}\int_{-\pi}^{\pi} dx \\ &= \frac{1}{j2} m_a\end{aligned}$$

- Case 2: $k \neq 0$

  Using the integration unit cell the integral can be rewritten with integration limits as:

$$\begin{aligned}\tilde{S}_{km} = \frac{1}{4\pi^2}\int_{-\pi}^{\pi} \Bigg(&\int_{-\pi}^{-\frac{\pi}{2}(1-m_a\sin(x))} e^{-j(kx+my)} dy - \int_{-\frac{\pi}{2}(1-m_a\sin(x))}^{\frac{\pi}{2}(1-m_a\sin(x))} e^{-j(kx+my)} dy \\ &+ \int_{\frac{\pi}{2}(1-m_a\sin(x))}^{\pi} e^{-j(kx+my)} dy \Bigg) dx\end{aligned}$$

  or

$$\tilde{S}_{km} = \frac{1}{4\pi^2}\int_{-\pi}^{\pi} \alpha + \beta + \delta \; dx$$

where

$$\begin{aligned}\alpha &= \int_{-\pi}^{-\frac{\pi}{2}(1-m_a\sin(x)} e^{-j(kx+my)}dy \\ &= \frac{e^{-jkx+\frac{1}{2}j\pi m(1-m_a\sin(x))}}{-jm} - \frac{e^{j\pi m-jkx}}{-jm} \\ &= \frac{je^{-jkx}}{m}\left(e^{\frac{1}{2}j\pi m(1-m_a\sin(x))} - e^{j\pi m}\right),\end{aligned}$$

$$\begin{aligned}\beta &= -\int_{-\frac{\pi}{2}(1-m_a\sin(x))}^{\frac{\pi}{2}(1-m_a\sin(x))} e^{-j(kx+my)}dy \\ &= -\frac{e^{-jkx-\frac{1}{2}j\pi m(1-m_a\sin(x))}}{-jm} + \frac{e^{-jkx+\frac{1}{2}j\pi m(1-m_a\sin(x))}}{-jm} \\ &= \frac{je^{-jkx}}{m}\left(e^{\frac{1}{2}j\pi m(1-m_a\sin(x))} - e^{-\frac{1}{2}j\pi m(1-m_a\sin(x))}\right)\end{aligned}$$

and

$$\begin{aligned}\delta &= \int_{\frac{\pi}{2}(1-m_a\sin(x))}^{\pi} e^{-j(kx+my)}dy \\ &= \frac{e^{-j\pi m-jkx}}{-jm} - \frac{e^{-jkx-\frac{1}{2}j\pi m(1-m_a\sin(x))}}{-jm} \\ &= \frac{je^{-jkx}}{m}\left(e^{-j\pi m} - e^{-\frac{1}{2}j\pi m(1-m_a\sin(x))}\right).\end{aligned}$$

Expanding;

$$\begin{aligned}\alpha+\beta+\delta &= \frac{je^{-jkx}}{m}\left(-e^{j\pi m} + e^{-j\pi m} + 2e^{\frac{1}{2}j\pi m(1-m_a\sin(x))} - 2e^{-\frac{1}{2}j\pi m(1-m_a\sin(x))}\right) \\ &= \frac{j2e^{-jkx}}{m}\left(e^{\frac{1}{2}j\pi m(1-m_a\sin(x))} - e^{-\frac{1}{2}j\pi m(1-m_a\sin(x))}\right) \\ &= \frac{j2}{m}\left(e^{-jkx}e^{\frac{1}{2}j\pi m}e^{-\frac{1}{2}j\pi m m_a\sin(x)} - e^{-jkx}e^{-j\frac{1}{2}\pi m}e^{\frac{1}{2}j\pi m m_a\sin(x)}\right)\end{aligned}$$

and substituting into the expression for $\tilde{S}_{km}$:

$$\begin{aligned}\tilde{S}_{km} &= \frac{1}{4\pi^2}\int_{-\pi}^{\pi} \alpha+\beta+\delta\, dx \\ &= \frac{j}{2\pi^2 m}\int_{-\pi}^{\pi} e^{-jkx}e^{\frac{1}{2}j\pi m}e^{-\frac{1}{2}j\pi m m_a\sin(x)} - e^{-jkx}e^{-j\frac{1}{2}\pi m}e^{\frac{1}{2}j\pi m m_a\sin(x)}dx\end{aligned}$$

The integral can be solved using Bessel functions of the first kind, defined in integral form as [5]:

$$2\pi J_n(x) = \int_{-\pi}^{\pi} e^{-jn\tau+jx\sin(\tau)}d\tau$$

Therefore, using the Bessel functions:

$$\tilde{S}_{km} = \frac{j}{\pi m}\left(e^{\frac{1}{2}j\pi m}J_k(-\frac{1}{2}\pi m m_a) - e^{-j\frac{1}{2}\pi m}J_k(\frac{1}{2}\pi m m_a)\right)$$

Using the identity that [5]

$$J_n(-x) = (-1)^n J_n(x),$$

the expression for $\tilde{S}_{km}$ can be rewritten as:

$$\tilde{S}_{km} = \frac{j}{\pi m} J_k(\frac{1}{2}\pi m m_a) \left((-1)^k e^{\frac{1}{2}j\pi m} - e^{-j\frac{1}{2}\pi m}\right)$$

Setting the derived $\tilde{S}_{km} = \tilde{\Psi}(k,m)$ the modulated duty cycle builder $\tilde{\Psi}(k,m)$ can be expressed as:

$$\tilde{\Psi}(k,m) = \begin{cases} \frac{-1}{j2} m_a & \text{when } m = 0, k = -1 \\ \frac{1}{j2} m_a & \text{when } m = 0, k = 1 \\ 0 & \text{when } m = 0, |k| \neq 1 \\ \frac{j}{\pi m} J_k(\frac{1}{2}\pi m m_a) \left((-1)^k e^{\frac{1}{2}j\pi m} - e^{-j\frac{1}{2}\pi m}\right) & \text{when } m \neq 0 \end{cases} \tag{A.6.6}$$

Using the coefficients the switching function can be reconstructed using the double Fourier series (A.6.5):

$$s(t) = \sum_{k=-\infty}^{\infty} \sum_{m=-\infty}^{\infty} \tilde{\Psi}(k,m) e^{j(kx+my)}$$

When the switching functions of a N-cell structure are interleaved the a^{th} carrier signal is shifted with respect to the reference by $\theta_c = \frac{2\pi a}{N}$. Substituting for x and y:

$$\begin{aligned} s_a(t) &= \sum_{k=-\infty}^{\infty} \sum_{m=-\infty}^{\infty} \tilde{\Psi}(k,m) e^{j(k(\omega_r t+\theta_r)+m(\omega_c t+\theta_c))} \\ &= \sum_{k=-\infty}^{\infty} \sum_{m=-\infty}^{\infty} \tilde{\Psi}(k,m) e^{jk\omega_r t} e^{jm\omega_c t} e^{jk\theta_r} e^{jm\theta_c} \\ &= \sum_{k=-\infty}^{\infty} \sum_{m=-\infty}^{\infty} \tilde{\Psi}(k,m) e^{jk\omega_r t} e^{jm\omega_c t} e^{jk\theta_r} \zeta_m^a \end{aligned} \tag{A.6.7}$$

where

$$\zeta_m^a = e^{j2\pi a m/N}. \tag{A.6.8}$$

A.6.5 Derivation of the Fourier Series Coefficients for the Interleaved Modulated Duty Cycle Case, Unipolar Switched Full-Bridge Converter

Let the switching PWM function be created through comparison of the reference signal f_r and a triangle carrier signal with frequency ω_c, as shown in Fig. A.7.

With reference to the switch assignments indicated in Fig. A.3 the switches in each leg, consisting of sw_1 and sw_2 (leg 1) and sw_3 and sw_4 (leg 2) are switched as complimentary pairs. The mapping of the switching function $s(t)$ describing the circuit operation to the switch states are indicated in Table A.2. Let the switching function of each leg be equal to 1 when the top switch is on and 0 when the bottom switch is on. The carrier and reference function, switching function of both legs and $s(t)$ are shown in Fig. A.4 for f_r = 0.5.

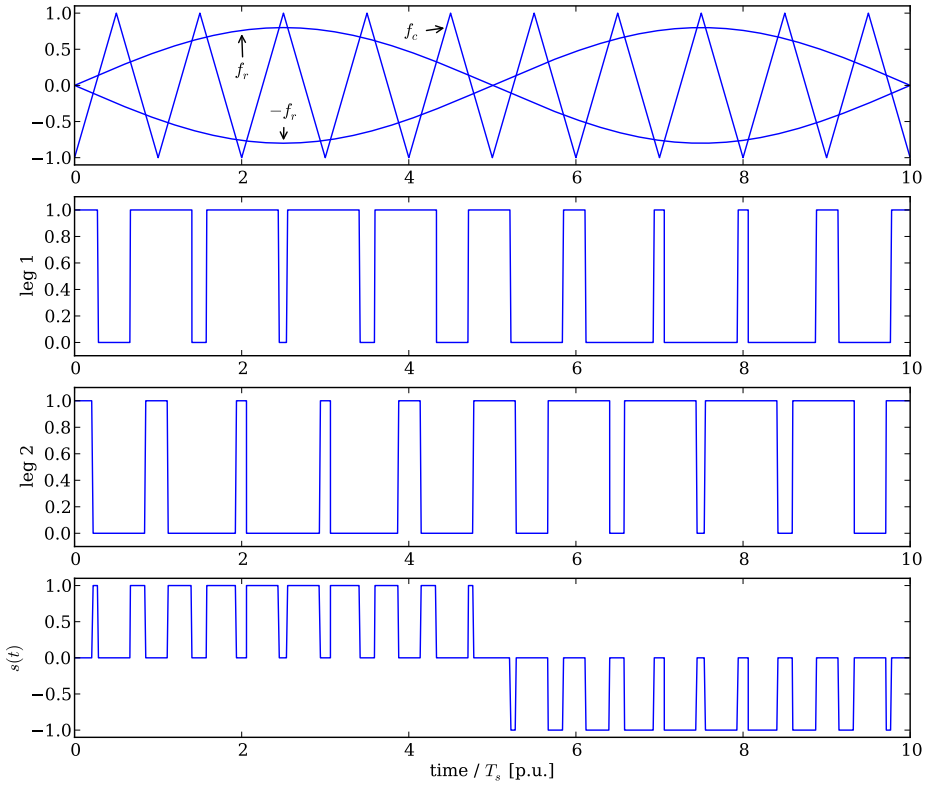

Figure A.7: Generation of a the unipolar switching signals

Table A.2: Map of the Switch States to $s(t)$

Switches on	$s(t)$	Condition
sw_1, sw_3	0	$f_r > f_c$ and $-f_r > f_c$
sw_1, sw_4	1	$f_r > f_c$ and $-f_r < f_c$
sw_2, sw_3	-1	$f_r < f_c$ and $-f_r > f_c$
sw_2, sw_4	0	$f_r < f_c$ and $-f_r < f_c$

A.6.5.1 Fourier Series Coefficients of Leg 1

Using the double Fourier series expression, in exponential form, as described in more detail in [5], the switching function s_1 for leg 1 can be expressed as, with the following definitions; $x(t) = \omega_r t + \theta_r$ and $y(t) = \omega_c t + \theta_c$:

$$s(t) = \sum_{k=-\infty}^{\infty} \sum_{m=-\infty}^{\infty} \tilde{S}_{km} e^{j(kx+my)} \tag{A.6.9}$$

where

$$\tilde{S}_{km} = \frac{1}{4\pi^2} \int_{-\pi}^{\pi} \int_{-\pi}^{\pi} F(x,y) e^{-j(kx+my)} dx dy.$$

The unit-cell integration area can be created as discussed in detail in [5; 28; 33] among others, and is indicated in Fig. A.8. The coefficients must be calculated for

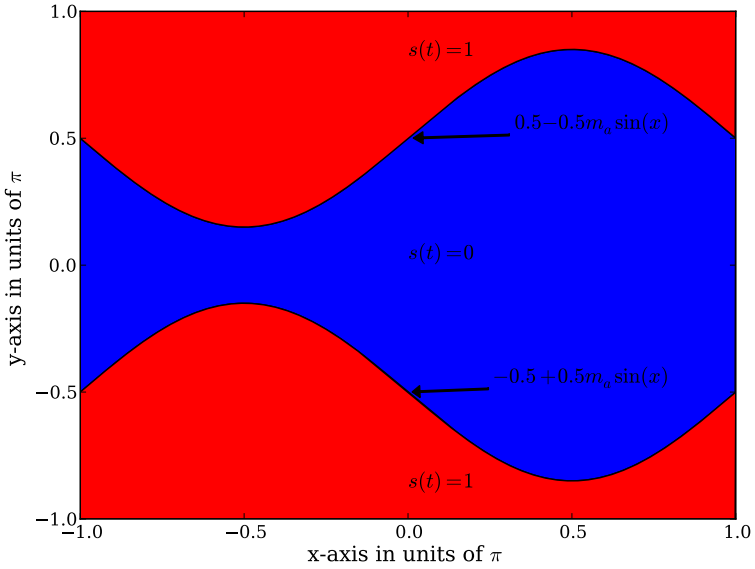

Figure A.8: Unit cell for unipolar switched PWM, leg 1

two cases: viz. when $m = 0$ and $m \neq 0$.

- Case 1: $m = 0$

  When $m = 0$ the expression for $\tilde{S}_{leg1(k,m)}$ can be rewritten as:

$$\tilde{S}_{leg1(k,0)} = \frac{1}{4\pi^2} \int_{-\pi}^{\pi} \int_{-\pi}^{\pi} F(x,y) e^{-jkx} dy dx$$

  Integrating over intervals, through the unit cell, yields:

$$\tilde{S}_{leg1(k,0)} = \frac{1}{4\pi^2} \int_{-\pi}^{\pi} \left(\int_{-\pi}^{-\frac{\pi}{2}(1-m_a \sin(x))} e^{-jkx} dy + \int_{\frac{\pi}{2}(1-m_a \sin(x))}^{\pi} e^{-jkx} dy \right) dx$$

  or

$$\tilde{S}_{leg1(k,0)} = \frac{1}{4\pi^2} \int_{-\pi}^{\pi} \alpha + \beta \, dx$$

  where

$$\begin{aligned} \alpha &= \int_{-\pi}^{-\frac{\pi}{2}(1-m_a \sin(x))} e^{-jkx} dy \\ &= e^{-jkx} \left(-\frac{\pi}{2}(1 - m_a \sin(x)) + \pi \right), \end{aligned}$$

$$\begin{aligned} \beta &= \int_{\frac{\pi}{2}(1-m_a \sin(x))}^{\pi} e^{-jkx} dy \\ &= e^{-jkx} \left(\pi - \frac{\pi}{2}(1 - m_a \sin(x)) \right). \end{aligned}$$

Expanding;

$$\begin{aligned}\alpha+\beta &= e^{-jkx}\left(-\frac{\pi}{2}(1-m_a\sin(x))+\pi+\pi-\frac{\pi}{2}(1-m_a\sin(x))\right)\\ &= \pi e^{-jkx}\big(1+m_a\sin(x)\big)\end{aligned}$$

and substituting into the expression for $\tilde{S}_{leg1(k,m)}$:

$$\begin{aligned}\tilde{S}_{leg1(k,0)} &= \frac{1}{4\pi^2}\int_{-\pi}^{\pi}\alpha+\beta\,dx\\ &= \frac{1}{4\pi}\int_{-\pi}^{\pi}e^{-jkx}\big(1+m_a\sin(x)\big)dx\end{aligned}$$

When $k=0$:

$$\begin{aligned}\tilde{S}_{leg1(0,0)} &= \frac{1}{4\pi}\int_{-\pi}^{\pi}\big(1+m_a\sin(x)\big)dx\\ &= \frac{1}{2}\end{aligned}$$

When $k\neq 0$, and using Euler's identity:

$$\begin{aligned}\tilde{S}_{leg1(k,0)} &= \frac{1}{4\pi}\int_{-\pi}^{\pi}e^{-jkx}+e^{-jkx}\frac{m_a}{2j}(e^{jx}-e^{-jx})dx\\ &= \frac{m_a}{j8\pi}\int_{-\pi}^{\pi}\frac{2j}{m_a}e^{-jkx}+e^{-jx(k-1)}-e^{-jx(k+1)}dx\end{aligned}$$

Since $\int_{-\pi}^{\pi}e^{-j\alpha x}dx=0$ for all nonzero values of α, only 2 cases remain, namely:

1. $k=-1$

$$\begin{aligned}\tilde{S}_{leg1(-1,0)} &= \frac{m_a}{j8\pi}\int_{-\pi}^{\pi}-1dx\\ &= \frac{-1}{j4}m_a\end{aligned}$$

2. $k=1$

$$\begin{aligned}\tilde{S}_{leg1(1,0)} &= \frac{m_a}{8j\pi}\int_{-\pi}^{\pi}1dx\\ &= \frac{1}{j4}m_a\end{aligned}$$

- Case 2: $k\neq 0$

  Using the integration unit cell the integral can be rewritten with integration limits as:

$$\tilde{S}_{leg1(k,m)}=\frac{1}{4\pi^2}\int_{-\pi}^{\pi}\left(\int_{-\pi}^{-\frac{\pi}{2}(1-m_a\sin(x))}e^{-j(kx+my)}dy+\int_{\frac{\pi}{2}(1-m_a\sin(x))}^{\pi}e^{-j(kx+my)}dy\right)dx$$

  or

$$\tilde{S}_{leg1(k,m)}=\frac{1}{4\pi^2}\int_{-\pi}^{\pi}\alpha+\beta\,dx$$

where

$$\begin{aligned}\alpha &= \int_{-\pi}^{-\frac{\pi}{2}(1-m_a\sin(x)} e^{-j(kx+my)}dy \\ &= \frac{e^{-jkx+\frac{1}{2}j\pi m(1-m_a\sin(x))}}{-jm} - \frac{e^{j\pi m-jkx}}{-jm} \\ &= \frac{je^{-jkx}}{m}\left(e^{\frac{1}{2}j\pi m(1-m_a\sin(x))} - e^{j\pi m}\right),\end{aligned}$$

$$\begin{aligned}\beta &= \int_{\frac{\pi}{2}(1-m_a\sin(x))}^{\pi} e^{-j(kx+my)}dy \\ &= \frac{e^{-j\pi m-jkx}}{-jm} - \frac{e^{-jkx-\frac{1}{2}j\pi m(1-m_a\sin(x))}}{-jm} \\ &= \frac{je^{-jkx}}{m}\left(e^{-j\pi m} - e^{-\frac{1}{2}j\pi m(1-m_a\sin(x))}\right).\end{aligned}$$

Expanding;

$$\begin{aligned}\alpha+\beta &= \frac{je^{-jkx}}{m}\left(-e^{j\pi m} + e^{-j\pi m} + e^{\frac{1}{2}j\pi m(1-m_a\sin(x))} - e^{-\frac{1}{2}j\pi m(1-m_a\sin(x))}\right) \\ &= \frac{je^{-jkx}}{m}\left(e^{\frac{1}{2}j\pi m(1-m_a\sin(x))} - e^{-\frac{1}{2}j\pi m(1-m_a\sin(x))}\right) \\ &= \frac{j}{m}\left(e^{-jkx}e^{\frac{1}{2}j\pi m}e^{-\frac{1}{2}j\pi mm_a\sin(x)} - e^{-jkx}e^{-j\frac{1}{2}\pi m}e^{\frac{1}{2}j\pi mm_a\sin(x)}\right)\end{aligned}$$

and substituting into the expression for $\tilde{S}_{km}$:

$$\begin{aligned}\tilde{S}_{leg1(k,m)} &= \frac{1}{4\pi^2}\int_{-\pi}^{\pi}\alpha+\beta\,dx \\ &= \frac{j}{4\pi^2 m}\int_{-\pi}^{\pi} e^{-jkx}e^{\frac{1}{2}j\pi m}e^{-\frac{1}{2}j\pi mm_a\sin(x)} - e^{-jkx}e^{-j\frac{1}{2}\pi m}e^{\frac{1}{2}j\pi mm_a\sin(x)}dx\end{aligned}$$

The integral can be solved using Bessel functions of the first kind, defined in integral form as [5]:

$$2\pi J_n(x) = \int_{-\pi}^{\pi} e^{-jn\tau+jx\sin(\tau)}d\tau$$

Therefore, using the Bessel functions:

$$\tilde{S}_{leg1(k,m)} = \frac{j}{2\pi m}\left(e^{\frac{1}{2}j\pi m}J_k(-\frac{1}{2}\pi mm_a) - e^{-j\frac{1}{2}\pi m}J_k(\frac{1}{2}\pi mm_a)\right)$$

Using the identity that [5]

$$J_n(-x) = (-1)^n J_n(x),$$

the expression for $\tilde{S}_{leg1(k,m)}$ can be rewritten as:

$$\tilde{S}_{leg1(k,m)} = \frac{j}{2\pi m}J_k(\frac{1}{2}\pi mm_a)\left((-1)^k e^{\frac{1}{2}j\pi m} - e^{-j\frac{1}{2}\pi m}\right)$$

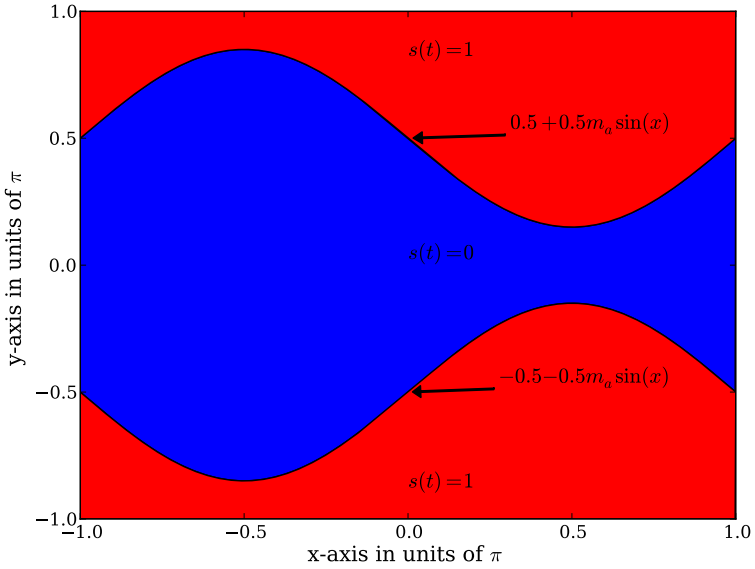

Figure A.9: Unit cell for unipolar switched PWM, leg 2

A.6.5.2 Fourier Series Coefficients of Leg 2

Using the unit-cell integration area indicated in Fig. A.9 The coefficients must be calculated for two cases: viz. when $m = 0$ and $m \neq 0$.

- Case 1: $m = 0$

  When $m = 0$ the expression for $\tilde{S}_{leg2(k,m)}$ can be rewritten as:

$$\tilde{S}_{leg2(k,0)} = \frac{1}{4\pi^2} \int_{-\pi}^{\pi} \int_{-\pi}^{\pi} F(x,y) e^{-jkx} dy dx$$

  Integrating over intervals, through the unit cell, yields:

$$\tilde{S}_{leg2(k,0)} = \frac{1}{4\pi^2} \int_{-\pi}^{\pi} \left(\int_{-\pi}^{-\frac{\pi}{2}(1+m_a \sin(x))} e^{-jkx} dy + \int_{\frac{\pi}{2}(1+m_a \sin(x))}^{\pi} e^{-jkx} dy \right) dx$$

  or

$$\tilde{S}_{leg2(k,0)} = \frac{1}{4\pi^2} \int_{-\pi}^{\pi} \alpha + \beta \, dx$$

  where

$$\begin{aligned} \alpha &= \int_{-\pi}^{-\frac{\pi}{2}(1+m_a \sin(x))} e^{-jkx} dy \\ &= e^{-jkx} \left(-\frac{\pi}{2}(1 + m_a \sin(x)) + \pi \right), \end{aligned}$$

$$\begin{aligned} \beta &= \int_{\frac{\pi}{2}(1+m_a \sin(x))}^{\pi} e^{-jkx} dy \\ &= e^{-jkx} \left(\pi - \frac{\pi}{2}(1 + m_a \sin(x)) \right). \end{aligned}$$

Expanding;

$$\begin{aligned}\alpha+\beta &= e^{-jkx}\left(-\frac{\pi}{2}(1+m_a\sin(x))+\pi+\pi-\frac{\pi}{2}(1+m_a\sin(x))\right)\\ &= \pi e^{-jkx}\big(1-m_a\sin(x)\big)\end{aligned}$$

and substituting into the expression for $\tilde{S}_{leg1(k,m)}$:

$$\begin{aligned}\tilde{S}_{leg2(k,0)} &= \frac{1}{4\pi^2}\int_{-\pi}^{\pi}\alpha+\beta\,dx\\ &= \frac{1}{4\pi}\int_{-\pi}^{\pi}e^{-jkx}\big(1-m_a\sin(x)\big)dx\end{aligned}$$

When $k=0$:

$$\begin{aligned}\tilde{S}_{leg2(0,0)} &= \frac{1}{4\pi}\int_{-\pi}^{\pi}\big(1-m_a\sin(x)\big)dx\\ &= \frac{1}{2}\end{aligned}$$

When $k\neq 0$, and using Euler's identity:

$$\begin{aligned}\tilde{S}_{leg2(k,0)} &= \frac{1}{4\pi}\int_{-\pi}^{\pi}e^{-jkx}-e^{-jkx}\frac{m_a}{2j}(e^{jx}-e^{-jx})dx\\ &= \frac{m_a}{j8\pi}\int_{-\pi}^{\pi}\frac{2j}{m_a}e^{-jkx}-e^{-jx(k-1)}+e^{-jx(k+1)}dx\end{aligned}$$

Since $\int_{-\pi}^{\pi}e^{-j\alpha x}dx=0$ for all nonzero values of α, only 2 cases remain, namely:

1. $k=-1$

$$\begin{aligned}\tilde{S}_{leg2(-1,0)} &= \frac{m_a}{j8\pi}\int_{-\pi}^{\pi}1dx\\ &= \frac{1}{j4}m_a\end{aligned}$$

2. $k=1$

$$\begin{aligned}\tilde{S}_{leg2(1,0)} &= \frac{m_a}{8j\pi}\int_{-\pi}^{\pi}-1dx\\ &= \frac{-1}{j4}m_a\end{aligned}$$

- Case 2: $k\neq 0$

  Using the integration unit cell the integral can be rewritten with integration limits as:

$$\tilde{S}_{leg2(k,m)}=\frac{1}{4\pi^2}\int_{-\pi}^{\pi}\left(\int_{-\pi}^{-\frac{\pi}{2}(1+m_a\sin(x))}e^{-j(kx+my)}dy+\int_{\frac{\pi}{2}(1+m_a\sin(x))}^{\pi}e^{-j(kx+my)}dy\right)dx$$

  or

$$\tilde{S}_{leg2(k,m)}=\frac{1}{4\pi^2}\int_{-\pi}^{\pi}\alpha+\beta\,dx$$

where

$$\begin{aligned}\alpha &= \int_{-\pi}^{-\frac{\pi}{2}(1+m_a\sin(x)} e^{-j(kx+my)}dy \\ &= \frac{e^{-jkx+\frac{1}{2}j\pi m(1+m_a\sin(x))}}{-jm} - \frac{e^{j\pi m-jkx}}{-jm} \\ &= \frac{je^{-jkx}}{m}\left(e^{\frac{1}{2}j\pi m(1+m_a\sin(x))} - e^{j\pi m}\right),\end{aligned}$$

$$\begin{aligned}\beta &= \int_{\frac{\pi}{2}(1+m_a\sin(x))}^{\pi} e^{-j(kx+my)}dy \\ &= \frac{e^{-j\pi m-jkx}}{-jm} - \frac{e^{-jkx-\frac{1}{2}j\pi m(1+m_a\sin(x))}}{-jm} \\ &= \frac{je^{-jkx}}{m}\left(e^{-j\pi m} - e^{-\frac{1}{2}j\pi m(1+m_a\sin(x))}\right).\end{aligned}$$

Expanding;

$$\begin{aligned}\alpha+\beta &= \frac{je^{-jkx}}{m}\left(-e^{j\pi m} + e^{-j\pi m} + e^{\frac{1}{2}j\pi m(1+m_a\sin(x))} - e^{-\frac{1}{2}j\pi m(1+m_a\sin(x))}\right) \\ &= \frac{je^{-jkx}}{m}\left(e^{\frac{1}{2}j\pi m(1+m_a\sin(x))} - e^{-\frac{1}{2}j\pi m(1+m_a\sin(x))}\right) \\ &= \frac{j}{m}\left(e^{-jkx}e^{\frac{1}{2}j\pi m}e^{\frac{1}{2}j\pi mm_a\sin(x)} - e^{-jkx}e^{-j\frac{1}{2}\pi m}e^{-\frac{1}{2}j\pi mm_a\sin(x)}\right)\end{aligned}$$

and substituting into the expression for $\tilde{S}_{leg2(k,m)}$:

$$\begin{aligned}\tilde{S}_{leg2(k,m)} &= \frac{1}{4\pi^2}\int_{-\pi}^{\pi} \alpha+\beta\, dx \\ &= \frac{j}{4\pi^2 m}\int_{-\pi}^{\pi} e^{-jkx}e^{\frac{1}{2}j\pi m}e^{\frac{1}{2}j\pi mm_a\sin(x)} - e^{-jkx}e^{-j\frac{1}{2}\pi m}e^{-\frac{1}{2}j\pi mm_a\sin(x)}dx\end{aligned}$$

Therefore, using the Bessel functions:

$$\tilde{S}_{leg2(k,m)} = \frac{j}{2\pi m}\left(e^{\frac{1}{2}j\pi m}J_k(\frac{1}{2}\pi mm_a) - e^{-j\frac{1}{2}\pi m}J_k(-\frac{1}{2}\pi mm_a)\right)$$

Using the identity that [5]

$$J_n(-x) = (-1)^n J_n(x),$$

the expression for $S_{leg2(k,m)}$ can be rewritten as:

$$\tilde{S}_{leg2(k,m)} = \frac{j}{2\pi m}J_k(\frac{1}{2}\pi mm_a)\left(e^{\frac{1}{2}j\pi m} - (-1)^k e^{-j\frac{1}{2}\pi m}\right)$$

A.6.5.3 Fourier Coefficients of the Complete Converter

The Fourier coefficients can be found as:

$$\tilde{S}_{km} = \tilde{S}_{leg1(k,m)} - \tilde{S}_{leg2(k,m)}$$

- Case 1: $m = 0$ When $k = 0$:

$$\begin{aligned}\tilde{S}_{0,0} &= \tilde{S}_{leg1(0,0)} - \tilde{S}_{leg2(0,0)} \\ &= \frac{1}{2} - \frac{1}{2} = 0\end{aligned}$$

When $k = -1$:

$$\begin{aligned}\tilde{S}_{-1,0} &= \tilde{S}_{leg1(-1,0)} - \tilde{S}_{leg2(-1,0)} \\ &= \frac{-1}{j4} m_a - \frac{1}{j4} m_a \\ &= \frac{j m_a}{2}\end{aligned}$$

When $k = 1$:

$$\begin{aligned}\tilde{S}_{1,0} &= \tilde{S}_{leg1(1,0)} - \tilde{S}_{leg2(1,0)} \\ &= \frac{1}{j4} m_a - \frac{-1}{j4} m_a \\ &= \frac{-j m_a}{2}\end{aligned}$$

- Case 2: $m \neq 0$

$$\begin{aligned}\tilde{S}_{km} &= \tilde{S}_{leg1(k,m)} - \tilde{S}_{leg2(k,m)} \\ &= \frac{j}{2\pi m} J_k(\frac{1}{2}\pi m m_a) \left((-1)^k e^{\frac{1}{2}j\pi m} - e^{-j\frac{1}{2}\pi m} - e^{\frac{1}{2}j\pi m} + (-1)^k e^{-j\frac{1}{2}\pi m}\right) \\ &= \frac{j}{2\pi m} J_k(\frac{1}{2}\pi m m_a) \Big((-1)^k \left(e^{\frac{1}{2}j\pi m} + e^{-j\frac{1}{2}\pi m}\right) - e^{-j\frac{1}{2}\pi m} - e^{\frac{1}{2}j\pi m}\Big) \\ &= \frac{j}{2\pi m} J_k(\frac{1}{2}\pi m m_a) \Big((-1)^k 2\cos(\frac{1}{2}\pi m) - 2\cos(\frac{1}{2}\pi m)\Big) \\ &= \frac{j}{\pi m} J_k(\frac{1}{2}\pi m m_a) \cos(\frac{1}{2}\pi m) \Big((-1)^k - 1\Big)\end{aligned}$$

The switching signal can thus be rewritten as:

$$s(t) = \sum_{k=-\infty}^{\infty} \sum_{m=-\infty}^{\infty} S_{(k,m)} e^{j(k\omega_r t + m\omega_c t)} \tag{A.6.10}$$

$$S_{(k,m)} = \tilde{\Psi}(k,m) \tag{A.6.11}$$

$$\tilde{\Psi}(k,0) = \begin{cases} \frac{j m_a}{2} & \text{when } k = -1 \\ \frac{-j m_a}{2} & \text{when } k = 1 \\ 0 & \text{when } |k| \neq 0 \end{cases} \tag{A.6.12}$$

$$\tilde{\Psi}(k,m) = \frac{j}{m\pi} J_k(\frac{\pi}{2} m m_a) \cos(\frac{\pi}{2} m)(-1^k - 1) \text{ when } m \neq 0 \tag{A.6.13}$$

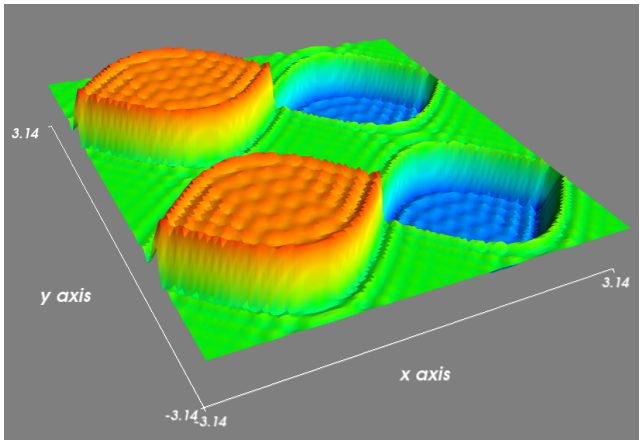

Figure A.10: Recreated unit cell for unipolar switched PWM

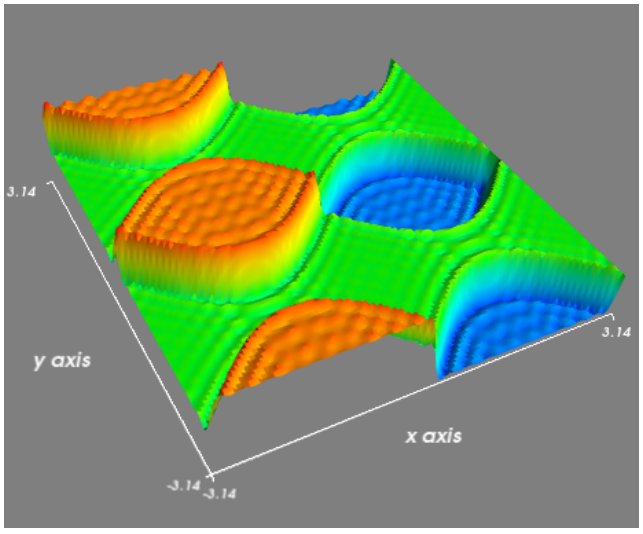

Figure A.11: Recreated unit cell for unipolar switched PWM: interleaved case

The presented coefficients were tested for accuracy by recreating the unit cell using the presented coefficients. The resulting unit cell is shown in Fig. A.10. The frequency doubling effect of unipolar switching is clearly evident. The unit cell for the two-cell interleaved case, using coefficients $S_{km} = j^m \tilde{\Psi}(k,m)$ is shown in Fig. A.11 as validation.

Appendix B

Selected Published Conference Papers

Two of the papers presented describe work done on natural balancing of converters that where deemed to fall outside of the scope of this dissertation. The papers will be included in this appendix.

It is suggested that Appendix A.6.3 and Appendix A.6.5 is read in conjunction with the papers. The details of the papers are summarised in Table B.1.

Table B.1: Details of the repeated papers

Title	Natural balancing of the two-cell back-to-back converter with specific application to the solid-state transformer concept.
Conference	IEEE Conference on Industrial Electronics and Applications (ICIEA)
Date	May 2009
Location	Xi'An, China
Title	An investigation of the natural balancing mechanisms of cascaded active rectifiers.
Conference	International Power Electronics and Motion Conference (EPE-PEMC)
Date	September 2010
Location	Ohrid, Macedonia

Furthermore, the text refers to references [19] and [20] co-authored by the author. The documents might be difficult to locate and are hence included here.

Natural Balancing of the Two-Cell Back-To-Back Multilevel Converter with Specific Application to the Solid-State Transformer Concept

Wim van der Merwe
Department of Electrical and Electronic Engineering
University of Stellenbosch
Stellenbosch, South Africa
email: wimvdmerwe@sun.ac.za

Toit Mouton
Department of Electrical and Electronic Engineering
University of Stellenbosch
Stellenbosch, South Africa
email: dtmouton@sun.ac.za

***Abstract*—This paper considers the voltage balancing of the two-level series stacked back-to-back converter topology. Firstly it is proven that the cell voltages will be balanced in steady state. Further insight into the balancing process is found through analysis of the rebalancing process following an external perturbation.**

I. Introduction

The oil-cooled steel core transformer is used globally in reticulation networks to provide galvanic isolation and voltage level transformation. This global use of the line frequency transformer (LFT) resulted in a very mature technology where any improvements to the system bring about marginal increases in parameters such as efficiency and system cost. Although the LFT is in global use many of its characteristics are undesirable such as the non-perfect voltage regulation. Currently additional network components such as FACTS devices and automatic tap changers are used in conjunction with the transformer to increase the total system power quality.

By using power electronic converters to change the incoming AC voltage to a high frequency signal, create electrical isolation with a high frequency transformer, and converters to recreate line frequency AC from the resulting signals, several benefits over traditional line frequency transformers can be gained, among others:

1) Output voltage quality is independent of input voltage.
2) Input current is balanced three phase with perfect power factor regardless of secondary load.
3) Perfect voltage regulation.
4) All measurements of currents, power and voltage are inherent to the system and hence available to the utility.
5) Ability to create other output frequencies, such as 60 Hz from a 50 Hz host system.
6) Ability to connect to a system with a different phase than the host system.
7) Voltage dip and sag ride through capability (with enough energy storage).

Some work on the solid-state transformer, also known as the intelligent universal transformer was done in recent years, with prototypes of the system constructed and tested [1]–[3].

The high voltage of the primary side necessitates the use of a multi-level power electronic converter. In [2] a diode-clamped multi-level converter was used. The modular nature of the series-input-parallel-output (SIPO) circuit [4] is attractive for high input voltage applications. In another study various topologies were investigated and compared with specific application to the SST; a hybrid cascaded-series stacked converter was proposed based on the results [5].

The main benefits of the proposed hybrid series stacked converter are:

- Cost is comparable to the diode clamped converter.
- Converter is modular thus readily expandable to higher voltages.
- The modular nature also increase system maintainability unlike the diode clamped converter.
- Number of converter switches rises linearly with voltage. The number of diodes for the diode clamped converter is a function of the square of the number of levels.

The main objection raised in literature against the use of the series stacked converter is the balancing of the cell voltages. In [6] it was proven that the cell-voltages of a three-cell series stacked converter, with series connected outputs, will balance naturally. As the topology proposed for the solid-state transformer concept implies a back to back connection of a cascaded power factor correcting rectifier and a series stacked dc-to-dc converter and the outputs are connected in parallel a measure of uncertainty of the applicability of [6] to the proposed converter exists. In another study [7] it is stated, although not rigorously proven, that a SIPO converter will balance even in the event of component mismatches. This paper aims to mathematically prove that the proposed two-cell converter will balance naturally.

Firstly the equivalent balancing circuit for the proposed converter will be developed. The converter will be investigated in steady state after which the rebalancing process after an external perturbation will be analysed.

978–1–4244–2800–7/09/$25.00 ©

II. Development of the Equivalent Circuit

The two cell converter under consideration is indicated in Fig. 1. In creating a workable approximation of the real circuit the source resistance and boost inductor resistance is lumped into r_b and the resistance of the transformer, filter inductor and switch elements into r.

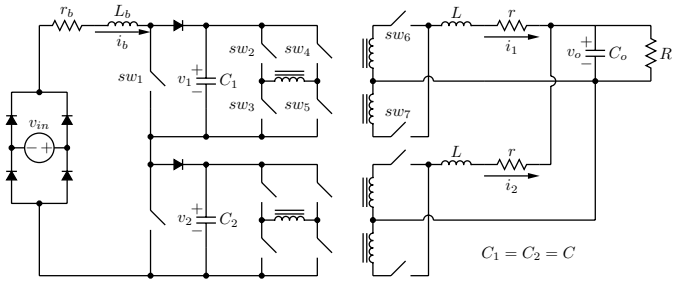

Fig. 1. General figure of a two cell series stacked converter

The boost and full bridge converters can be approximated by perfect, non saturable, transformers with a time dependant turns ratio as used and defined in [8]. It is important to note that the turns ratio in this application is not the time averaged value of the duty cycle. In Fig. 1 the switches of the topmost converter are labeled as 1-7. The back-to-back connection of the boost (switch 1 and diode) and the synchronously rectified full bridge (switches 2-7) can be identified. If each of the converters is substituted by a perfect transformer the operation of the circuit in Fig. 1 can be described without any loss of information as long as the switching functions s_{b1}, s_{b2}, s_1, and s_2 are complete representations of the switching behaviour of the respective converters.

The switching functions of the topmost converter, with reference to the switching behaviour of the respective switches, are indicated in Table I. Let a denote the turns-ratio of the full bridge transformer and assume all switches to be in the off-state unless mentioned otherwise. The full-bridge converter is assumed to operate with bipolar switching whereby 3 states can be identified, two energy transfer states (2,5,6 on) and (3,4,7 on) and a free-flow state (6,7 on). The definitions in Table I can be adjusted to accommodate any other switching scheme such as the phase shifted resonant scheme. It is important to note that the effective frequency of the full bridge switching function is twice that of the individual switches. The information presented can be extended to s_{b2} and s_2.

TABLE I
Definition of Switching Functions

Switch Information	s_{b1}	s_1
1 (on)	0	
1 (off)	1	
2,5,6 (on)		a
3,4,7 (on)		a
6,7 (on)		0

With the switching functions defined the circuit of Fig 1 can be redrawn with the converters replaced with the perfect, variable turns ratio transformers as indicated in Fig. 2. Using this representation the system of differential equations describing the operation of the converter can be expressed as:

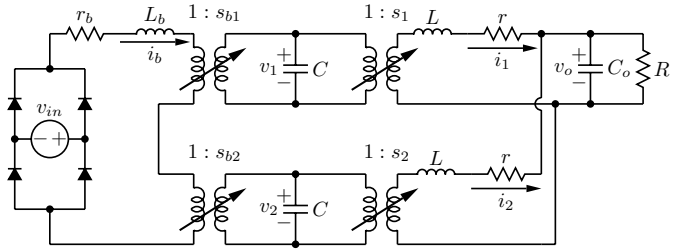

Fig. 2. The two cell series circuit expressed in terms of the two port circuits

$$\frac{d}{dt}\begin{bmatrix} L_b \cdot i_b \\ C \cdot v_1 \\ C \cdot v_2 \\ L \cdot i_1 \\ L \cdot i_2 \\ C_o \cdot v_o \end{bmatrix} = \begin{bmatrix} -r_b & -s_{b1} & -s_{b2} & 0 & 0 & 0 \\ s_{b1} & 0 & 0 & -s_1 & 0 & 0 \\ s_{b2} & 0 & 0 & 0 & -s_2 & 0 \\ 0 & s_1 & 0 & -r & 0 & -1 \\ 0 & 0 & s_2 & 0 & -r & -1 \\ 0 & 0 & 0 & 1 & 1 & \frac{-1}{R} \end{bmatrix} \begin{bmatrix} i_b \\ v_1 \\ v_2 \\ i_1 \\ i_2 \\ v_o \end{bmatrix} + \begin{bmatrix} |v_{in}| \\ 0 \\ 0 \\ 0 \\ 0 \\ 0 \end{bmatrix} \quad (1)$$

The following variables are defined in order to study the unbalance in the circuit:

$$s_d = \frac{s_1 - s_2}{2} \qquad s_{bd} = \frac{s_{b1} - s_{b2}}{2}$$
$$v_d = v_1 - v_2 \qquad i_d = i_1 - i_2$$

and

$$s_t = \frac{s_1 + s_2}{2} \qquad s_{bt} = \frac{s_{b1} + s_{b2}}{2} \quad (2)$$
$$v_t = v_1 + v_2 \qquad i_t = i_1 + i_2$$

The differential equation of (1) can be rewritten in terms of the definitions in (2) resulting in:

$$\frac{d}{dt}\begin{bmatrix} L_b \cdot i_b \\ C \cdot v_t \\ C \cdot v_d \\ L \cdot i_t \\ L \cdot i_d \\ C_o \cdot v_o \end{bmatrix} = \begin{bmatrix} -r_b & -s_{bt} & -s_{bd} & 0 & 0 & 0 \\ 2s_{bt} & 0 & 0 & -s_t & -s_d & 0 \\ 2s_{bd} & 0 & 0 & -s_d & -s_t & 0 \\ 0 & s_t & s_d & -r & 0 & -2 \\ 0 & s_d & s_t & 0 & -r & 0 \\ 0 & 0 & 0 & 1 & 0 & \frac{-1}{R} \end{bmatrix} \begin{bmatrix} i_b \\ v_t \\ v_d \\ i_t \\ i_d \\ v_o \end{bmatrix} + \begin{bmatrix} |v_{in}| \\ 0 \\ 0 \\ 0 \\ 0 \\ 0 \end{bmatrix} \quad (3)$$

The circuit of the two-cell series stacked converter in terms of d and t parameters can be expressed as shown in Fig. 3. The proposed circuit is equivalent to the original circuit of Fig. 1 but the bus voltages and currents are expressed in terms of total and difference values. This representation allows for clear understanding of the balancing process.

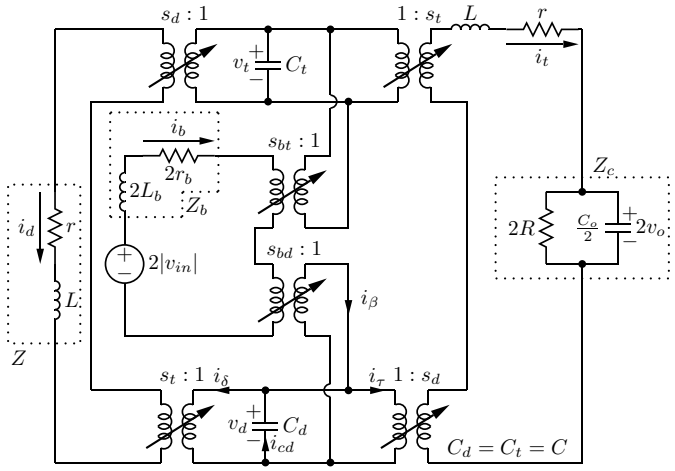

Fig. 3. 2-Level series stacked converter circuit in terms of d and t parameters

III. Harmonic Content of Switching Signals

The non-linear behaviour of the system can best be analysed in the frequency domain. The following assumptions are made:

1) The two cells are operating at the same switching frequency.
2) The PWM signals are generated through comparison of a PWM reference signal with a sawtooth carrier.
3) The two cells operate with interleaved switching whereby the carrier waves are shifted by $180°$.
4) The PWM reference signals of the two cells are equal.
5) The full-bridge converters are operating at constant duty cycle, defined as d.
6) The boost switching function is derived by a main controller using the value of v_{in} and v_t.
7) Isolation transformer turns ratio is assumed to be 1:1.

A. Boost Converter Signals

The boost converters act as power factor correcting units. The converters typically operate with a inner current loop and a outer voltage loop. The inner current loop controls the current i_b, with reference to Fig. 1, to be sinusoidal and in phase with the input voltage v_{in}. The outer voltage loop controls the sum of voltages v_1 and v_2, in other words v_t, to conform to a set level.

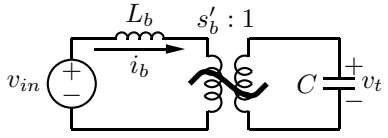

Fig. 4. Approximation of the Boost-Converters

Due to the interaction of the two control loops it is very difficult to derive an exact expression for the switching function of the converters. A workable approximation can be found through neglecting the, primarily second order, harmonics of the line frequency on the bus voltages. If the boost converter is approximated by a dc-transformer, Fig. 4, an expression for the inverted reference function f_r' can be found for a half-cycle as

$$f_r' = \frac{v_{in}}{v_t}\sin(\omega_L t) - \frac{L_b i_b \omega_L}{v_t}\cos(\omega_L t) \tag{4}$$

where ω_L represents the frequency of the line voltage. As, in general, $v_{in} \gg L_b i_b \omega_L$ the PWM reference function can safely be approximated by:

$$f_r = 1 - \frac{v_{in}}{v_t}|\sin(\omega_L t)| \tag{5}$$

1) Fourier Series Representation: Let the boost switching PWM function be created through comparison of the reference signal f_r and a sawtooth carrier signal with frequency ω_c. Define $x(t) = \omega_L t + \theta_L$ and $y(t) = \omega_c t + \theta_c$. Using the double Fourier series expression, in exponential form, as described in more detail in [9], the switching function s_{b1} can be expressed as:

$$s_{b1}(t) = \sum_{k=-\infty}^{\infty}\sum_{m=-\infty}^{\infty} K_{km} e^{j(kx+my)} \tag{6}$$

where

$$K_{km} = \frac{1}{4\pi^2}\int_0^{2\pi}\int_0^{2\pi} F(x,y)e^{-j(kx+my)}dxdy. \tag{7}$$

A unit cell of the background function $F(x,y)$ is indicated in Fig. 5. A complete discussion of the development of a general background function can be found in [9].

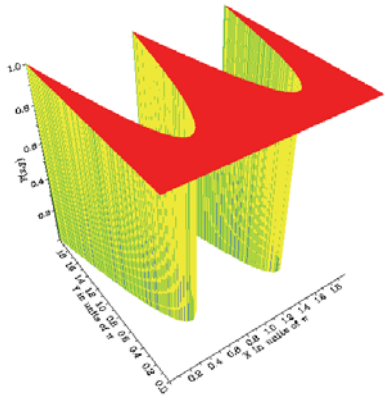

Fig. 5. Background function unit cell, $F(x,y)$ used to calculate the boost switching function

The double integral is evaluated over the area as indicated by Fig. 5. As an analytical expression for K_{km} is not readily forthcoming a numerical solution was found through implimentation of a Python (with numpy) script.

With reference to (7) it is important to note that:

1) The counter k denotes steps in the frequency domain with size ω_L.

2) Likewise m denotes steps with size ω_c.
3) K_{k0} would therefore describe the low frequency harmonics of the switching function, centred about the fundamental component of the switching function.
4) As $\omega_c \lll \omega_L$ the groups of harmonics do not overlap.
5) Harmonics decay as $|m|$ increase.

B. Full Bridge Signals

As the switching function of the full-bridge converter is not modulated the exponential Fourier series can be used to represent the harmonic content of the signal. The switching function $s_1(t)$ can be expressed in exponential Fourier series form as:

$$s_1(t) = \sum_{n=-\infty}^{\infty} C_{1(n)} e^{jn\omega_c t} \tag{8}$$

where,

$$C_{1(n)} = \frac{1}{T_s} \int_{t_0}^{t_0+T_s} s_1(t) e^{-jn\omega_c t} dt. \tag{9}$$

Similarly switching function s_2 maps to coefficients $C_{2(n)}$. The Fourier series coefficients of the two interleaved converters, for a duty cycle d, can be expressed as:

$$C_{1(n)} = \Psi(n) \tag{10}$$

$$C_{2(n)} = -1^n \Psi(n) \tag{11}$$

where

$$\Psi(n) = \begin{cases} \frac{j}{2\pi n}\left(e^{-j2\pi nd} - 1\right) & \text{for } n \neq 0 \\ d & \text{for } n = 0 \end{cases} \tag{12}$$

The frequency ω_c in this case denotes the effective frequency at the output of the rectifier, or double the switching frequency of the switching elements. This frequency will also be a multiple of the original sawtooth carrier, depending on the method used to generate the switching signals.

C. Combined Switching Functions

The total and difference switching functions as defined in (2) can only be investigated analytically for the full-bridge case as the harmionic content of the modulated PWM at the boost converters was found numerically. Investigating the full-bridge signals reveals, for $\vartheta \in \mathbb{Z}$:

$$S_{t(n)} = \begin{cases} \Psi(n) & \text{for } n = 2\vartheta \\ 0 & \text{otherwise} \end{cases} \tag{13}$$

$$S_{d(n)} = \begin{cases} 0 & \text{for } n = 2\vartheta \\ \Psi(n) & \text{otherwise} \end{cases} \tag{14}$$

This result for the constant duty-cycle case can be extrapolated to the modulated PWM case, as described in [6] and [10], resulting in,

$$S_{bt(k,m)} = \begin{cases} K_{km} & \text{for } m = 2\vartheta,\ k \in \mathbb{Z} \\ 0 & \text{otherwise} \end{cases} \tag{15}$$

$$S_{bd(k,m)} = \begin{cases} 0 & \text{for } m = 2\vartheta,\ k \in \mathbb{Z} \\ K_{km} & \text{otherwise} \end{cases} \tag{16}$$

IV. The Converter in Steady-State

With the assumption that the cell bus capacitance is very large the harmonic content of the cell voltages can be neglected. With reference to Fig. 3 the currents $I_t(\omega)$, $I_d(\omega)$ and $I_b(\omega)$ can be found as:

$$I_t(\omega) = \frac{1}{Z(\omega) + Z_c(\omega)} \left(V_t S_t(\omega) + V_d S_d(\omega)\right) \tag{17}$$

$$I_d(\omega) = \frac{1}{Z(\omega)} \left(V_t S_d(\omega) + V_d S_t(\omega)\right) \tag{18}$$

$$I_b(\omega) = \frac{1}{Z_b(\omega)} \left(2|V_{in}(\omega)| - V_t S_{bt}(\omega) - V_d S_{bd}(\omega)\right) \tag{19}$$

where

$$Z(\omega) = j\omega L + r,\ Z_b(\omega) = j2\omega L_b + 2r_b \text{ and } Z_c(\omega) = \frac{2R}{j\omega C_o R + 1}. \tag{20}$$

Let $I_{cd}(\omega)$ denote the current through the the C_d capacitor, as shown in Fig. 3. An expression for $I_{cd}(\omega)$ can be found as:

$$I_{cd}(\omega) = S_t(\omega) * I_d(\omega) + S_d(\omega) * I_t(\omega) - I_b(\omega) * S_{bd}(\omega) \tag{21}$$

In steady state the average of the current through a capacitor is equal to zero. Therefore, with $\omega = 0$, and substituting (17)-(19) into (21) and rearranging:

$$V_d A(\omega)|_{\omega=0} = \left(V_t B(\omega) + \frac{2|V_{in}(\omega)|}{Z_b(\omega)} * S_{bd}(\omega)\right)\Bigg|_{\omega=0} \tag{22}$$

where

$$A(\omega) = \frac{S_t(\omega)}{Z(\omega)} * S_t(\omega) + \frac{S_d(\omega)}{Z(\omega) + Z_c(\omega)} * S_d(\omega) + \frac{S_{bd}(\omega)}{Z_b(\omega)} * S_{bd}(\omega)$$

and

$$B(\omega) = -\frac{S_d(\omega)}{Z(\omega)} * S_t(\omega) - \frac{S_d(\omega)}{Z(\omega) + Z_c(\omega)} * S_t(\omega) - \frac{S_{bt}(\omega)}{Z_b(\omega)} * S_{bd}(\omega).$$

At $\omega = 0$ the convolution of two frequency domain signals, expressed in exponential Fourier series form, can be expressed as:

$$(F(\omega) * G(\omega))|_{\omega=0} = \sum_{\xi=-\infty}^{\infty} F_{(\xi)} G_{(-\xi)} \tag{23}$$

Using the characteristics from (13) and (14) and substituting into (23) it can be shown that

$$\left(\frac{S_d(\omega)}{Z(\omega)} * S_t(\omega)\right)\Bigg|_{\omega=0} = 0. \tag{24}$$

For the harmonic rich modulated PWM case (23) is better expressed as:

$$(F(\omega) * G(\omega))|_{\omega=0} = \sum_{\xi=-\infty}^{\infty} \sum_{\varrho=-\infty}^{\infty} F_{(\xi,\varrho)} G_{(-\xi,-\varrho)} \tag{25}$$

Under the premise that ω_c is sufficiently larger than ω_L such that the harmonic groups do not over lap

$$\left(\frac{S_{bt}(\omega)}{Z_b(\omega)} * S_{bd}(\omega)\right)\Bigg|_{\omega=0} = 0. \tag{26}$$

Therefore it follows that:

$$B(\omega)|_{\omega=0} = 0 \tag{27}$$

$V_{in}(\omega)$ contains harmonics of ω_L centred around zero. With the assumption that the switching frequency is sufficiently large

$$\left(\frac{2|V_{in}(\omega)|}{Z_b(\omega)} * S_{bd}(\omega)\right)\Big|_{\omega=0} = 0. \tag{28}$$

From the characteristics in (13) and (14) and using (23) it can be shown that:

$$A(\omega)|_{\omega=0} = A_0 \neq 0 \tag{29}$$

Therefore (20) can be rewritten as

$$V_d = \frac{0}{A_0} V_t + 2\frac{0}{A_0} V_{in}. \tag{30}$$

Implying the cell voltages will be balanced in steady state.

V. Rebalancing Mechanism

Having established that the cell voltages will be balanced in steady state it is appropriate to investigate the circuit response to an external perturbation.

Let $I_\tau(\omega)$, $I_\delta(\omega)$ and $I_\beta(\omega)$ be the reflected currents from the $I_t(\omega)$, $I_d(\omega)$ and $I_b(\omega)$, as indicated in Fig. 3. If the capacitor is sufficiently large, insight into the charging current can be found through investigating the dc components of $I_\tau(\omega)$, $I_\delta(\omega)$ and $I_\beta(\omega)$. The currents can be expressed as:

$$I_\tau(\omega) = \left(\frac{V_t S_t(\omega) + V_d S_d(\omega)}{Z(\omega) + Z_c(\omega)}\right) * S_d(\omega) \tag{31}$$

$$I_\delta(\omega) = \left(\frac{V_t S_d(\omega) + V_d S_t(\omega)}{Z(\omega)}\right) * S_t(\omega) \tag{32}$$

$$I_\beta(\omega) = \left(\frac{2|V_{in}(\omega)| - V_t S_{bt}(\omega) - V_d S_{bd}(\omega)}{Z_b(\omega)}\right) * S_{bd}(\omega) \tag{33}$$

Using the results derived in the previous section the dc components of the currents can be rewritten as:

$$I_\tau(\omega)|_{\omega=0} = -V_d \sum_{\xi=\infty}^{\infty} \frac{S_d(\xi)}{Z(\xi\omega_c) + Z_c(\xi\omega_c)} S_d(-\xi) \tag{34}$$

$$I_\delta(\omega)|_{\omega=0} = -V_d \sum_{\xi=\infty}^{\infty} \frac{S_t(\xi)}{Z(\xi\omega_c)} S_t(-\xi) \tag{35}$$

$$I_\beta(\omega)|_{\omega=0} = -V_d \sum_{\xi=-\infty}^{\infty} \sum_{\varrho=-\infty}^{\infty} \frac{S_{bd(\xi,\varrho)}}{Z_b(\xi\omega_c + \varrho\omega_L)} S_{bd(-\xi,-\varrho)} \tag{36}$$

It is clear that the balancing process separates into three distinct parts each associated with one of subcircuits as identified by i_t, i_d and i_b in Fig. 3. Using the superposition principle the contribution to the balancing process each of the subcircuits can be investigated independently.

In general the filter inductor is chosen to provide a considably large impedance at the switching frequency. Since S_d and S_{bd} does not contain dc components it follows that the $Z(\omega)$ term will dominate in (36) and (34). In contrast $S_t(\omega)$ contains a dc term and it follows that

$$I_\delta(\omega)|_{\omega=0} \lggg I_\tau(\omega)|_{\omega=0}\,,\, I_\beta(\omega)|_{\omega=0} \tag{37}$$

The conclusion of this argument holds that the dc term of I_δ should dominate the harmonic components the total contribution of i_δ. The relative contribution of the dc term in I_δ to the total capacitor charging current can be found as,

$$\varepsilon = \frac{dI_d(0)}{(I_\tau(\omega) + I_\beta(\omega) + I_\tau(\omega))|_{\omega=0}}. \tag{38}$$

Although a simplified expression for ε is not readily forthcomming the value was calculated with the reference design of Table II to be in excess of 0.99. Since the charging current is dominated by the dc-component, the circuit can be analysed using an averaging technique.

With reference to Fig. 3 the balancing process via the i_d subcircuit of the converter is governed by a RLC circuit described by C, L and r. Using time averaging of the S_t switching function the rebalancing equivalent circuit can be expressed as shown in Fig. 6. The balancing process can thus be expressed as:

$$0 = L'\frac{di}{dt} + r'i + \frac{1}{C}\int_0^t i d\tau \tag{39}$$

where

$$L' = \frac{L}{d^2}\ ,\ r' = \frac{r}{d^2} \tag{40}$$

$$i(0) = dI_d(0)\ ,\ v(0) = v_d(0) \tag{41}$$

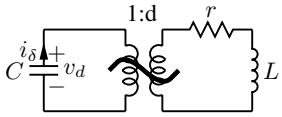

Fig. 6. Equivalent rebalancing circuit

The second order ordinary differential equation (ODE), with the indicated boundary conditions, describing the rebalancing RLC circuit can be analysed analytically.

VI. Results

The theory presented was tested by comparing the predicted results with the results of a detailed Ansoft Simplorer simulation. The parameter values used in the simulation are summarised in Table II.

Fig. 7 compares the V_d voltage during rebalancing found through detailed simulation to the solution found to the ODE described in (39) - (41). The corresponding waveforms of the reflected difference current (I_δ) are shown in Fig. 8. The theory presented corresponds very well with the converter behaviour. In Fig. 8 the effect of the averaging technique is clearly visible.

The theory presented does not, at first glance, indicate the strength of the balancing mechanism. In a second simulation a resistor of 320 Ω (representing more than 50 % of the output power) was connected in shunt with the cell capacitor, C_2,

TABLE II
CIRCUIT VALUES USED

Item	Value	
Sec. Filter Inductor	L	1 mH
Lumped Sec. Resistance	r	0.5 Ω
Bus Capacitors	C	1 mF
Boost Inductor	L_b	6 mH
Boost Resistance	r_b	1 Ω
Duty cycle	d	80 %
Total Voltage	V_t	2 000 V
Initial Difference Voltage	V_d	200 V
Line frequency	$\frac{\omega_L}{2\pi}$	50 Hz
Switching frequency	$\frac{\omega_c}{2\pi}$	50 kHz

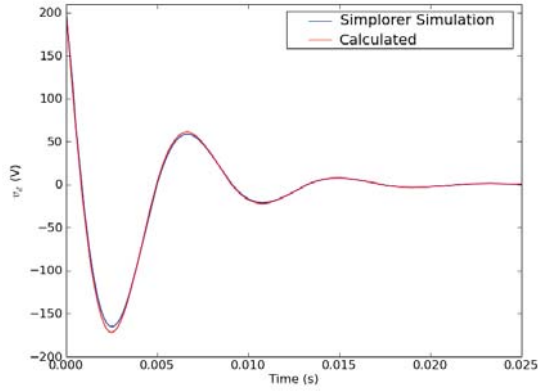

Fig. 7. Rebalancing of V_d after an initial perturbation of 200 V

in Fig. 1. The simulated rebalancing response of the modified circuit is compared with the response of the unmodified circuit in Fig. 9. Although the resistor represents a driver towards unbalance, it is clear that the circuit still rebalances.

VII. CONCLUSION

A series stacked back to back converter topology was identified for use in the solid-state transformer concept. The main objection in literature to the use of this topology is the question of maintaining voltage balancing among the series stacked cells. Although the concept of natural balancing had been proven for other topologies the mechanisms for the series connected back to back case still remain largely unexplored.

In this paper the two-cell converter, with synchronous rectification, was investigated. An equivalent circuit of the system in terms of d and t parameters was developed. With the aid of the circuit it was proven that the system will be balanced in steady state.

The rebalancing process was also investigated and an equivalent circuit describing the rebalancing of the circuit, after an external perturbation, was developed. The results were compared with a detailed Ansoft Simplorer simulation and found to correspond to an acceptable degree.

REFERENCES

[1] J. Lai, A. Maitra, and F. Goodman, "Performance of a distribution intelligent universal transformer under source and load disturbances," in *Conference Record of the 2006 IEEE 41st IAS Annual Meeting*, vol. 2, 8-12 October 2006.

[2] J. Lai, A. Maitra, A. Mansoor, and F. Goodman, "Multilevel intelligent universal transformer for medium voltage applications," in *Conference Record of the 2005 IEEE 40th IAS Annual Meeting*, vol. 3, 2-6 October 2005, pp. 1893–1899.

[3] E. Ronan, S. Sudhoff, S. Glover, and D. Galloway, "A power-electronic based distribution transformer," *IEEE Transactions on Power Delivery*, vol. 17, no. 2, pp. 537–543, Apr. 2002.

[4] J.-W. Kim, J.-S. You, and B. Cho, "Modeling, control, and design of input-series-output-parallel-connected converter for high speed train power system," *IEEE Transactions on Industrial Electronics*, vol. 48, no. 3, pp. 536–544, June 2001.

[5] J. van der Merwe and H. d. T. Mouton, "Solid-state transformer topology selection," in *Conference Record of the 2009 IEEE International Conference on Industrial Technology*, 10-13 February 2009.

[6] H. d. T. Mouton, J. Enslin, and H. Akagi, "Natural balancing of series-stacked power quality conditioners," *IEEE Transactions on Power Electronics*, vol. 18, no. 1, pp. 198–207, Jan. 2003.

[7] R. Giri, V. Choudhary, R. Ayyanar, and N. Mohan, "Common-duty-ratio control of input-series connected modular dc-dc converters with active input voltage and load-current sharing," *IEEE Transactions on Industry Applications*, vol. 42, no. 4, pp. 1101–1111, 2006.

[8] R. Erickson and D. Maksimović, *Fundamentals of Power Electronics*. Kluwer Academic Publishers, 2001.

[9] D. Holmes and T. Lipo, *Pulse Width Modulation For Power Converters, Principles and Practice*. IEEE Press, 2003.

[10] R. Wilkinson, T. Meynard, and H. d. T. Mouton, "Natural balance of multicell converters: The general case," *IEEE Transactions on Power Electronics*, vol. 21, no. 6, pp. 1658–1666, Nov. 2006.

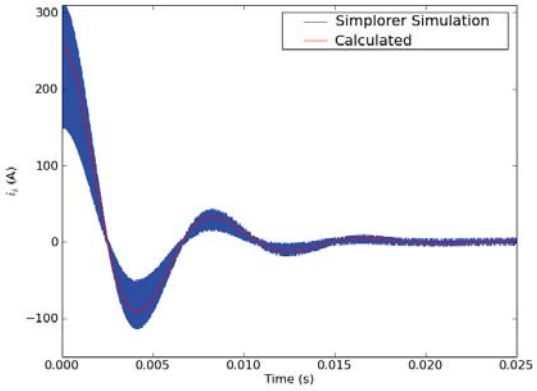

Fig. 8. Reflected difference current I_δ during rebalancing

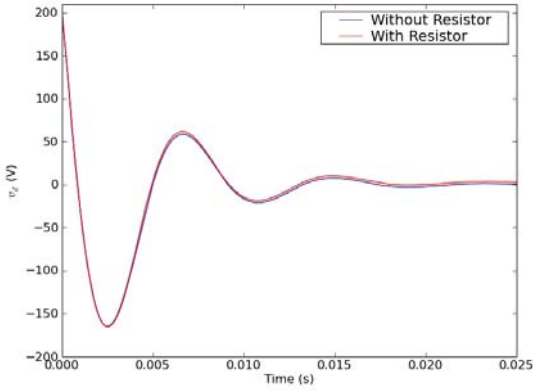

Fig. 9. Rebalancing with a resistor placed across one of the cells

An Investigation of the Natural Balancing Mechanisms of Cascaded Active-Rectifiers

J.W. van der Merwe
Department of Electrical and Electronic Engineering
University of Stellenbosch
Stellenbosch, South Africa
Email: wimvdmerwe@sun.ac.za

H. du T. Mouton
Department of Electrical and Electronic Engineering
University of Stellenbosch
Stellenbosch, South Africa
Email: dtmouton@sun.ac.za

***Abstract*—The natural balancing processes of a 2-cell cascaded active rectifier converter is investigated in the frequency domain. Two balancing mechanisms are identified, weak and strong. Expressions for the time constant of both mechanisms are derived. The limitations and applicability of both mechanisms are discussed. The results are compared to time domain simulation results for the constant duty cycle case. Finally the measured results of a practical system operating as power factor correcting rectifier are presented.**

I. Introduction

Multilevel converters (MC) attract considerable interest, mainly due to the ability to operate at voltages higher than the ratings of the individual switches. In comparison with conventional converters MCs also provide higher efficiencies, power densities and lower filter requirements in part due to the ability to increase the apparent switching frequency through interleaving of the different levels [1]. However, all MC topologies require some mechanism to clamp the voltages over the individual switches to the same value, effectively sharing, or balancing, the total applied voltage equally among the different levels.

In this paper the voltage balancing of the cascaded active rectifier converter, CARC, is discussed. In literature several methods of actively balancing the voltages are discussed [2]–[5]. However, a natural balancing mechanism exists that might be sufficient for many applications. In a previous study [6] the natural balancing of a CARC with modular converters connected in output-parallel as loads was investigated. This type of converter typically finds application in grid-connected converters. However, the natural balancing of the output-parallel connected converters dominated the inherent balancing mechanism of the CARC. This study investigates the natural balancing of the CARC with resistive loads. The voltage sharing under unequal loading is discussed and two balancing mechanisms, weak and strong, are identified and quantified.

For the constant duty cycle case the theory presented is verified through comparison with a simulation of the circuit. The presented theory is also valid when the CARC is operational as a power factor correcting active rectifier. Measurements of a practical system showing the rebalancing of such a system are included.

II. Equivalent Balancing Circuit of the CARC

A 2-level CARC is shown in Fig. 1. The following assumptions are made:

1) The switches and diodes are assumed to be ideal.
2) The source and inductor ESR resistances are lumped together as r.
3) The filter capacitor ESR is ignored.
4) The filter capacitances of the two cells are equal.
5) Allowance is made for different loads, R_1 and R_2, to be connected.
6) The effects of dead time are ignored.
7) The reference function used to determine the duty cycle is equal for both cells.

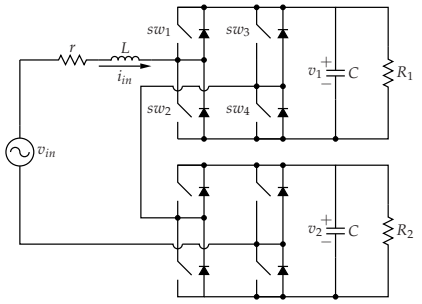

Fig. 1. 2-Level Cascaded Active Rectifier Converter Circuit

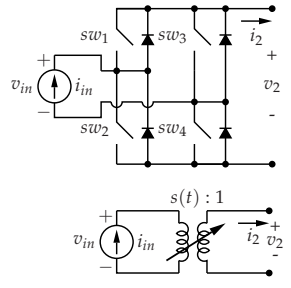

Fig. 2. Model of the Full-Bridge Circuit

The full bridge converter can be modelled as an ideal transformer with a time varying turns-ratio. Let the converter

operate with unipolar switching [7] and therefore each phase leg is switched as a complimentary pair. The switching signals are created through comparison of a reference function (f_r) with a triangular carrier (f_c). The carrier is described, with a switching frequency of f_s and a phase shift of θ_s, as:

$$f_c(t) = \frac{2}{\pi}\arcsin(\sin(2\pi f_s t + \theta_s)) \tag{1}$$

Referring to Fig. 2 the states of switches 1-4 can be mapped to $s(t)$ as shown in Table I.

TABLE I
MAP OF THE SWITCH STATES TO $s(t)$

Switches on	$s(t)$	Condition
sw_1, sw_3	0	$f_r > f_c$ and $-f_r > f_c$
sw_1, sw_4	1	$f_r > f_c$ and $-f_r < f_c$
sw_2, sw_3	-1	$f_r < f_c$ and $-f_r > f_c$
sw_2, sw_4	0	$f_r < f_c$ and $-f_r < f_c$

The operation of the circuit can be described by the following system of differential equations:

$$\frac{d}{dt}\begin{vmatrix} Li_{in} \\ Cv_1 \\ Cv_2 \end{vmatrix} = \begin{vmatrix} -r & -s_1 & -s_2 \\ s_1 & \frac{-1}{R_1} & 0 \\ s_2 & 0 & \frac{-1}{R_2} \end{vmatrix} \begin{vmatrix} i_{in} \\ v_1 \\ v_2 \end{vmatrix} + \begin{vmatrix} v_{in} \\ 0 \\ 0 \end{vmatrix} \tag{2}$$

To study the unbalance in the circuit the following variables are defined:

$$s_t = \frac{1}{2}(s_1 + s_2) \qquad s_d = \frac{1}{2}(s_1 - s_2)$$
$$v_t = v_1 + v_2 \qquad v_d = v_1 - v_2$$
$$G_t = \frac{R_1 + R_2}{2R_1R_2} \qquad G_d = \frac{R_1 - R_2}{2R_1R_2}$$

Where v_d now describes the unbalance voltage. Using these variables the system of equations (2) can be rewritten as:

$$\frac{d}{dt}\begin{vmatrix} Li_{in} \\ Cv_t \\ Cv_d \end{vmatrix} = \begin{vmatrix} -r & -s_t & -s_d \\ 2s_t & -G_t & G_d \\ 2s_d & G_d & -G_t \end{vmatrix} \begin{vmatrix} i_{in} \\ v_t \\ v_d \end{vmatrix} + \begin{vmatrix} v_{in} \\ 0 \\ 0 \end{vmatrix} \tag{3}$$

The equivalent circuit of Fig. 1 can be redrawn in terms of the balancing parameters as shown in Fig 3.

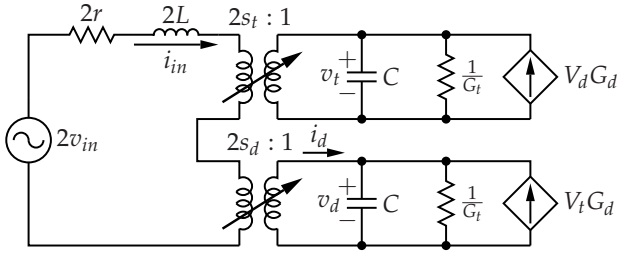

Fig. 3. 2-Level Cascaded Active Rectifier Converter Circuit in Terms of d and t Parameters

III. FREQUENCY DOMAIN ANALYSIS

For reasons that will become apparent later the circuit is analysed in the frequency domain. As a logical point of departure it is assumed that both rectifiers operate with equal and unmodulated (i.e. constant) duty cycle and that the source v_{in} is a DC source. The function $s(t)$ can be expressed in the frequency domain, where $\Psi(n)$ is the exponential Fourier coefficients, ω_s the radian switching frequency of the switches and $d = f_r$, as

$$s_1(t) = \sum_{n=-\infty}^{\infty} S_{1(n)} e^{j2n\omega_s t} \tag{4}$$
$$S_{1(n)} = \Psi(n) \tag{5}$$
$$S_{2(n)} = (-1)^n \Psi(n) \tag{6}$$
$$\Psi(n) = \begin{cases} \frac{1}{\pi n}\sin(n\pi d) & \text{for } n \neq 0 \\ d & \text{for } n = 0, \end{cases} \tag{7}$$

when the two rectifiers are operating with interleaved switching. When the two rectifiers are operational with ordinary switching (no interleaving of the two carriers) it follows logically that $S_{1(n)} = S_{2(n)} = \Psi(n)$.

It is assumed that the filter capacitances are large enough that the switching frequency voltage ripple of v_1 and v_2 are small enough to be ignored. With reference to Fig. 3 the current I_{in} can be found, with $Z(\omega) = r + j\omega L$, as:

$$I_{in}(\omega) = \frac{V_{in} - V_t S_t(\omega) - V_d S_d(\omega)}{Z(\omega)} \tag{8}$$

The current I_d can now be written as, where $*$ denotes the convolution operator:

$$I_d(\omega) = A(\omega) + B(\omega) + D(\omega) \tag{9}$$
$$A(\omega) = 2\frac{V_{in}}{Z(\omega)} * S_d(\omega) \tag{10}$$
$$B(\omega) = -2V_t\frac{S_t}{Z(\omega)} * S_d(\omega) \tag{11}$$
$$D(\omega) = -2V_d\frac{S_d}{Z(\omega)} * S_d(\omega) \tag{12}$$

In the steady-state the average current through a capacitor is zero. In the next subsections the influence of the three contributors to I_d will be investigated when $\omega = 0$.

A. The Influence of $A(\omega)$ on $I_d(\omega)$ in the Steady-State

Substituting (4)-(7) into the definition of s_d reveals, for interleaved switching:

$$S_{d(n)} = \begin{cases} \Psi(n) & \text{for } |n| = 1, 3, 5 \ldots \\ 0 & \text{for } |n| = 0, 2, 4 \ldots \end{cases} \tag{13}$$

For ordinary switching $S_d = 0$. The convolution operator evaluated at $\omega = 0$ can be expressed as:

$$S_1(\omega) * S_2(\omega)\Big|_{\omega=0} = \sum_{\xi=-\infty}^{\infty} S_{1(\xi)} S_{2(-\xi)} \tag{14}$$

Since the source V_{in} does not contain any harmonics at the multiples of the switching frequency (10) evaluates to zero. Therefore the source V_{in} has no influence on the current I_d.

B. The Influence of $B(\omega)$ on $I_d(\omega)$ in the Steady-State

From (7) it is clear that

$$\Psi(n) = \Psi(-n). \tag{15}$$

Evaluation of the convolution sum reveals:

$$\begin{aligned}
&-\frac{S_t(\omega)}{Z(\omega)} * 2S_d(\omega)\Big|_{\omega=0} \\
&= \sum_{\xi=-\infty}^{\infty} -\frac{S_{1(\xi)} + S_{2(\xi)}}{2Z(\xi 2\omega_s)}\Big(S_{1(-\xi)} - S_{2(-\xi)}\Big) \\
&= \sum_{\xi=-\infty}^{\infty} -\frac{\Psi(\xi)\Big(1+(-1)^{\xi}\Big)}{2Z(\xi 2\omega_s)}\Psi(-\xi)\Big(1-(-1)^{-\xi}\Big) \\
&= \sum_{\xi=-\infty}^{\infty} -\frac{\Psi(\xi)^2}{2Z(\xi 2\omega_s)}\Big(1+(-1)^{\xi}\Big)\Big(1-(-1)^{-\xi}\Big) \\
&= \sum_{\xi=-\infty}^{\infty} -\frac{\Psi(\xi)^2}{2Z(\xi 2\omega_s)}0 = 0
\end{aligned} \tag{16}$$

It follows that in the steady-state the value of V_t has no influence on the current I_d.

C. The Influence of $D(\omega)$ on $I_d(\omega)$ in the Steady-State

Evaluation of the convolution sum reveals, for interleaved switching:

$$\begin{aligned}
&-\frac{S_d(\omega)}{Z(\omega)} * 2S_d(\omega)\Big|_{\omega=0} \\
&= \sum_{\xi=-\infty}^{\infty} -\frac{\Psi(\xi)^2}{2Z(\xi 2\omega_s)}\Big(1-(-1)^{\xi}\Big)\Big(1-(-1)^{-\xi}\Big) \\
&= \sum_{\xi=-\infty}^{\infty} -\frac{\Psi(\xi)^2}{Z(\xi 2\omega_s)}\Big(1-(-1)^{\xi}\Big)
\end{aligned} \tag{17}$$

The sum can be simplified by adding the positive and negative parts of the sum together:

$$\begin{aligned}
&-\frac{S_d(\omega)}{Z(\omega)} * 2S_d(\omega)\Big|_{\omega=0} \\
&= \sum_{\xi=1,3,5}^{\infty} -2\frac{\Psi(\xi)^2}{Z(\xi 2\omega_s)} - 2\frac{\Psi(-\xi)^2}{Z(-\xi 2\omega_s)} \\
&= 2\sum_{\xi=1,3,5}^{\infty} \frac{-\Psi(\xi)^2 Z(-\xi 2\omega_s) - \Psi(\xi)^2 Z(\xi 2\omega_s)}{|Z(\xi 2\omega_s)|^2} \\
&= -4\sum_{\xi=1,3,5}^{\infty} \frac{\Psi(\xi)^2}{|Z(\xi 2\omega_s)|^2}\mathrm{Re}\{Z(\xi 2\omega_s)\}
\end{aligned} \tag{18}$$

Realising that in general $\omega L \gg r$ at the odd multiples of the switching frequency and substituting

$$\Psi(n)^2 = \frac{\sin^2(\pi n d)}{\pi^2 n^2}, \tag{19}$$

yields:

$$-\frac{S_d(\omega)}{Z(\omega)} * 2S_d(\omega)\Big|_{\omega=0} = -\sum_{\xi=1,3,5}^{\infty} \frac{\sin^2(\pi\xi d)r}{4\pi^4 L^2 f_s^2 \xi^4}. \tag{20}$$

It is clear that the convolution sum terms are always positive, resulting in a negative current, therefore the current I_d will always extract unbalance energy from the v_d capacitor. It is also clear that the convolution sum entries decrease with ξ^4, the second summation term is in the region of a 81^{th} of the first entry; for the remainder of the text only the first entry will be used to approximate the convolution sum.

With ordinary switching $s_d = 0$ and $I_d = 0$ under all circumstances.

IV. The Effect of Unequal Loads

When the loads R_1 and R_2 are unequal, the conductance $G_d \neq 0$. From Fig. 3 and using the results from the previous section the following expression for V_d in the steady state is found:

$$V_d G_t + V_d \frac{\sin^2(\pi d)r}{4\pi^4 L^2 f_s^2} = V_t G_d \tag{21}$$

It is true that in general

$$\frac{\sin^2(\pi d)r}{4\pi^4 L^2 f_s^2} \ll G_t. \tag{22}$$

Neglecting the effects of the harmonics, or equivalently assuming the circuit is operational with ordinary switching yields:

$$\begin{aligned}
V_d &= V_t \frac{G_d}{G_t} \\
&= V_t \frac{R_1 - R_2}{R_1 + R_2}
\end{aligned} \tag{23}$$

Translation of this result to the original circuit reveals,

$$\frac{V_1}{V_2} = \frac{R_1}{R_2} \tag{24}$$

similar to a resistive voltage divider. This result ignores the effect of the weak rebalancing mechanism (22), which will be discussed in the next section. Since the rebalancing mechanism is ignored this result gives the maximum voltage deviation due to unbalanced loads. As can be seen in the results of Fig. 7 the weak rebalancing mechanism limits the difference voltage under unequal load conditions.

V. Rebalancing Mechanisms

Having established that the steady-state value of V_d is zero when the loads are equal and a function of the respective loads when they are unequal, the reaction of the circuit to an external perturbation can be studied. Let $V_d(0)$ denote the initial deviation from the steady-state value of V_d, using the results from the previous sections, from Fig. 3 it follows that during rebalancing:

$$-C\frac{dV_d}{dt} = V_d G_t + V_d \sum_{\xi=1,3,5}^{\infty} \frac{\sin^2(\pi\xi d)r}{4\pi^4 L^2 f_s^2 \xi^4} \tag{25}$$

First consider the case when the circuit is operational with ordinary switching. As stated previously since $s_d = 0$ the current $I_d = 0$ and (25) simplifies to:

$$-C\frac{dV_d}{dt} = V_d G_t \tag{26}$$

With solution:

$$v_d(t) = V_d(0)e^{-\frac{t}{\tau}} \tag{27}$$

$$\tau = \frac{C}{G_t} \tag{28}$$

Since this rebalancing mechanism is always present, irrespective of switching regime, it is termed the strong rebalancing mechanism.

The weak rebalancing mechanism can best be studied in the theoretical case were both converters are unloaded, i.e. $R_1, R_2 \to \infty$ and $G_t \to 0$. In this case (25) can be rewritten as:

$$-C\frac{dV_d}{dt} = V_d \sum_{\xi=1,3,5}^{\infty} \frac{\sin^2(\pi\xi d)r}{4\pi^4 L^2 f_s^2 \xi^4} \tag{29}$$

With solution, using only the first term of the sum as approximation,

$$v_d(t) = V_d(0)e^{-\frac{t}{\tau}} \tag{30}$$

$$\tau \approx \frac{4\pi^4 L^2 f_s^2 C}{\sin^2(\pi d)r}, \tag{31}$$

when the circuit operates with interleaved switching. When ordinary switching is used no rebalancing is possible. This result illustrates the need to study the circuit in the frequency domain, if time averaging techniques are used the effect of the rebalancing due to the interleaving can not be identified.

In general when the circuit is operational with interleaved switching the rebalancing will be due to a combination of the strong and weak balancing mechanisms. However, due to the dimensioning of the filter components (determining the strength of the weak rebalancing mechanism) and the load (determining the strength of the strong rebalancing mechanism) the strong rebalancing mechanism dominates.

VI. Simulation Results

The theory presented was verified through comparison with a detailed time-domain simulation. A 2-cell CARC with the parameters tabulated in Table II was simulated. The inductor ESR might seem high but the converter dimensioning is such that the losses in it represents a 1.3% of the output power at full load. Likewise the inductance seems small, but due to interleaving of the cells and the operation at duty-cycles close to 50%, the ripple current is small. It can be shown that the converter is operational with a duty-cycle of 50% no current ripple is observed.

TABLE II
Component Values for a the CARC

V_t	1.65 kV	C	50 μF
L	1 mH	r	5 Ω
v_{in}	1 kV	f_s	10 kHz
R	500 Ω	ΔR	250 Ω
P	2.8 kW	d	40 %

Initially the loads are equal, $R_1 = R_2 = R$. At 50 ms a load unbalance of ΔR is introduced through adjusting the loads as follow:

$$R_1 = R + \frac{\Delta R}{2} \tag{32}$$

$$R_2 = R - \frac{\Delta R}{2} \tag{33}$$

This unbalance is removed again at 200 ms. First the effect of only the strong rebalancing mechanism is investigated by operating the cells with ordinary switching. In Fig. 4 it can be seen that the voltages balance initially and that during the perturbation the voltages share according to the estimation discussed in section IV. The rebalancing is shown in Fig. 5. It is clear that strong balancing is the only rebalancing mechanism, especially in comparison with Fig. 7.

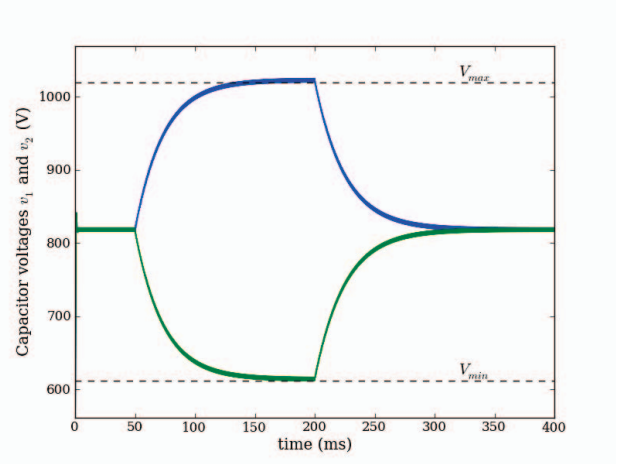

Fig. 4. The Two Cell Voltages During Perturbation: Ordinary Switching

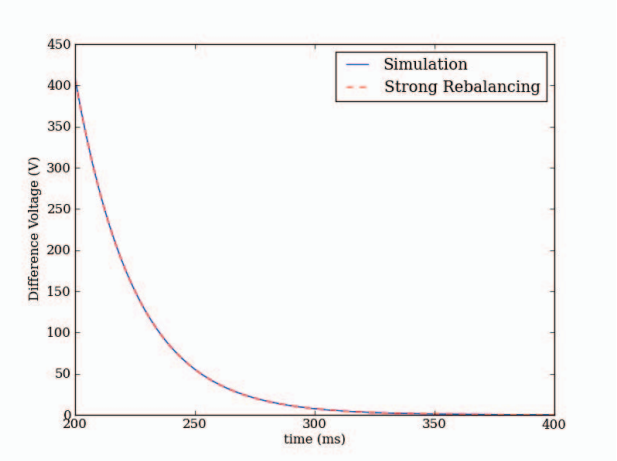

Fig. 5. Difference Voltage During Rebalancing: Ordinary Switching

The test is repeated with the cells operational with interleaved switching. The effect of the weak rebalancing mechanism on the steady state voltages during perturbation is clear in Fig. 6. The weak rebalancing limits the V_d voltage and hence the voltages do not deviate to the limits predicted by (24) unlike the full deviation with ordinary switching, Fig. 4. The

rebalancing of the difference voltage shown in Fig. 7 shows the effect of the weak balancing mechanism as the actual rebalancing is faster than that of the strong mechanism alone.

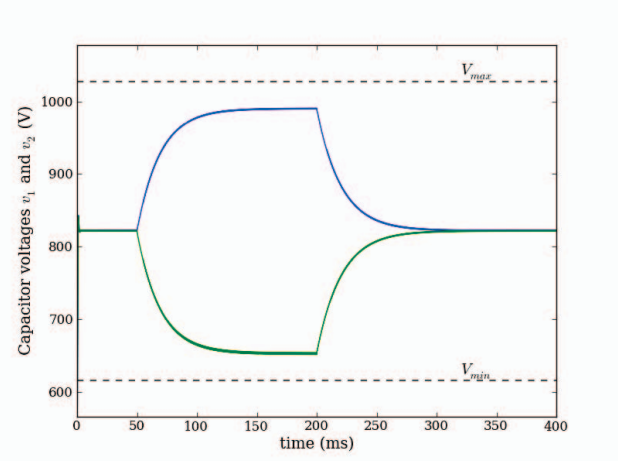

Fig. 6. The Two Cell Voltages During Perturbation: Interleaved Switching

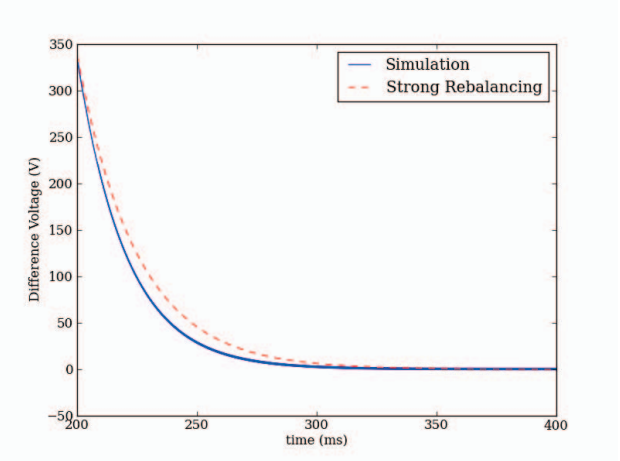

Fig. 7. Difference Voltage During Rebalancing: Interleaved Switching

VII. Addition of a Balance Booster

From (18) it is clear that the rebalancing current i_d is proportional to the ratio of the real part of the input filter impedance to the square of the absolute value of the impedance at the odd harmonics of $2f_s$. A notch filter, with a low impedance at $2f_s$, added in shunt with the filter impedance is often used with the flying capacitor converter, FCC, to adjust this ratio hence increasing the strength of the weak balancing mechanism. As with other multilevel converters the FCC exhibits natural balancing properties [8]–[10]. However, only the weak balancing mechanism is applicable to the FCC. When the notch filter, called a balance booster [9], [10], is well designed it provides a low and nearly real impedance path to the unbalance current, hence promoting rebalancing. Due to the effects of interleaving the balance booster conducts very little current unless unbalance in the circuit is present.

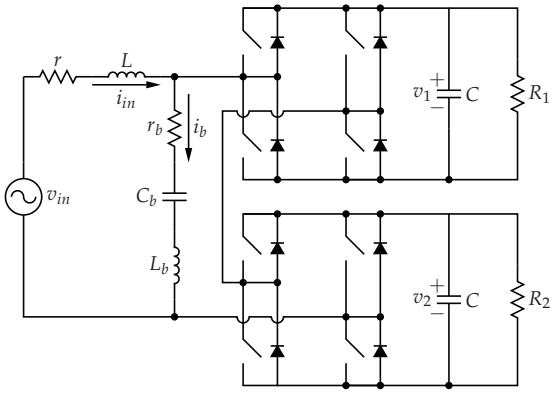

Fig. 8. 2-Level Cascaded Active Rectifier Converter Circuit with Additional Balance Booster

VIII. Modulated Duty Cycle

In most applications the CARC is used as a power factor correcting, PFC, rectifier; implying the use of a modulated duty cycle. The investigation of the circuit operation in the frequency domain, with modulated duty cycle, is possible by expressing the switching functions in Fourier series form using the double Fourier series method, [11].

For the purposes of the following discussion assume that the switching signals of the CARC operating as PFC rectifier is created through the comparison of a reference function and two interleaved triangular carrier signals as defined in (1). Under ideal conditions the reference function would be sinusoidal

$$f_r(t) = m_a \sin(\omega_r t), \tag{34}$$

and the harmonic content of the switching functions could be expressed analytically, where $J_k(x)$ denotes the Bessel function of the first kind [11], as:

$$s(t) = \sum_{k=-\infty}^{\infty} \sum_{m=-\infty}^{\infty} S_{(k,m)} e^{j(k\omega_r t + m\omega_c t)} \tag{35}$$

$$S_{1(k,m)} = \tilde{\Psi}(k,m) \tag{36}$$

$$S_{2(k,m)} = j^m \tilde{\Psi}(k,m) \tag{37}$$

$$\tilde{\Psi}(k,0) = \begin{cases} \frac{jm_a}{2} & \text{when } k=-1 \\ \frac{-jm_a}{2} & \text{when } k=1 \\ 0 & \text{when } |k| \neq 0 \end{cases} \tag{38}$$

$$\tilde{\Psi}(k,m) = \frac{j}{m\pi} J_k(\frac{\pi}{2} m m_a) \cos(\frac{\pi}{2} m)(-1^k - 1) \text{ when } m \neq 0 \tag{39}$$

The $\cos(\frac{\pi}{2}m)$ term in the expression for $\tilde{\Psi}(k,m)$ implies that the harmonic content for odd values of m will be zero. The carrier signals for the two cells are interleaved by adding a phase shift of, with reference to (1), $\theta_s = \frac{\pi}{2}$ to the carrier of the second cell, with the result that $S_{2(k,m)} = j^m S_{1(k,m)}$.

Assuming that the switching frequency is much higher than the highest frequency present in the reference function, the harmonics of the switching function will appear in clusters around the harmonics of the switching frequency [9], [11]. The harmonic content of selected functions are shown in Fig.9, for $f_s = 2$ kHz, $f_r = 50$ Hz and $m_a = 0.7$. It is important to note that:

1) The harmonic content of S_1 are arranged in clusters centred around multiples of 4 kHz. This is due to the apparent switching frequency doubling when unipolar switching is used [7].
2) The different clusters do not overlap, even in the case of a relatively low switching frequency of 2 kHz.
3) The function S_t contains only harmonic groups centred around multiples of 8 kHz. Similar to the results of the constant duty cycle case.
4) The function S_d contain only harmonic groups centred around the odd multiples of 4 kHz, again similar to the result of (13).

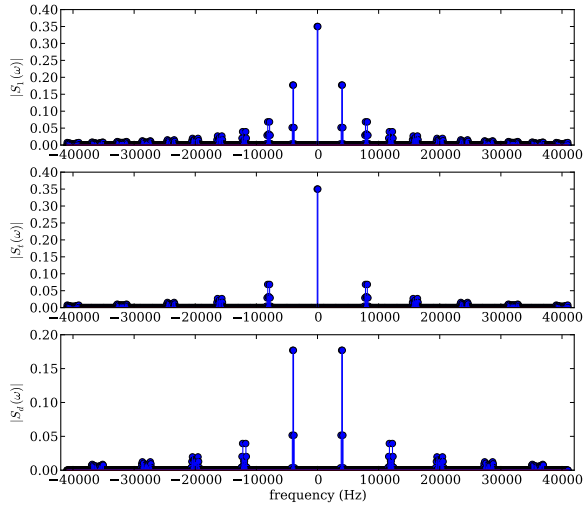

Fig. 9. Harmonic Spectrum of $|S_1(\omega)|$, $|S_t(\omega)|$ and $|S_d(\omega)|$.

It is clear that since the harmonic content of S_t and S_d occur at different frequencies that

$$\frac{S_t(\omega)}{Z(\omega)} * S_d(\omega)\bigg|_{\omega=0} = 0. \tag{40}$$

Likewise it is clear that for any source v_{in} with a harmonic spectrum bounded by the switching frequency

$$\frac{V_{in}(\omega)}{Z(\omega)} * S_d(\omega)\bigg|_{\omega=0} = 0. \tag{41}$$

Therefore, the rebalancing process can be expressed as:

$$-C\frac{dV_d}{dt} = V_d G_t + V_d \left.\frac{S_t(\omega)}{Z(\omega)} * 2S_d(\omega)\right|_{\omega=0} \tag{42}$$

TABLE III
COMPONENT VALUES FOR THE CARC

V_t	200 V	C	50 μF
L	6 mH	r	7 Ω
v_{in}	110 V_{rms}	f_s	6 kHz
R	1 600 Ω		

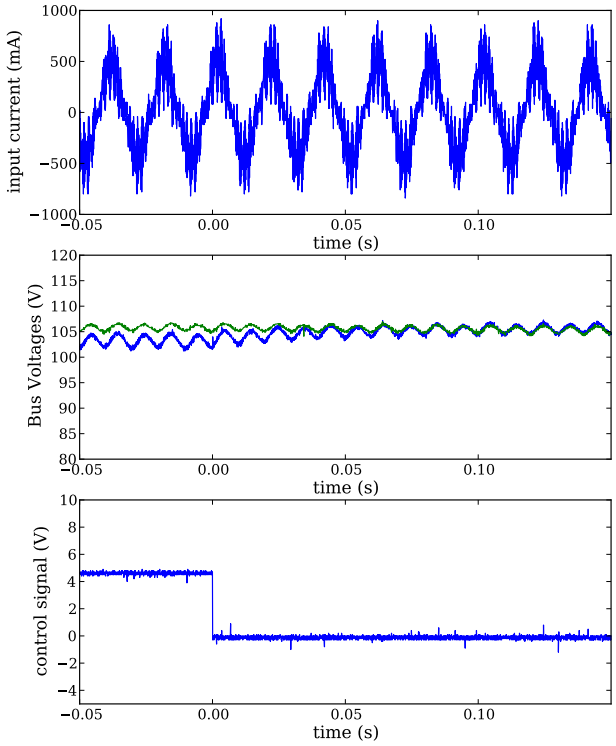

Fig. 10. Input Current, Bus Voltages and Control Signal Measurements of a PFC CARC Practical System

IX. PRACTICAL RESULTS

In this section practical measurements of a 2-cell CARC operational as a PFC is presented. The circuit parameters of the system are tabulated in Table III.

The system is operational with the conventional PFC control system with a fast inner current loop and slower outer voltage loop [12]. Each cell has an independent FPGA cell controller that accepts a reference function value and triangular carrier synchronisation marker from the main controller via a fibre optic link. Each cell controller uses the synchronisation marker to generate individual carrier signals that are compared to the reference function value to generate the switch PWM signals. In turn each controller measures the bus voltage of the cell and provides the measurement to the main controller. The main controller, also implemented in a FPGA, measures the input voltage, input current and receives the bus voltage measurements from the cell controllers. Through implementation of the

two loop control algorithm it calculates a reference function value that is send to both cell controllers. By interleaving the synchronisation pulses send to the two cell controllers the two cells can be operated with interleaved switching. An in depth discussion of the control implementation can be found in [13], [14].

The cell voltages are forced into an unbalanced state by multiplying the reference function value of cell 1 by a factor 1.1 for a certain period. After this period, as indicated by the control signal in Fig. 10, the same reference function is send to both cells. It is clear from Fig. 10 that the voltages rebalances as soon as the external disturbance is removed. The input current remains sinusoidal throughout.

The test is repeated for both interleaved and ordinary switching. The resulting difference voltages are shown in Fig. 11. It can be seen that the system operating with interleaved switching rebalances slightly quicker than when operational with ordinary switching.

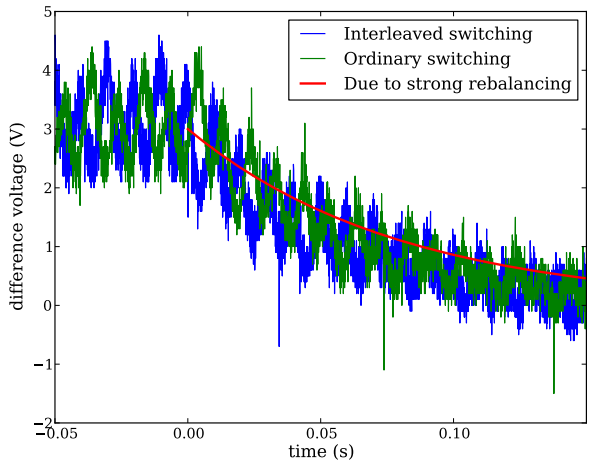

Fig. 11. Measured Difference Voltages During Rebalancing; Interleaved Switching and Ordinary Switching

X. Conclusion

A model for the natural balancing process of the 2-cell CARC was created in the frequency domain. Using this model two rebalancing mechanisms, weak and strong, were identified. Expressions for the respective balancing time constants were found. The presented theory, for the constant duty cycle case, was verified through comparison with detailed simulations.

The limitations of the rebalancing mechanisms were discussed. It was found that although the weak rebalancing mechanism have little influence on the rebalancing time constant it plays a large part in limiting the difference voltage when unequal loads are applied to the two cells. It is also possible to increase the strength of the weak balancing mechanism through the inclusion of a balance booster.

However, in most applications the CARC would operate with modulated duty cycle, such as when used in a PFC active rectifier. It is possible to express the rebalancing process for the modulated case in similar fashion as in the constant duty cycle case through use of the double Fourier series. It was shown that the results of the constant duty cycle case can be extended to the modulated case. Practical measurements of a PFC CARC are included as validation.

Acknowledgment

The authors would like to thank Louis Schietekat and Francois Breet for their help with the practical setup and measurements.

References

[1] J.-S. Lai and F. Z. Peng, "Multilevel converters-a new breed of power converters," *IEEE Transactions on Industry Applications*, vol. 32, pp. 509–517, May / June 1996.

[2] H. Iman-Eini, J.-L. Schanen, S. Farhangi, and J. Roudet, "A modular strategy for control and voltage balancing of cascaded h-bridge rectifiers," *Power Electronics, IEEE Transactions on*, vol. 23, no. 5, pp. 2428–2442, Sept. 2008.

[3] P. Zanchetta, D. Gerry, V. Monopoli, J. Clare, and P. Wheeler, "Predictive current control for multilevel active rectifiers with reduced switching frequency," *Industrial Electronics, IEEE Transactions on*, vol. 55, no. 1, pp. 163–172, Jan. 2008.

[4] P. Lezana, J. Rodriguez, and D. Oyarzun, "Cascaded multilevel inverter with regeneration capability and reduced number of switches," *Industrial Electronics, IEEE Transactions on*, vol. 55, no. 3, pp. 1059–1066, March 2008.

[5] C. Cecati, A. Dell'Aquila, M. Liserre, and V. Monopoli, "A passivity-based multilevel active rectifier with adaptive compensation for traction applications," *Industry Applications, IEEE Transactions on*, vol. 39, no. 5, pp. 1404–1413, Sept.-Oct. 2003.

[6] W. van der Merwe and T. Mouton, "Natural balancing of the two-cell back-to-back multilevel converter with specific application to the solid-state transformer concept," in *Industrial Electronics and Applications, 2009. ICIEA 2009. 4th IEEE Conference on*, May 2009, pp. 2955–2960.

[7] N. Mohan, T. Undeland, and W. Robbins, *Power electronics: converters, applications, and design*. Wiley New York, 2007.

[8] R. Wilkinson, T. Meynard, and H. du T. Mouton, "Natural balance of multicell converters: The general case," *IEEE Transactions on Power Electronics*, vol. 21, no. 6, pp. 1658–1666, Nov. 2006.

[9] R. Wilkinson, T. Meynard, and H. du Toit Mouton, "Natural balance of multicell converters: The two-cell case," *Power Electronics, IEEE Transactions on*, vol. 21, no. 6, pp. 1649–1657, Nov. 2006.

[10] T. Meynard, M. Fadel, and N. Aouda, "Modeling of multilevel converters," *Industrial Electronics, IEEE Transactions on*, vol. 44, no. 3, pp. 356–364, Jun 1997.

[11] D. Holmes and T. Lipo, *Pulse Width Modulation For Power Converters, Principles and Practice*. IEEE Press, 2003.

[12] P. Todd, "UC3854 controlled power factor correction circuit design," *Unitrode Application Note U-134*, 1997.

[13] C. Breet, H. du T. Mouton, and J. van der Merwe, "Modular cell controller and measurement system design for implementation in a solid-state transformer," in *Proceedings of the 19th South African Power Engineering Conference*, Johannesburg, South Africa, Jan 2010.

[14] L. Schietekat, H. du T. Mouton, and J. van der Merwe, "Design of a cascaded rectifier control strategy, implemented in the main controller of a solid-state transformer," in *Proceedings of the 19th South African Power Engineering Conference*, Johannesburg, Jan 2010.

MODULAR CELL CONTROLLER AND MEASUREMENT SYSTEM DESIGN FOR IMPLEMENTATION IN A SOLID-STATE TRANSFORMER

C.F. Breet, H. du T. Mouton and J.W. van der Merwe

Stellenbosch University, Department of Electrical and Electronic Engineering, Private Bag X1, Matieland, Stellenbosch, 7602, South Africa.

Abstract. This paper presents the measurement and control system designed to monitor and control the individual converter modules of a solid state transformer. Special consideration is given to the modularity of the design and the inherent advantages of such a system. Further information on the control and measurement circuitry is also provided, with particular reference to the central control and measurement systems.

Key Words. Solid-State Transformer; Input-Series-Output-Parallel; Modular; Controller; Measurement.

1. INTRODUCTION

With the ever-increasing demands placed on electricity distribution networks to conserve energy and to deliver reliable and especially more versatile energy options, it is increasingly necessary to develop a grid that facilitates these requirements. This resulted in the proposal of a smart grid model [1]. The model is aimed at establishing complete controllability and interconnectivity over a variety of distribution networks. With businesses, and even households, starting to produce their own electricity supplies, either as renewable or backup solutions, the central grid can be enhanced even further by selling excess power to the utility. With the improved information sharing capabilities of the smart grid, additional network controllability is gained, also referred to as cloud-based smart grid control [2]. This system suggests the use of web-based middleware to monitor and control interconnected networks, thus increasing the expansion capabilities of the network while minimizing the interruption of ongoing network operations. Although the system shows great promise, there is still a significant amount of research and development required to study the feasibility of these solutions.

With the smart grid in sight, the solid-state transformer (SST) aims to fit into this future network. The concept of the SST, also known as the intelligent universal transformer, was first introduced in 1980 with the objective of overcoming the various disadvantages of the line frequency transformer (LFT) [3], [4] and [5].

Fig. 1 illustrates the basic SST outline, which consists of three segments: converter(s) used to convert the incoming line frequency AC to the desired high frequency AC, a high frequency transformer used for galvanic isolation and lastly converter(s) to recreate the line frequency at the desired voltage [5].

The chosen SST topology, as discussed in [6], is shown in Fig. 2. An Input-Series-Output-Parallel (ISOP) configuration is used to overcome the problems caused by the high voltage side and to

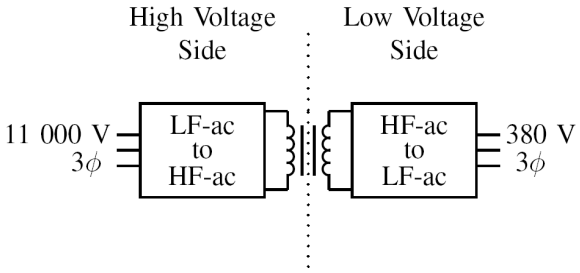

Fig. 1: Basic Solid-State Transformer Outline

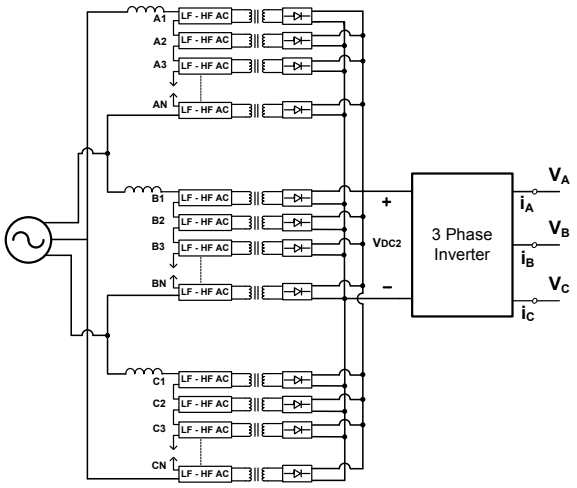

Fig. 2: SST Topology

achieve the required high to low voltage power conversion [5]. This is followed by a three phase inverter on the output stage of the SST.

Given the above mentioned SST configuration, illustrated in Fig. 2, it is required to develop a control strategy for this system. This paper will firstly discuss the desired modular system design parameters and the inherent advantages of increasing system modularity. Secondly, the measurement and control system that was developed to monitor and control the individual cells of the SST will be introduced followed by measurement results to validate the accuracy of the measurement acquisition system.

2. MODULAR CELL DESIGN

Functionality, complexity and cost are the most important factors to consider when designing a large and complex system like the SST. These parameters are often directly proportional to each other since, for example, an increase in functionality directly translates into an increase in complexity and cost. This section will discuss and elaborate on these factors, as well as present the chosen modular cell design and the advantages of a standardized system implementation.

Studies into the traditional implementation of ISOP stacked converter topologies have been under rigorous investigation in recent years [7], [8]. Various control techniques have been devised to achieve improved voltage balancing and current sharing between the modules [8], [9]. Considering the increased complexity of the solutions, a universal, more reliable and less complex solution is desired. Research on the natural balancing of similar converters in terms of duty cycle and transformer turns ratio mismatches showed promising results [10]. By switching the series connected cells in an interleaved pattern balance was obtained between the units.

A complete modular system design was desired to realize the SST. This would allow the SST to be as flexible as possible during its development and evaluation stages. It was thus decided to design standardized cells that would be stacked in a multilevel cascaded ISOP configuration to implement the SST (see Fig. 2). A generalized cell configuration was selected to increase the functionality of the cells. Each cell consists of two, back-to-back, full-bridge converters, as shown in Fig. 3 [11]. The first acts as an active rectifier, which is switched in a boost converter configuration and is used to control and maintain the desired inductor current of the SST as well as the DC-bus voltage of the cell [12]. This is followed by a DC-DC converter that transfers the power across the isolation barrier. The added benefit of this generalized configuration is the increase in its modularity, since it can be used in several other configurations.

Increasing the modularity of SST is especially important because it allows an increase in the redundancy, flexibility and thus functionality of the system. If all the cells are identical, a faulty cell can be isolated and simply replaced by another unit. By introducing redundant cells, the system can continue to function even if a cell fails, which also improves system reliability [5], [13]. Enhancing the controllability of each cell is thus also desired, since this will add to the isolation capabilities of the SST.

The designed SST control configuration, Fig. 4, consists of three main controllers, one per phase [14]. Each cell module has its own control and measurement system, which greatly reduces the control load of the main SST controllers and provides

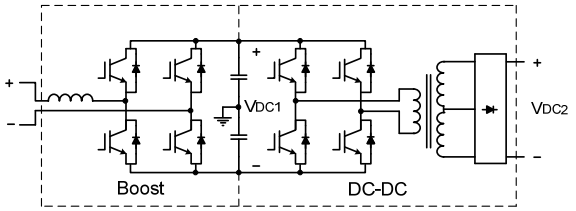

Fig. 3: Circuit Diagram of a Cell

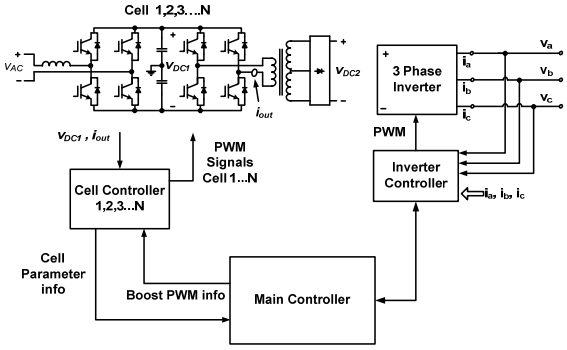

Fig. 4: SST Control Configuration

further monitoring capabilities. The main controllers will thus communicate with every cell controller and provide them with the necessary PWM information. Adding a dedicated controller for each cell also provides extra control lines, which enhances the functionality and reliability of the module. Additionally, this produces more accurate measurements, since the noise susceptibility of the measurement signals is significantly reduced due to the close proximity of the controller with relation to the measurement circuit.

A FPGA based control system was chosen because of its high-speed and parallel processing capabilities. By using such a controller, the various cell components can be managed almost simultaneously, with the only noteworthy delay being commands received from the main controller.

Due to the constant communication between the main controllers and their respective cells, additional isolation capabilities are also achieved. If communication with the main controller is lost, a cell can continue to function for a given period. If cell communication is not restored within a certain time frame, it can be shut down and isolated by its respective controller, and the utility informed to rectify the problem. This complete controllability of the cell can allow real-time data to be relayed to the utility, enabling increased monitoring capabilities for the SST.

As a result of this topology's completely modular nature the SST becomes fully scalable; this is particularly helpful during the development and experimentation stages of the SST. The additional application capabilities are an added benefit of the integrated cell, control and measurement module. The module can, for instance, be used as a standalone unit, or in various stacked topologies, such as ISOP and input-parallel-output-parallel (IPOP).

A significant limiting factor in respect of the design and development of the SST is cost. With the above mentioned modular cell design costs can be considerably reduced if the modules are created in sufficiently large enough quantities. Further integration of the cell's control circuitry, with the use of application-specific integrated circuits (ASICs), will greatly reduce the price and also increase the reliability of each module. Due to the high functionality of the design, it can be applied to various other operations, so it is not unreasonable to assume a significant decrease in cost, as soon as the technology has matured enough, which will result in an increase of the adoption rate of the module.

3. MEASUREMENT SYSTEM

Given the universal design of each cell module, various measurements are needed to ensure the correct operation and controllability of the SST. This section will discuss the measurement circuits used and the design criteria that were followed to create a fully modular cell design.

The measurement system layout, used to monitor the cell, is show in Fig. 5. This system consists of three types of measurement circuits, i.e. current measurement, voltage measurement and temperature measurement circuits.

3.1 Central Measurement Circuits

The primary measurement circuits are used to measure the current and voltage values of a cell.

Taking into consideration the noisy environment within which the measurement system must function, appropriate signal conditioning techniques are required to maximize the accuracy of the measurements and to reduce or eliminate any noise that gathers along the measurement paths. Since the measurement path includes an IDC interface that connects the measurement and control system, special attention should be paid to noise that may accumulate on the interface cable. By using a differential measurement acquisition system, any noise accumulated on the common-mode (CM) voltage of the signals can be discarded by using a differential analog-to-digital converter (ADC). This characteristic creates a system that is extremely immune to noise and also improves the distortion performance obtained, since differential signals eliminate all even order harmonics [15].

3.1.1 Current Measurement Circuit

Fig. 6 illustrates the circuit used to measure the primary transformer current, i_{out} (on the output of the DC-DC converter), shown in Fig. 4. This circuit utilizes a current transducer to generate a single-ended voltage that represents the measured transformer current. This measurement is then converted into a differential signal pair by a fully differential amplifier, which also serves to buffer the measurement signal.

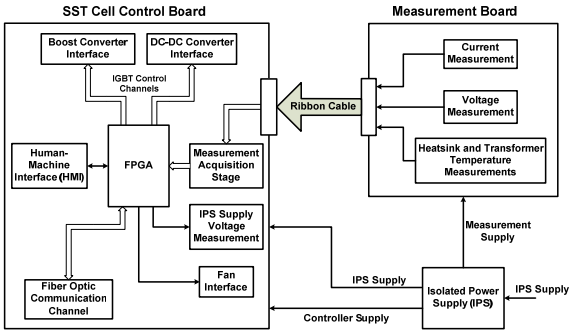

Fig. 5: Cell Control and Measurement System

To increase the accuracy and CM rejection of the measurement, an external, high accuracy reference chip is used to provide the required CM voltage. This reference voltage is applied to both the current transducer and op amp to decrease the deviations from the preferred reference voltage that cause unwanted offset errors on the measurement signal.

By adding a first-order differential low-pass filter (LPF), R5, R6 and C1 on the output of the measurement circuit, any unwanted high frequency noise can be eliminated. Care should be taken when driving capacitive loads with this circuit. The datasheet of the differential amplifier usually states the maximum capacitive load, or provides a diagram of the load resistance versus capacitive load, that can be connected to each of the outputs and still ensure accurate operation. R5 and R6 thus also serve to isolate the capacitive load from the loop gain path. By doing so the load is prevented from interacting with the output impedance of the differential amplifier, which could cause a phase shift in the loop gain. This phase shift, in turn, causes a reduction in the phase margin of the circuit, which results in oscillations on the output signals. (Overshoot, undershoot and ringing can also be expected when measuring a square-wave signal.) It is therefore advised to place the resistors as close as possible to the outputs of the op amp circuit.

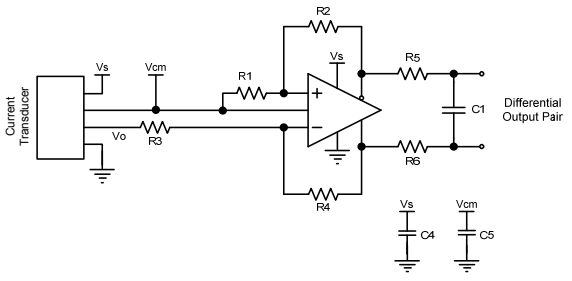

Fig. 6: Current Measurement Circuit

3.1.2 Voltage Measurement Circuit

Consider the circuit used to measure the DC-bus voltage of the cell shown in Fig. 7. Note that the ground used by the cell control and measurement system is situated in the centre of the DC-bus of the respective cell. Using this connection scheme enabled the differential measurement of the bus

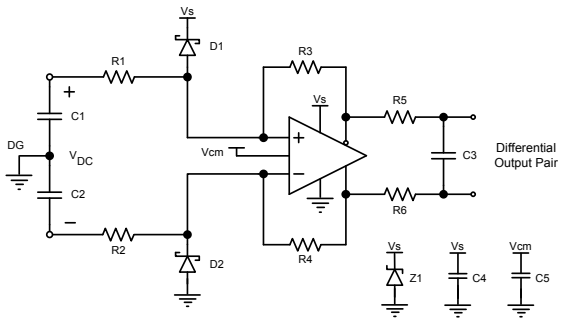

Fig. 7: Voltage Measurement Circuit

voltage. A fully differential amplifier is utilized to perform a differential-to-differential conversion which scales and level-shifts the measurement signals to the required values. The filter configuration implemented in this circuit is the same as discussed in section 3.1.1.

Various safeguards have been introduced to protect and ensure the safety of the measurement circuit. Schottky diodes, D1 and D2, have been placed to protect the op amp inputs against overvoltage fault conditions that may occur on the DC-bus side. A zener diode has also been placed to protect the measurement board's supply voltage, Vs, during possible faults.

3.2 Secondary Measurement Circuits

When considering the cell assembly, there are two temperature values that are of interest, namely the IGBT heatsink and high frequency transformer temperatures. These measurements only function as a safety measure and can be used to disable the SST if inadequate ventilation is present.

Fig. 8 shows the straightforward buffering circuit used to measure the desired temperatures of each cell. The circuit consists of an integrated-circuit (IC) temperature sensor, which provides a voltage value that is linearly proportional to the connected surface temperature. Since a cable is used to connect the sensor to the measurement board, three LPFs are used to filter the temperature sensor interface, and they are placed as close as possible to this interface.

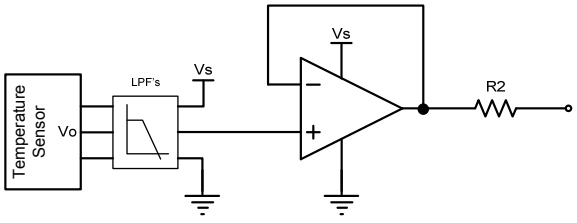

Fig. 8: Temperature Measurement Circuit

4. CELL CONTROL SYSTEM

The FPGA based control system that has been developed to monitor and control a cell is shown on the left hand side of Fig. 5. The majority of the components are self-explanatory. This section will provide supplementary information concerning the main components of the measurement acquisition stage, the isolated power supply (IPS) monitoring system and the fiber optic communication channel.

4.1 Measurement Acquisition Stage

The measurement acquisition stage consists of a variety of ADCs to acquire the measurement data received from the measurement board. This subsection will discuss the signal conditioning required by the primary ADC configuration circuitry.

Consider the ADC configuration (see Fig. 9) that is used to acquire the primary measurements provided by the measurement system, as discussed in section 3.1. This circuit uses a fully differential amplifier to drive the inputs of a high speed, pipelined, ADC with parallel outputs. By using the CM voltage output of the ADC to drive the reference input of the op amp, which performs a differential-to-differential conversion, it is ensured that the correct DC voltage is used to bias the differential inputs of the respective ADC.

As the ADC input is capacitive by nature, it is advisable to include small series resistors, R5 and R6, to isolate the ADC from its source, as discussed in section 3.1.1. These resistors also reduce the transient currents caused by the ADC's switched capacitive front end. By introducing a shunt capacitor, C1, the final measurement is limited to the desired bandwidth before concluding the measurement acquisition stage. To reduce the sampling noise of the ADC inputs even further, additional capacitors, C2 and C3, are also added.

Appropriate biasing of reference voltages is always required. This ensures that the voltages stay stable and it minimizes clock feed-through. Low inductance 100nF capacitors, C4 and C5, are recommended and should be placed as close as possible to the corresponding reference pins.

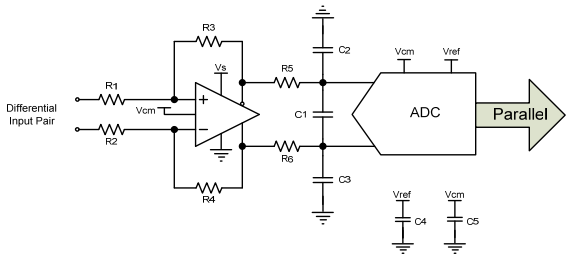

Fig. 9: Central ADC Configuration

4.2 Isolated Power Supply

Bearing in mind the series stacked configuration used to implement the SST, each cell module requires an IPS (see Fig. 5) [16]. As it is crucial for the cell module to be powered at all times, it was decided to implement a supervisory circuit for the supply's input voltage. The IPS supply measurement circuit utilizes an ADC to monitor the input voltage of the IPS. If the supply voltage drops below a certain threshold,

the main controller is notified to take corrective action.

4.3 Fiber Optic Communication Channel

The fiber optic channel is used for serial communication between the SST cells and their respective main controllers. This communication consists of PWM information concerning the boost converter, sent by the main controllers, and cell parameter information, sent by the individual cell controllers, as depicted in Fig. 4. Using fiber optics for data communication increases the reliability and safety of the system, since the main controllers are fully isolated from the core SST components.

PWM boost information is sent every switching period and consists of synchronization commands, used to synchronize the carrier signals of the controllers, and reference information, used to generate the IGBT gating signals.

Cell parameter information, in contrast, is sent multiple times every switching period, depending on the amount of information required, and consists of the requested measurement data and/or acknowledge commands to confirm instructions received from the main controller. Various error or warning messages are also sent if appropriate. The parameter information is then analyzed by the main controller and sent via a USB interface to a PC for data logging.

5. MEASUREMENTS

This section will present the measurement results, obtained from the primary measurement acquisition systems of a single cell module, as described in sections 3.1 and 4.1.

The following results were obtained by applying a DC voltage of 450V to the input of a cell, disabling the boost converter and switching the DC-DC converter of the module at a constant duty cycle.

Fig. 10 shows the DC-bus voltage, V_1, obtained with a high voltage differential probe, while Fig. 13 shows the primary transformer current, I_1, obtained with a DC coupled current probe. The corresponding measurements, obtained via the cell's primary measurement systems and extracted using the FPGA's Joint Test Action Group (JTAG) boundary-scan test (BST) interface, are shown in Fig. 11 and Fig. 14, respectively.

V_1 and V_2 both verify the bus voltage of 450V. Fig. 12 provides a comparison of V_1 and V_2. The voltage measurement, V_2, is extremely accurate since no additional peripheral devices were used to adapt the bus voltage to a lower, measureable value, with the only notable inaccuracies caused by the quantization noise of the ADC.

The current measurement, I_2 is relatively accurate when compared to I_1. Due to the lower bandwidth of the current transducer, I_2 does however display some measurement mismatches at the positions where the current changes are too quick.

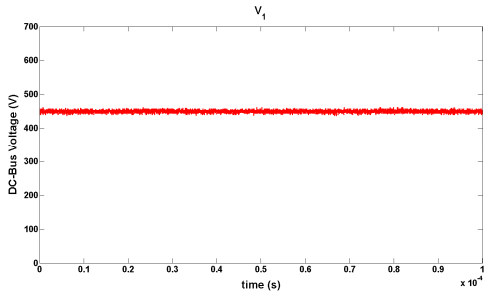

Fig. 10: DC-Bus Voltage, measured using Oscilloscope

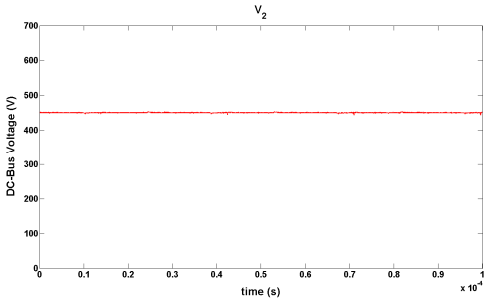

Fig. 11: DC-Bus Voltage, measured using measurement system

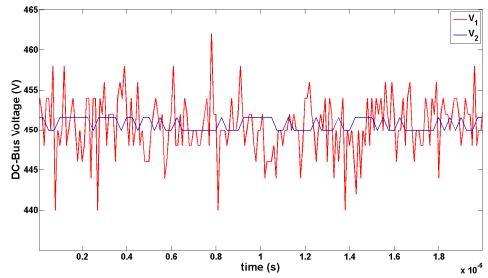

Fig. 12: DC-Bus voltage comparison

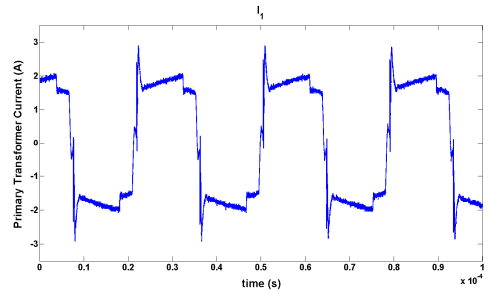

Fig. 13: Primary transformer current, measured using Oscilloscope

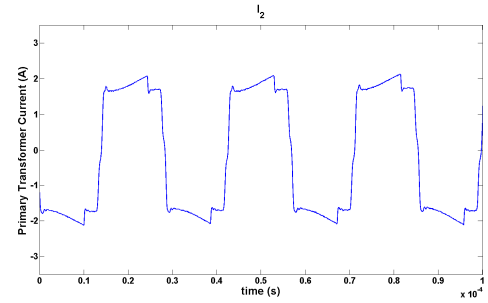

Fig. 14: Primary transformer current, measured using measurement system

CONCLUSION

The modularity of the series stacked configuration is of significant importance when assessing which topology should be used to realize the SST system, since the modularity greatly improves the maintainability and scalability of the SST [6]. By switching cells in an interleaving pattern, reliable natural balancing can be accomplished between the modules, which made it possible to design a modular SST system. This article discussed the modular cell design methodology which was followed, and the hardware development that was done, to implement a complete modular and reliable SST system. Further elaboration on the inherent advantages of such a universal system was also provided.

Measurement data of the designed measurement system illustrated the accuracy, noise resilience and thus reliability of the circuitry and signal conditioning techniques that were used. Further enhancements may involve increasing the bandwidth of the current measurement circuit, but this is not necessary at present.

ACKNOWLEDGEMENTS

The authors would just like to thank the South African National Energy Research Institute (SANERI) for their financial assistance during the development of the SST.

REFERENCES

[1] S. M. Amin and B.F. Wollenberg, "Toward a Smart Grid", *IEEE Power and Energy Magazine*, Vol.3, No. 5, pp. 34-41, September/October 2005.

[2] A. Ipakchi and F. Albuyeh, "Grid of the future", *IEEE Power and Energy Magazine*, Vol. 7, No. 2, pp. 52-62, March/April 2009.

[3] J. Brooks, "Solid state transformer concept development," Naval Material Command, Civil Engineering Laboratory, Naval Construction Battalion Center, Port Hueneme, CA, Tech. Rep., 1980.

[4] J.S. Lai, "Designing the Next Generation Distribution Transformers: New Power Electronic Based Hybrid and Solid State Design Approaches", *in Proceedings of the IASTED International Conference*. Palm Springs, CA, USA, 24-26 Feb 2003.

[5] J.W. van der Merwe and H. du T. Mouton, "The Solid-State Transformer Concept: A New Era in Power Distribution", i*n Proceedings of the IEEE Africon Conference*, Nairobi, Kenya, 23-25 Sep 2009.

[6] J.W. van der Merwe and H. du T. Mouton, "Solid-State Transformer Topology Selection", in *Proceedings of the IEEE International Conference on Industrial Technology*, Gippsland, Australia, 10-13 Feb 2009.

[7] V. Vorpérian, "Synthesis of Medium voltage dc-to-dc Converters From low-voltage, High Frequency PWM Switching Converters", *IEEE Transactions on Power Electronics*, Vol. 22, No. 5, pp. 1619- 1635, 2007.

[8] X. Ruan, L. Cheng, and T. Zhang, "Control strategy for input-series output-paralleled converter," *in Conference Record of the 2006 IEEE 37th Power Electronics Specialists Conference*, 18-22 June 2006, pp. 1 – 8.

[9] J.-W. Kim, J.-S. You, and B. Cho, "Modeling, control, and design of input-series-output-parallel-connected converter for high speed train power system*," IEEE Transactions on Industrial Electronics*, Vol. 48, No. 3, pp. 536–544, June 2001.

[10] J.W. van der Merwe and H. du. T. Mouton, "Balancing of a 2-Cell Modular Input-Series-Output-Parallel Converter with Common Duty Ratio Control under Converter Mismatch", *in Proceedings of the South African Universities Power Engineering Conference (SAUPEC) Conference*, Stellenbosch, South Africa, 28-29 Jan 2009.

[11] M. Wolf, "Design and Implementation of a Modular Converter with Application to a Solid State Transformer", Master's thesis, Stellenbosch University, 2008.

[12] J.W. van der Merwe and H. du T. Mouton, "Natural Balancing of the Two-Cell Back-To-Back Multilevel Converter with Specific Application to the Solid-State Transformer Concept"*, in 4th IEEE Conference on Industrial Electronics and Applications*. Xi'an, China, 25-27 May 2009.

[13] E. Choudhary, V. Ledezma, R. Ayyanar, and R. Button, "Fault tolerant circuit topology and control method for input-series and ouput-parallel modular DC-DC converters", *IEEE Transactions on Power Electronics*, Vol. 23, No. 1, pp. 402–411, 2008.

[14] L.M. Schietekat and H. du T. Mouton, J.W. van der Merwe, "Design of a Cascaded Rectifier Control Strategy, Implemented in the Main Controller of a Solid-State Transformer", *Submitted for review for the SAUPEC conference*, 2010.

[15] S. Paterson, "Maximize performance when driving differential ADCs", *EDN Design Engineering Magazine Article*, June 2003. www.edn.com

[16] P.S. Kemp and H. du T. Mouton, J.W. van der Merwe, "Design of an Isolated Resonant Switch-Mode Power Supply for a Modular Solid-State Transformer", *Submitted for review for the SAUPEC conference*, 2010.

Design of a Cascaded Active-Rectifier Control Strategy, Implemented in the Main Controller of a Solid-State Transformer.

L.M. Schietekat, H. du T. Mouton and J.W. van der Merwe

Department of Electrical and Electronic engineering, University of Stellenbosch, Private Bag X1, Matieland, 7602.

Abstract. This paper presents power-factor correction control applied to cascaded active-rectifiers. The control implements a double-loop strategy where the inner loop utilises average current mode control. The physical implementation of the control is discussed and the issues as well as the applied solutions thereof are presented. Emphasis is placed on the hardware computing power as well as the methods used to accomplish multisampling PWM.

Key Words. Power-Factor Correction Control, Multisampling PWM, Cascaded Active-Rectifiers.

1. INTRODUCTION

The line-frequency transformer (LFT) is the traditional method for transforming voltage levels in the power distribution grid. Due to the maturity of this technology, this method is both effective and cheap. However, as explained in [1], it introduces unwanted characteristics into the grid.

The solid-state transformer (SST) consists of three main sections, namely, a converter(s) section to create high-frequency AC from the input line-frequency AC, an isolation section with a high-frequency transformer, and lastly, another converter(s) section to create line-frequency AC output again. The SST, as an alternative to the LFT, addresses some of the distribution-system problems and all of the LFT problem areas. A few of the prominent advantages of the SST in comparison to the LFT, as stated in [1], are summarized below:

(i) Output-voltage regulation: The output voltage is immune to input-voltage sags and dips and free of power frequency harmonics. The output voltage is also regulated throughout the load range.

(ii) Input power-factor correction: The input current is controlled to be sinusoidal and in phase with the input voltage. The input of the SST is thus seen as a variable resistor.

(iii) Protection: The different controllers measure and have control over most operational parameters. This enables the SST to act as a fault barrier, between the input and output, able to make real time decisions regarding power flow during fault conditions.

(iv) Communication: The utility can be informed in the event of input faults such as voltage unbalancing or voltage sag, for corrective action. Certain SST outputs can be remotely controlled. Real-time and stored operational data can be available to the utility to be used for preventative maintenance.

The challenging aspects of the SST are the high-voltage (HV) side converter (because of the high voltage) and the high-frequency transformer (because of isolation and parasitic issues). Three well-known SST topologies are compared in [2]. These are the cascaded, diode-clamped and flying-capacitor converter topologies. It is concluded that the cascaded converter topology is the most feasible as a result of its cost and its modular nature.

This nature yields the implementation of the modular cell. In this paper the power-electronic configuration of the SST is briefly discussed as introduction to the controller-hardware configuration that enables all the added functionality of the SST. The hardware focus is on the main controller, whereas the software focus is on the active-rectifier control strategy.

2. POWER-ELECTRONIC CONFIGURATION

2.1 Three-phase SST topology

The three-phase SST, shown in Fig. 1, comprises three groups of N cascaded cells, one group per phase. The three-phase HV line-frequency AC input is connected in delta and the $3 \cdot N$ cell low-voltage (LV) DC outputs are connected in parallel. This is the LV bus voltage, V_{DC2}, of the three-phase inverter which, in turn, has a three-phase LV line-frequency AC output. As mentioned in [2], the modularity of this topology introduces scalability and improves maintainability.

2.2 Cell configuration

As mentioned, the cell consists of two back-to-back full-bridge converters. The front end converter is operated as an active-rectifier switched in a boost configuration. The active-rectifier ensures that the input current is sinusoidal and in phase with the input voltage and it also regulates the cell bus-voltage, V_{DC1}. This control is discussed in greater depth later in this paper. The second converter is a DC-DC converter that transfers the power across the isolation barrier. It consists of a full-bridge converter, an isolation transformer and a passive-rectifier. According to [3], the frequency of the DC-DC converter is limited by switching losses and parasitic inductances in the circuit. The cell configuration is shown in Fig. 2.

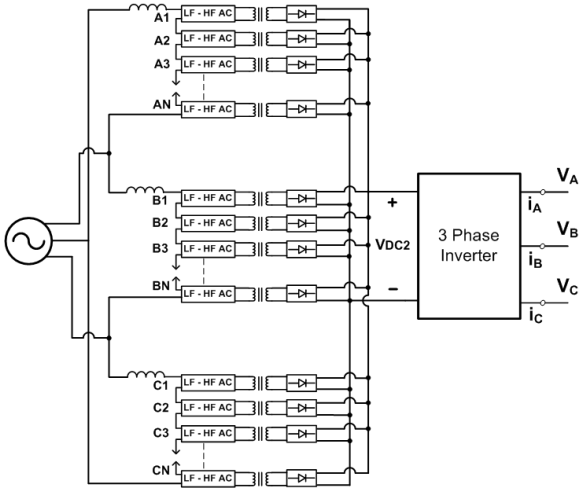

Fig. 1: Three-phase SST topology.

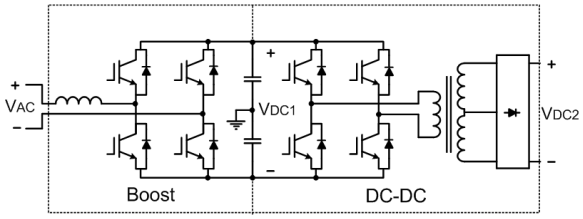

Fig. 2: Cell configuration.

3. CONTROL HARDWARE CONFIGURATION

There are three types of controllers present in the SST, namely, cell controllers (one for each cell), three main controllers (one for each phase) and an inverter controller.

3.1 Cell controller

The cell controller acts as the link between the main controller and each cell in the respective phase. The cell controller measures and monitors the operational parameters of the cell and sends regular status reports to the main controller. These reports indicate if the isolation-transformer input current and both the insulated gate bipolar transistors (IGBT) heat sink and transformer-core temperatures are within acceptable operating ranges. The report also relays the V_{DC1} measurement to the main controller, which is used in the active-rectifier control strategy. The cell controller also receives pulse width modulation (PWM) information from the main controller, which is used to generate duty cycles for the respective IGBTs.

3.2 Inverter controller

The inverter controller is responsible for one of the prominent advantages of the SST, namely the near perfect output voltage regulation. This is achieved with a double loop control strategy, for faster response. The strategy is developed in [3]. The inner loop controls the inductor current, whereas the outer loop controls the line-frequency AC load voltage. Communication is also available between one of the main controllers and the inverter controller.

3.3 Main controller

The main controller is the main hardware focus of this paper. It consists of five printed circuit boards (PCBs): The controller board, the fiber optic interface board and three measurement boards. The measurements taken by the latter are the input inductor current, I_L, at the front end of the cascaded cell group, the input voltage, V_{AC}, and the three-phase inverter bus voltage, V_{DC2}. The fiber optic interface PCB enables communication between the main controller and all the cell controllers in the respective phase and between the main controllers of each phase. Fiber optics are used because of immunity to system noise and to isolate the main controller from the cell controllers. As shown in Fig. 3, the controller PCB consists of a field programmable gate array (FPGA), three high-speed analog to digital converters (ADCs), flash memory, double data rate (DDR) memory, a real-time clock, a soft-start system interface and a USB interface.

The FPGA is configured using VHDL. This means that one actually creates logic, which has two very important advantages. The first is the ability to perform separate functions in a parallel fashion. For example, status reports can be received from multiple cell controllers at the same time, while a control strategy is implemented and while operational data is being stored etc. The second advantage is the speed at which operations can be executed. The high-speed FPGA together with the high-speed ADCs (53MSPS) enable the main controller to implement a high-speed control strategy (10MHz) to achieve multisampling PWM.

A Nios II embedded processor system is implemented to manage housekeeping on the main controller. As stated in [4], such a system can be implemented on a single Atera® chip; it includes a Nios II processor core, a set of on-chip peripherals, on-chip memory and off-chip memory interfaces. The DDR memory serves as an extension of the on-chip memory. Housekeeping involves, for example, the management of operational data and communication. The Nios II processor manages the

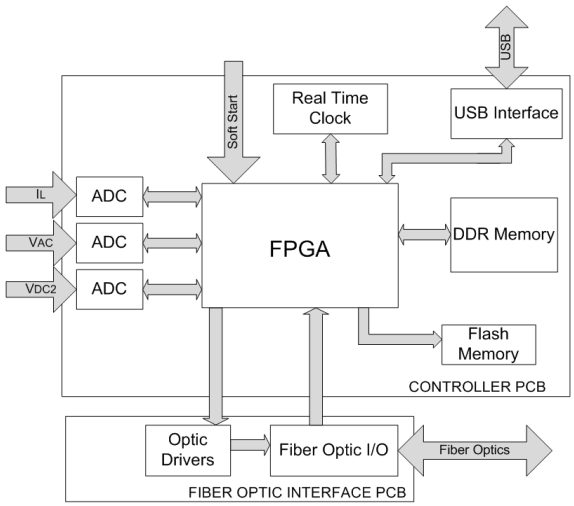

Fig. 3: Main controller block diagram.

communication interfaces between the FPGA, real-time clock, flash memory, DDR memory and USB interface device. The Nios II processor also gathers measurement data, uses the real-time clock to add time stamps and saves the data in flash memory. Using this combination of the FPGA and the Nios II processor thus yields the functionality to implement the fast, parallel input/output, control strategy, while still having the ease of use of a micro controller for housekeeping functions.

The soft-start system enables the SST to start up without damaging transition-stage currents.

The USB interface adds functionality as listed below:

(i) Measurements from the measurement PCBs and the cell controllers can be sent to a PC for analysis during the SST design and testing phase.

(ii) Operational data stored in flash memory can be downloaded to a laptop or any other data-capture device.

(iii) A GSM or Bluetooth module can be included enabling remote control of the system as well as communication with the utility. The utility can thus be informed of the nature and extent of faults.

4. CASCADED ACTIVE-RECTIFIER CONTROL STRATEGY

This strategy is aimed at regulating the power flow by regulating the active rectifier output voltage, V_{DC1}, as well as the unity power factor, by ensuring that I_L is sinusoidal and in phase with V_{AC}. The control discussed in this section pertains solely to the front end of the cell, being the active-rectifier.

Average current mode control is implemented as opposed to peak current mode control and it incorporates a high gain integrator into the current loop. As discussed in [5], this control method enables the inductor current to track its reference with a high level of accuracy and also supplies the control system with a high level of noise immunity.

Fig. 4 is a block diagram of the power factor correction control strategy. As discussed in [6], the current loop is controlled by the input voltage, V_{AC}, so that the converter appears to be resistive. V_{DC1}, in contrast, is controlled by varying the current-reference amplitude. To maximize the power factor, the current reference must match V_{AC} as closely as possible. If the voltage-loop bandwidth is too large, it will try to keep V_{DC1} constant and thus distort I_L.

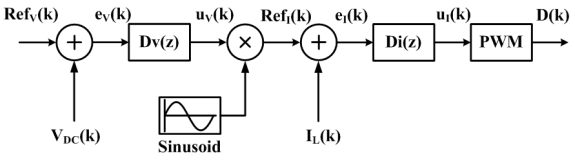

Fig. 4: Power-factor correction control strategy.

Conversely, the bandwidth should be as large as possible to minimize the output voltage transient response. The voltage-loop bandwidth is thus set to less than the input line frequency; however, the current loop needs a much larger bandwidth, as large as possible without causing system instability.

The only way to use this control strategy on a set of cascaded active-rectifiers is to have a single double loop system sending switching signals to all the active-rectifiers. As is explained in section 4.2 below, the active rectifier switching is interleaved. Fig. 5 shows the equivalent circuit of a group of cascaded active-rectifiers, for simulation purposes, and Fig. 6 shows the physical implementation of this control strategy.

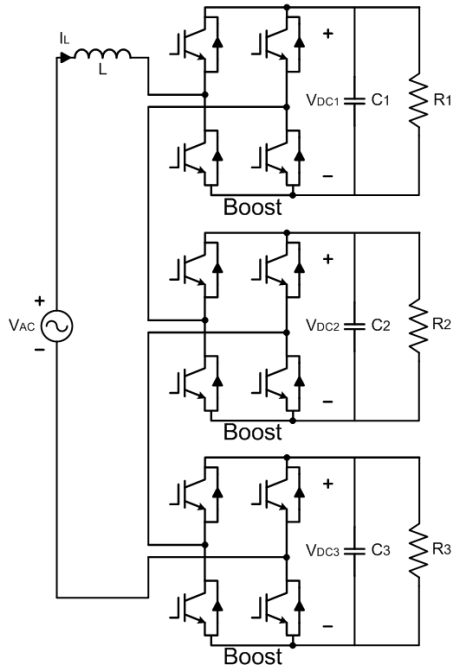

Fig. 5: Cascaded active rectifier circuit diagram.

4.1 Current loop

The inductor current, I_L, is measured, as an analog signal, with one of the three measurement channels. This channel consists of a LEM current transducer that converts the I_L measurement to a voltage. This voltage is then converted to a differential signal-pair, V_{ILdiff}, by the measurement PCB. It is carried to the controller PCB in differential mode because of its resistance to system noise. On the controller PCB, the signal is fed to one of the high-speed ADCs to be converted to a 12-bit digital signal.

This signal is compared to a current reference, Ref_I, and the error, e_I, is fed to the controller block $D_I(z)$. The controller block output, u_I, is the PWM reference. This signal is compared to two PWM carrier-signals per cell. The reference value, where the reference intercepts either of the carriers, is sent to the corresponding cell controller via the implemented serial communication interface (SCI) and the fiber optic interface PCB. The signal is thus converted from a digital signal to a serial optic signal.

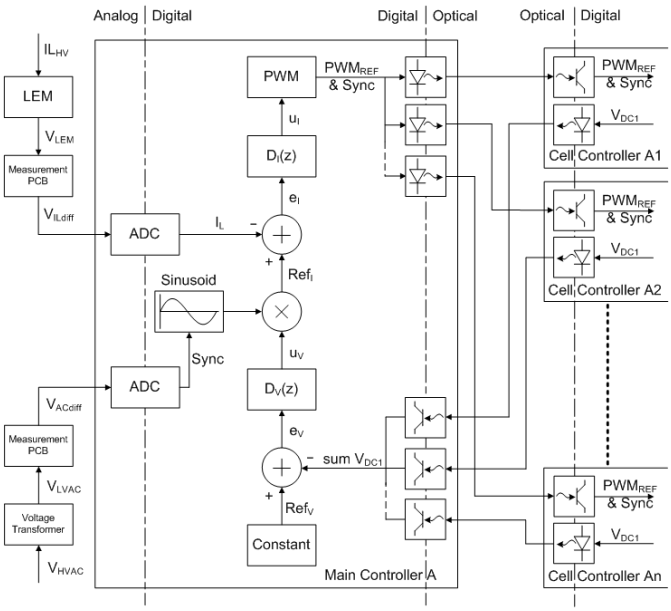

Fig. 6: Physical implementation of the active rectifier control strategy.

4.2 PWM generation

The active-rectifier switching frequency is 10 kHz, which means that the two carrier signals have a frequency of 10 kHz. There are two carrier signals because of the unipolar switching scheme. In this scheme, the two carrier signals are shifted 180° with respect to each other, which yields an effective active-rectifier switching frequency of 20 kHz. The respective cells in the phase group, however, are switched in an interleaved fashion, resulting in an effective phase group switching frequency of N·20 kHz.

Saw-tooth PWM carriers are used, thus implementing asymmetrical PWM. The alternative would be to use triangular carriers and thus implementing symmetrical PWM. The saw-tooth carrier yields more harmonics, but these are acceptable, given the high effective switching frequency. Added advantages of asymmetrical PWM are that it simplifies the analysis of the system and makes the PWM less vulnerable to reference ripple. As indicated by [7], PWM reference ripple compensation is also simpler to implement with asymmetrical PWM. This ripple component is caused by the high bandwidth of the current loop, and the ripple amplitude is thus proportional to the current-loop gain, as discussed in [5].

Fig. 7 shows exactly how the PWM switching information is sent from the main controller, where the control is implemented, to the cell controller, where duty cycles are generated and sent to the respective IGBT drivers on the cell itself. The main controller sends two types of data packages, viz. a synchronize package and a reference package. The synchronize package is sent on the falling edge of the main controller's carrier1 signal, which triggers the cell controller to wait t_{delay1} seconds before resetting its carrier signals. The communication delay, caused by the respective buffers and fiber optic drivers and receivers, is depicted as t_{delay2}. This results in the cell controller carrier signals being $t_{delay1} + t_{delay2}$ seconds behind the main controller carrier signals. The reference package is sent at the same time as a main controller reference-carrier-crossing, which results in a cell controller reference update with a delay of t_{delay2} seconds, well before a cell controller reference-carrier-crossing. Defining t_{delay1} ensures the continual implementation of multisampling PWM. The only difference between the reference-carrier-crossings of the two controllers is caused by aliasing effects in the main controller. It can clearly be seen how this communication method is less vulnerable to the reference ripple by effectively sampling exactly at a reference-carrier-crossing. An effective reference is thus created on the cell controller, as depicted by the dotted line in Fig. 7.

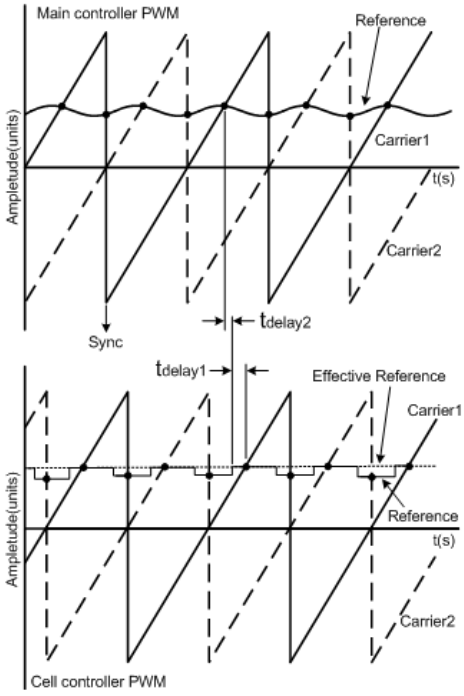

Fig. 7: PWM information communication protocol.

4.3 Voltage loop

The active-rectifier output voltages, V_{DC}, are measured as analog values and converted to digital signals by the respective cell controllers. The measurements are passed on to the main controller, once a switching period, via the implemented SCI interface and the fiber optic interface PCB. It is thus converted to a serial optic signal and then back to a 12-bit digital signal on the main controller.

The signals received from all the cell controllers, in the respective phase, are added together to represent the total output voltage, sum V_{DC}. This signal is compared to the constant voltage reference, Ref_V. The error, e_V, is fed to the controller block $D_V(z)$, and the controller block output, u_V, is multiplied with a unit amplitude sinusoid signal, synchronized with V_{AC} to generate the current reference of the current loop, Ref_I, in phase with V_{AC}.

This means that the current is always forced to follow a sinusoid, although the amplitude of this sinusoid is determined by the voltage loop, indirectly forcing the V_{DC} to follow a voltage reference.

5. SIMULATION RESULTS

The current and voltage loops are tested by means of time-domain simulations. Simplorer 8 from Ansoft LLC was used to simulate the interleaved switching of the cascaded active-rectifier circuit shown in Fig. 4 and the circuit parameters are listed in Table 1. I_L tracking Ref_I is shown in Fig. 8. The inductor current ripple is the sum of the ripples caused by each of the three active rectifiers and, as Fig. 9 indicates, the three separate ripples cancel out at certain time instances.

Table 1: Simulation parameters.

V_{AC}	2.5kV	Pout	2kW
L	21.07mH	V_{DCA1-3}	1000V
C_{A1-3}	50µF	R_{A1-3}	500Ω

The V_{DC} ripple amplitude, however, is determined by the cell bus capacitor size and, as shown in Fig. 10, is 60V. This figure also indicates the V_{DC} settling time if the bus capacitors are charged to V_{DC} before switching begins. The settling time is determined by the gain component of controller block $D_V(z)$. As mentioned, there is a tradeoff between V_{DC} settling time and Ref_I distortion with regard to this gain component. Fig. 11 shows that the $D_V(z)$ output, u_V, is effectively not as constant as ideally required, and the gain component determines the ripple amplitude present on this signal. Because this ripple is multiplied with the unit-amplitude sinusoid, Ref_I is distorted. A sinusoid with the same amplitude as Ref_I is added in Fig. 11 to show clearly the slight Ref_I 3rd harmonic distortion created by a $D_V(z)$ gain of 1 unit.

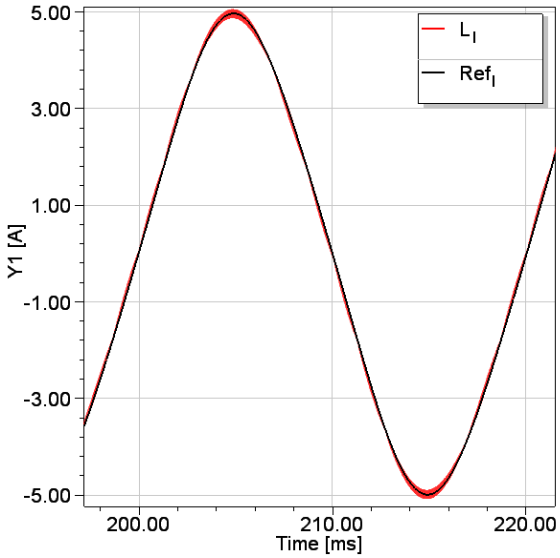

Fig. 8: Input inductor current tracking the current reference.

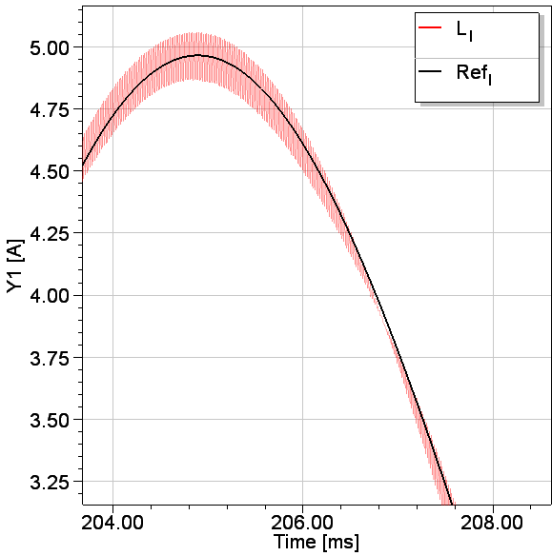

Fig. 9: Inductor current ripple and ripple cancelation.

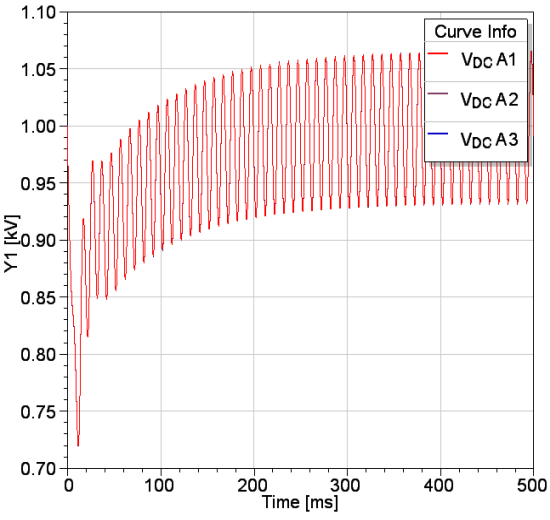

Fig. 10: Bus voltage ripple and transient response.

The result of the natural voltage balancing mechanisms of cascaded active-rectifiers can be seen in Fig. 12, where a load-step is implemented in one

of the active-rectifiers. The load R_{A1} is stepped down from 500Ω to 250Ω at Time = 300ms and stepped back up to 500Ω at Time = 450ms. The two balancing mechanisms present are the strong balancing mechanism, determined by the load, and the weak balancing mechanism, determined by the filter components, as discussed in [8].

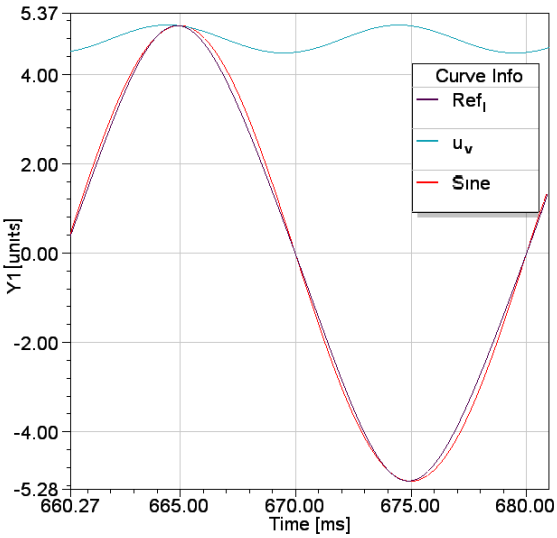

Fig. 11: Current reference 3rd harmonic distortion.

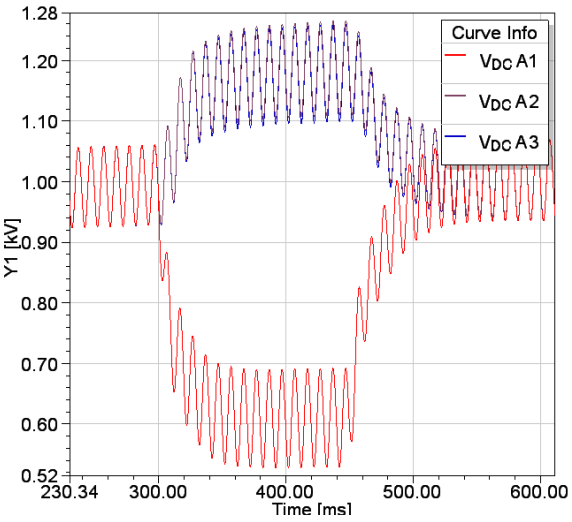

Fig. 12: Natural voltage balancing.

6. CONCLUSION

A power-factor correction control strategy, incorporating average current mode control, is applied to a set of cascaded active-rectifiers. The physical implementation of this control strategy is discussed with emphasis on the computing power that enables multisampling PWM. Simulation results are obtained to verify the functionality of this strategy and to confirm the presence of voltage balancing mechanisms introduced by interleaved switching.

ACKNOWLEDGEMENTS

The authors would like to thank SANERI for their ongoing financial support for the development of the SST.

REFERENCES

[1] van der Merwe, W. and Mouton, H du T.: The Solid-State Transformer Concept: A New Era in Power Distribution. In: *Proceedings of the IEEE Africon Conference*. Nairobi, Kenya, 23-25 Sep 2009.

[2] van der Merwe, W. and Mouton, H. du T.: The Solid-State Transformer Topology Selection. In: *Proceedings of the IEEE International Conference on Industrial Technology*. Churchill, Victoria 3842 Australia, 10-13 Feb 2009.

[3] Wolf, M.: *Design and implementation of a Modular Converter with Application to a Solid- State Transformer*. Master's thesis, Stellenbosch University, 2009.

[4] *Nios II Processor Reference Handbook*. Altera Corporation. Available at: http://www.altera.com. May 2004.

[5] Dixon, L.: Average Current Mode Control of Switching Power Supplies, Application note. Unitrode Application handbook, U-140.

[6] Todd, P. C.: Controlled Power Factor Correction Circuit Design, Application note. Unitrode Application handbook, U-134.

[7] Mouton, H. du T. and Putzeyz, B.: Digital Control of a PWM Switching Amplifier with Global Feedback. In: *Proceedings of the AES 37th international conference*. Hillerød, Denmark, 28-30 Aug 2009.

[8] van der Merwe, W. and Mouton, H du T.: An Investigation of Natural Balancing Mechanisms of Cascaded Active-Rectifiers. To be reviewed.

Appendix C

Selected Python Programs

C.1 ISOP Converter

C.1.1 Time Domain Simulations

```
from __future__ import division
from pylab import*
from scipy.integrate import odeint

# This file simulates the 2-cell isop converter using the scipy odeint function
# Capabilities are built in to simulate:
#   Cells with different duty-cycles
#   Keeping the unbalance voltage constant to investigate rebalancing current
#   Changing the interleaving of the cells
#   Changing the paramter values of the different cell parameters to investigate their influence
#
# Wim van der Merwe
# 2 February 2010

#################################################################
## Input of circuit parameters and initial values              ##
#################################################################

# Circuit Parameters

similar = 1             # Boolean to state if the cells are similar (0 => FALSE)
interleaved = 1         # Boolean to state if the cells are interleaved
circular = 1            # Set boolean to test circulating currents
L1 = L2 = 1e-3          # Inductance
r1 = r2 = 0.5           # resistance
C1 = C2 = 500e-6        # Capacitance
d1 = d2 = 0.8           # Duty cycle
Ls = 50e-9              # Source inductance
rs = 0.2                # Source resistance
C = 4700e-6             # Output Capacitor
R = 300                 # Load resistance


fs = 10000              # Switching Frequency
tend = 0.08             # Simulation time end
dt = 500e-9             # time step

Vin = 1600              # input voltage
dV = 200                # Change in voltage during unbalance
t0 = 0.05               # time point where unbalance is introduced

# Initial Values
```

```
i_in0 = 0
v_10 = 0
v_20 = 0
i_10 = 0
i_20 = 0
v_o0 = 0

x0 = array([i_in0, v_10, v_20, i_10, i_20, v_o0])



#####################################################################
## Change of circuit parameters if the cells are not similar  ##
#####################################################################

if not(similar):
    L2 = 300e-6
    r2 = 0.4
    C2 = 400e-6
    d2 = 0.8

#####################################################################
## Function that determines the derivative of the states      ##
## at every point in time. Generates switching states from    ##
## time stamp and returns derivative as vector.               ##
#####################################################################



def F(y,t):
    carrier1 = (2/pi)*arctan(tan(2*pi*fs*t))+0.5
    if interleaved:
        carrier2 = (2/pi)*arctan(tan(2*pi*fs*t+0.5*pi))+0.5
    else:
        carrier2 = carrier1

    ## With the switching function definitions, the arctan(tan(x)) yields a sawtooth with
    ## frequency twice x. This is desireable since the full-bridge converter modelled by
    ## the perfect transformers also implies a doubling frequency. The addition of 0.5*pi
    ## to force the interleaving due to this frequency doubling. It yields a 180deg shift.

    if t < 10e-3:
        d1e = (t/10e-3)*d1
        d2e = (t/10e-3)*d2              # Soft start
    else:
        d1e = d1
        d2e = d2
    s1 = carrier1<d1e
    s2 = carrier2<d2e      # generate the switching functions

    # Calculate derivatives

    [Is, v1, v2, i1, i2, vo] = y
    dIs = (1/Ls)*(Vin - v1 - v2 - rs*Is)
    dv1 = (1/C1)*(Is - s1*i1)
    dv2 = (1/C2)*(Is - s2*i2)
    if circular:
        if t > t0:
            dv1 = dv2 = 0
    di1 = (1/L1)*(s1*v1 - r1*i1 - vo)
    di2 = (1/L2)*(s2*v2 - r2*i2 - vo)
    dvo = (i1 + i2 - vo/R)/C

    return array([dIs, dv1, dv2, di1, di2, dvo])
```

```
t1 = arange(0,t0,dt)

y1 = odeint(F,x0,t1)

[Is, v1, v2, i1, i2, vo] = y1[-1,:]
v1 = v1 + 0.5*dV
v2 = v2 - 0.5*dV


y0 = array([Is, v1, v2, i1, i2, vo])
t2 = arange(t0,tend,dt)
y2 = odeint(F,y0,t2)

vdint = y2[:,1] - y2[:,2]
id = y2[:,3] - y2[:,4]

if not(circular):
    tau = 2*L1/r1
    energy = [0]
    for n in range(1,size(t2)):
        energy.append(energy[n-1] + id[n]**2*r1*dt)


    figure()
    plot(1000*t2-50,y2[:,3],'b')
    plot(1000*t2-50,y2[:,4],'g')
    ylabel('Cell output current (A)')
    xlabel('time (ms)')
    legend(('Current $i_1$','Current $i_2$'))
    axis([0,30,-60,60])

    figure()
    plot(1000*t2-50,vdint)
    plot(1000*t2-50,200*exp(-(t2-t0)/tau),'g')
    legend(('Simulated value','Time constant approximation'))
    plot(1000*t2-50,-200*exp(-(t2-t0)/tau),'g')
    xlabel('time (ms)')
    ylabel('difference voltage (V)')
    axis([0,30,-100,250])

    fig = figure()
    ax1 = fig.add_subplot(111)
    ax1.plot(1000*(t2-t0),energy,'b', linewidth=2)
    ax1.set_xlabel('time (ms)')
    # Make the y-axis label and tick labels match the line color.
    ax1.set_ylabel('Energy (J)', color='b')
    plot(0,0,'g')
    legend(('Energy dissipated in $r$','Difference current'),loc = 4)
    for tl in ax1.get_yticklabels():
        tl.set_color('b')

    ax2 = ax1.twinx()

    ax2.plot(1000*(t2-t0), id, 'g')
    ax2.set_ylabel('Difference current (A)', color='g')
    for tl in ax2.get_yticklabels():
        tl.set_color('g')

else:
    figure()
    plot(1000*t1,y1[:,3],'b',label='Current $i_1$')
    plot(1000*t1,y1[:,4],'g',label='Current $i_2$')
    plot(1000*t2,y2[:,3],'b')
    plot(1000*t2,y2[:,4],'g')
    legend(loc=2)
```

```
    xlabel('time (ms)')
    ylabel('Current (A)')
    axis([30,80,-150,150])

    figure()
    plot(1000*t1,y1[:,-1],'b')
    plot(1000*t2,y2[:,-1],'b')
    ylabel('Output voltage (V)')
    xlabel('time (ms)')

show()
```

C.2 Flying Capacitor Converter

C.2.1 Flying Capacitor Toolkit

```
from pylab import*
from scipy.special import jn

def Generate_Frequency_Vector(k,m,fr,fc):
    f = []                  # Create empty list
    for x in m:             # Steps in fc
        for y in k:         # Steps in fr
            f.append(x*fc+y*fr)
    return array(f)

def Modulated_Fourier_Coef(k,m,ma,a,N):
    # k : Steps in fr
    # m : Steps in fs
    # ma : Amplitude modulation index
    # a : ath cell in a... (0<= a <= N-1)
    # N : N-cell structure
    C = []              # Create empty list
    for x in m:         # Steps in fc
        if x <> 0:
            for y in k:     # Steps in fr
                B = jn(y,0.5*pi*x*ma)*(1j)/(x*pi)
                B = B*exp(1j*a*2*pi*x/N)
                C.append(B*(exp(1j*pi*x/2)*exp(1j*pi*y) - exp(-1j*pi*x/2)))
        else:
            for y in k:
                if y == -1:
                    C.append(1j*ma/2)
                elif y == 1:
                    C.append(-1j*ma/2)
                else:
                    C.append(0)
    return array(C)

def Const_Fourier_Coef(n,D,a,N):
    # n : Steps in fs
    # D : Duty cycle
    # a : ath cell in a... (0<= a <= N-1)
    # N : N-cell structure
    C = []
    for x in n:
        if x!=0:
            B = (1j/(pi*x))*(exp(-1j*x*2*pi*D)-1)
            C.append(B*exp(-1j*a*2*pi*x/N))
        else:
            C.append(2*D-1)
    return array(C)

def ZCalc_inductive(f,L,r):
    # f : Frequency vector
```

```
    # L : Inductance
    # r : Inductance ESR
    Z = r + 1j*2*pi*f*L
    return array(Z)

def ZCalc_LCFilter(f,L,r,C,R):
    # f : Frequency vector
    # L : Inductance
    # r : Inductance ESR
    # C : Filter capacitor
    # R : Load resistance
    w = 2*pi*f
    Z = (R +r + 1j*w*L + 1j*w*C*R*r - ((w)**2)*C*R*L)/(1+1j*w*C*R)
    return array(Z)

def ZCalc_LCFilter_BB(f,L,r,C,R,rb,Lb,Cb):
    # f : Frequency vector
    # L : Inductance
    # r : Inductance ESR
    # C : Filter capacitor
    # R : Load resistance
    # rb : Balance booster resistance
    # Lb : Balance booster inductance
    # Cb : Balance booster capacitance
    w = 2*pi*f
    Zl = (R +r + 1j*w*L + 1j*w*C*R*r - ((w)**2)*C*R*L)/(1+1j*w*C*R)
    Zb = (-(w**2)*Lb*Cb + 1j*w*Cb*rb + 1)/(1j*w*Cb)
    Z = 1/(1/Zb + 1/Zl)
    return array(Z)

def ZCalc_inductive_BB(f,L,r,rb,Lb,Cb):
    # f : Frequency vector
    # L : Inductance
    # r : Inductance ESR
    # rb : Balance booster resistance
    # Lb : Balance booster inductance
    # Cb : Balance booster capacitance
    w = 2*pi*f
    Zl = r + 1j*w*L
    Zb = (-(w**2)*Lb*Cb + 1j*w*Cb*rb + 1)/(1j*w*Cb)
    Z = 1/(1/Zb + 1/Zl)
    Z[size(Z)//2] = 1e9
    return array(Z)

def Sd_Calculator(k,m,ma,N):
    # k : Steps in fr
    # m : Steps in fs
    # ma : Amplitude modulation index
    # N : N-cell structure
    C = []
    for a in range(0,N):
        C.append(Modulated_Fourier_Coef(k,m,ma,a,N))
    Cd = []
    for a in range(1,N):
        Cd.append((C[a] - C[a-1])/2)
    return Cd

def Sd_Calculator_const(n,d,N):
    # n : Steps in fs
    # d : Duty cycle
    # N : N-cell structure
    C = []
    for a in range(0,N):
        C.append(Const_Fourier_Coef(n,d,a,N))
    Cd = []
    for a in range(1,N):
```

```
        Cd.append((C[a] - C[a-1])/2)
    return Cd,C

def freq_base_change(k,m,fc,fr,Cd,N):
    # k : Steps in fr
    # m : Steps in fs
    # ma : Amplitude modulation index
    # N : N-cell structure
    f = Generate_Frequency_Vector(k,m,fr,fc)
    fnew = arange(f.min(),f.max()+fr,fr)
    Cdnew = []
    for a in range(1,N):
        Cdnew.append([])
    for F in fnew:
        if (F == f).any():
            for a in range(0,N-1):
                Cdnew[a].append(Cd[a][F==f][0])
        else:
            for a in range(0,N-1):
                Cdnew[a].append(0)
    Cda = []
    for a in range(0,N-1):
        Cda.append(array(Cdnew[a]))
    return fnew,Cda

def Lambda_Matrix_Generator(Cd,N,Z):
    # Cd : List of Cd functions
    # N : N-Cell structure
    # Z : Impedance vector
    Lambda_mat = zeros([N-1,N-1])
    index = size(Cd[0])-1
    for x in range(0,N-1):
        for y in range(0,N-1):
            Lambda_mat[y,x] = convolve(Cd[x]/Z,Cd[y])[index]
    return Lambda_mat
```

C.2.2 Time Constant Calculation: Constant Duty Cycle Case

```
from pylab import*
from scipy.special import jn
import FCCToolkit as FCC


##############################################################################
## Full approximation of the N-Cell FCC Converter rebalancing time constant,  ##
## with the FCC operating with modulated duty cycle. This approximation is    ##
## valid when:                                                                ##
##  1. The modulation frequency is much lower than the switching frequency.   ##
##  2. The exponential Fourier series coefficients used here does not make    ##
##  allowance for reference functions more complex than a pure sinusoid of    ##
##  frequency f_r, nor over-modulation, viz. m_a > 1.                         ##
##  3. Allowance is made in this code for 3 types of load, pure inductive     ##
##  (with ESR), Resistive load, with LC filter, and Resistive load, with LC   ##
##  filter and a balance booster. However, the source code could be adapted   ##
##  for any other type of load.                                               ##
##                                                                            ##
## Wim van der Merwe                                                          ##
## 2010                                                                       ##
##############################################################################


##############################################################################
## User defined variables.                                                    ##
##############################################################################

fc = 3e3                            # Switching frequecy
```

```
d = 0.82                            # Duty cycle
N = 4                              # Number of cells

C = 94e-6                           # Flying capacitor [F]

L = 2.15e-3                         # Filter inductor [H]
r = 3.5                            # Filter inductor ESR [Ohm]

Co = 50e-6                         # Filter capacitor [F]
R = 32                              # Load resistance [Ohm]

Rb = 2                              # Balance booster resistance [Ohm]
                                    # include balance booster capacitance
                                    # and inductance ESR in this value!
Cb = 4.3e-6                         # Balance booster capacitance [F]
Lb = 237e-6                         # Balance booster inductance [H]

load_type = 1                       # Load type, valid values are:
                        #   0: Pure inductive load e.g. induction machine.
                        #   1: Resistive load, with LC filter.
                        #   2: Resistive load, with LC filter
                        #   and balance booster.


mmax = 40                   # Maximum number of harmonics of fc to use
                            # in calculations, suggested value is 40.


##  Generation of the exponential Fourier series coefficients.  ##


m = range(-mmax,mmax+1)             # Generate indexes

Cd,S = FCC.Sd_Calculator_const(m,d,N)     # Calculate Cd vectors
f = fc*array(m)

if load_type == 0:
    Z = FCC.ZCalc_inductive(f,L,r)
elif load_type == 1:
    Z = FCC.ZCalc_LCFilter(f,L,r,Co,R)
elif load_type == 2:
    Z = FCC.ZCalc_LCFilter_BB(f,L,r,Co,R,rb,Lb,Cb)
else:
    print "Incorrect selection for load type! Assuming inductive load. \n"
    Z = FCC.ZCalc_inductive(f,L,r)

Lambda_mat = FCC.Lambda_Matrix_Generator(Cd,N,Z)
eigv = real(eig(Lambda_mat)[0]).min()
print eig(Lambda_mat)[0]
tau = -C/eigv
print Lambda_mat

eigvm = real(eig(Lambda_mat)[0]).max()
taum = -C/eigvm

LambdaR = 0.5*(Lambda_mat + Lambda_mat.T)
eigvE = real(eig(LambdaR)[0]).min()
tauE = -C/eigvE

print 'Voltage time constant:', tau, 's'
print 'Energy time constant:', tauE, 's'
print taum
print eig(Lambda_mat)[0]
```

C.2.3 Time Constant Calculation: Modulated Duty Cycle Case

```
from pylab import*
from scipy.special import jn
import FCCToolkit as FCC


##############################################################################
## Full approximation of the N-Cell FCC Converter rebalancing time constant,  ##
## with the FCC operating with modulated duty cycle. This approximation is    ##
## valid when:                                                                ##
##  1. The modulation frequency is much lower than the switching frequency.   ##
##  2. The exponential Fourier series coefficients used here does not make    ##
##  allowance for reference functions more complex than a pure sinusoid of    ##
##  frequency f_r, nor over-modulation, viz. m_a > 1.                         ##
##  3. Allowance is made in this code for 3 types of load, pure inductive     ##
##  (with ESR), Resistive load, with LC filter, and Resistive load, with LC   ##
##  filter and a balance booster. However, the source code could be adapted   ##
##  for any other type of load.                                               ##
##                                                                            ##
## Wim van der Merwe                                                          ##
## 2010                                                                       ##
##############################################################################


##############################################################################
## User defined variables.                                                   ##
##############################################################################

fc = 5e3                            # Switching frequecy
fr = 50                             # Modulation frequency
ma = 0.8                            # Amplitute modulation index
N = 5                               # Number of levels

C = 20e-6                           # Flying capacitor [F]

L = 27.9e-3                          # Filter inductor [H]
r = 4.9                             # Filter inductor ESR [Ohm]

Cf = 75e-6                         # Filter capacitor [F]
R = 10                              # Load resistance [Ohm]

Rb = 2                              # Balance booster resistance [Ohm]
                                    # include balance booster capacitance
                                    # and inductance ESR in this value!
Cb = 4.7e-6                         # Balance booster capacitance [F]
Lb = 250e-6                         # Balance booster inductance [H]

load_type = 3                       # Load type, valid values are:
                        #   0: Pure inductive load e.g. induction machine.
                        #   1: Resistive load, with LC filter.
                        #   2: Resistive load, with LC filter
                        #   and balance booster.
                        #   3: Inductive load with balance booster.

kmax = 20                   # Maximum number of harmonics of fr to use
                            # in calculations, suggested value is 20.
mmax = 10                   # Maximum number of harmonics of fc to use
                            # in calculations, suggested value is 10.


##  Generation of the exponential Fourier series coefficients.  ##


k = range(-kmax,kmax+1)
m = range(-mmax,mmax+1)             # Generate indexes

Cd = FCC.Sd_Calculator(k,m,ma,N)     # Calculate Cd vectors
```

```
f,Cd = FCC.freq_base_change(k,m,fc,fr,Cd,N)    # Change the frequecy base
                        # of the Cd vectors to enable the convolution calculation.

if load_type == 0:
    Z = FCC.ZCalc_inductive(f,L,r)
elif load_type == 1:
    Z = FCC.ZCalc_LCFilter(f,L,r,C,R)
elif load_type == 2:
    Z = FCC.ZCalc_LCFilter_BB(f,L,r,C,R,Rb,Lb,Cb)
elif load_type == 3:
    Z = FCC.ZCalc_inductive_BB(f,L,r,Rb,Lb,Cb)
else:
    print "Incorrect selection for load type! Assuming inductive load. \n"
    Z = FCC.ZCalc_inductive(f,L,r)

Lambda_mat = FCC.Lambda_Matrix_Generator(Cd,N,Z)
eigv = real(eig(Lambda_mat)[0]).min()
tau = -C/eigv

LambdaR = 0.5*(Lambda_mat + Lambda_mat.T)
eigvE = real(eig(LambdaR)[0]).min()
tauE = -C/eigvE

print 'Voltage time constant :', tau, 's'
print 'Energy time constant :', tauE, 's'
```

C.2.4 Balance Booster Design

```
from __future__ import division
from pylab import*
#################################################################
## This program is intended as a design aid for a balance    ##
## booster. It used the user supplied component values of    ##
## the load to create a plot of Re{Z} vs Im{Z} at the        ##
## frequencies of interest.                                  ##
##                                                           ##
## Wim vd Merwe                                              ##
## 2009                                                      ##
#################################################################

#################################################################
## User defined variables.                                   ##
#################################################################


L = 153e-6              # Filter Inductance
C = 50e-6               # Filter Capacitance
R =1e9                   # Load resistance
Lb = 210e-6             # Balance Booster Inductance
Cb = 3e2               # Balance booster capacitance
Rb = 2                  # Balance booster resistance
r = 0.1                 # ESR of filter inductance
fs = 5000               # switching frequency

N = 2                   # Number of cells.


## Generate Load Curves                                     ##

ws = arange(0*pi*fs,5*pi*2*fs,1)
Zls = (R +r + 1j*ws*L + 1j*ws*C*R*r - ((ws)**2)*C*R*L)/(1+1j*ws*C*R)
Zb = (-(ws**2)*Lb*Cb + 1j*ws*Cb*Rb + 1)/(1j*ws*Cb)
Zt = (Zls*Zb)/(Zb + Zls)

## Summation Index ##
M = range(0,6)
```

```
i = range(0,6,N)
i.reverse()
for x in i:
    M.pop(x)
M = array(M)
wm = 2*pi*fs*M
Zlm = (R +r + 1j*wm*L + 1j*wm*C*R*r - ((wm)**2)*C*R*L)/(1+1j*wm*C*R)
Zbm = (-(wm**2)*Lb*Cb + 1j*wm*Cb*Rb + 1)/(1j*wm*Cb)
Ztm = (Zlm*Zbm)/(Zbm + Zlm)

## Plot Parametric Curves ##

fig = figure(1)
ax = fig.add_subplot(111)
plot(real(Zls),imag(Zls))
plot(real(Zt),imag(Zt),'r')

plot(real(Zlm),imag(Zlm),'ob')
plot(real(Ztm),imag(Ztm),'or')


ax.annotate('$f_s$',size = 'x-large', xy=(real(Zlm[0]), imag(Zlm[0])),
                xycoords='data',
                xytext=(50, -30),textcoords='offset points',
                arrowprops=dict(arrowstyle="->")
                )
ax.annotate('$3f_s$',size = 'x-large', xy=(real(Zlm[1]), imag(Zlm[1])),
                xycoords='data',
                xytext=(50, 10), textcoords='offset points',
                arrowprops=dict(arrowstyle="->")
                )
ax.annotate('$5f_s$',size = 'x-large', xy=(real(Zlm[2]), imag(Zlm[2])),
                xycoords='data',
                xytext=(50, -30), textcoords='offset points',
                arrowprops=dict(arrowstyle="->")
                )
ax.annotate('$f_s$',size = 'x-large', xy=(real(Ztm[0]), imag(Ztm[0])),
                xycoords='data',
                xytext=(50, -10), textcoords='offset points',
                arrowprops=dict(arrowstyle="->")
                )
ax.annotate('$3f_s$',size = 'x-large', xy=(real(Ztm[1]), imag(Ztm[1])),
                xycoords='data',
                xytext=(50, -10), textcoords='offset points',
                arrowprops=dict(arrowstyle="->")
                )
ax.annotate('$5f_s$',size = 'x-large', xy=(real(Ztm[2]), imag(Ztm[2])),
                xycoords='data',
                xytext=(50, -20), textcoords='offset points',
                arrowprops=dict(arrowstyle="->")
                )

grid(1<2)
legend(('Load','Load with Balance Booster'),loc=1)
xlabel('Real Part of Z').set_size('large')
ylabel('Imaginary part of Z').set_size('large')
#axis([-0.2,7,-5,28])

show()
```

Appendix D

Practical Hardware

Several similar power electronic cells were used for the measurements of both the ISOP and the SISO DC-DC converters. A circuit diagram of the converter is shown in Fig. D.1. Although the cell consists of two back-to-back DC-DC converters the DC bus is accessible. The first full bridge converter was kept in the off state for all tests. The cell specifications are indicated in Table D.1 and a photograph of the converter is shown in Fig. D.2.

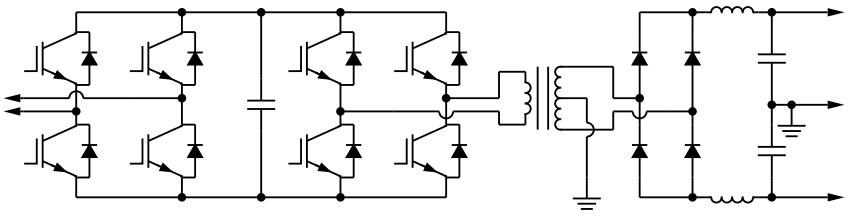

Figure D.1: Circuit diagram of the converter

Table D.1: Cell parameters

Rated Power	3.5 kW	Rated DC bus voltage	800 V
Transformer insulation rating	8 kV	Output voltage	800 V
DC bus capacitance	100 μF	Filter inductor	2.2 mH
Switching frequency	15 - 35 kHz		

The FCC used for the measurements is located at Ghent University in Belgium. A photograph is shown in Fig. D.3. The specifications of the converter are listed in Table D.2.

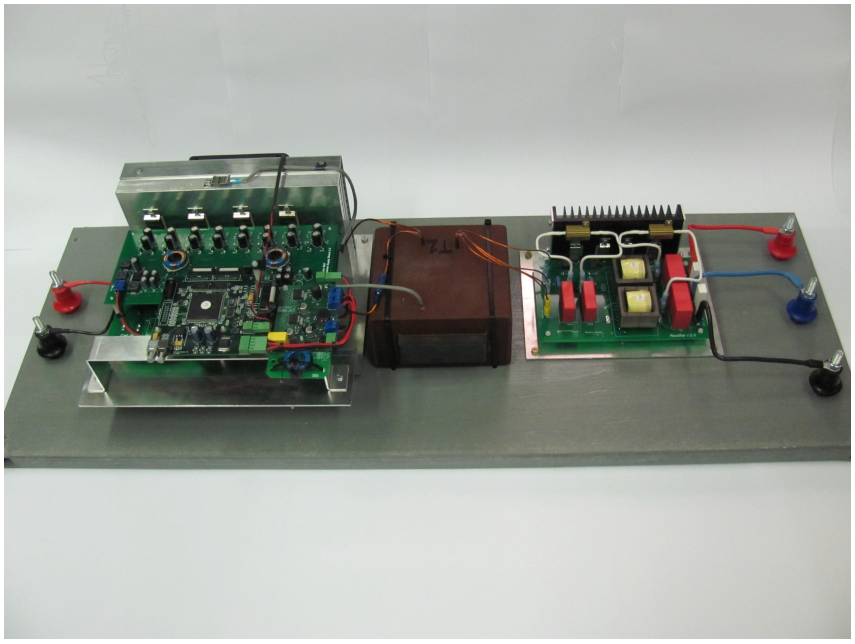

Figure D.2: Photograph of the converter

Table D.2: Practical FCC parameters

C	94 μF	C_f	50 μF
L	2.2 mH	f_s	3 kHz
r_{dc}	0.75 Ω	r_{75kHz}	8 Ω
R_{large}	8 Ω	R_{small}	32 Ω

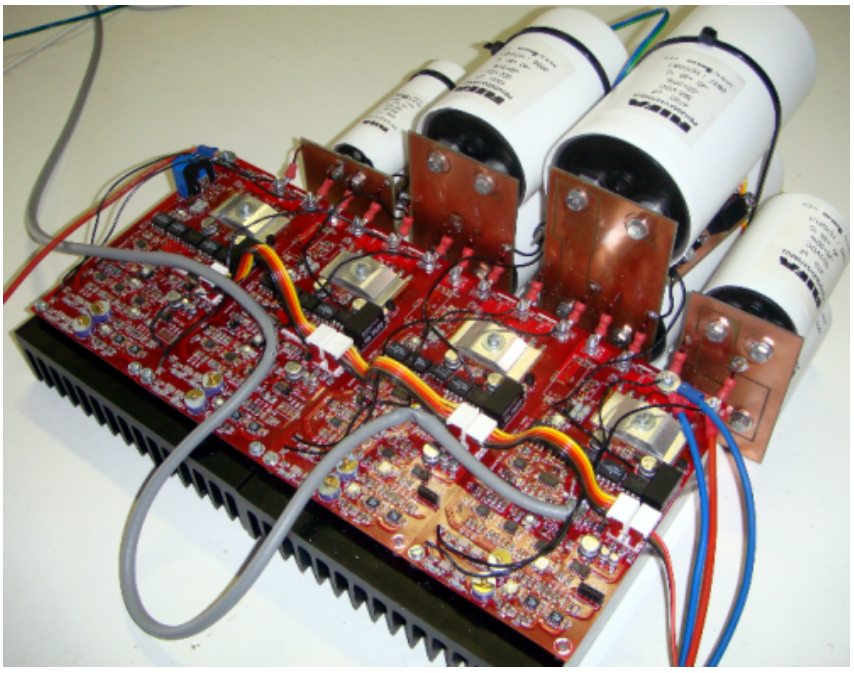

Figure D.3: Photograph of the FCC converter

Appendix E

Rebalancing Time Constant Reference Tables

Table E.1: Rebalancing time constant, 3-cell case with constant duty cycle

duty cycle	τ_r	duty cycle	τ_r
0.0	∞	0.5	129.60155076
0.01	91550.2755705	0.51	129.694887221
0.02	23199.907582	0.52	129.975866199
0.03	10473.0745829	0.53	130.446826151
0.04	5984.50356719	0.54	131.111916755
0.05	3892.11191018	0.55	131.977138125
0.06	2747.38358213	0.56	133.05015849
0.07	2052.28024805	0.57	134.341091674
0.08	1598.06177244	0.58	135.862043249
0.09	1284.55169173	0.59	137.62796563
0.1	1058.84704846	0.6	139.65684237
0.11	890.798601697	0.61	141.969896724
0.12	762.208524969	0.62	144.59294677
0.13	661.557584252	0.63	147.556127783
0.14	581.254289968	0.64	150.895942452
0.15	516.137037293	0.65	154.655798055
0.16	462.58910595	0.66	158.887598214
0.17	418.017513891	0.67	163.654722262
0.18	380.522849626	0.68	169.022361667
0.19	348.686425073	0.69	175.053416599
0.2	321.432821202	0.7	181.820290042
0.21	297.93324778	0.71	189.410165925
0.22	277.541433998	0.72	197.926356655
0.23	259.747278676	0.73	207.492892842
0.24	244.143638422	0.74	218.258551263
0.25	230.402813887	0.75	230.402813887
0.26	218.258551263	0.76	244.143638422
0.27	207.492892842	0.77	259.747278676
0.28	197.926356655	0.78	277.541433998
0.29	189.410165925	0.79	297.93324778
0.3	181.820290042	0.8	321.432821202
0.31	175.053416599	0.81	348.686425073
0.32	169.022361667	0.82	380.522849626
0.33	163.654722262	0.83	418.017513891
0.34	158.887598214	0.84	462.58910595
0.35	154.655798055	0.85	516.137037293
0.36	150.895942452	0.86	581.254289968
0.37	147.556127783	0.87	661.557584251
0.38	144.59294677	0.88	762.208524969
0.39	141.969896724	0.89	890.798601697
0.4	139.65684237	0.9	1058.84704846
0.41	137.62796563	0.91	1284.55169173
0.42	135.862043249	0.92	1598.06177244
0.43	134.341091674	0.93	2052.28024805
0.44	133.05015849	0.94	2747.38358213
0.45	131.977138125	0.95	3892.11191018
0.46	131.111916755	0.96	5984.50356719
0.47	130.446826151	0.97	10473.0745829
0.48	129.975866199	0.98	23199.907582
0.49	129.694887221	0.99	91550.2755705
		1.0	∞

Table E.2: Rebalancing time constant, 4-cell case with constant duty cycle

duty cycle	$\check{\tau}$	duty cycle	$\check{\tau}$
0.0	∞	0.5	∞
0.01	163302.448374	0.51	82540.8148652
0.02	41493.0147207	0.52	21181.8079956
0.03	18793.6100245	0.53	9713.98112583
0.04	10777.3918739	0.54	5647.5404669
0.05	7036.39350199	0.55	3743.37886168
0.06	4987.7543583	0.56	2697.63473719
0.07	3742.75426941	0.57	2060.78028298
0.08	2928.79937092	0.58	1644.04806176
0.09	2366.87004481	0.59	1356.48299402
0.1	1962.42373679	0.6	1150.01912113
0.11	1661.53935462	0.61	997.180416377
0.12	1431.65343445	0.62	881.361209256
0.13	1252.16807659	0.63	792.0651536
0.14	1109.49522908	0.64	722.36344666
0.15	994.418859254	0.65	667.581481356
0.16	900.48812582	0.66	624.4601517
0.17	823.095015554	0.67	590.696048519
0.18	758.893152954	0.68	564.647980043
0.19	705.401211883	0.69	545.125906085
0.2	660.78349069	0.7	531.295069644
0.21	623.662492918	0.71	522.570650366
0.22	593.022192534	0.72	518.580178906
0.23	568.139644249	0.73	519.13535839
0.24	548.52008696	0.74	524.197048924
0.25	533.91921658	0.75	533.91921658
0.26	524.197048924	0.76	548.52008696
0.27	519.13535839	0.77	568.139644249
0.28	518.580178906	0.78	593.022192534
0.29	522.570650366	0.79	623.662492918
0.3	531.295069644	0.8	660.78349069
0.31	545.125906085	0.81	705.401211883
0.32	564.647980043	0.82	758.893152954
0.33	590.696048519	0.83	823.095015554
0.34	624.4601517	0.84	900.48812582
0.35	667.581481356	0.85	994.418859253
0.36	722.363446659	0.86	1109.49522908
0.37	792.065153601	0.87	1252.16807659
0.38	881.361209256	0.88	1431.65343445
0.39	997.180416378	0.89	1661.53935462
0.4	1150.01912113	0.9	1962.42373679
0.41	1356.48299402	0.91	2366.87004481
0.42	1644.04806176	0.92	2928.79937092
0.43	2060.78028298	0.93	3742.75426941
0.44	2697.63473719	0.94	4987.7543583
0.45	3743.37886168	0.95	7036.39350199
0.46	5647.5404669	0.96	10777.3918739
0.47	9713.98112582	0.97	18793.6100245
0.48	21181.8079957	0.98	41493.0147206
0.49	82540.8148652	0.99	163302.448374
		1.0	∞

Table E.3: Rebalancing time constant, 5-cell case with constant duty cycle

duty cycle	τ_r	duty cycle	τ_r
0.0	∞	0.5	5118.38283232
0.01	256082.941764	0.51	5066.6447661
0.02	65264.5556558	0.52	4917.61898497
0.03	29670.3710291	0.53	4688.14202572
0.04	17082.6773318	0.54	4401.3110455
0.05	11201.5126442	0.55	4081.27044542
0.06	7977.72436331	0.56	3749.44176099
0.07	6017.13436367	0.57	3422.30096754
0.08	4734.94661345	0.58	3111.0344678
0.09	3849.87686551	0.59	2822.36457895
0.1	3213.38289387	0.6	2559.25761359
0.11	2740.6708657	0.61	2323.22058268
0.12	2380.53678028	0.62	2115.44737586
0.13	2100.62696049	0.63	1935.34616476
0.14	1879.59853254	0.64	1780.65952537
0.15	1703.05380807	0.65	1648.70321436
0.16	1560.95333835	0.66	1536.7186836
0.17	1446.21424032	0.67	1442.1684665
0.18	1353.81266557	0.68	1362.86517494
0.19	1280.12724715	0.69	1296.93318501
0.2	1222.73726569	0.7	1242.86815681
0.21	1179.7388018	0.71	1199.45887284
0.22	1149.13852115	0.72	1165.78358002
0.23	1129.27835674	0.73	1141.19729594
0.24	1119.09534717	0.74	1125.28057075
0.25	1117.88530711	0.75	1117.88530711
0.26	1125.28057075	0.76	1119.09534717
0.27	1141.19729594	0.77	1129.27835674
0.28	1165.78358002	0.78	1149.13852115
0.29	1199.45887284	0.79	1179.7388018
0.3	1242.86815681	0.8	1222.73726569
0.31	1296.93318501	0.81	1280.12724715
0.32	1362.86517494	0.82	1353.81266557
0.33	1442.1684665	0.83	1446.21424032
0.34	1536.7186836	0.84	1560.95333835
0.35	1648.70321436	0.85	1703.05380807
0.36	1780.65952537	0.86	1879.59853254
0.37	1935.34616476	0.87	2100.62696049
0.38	2115.44737586	0.88	2380.53678028
0.39	2323.22058268	0.89	2740.6708657
0.4	2559.25761359	0.9	3213.38289387
0.41	2822.36457895	0.91	3849.87686552
0.42	3111.0344678	0.92	4734.94661345
0.43	3422.30096754	0.93	6017.13436367
0.44	3749.44176099	0.94	7977.7243633
0.45	4081.27044543	0.95	11201.5126442
0.46	4401.31104549	0.96	17082.6773318
0.47	4688.14202572	0.97	29670.3710291
0.48	4917.61898498	0.98	65264.5556558
0.49	5066.64476611	0.99	256082.941764
		1.0	∞

Table E.4: Rebalancing time constant, 6-cell case with constant duty cycle

duty cycle	τ_r	duty cycle	τ_r
0.0	∞	0.5	∞
0.01	370008.043288	0.51	186742.286939
0.02	94634.2991477	0.52	48433.0608238
0.03	43193.3991729	0.53	22568.0363882
0.04	24976.0546787	0.54	13424.3610886
0.05	16456.3054789	0.55	9193.58915857
0.06	11782.210845	0.56	6943.98125617
0.07	8939.16872184	0.57	5683.88666671
0.08	7080.68051626	0.58	5025.9758712
0.09	5799.7661278	0.59	4830.22238114
0.1	4881.48779805	0.6	5090.98506107
0.11	4203.0862404	0.61	5922.29771609
0.12	3690.88096123	0.62	7653.48803452
0.13	3298.38297822	0.63	11199.2693784
0.14	2995.55777249	0.64	19541.5601271
0.15	2762.72351995	0.65	46898.6992896
0.16	2587.12636209	0.66	280654.854424
0.17	2461.48154085	0.67	1114777.2151
0.18	2380.71291017	0.68	71940.3272866
0.19	2340.72153698	0.69	24816.5680142
0.2	2340.59233018	0.7	12967.90064
0.21	2383.05802616	0.71	8245.69412467
0.22	2474.73719127	0.72	5896.47662484
0.23	2627.97010584	0.73	4564.44852905
0.24	2863.32575825	0.74	3745.57685226
0.25	3215.69133066	0.75	3215.69133066
0.26	3745.57685226	0.76	2863.32575825
0.27	4564.44852905	0.77	2627.97010584
0.28	5896.47662484	0.78	2474.73719127
0.29	8245.69412466	0.79	2383.05802616
0.3	12967.90064	0.8	2340.59233018
0.31	24816.5680141	0.81	2340.72153698
0.32	71940.3272863	0.82	2380.71291017
0.33	1114777.21501	0.83	2461.48154085
0.34	280654.854416	0.84	2587.12636209
0.35	46898.6992898	0.85	2762.72351994
0.36	19541.5601271	0.86	2995.55777249
0.37	11199.2693784	0.87	3298.38297822
0.38	7653.48803454	0.88	3690.88096123
0.39	5922.29771607	0.89	4203.0862404
0.4	5090.98506106	0.9	4881.48779805
0.41	4830.22238114	0.91	5799.7661278
0.42	5025.9758712	0.92	7080.68051626
0.43	5683.8866667	0.93	8939.16872184
0.44	6943.98125616	0.94	11782.210845
0.45	9193.58915858	0.95	16456.3054789
0.46	13424.3610887	0.96	24976.0546787
0.47	22568.0363883	0.97	43193.3991729
0.48	48433.0608237	0.98	94634.2991478
0.49	186742.286936	0.99	370008.043288
		1.0	∞

Table E.5: Rebalancing time constant, 7-cell case with constant duty cycle

duty cycle	τ_r	duty cycle	τ_r
0.0	∞	0.5	40447.3567536
0.01	505521.444226	0.51	36477.2295619
0.02	129734.177741	0.52	28331.9775919
0.03	59461.4119058	0.53	20932.7153093
0.04	34541.9124631	0.54	15674.9165035
0.05	22878.0979776	0.55	12219.2672063
0.06	16476.5412592	0.56	10010.5523228
0.07	12584.5378177	0.57	8641.33433847
0.08	10044.6772056	0.58	7861.70723387
0.09	8300.42625776	0.59	7523.23807321
0.1	7058.41969096	0.6	7532.32508463
0.11	6151.43473508	0.61	7837.87067161
0.12	5480.37347623	0.62	8423.45570023
0.13	4983.83963781	0.63	9298.98235958
0.14	4624.77424076	0.64	10488.5658431
0.15	4381.13933663	0.65	12008.1550852
0.16	4235.22395966	0.66	13821.9777574
0.17	4173.96826453	0.67	15756.2521834
0.18	4192.61128686	0.68	17415.3266062
0.19	4292.58902756	0.69	18203.7187563
0.2	4481.70396025	0.7	17663.2491249
0.21	4775.13343043	0.71	15877.6372103
0.22	5196.80812552	0.72	13448.0014752
0.23	5783.40720619	0.73	11085.9323391
0.24	6587.1116838	0.74	9154.06246974
0.25	7680.84477858	0.75	7680.84477858
0.26	9154.06246973	0.76	6587.1116838
0.27	11085.9323391	0.77	5783.40720619
0.28	13448.0014752	0.78	5196.80812551
0.29	15877.6372102	0.79	4775.13343043
0.3	17663.2491249	0.8	4481.70396025
0.31	18203.7187563	0.81	4292.58902756
0.32	17415.3266063	0.82	4192.61128685
0.33	15756.2521834	0.83	4173.96826453
0.34	13821.9777574	0.84	4235.22395966
0.35	12008.1550852	0.85	4381.13933663
0.36	10488.5658431	0.86	4624.77424076
0.37	9298.98235958	0.87	4983.83963781
0.38	8423.45570021	0.88	5480.37347623
0.39	7837.8706716	0.89	6151.43473508
0.4	7532.32508462	0.9	7058.41969096
0.41	7523.2380732	0.91	8300.42625776
0.42	7861.70723387	0.92	10044.6772056
0.43	8641.33433846	0.93	12584.5378177
0.44	10010.5523228	0.94	16476.5412592
0.45	12219.2672063	0.95	22878.0979776
0.46	15674.9165036	0.96	34541.9124631
0.47	20932.7153091	0.97	59461.4119059
0.48	28331.9775919	0.98	129734.177741
0.49	36477.2295618	0.99	505521.444226
		1.0	∞

Table E.6: Rebalancing time constant, 8-cell case with constant duty cycle

duty cycle	τ_r	duty cycle	τ_r
0.0	∞	0.5	∞
0.01	663176.972957	0.51	335193.602189
0.02	170703.931196	0.52	87997.7403417
0.03	78581.3419906	0.53	41804.9654663
0.04	45874.06331	0.54	25528.8276641
0.05	30555.2426817	0.55	18101.3703657
0.06	22150.3469989	0.56	14298.5940964
0.07	17046.9823805	0.57	12368.5990496
0.08	13729.5562794	0.58	11648.6268777
0.09	11467.7715668	0.59	11924.9749738
0.1	9879.93803347	0.6	13242.1755147
0.11	8750.9301435	0.61	15864.5713443
0.12	7958.25102271	0.62	20237.1021938
0.13	7435.01234643	0.63	26572.4404152
0.14	7137.59728103	0.64	33850.8919156
0.15	7038.93411001	0.65	38995.725991
0.16	7140.64447513	0.66	38704.3784537
0.17	7478.23850387	0.67	33744.7220265
0.18	8135.74901572	0.68	27687.8165145
0.19	9293.72557045	0.69	22854.3053773
0.2	11339.1737921	0.7	20113.3240388
0.21	15203.8271085	0.71	20351.5007838
0.22	23580.5936248	0.72	26304.0478304
0.23	47170.702011	0.73	48509.3415823
0.24	172684.217591	0.74	173232.599262
0.25	∞	0.75	∞
0.26	173232.599264	0.76	172684.217593
0.27	48509.3415824	0.77	47170.7020111
0.28	26304.0478304	0.78	23580.5936248
0.29	20351.5007839	0.79	15203.8271085
0.3	20113.3240389	0.8	11339.1737921
0.31	22854.3053774	0.81	9293.72557045
0.32	27687.8165145	0.82	8135.74901572
0.33	33744.7220264	0.83	7478.23850387
0.34	38704.3784537	0.84	7140.64447512
0.35	38995.7259911	0.85	7038.93411001
0.36	33850.8919157	0.86	7137.59728103
0.37	26572.4404152	0.87	7435.01234643
0.38	20237.1021938	0.88	7958.25102272
0.39	15864.5713443	0.89	8750.9301435
0.4	13242.1755147	0.9	9879.93803347
0.41	11924.9749738	0.91	11467.7715668
0.42	11648.6268777	0.92	13729.5562794
0.43	12368.5990497	0.93	17046.9823805
0.44	14298.5940964	0.94	22150.3469989
0.45	18101.3703657	0.95	30555.2426816
0.46	25528.8276641	0.96	45874.06331
0.47	41804.9654663	0.97	78581.3419905
0.48	87997.7403416	0.98	170703.931196
0.49	335193.602189	0.99	663176.972956
		1.0	∞

Table E.7: Rebalancing time constant, 2-cell case with modulated duty cycle

modulation index	$tilde\tau_r$	modulation index	$\tilde{\tau}_r$
0.0	48.0077330542	0.5	65.661146454
0.01	48.0146436308	0.51	66.4480245667
0.02	48.0353657682	0.52	67.2578024824
0.03	48.0698711364	0.53	68.0909614178
0.04	48.1181139855	0.54	68.9479888686
0.05	48.1800332765	0.55	69.8293788737
0.06	48.2555555263	0.56	70.735632199
0.07	48.3445982404	0.57	71.6672563032
0.08	48.4470737766	0.58	72.6247649437
0.09	48.5628934708	0.59	73.6086772897
0.1	48.6919718417	0.6	74.6195164278
0.11	48.8342306959	0.61	75.657807172
0.12	48.9896029625	0.62	76.7240731258
0.13	49.1580361057	0.63	77.8188329851
0.14	49.3394949896	0.64	78.9425961099
0.15	49.5339641026	0.65	80.0958574345
0.16	49.741449087	0.66	81.279091821
0.17	49.9619775561	0.67	82.4927479835
0.18	50.1955992222	0.68	83.737242128
0.19	50.4423853967	0.69	85.012951449
0.2	50.7024279519	0.7	86.3202076104
0.21	50.9758378644	0.71	87.6592903046
0.22	51.2627434729	0.72	89.0304209382
0.23	51.5632885962	0.73	90.4337564345
0.24	51.8776306528	0.74	91.8693830755
0.25	52.2059389174	0.75	93.3373102379
0.26	52.5483930289	0.76	94.8374638068
0.27	52.9051818427	0.77	96.369678997
0.28	53.2765026883	0.78	97.9336922667
0.29	53.6625610622	0.79	99.5291319882
0.3	54.0635707521	0.8	101.15550755
0.31	54.4797543576	0.81	102.812196602
0.32	54.9113441417	0.82	104.498430234
0.33	55.3585831285	0.83	106.213275982
0.34	55.8217263434	0.84	107.955618696
0.35	56.3010420855	0.85	109.72413948
0.36	56.7968131225	0.86	111.517293096
0.37	57.3093377052	0.87	113.333284417
0.38	57.8389303182	0.88	115.170044711
0.39	58.3859221015	0.89	117.025208722
0.4	58.950660907	0.9	118.896093651
0.41	59.5335109824	0.91	120.77968124
0.42	60.1348523048	0.92	122.672604225
0.43	60.7550796104	0.93	124.571138371
0.44	61.3946011944	0.94	126.471201235
0.45	62.0538375669	0.95	128.368358603
0.46	62.7332200635	0.96	130.257839294
0.47	63.4331895066	0.97	132.134558731
0.48	64.1541950086	0.98	133.993151263
0.49	64.8966929885	0.99	135.828010863
		1.0	137.633339393

Table E.8: Rebalancing time constant, 3-cell case with modulated duty cycle

modulation index	$\tilde{\tau}_r$	modulation index	$\tilde{\tau}_r$
0.0	129.617415418	0.5	166.601653783
0.01	129.628944145	0.51	168.430650868
0.02	129.663554279	0.52	170.320514314
0.03	129.721316741	0.53	172.272535457
0.04	129.802346675	0.54	174.288030801
0.05	129.906799146	0.55	176.368340192
0.06	130.034863662	0.56	178.514825001
0.07	130.186758008	0.57	180.728866322
0.08	130.362721941	0.58	183.011863043
0.09	130.563011346	0.59	185.365229592
0.1	130.787893374	0.6	187.790393079
0.11	131.037643061	0.61	190.288789492
0.12	131.312541795	0.62	192.86185862
0.13	131.612877838	0.63	195.511037372
0.14	131.938948984	0.64	198.237751233
0.15	132.291067219	0.65	201.043403686
0.16	132.669565128	0.66	203.929363548
0.17	133.07480362	0.67	206.896950285
0.18	133.507180431	0.68	209.947417512
0.19	133.967138812	0.69	213.081934966
0.2	134.455175744	0.7	216.301569342
0.21	134.971849091	0.71	219.607264395
0.22	135.517783113	0.72	222.999820675
0.23	136.093671921	0.73	226.479875202
0.24	136.700280567	0.74	230.04788121
0.25	137.33844363	0.75	233.704087913
0.26	138.009061348	0.76	237.448519989
0.27	138.7130935	0.77	241.280956262
0.28	139.451551397	0.78	245.200906768
0.29	140.225488475	0.79	249.207587242
0.3	141.035990047	0.8	253.299889893
0.31	141.884162852	0.81	257.476349333
0.32	142.771124991	0.82	261.735102583
0.33	143.697996841	0.83	266.073842349
0.34	144.665893416	0.84	270.489763108
0.35	145.675918554	0.85	274.979500088
0.36	146.729161159	0.86	279.539061844
0.37	147.826693589	0.87	284.163757886
0.38	148.969572109	0.88	288.848123577
0.39	150.158839242	0.89	293.585845275
0.4	151.395527671	0.9	298.369689384
0.41	152.680665325	0.91	303.191439529
0.42	154.015281188	0.92	308.041846383
0.43	155.400411373	0.93	312.910594771
0.44	156.837105034	0.94	317.786292408
0.45	158.326429739	0.95	322.656484076
0.46	159.869475992	0.96	327.507694135
0.47	161.46736073	0.97	332.325499063
0.48	163.121229691	0.98	337.094630258
0.49	164.832258672	0.99	341.799105774
		1.0	346.422387999

Table E.9: Rebalancing time constant, 4-cell case with modulated duty cycle

modulation index	$\tilde{\tau}_r$	modulation index	$\tilde{\tau}_r$
0.0	∞	0.5	671.685655706
0.01	686407.272295	0.51	665.373480656
0.02	171967.634081	0.52	660.017367798
0.03	76699.8574062	0.53	655.573304936
0.04	43354.7579363	0.54	652.000347969
0.05	27919.2489025	0.55	649.260380453
0.06	19532.9732393	0.56	647.317982634
0.07	14474.7299046	0.57	646.140386876
0.08	11190.1486148	0.58	645.697496382
0.09	8936.68134976	0.59	645.961944503
0.1	7323.25587852	0.6	646.909172775
0.11	6128.02123375	0.61	648.517507344
0.12	5217.53038361	0.62	650.768215607
0.13	4507.6153303	0.63	653.645527773
0.14	3943.06892084	0.64	657.136611644
0.15	3486.46855025	0.65	661.231493032
0.16	3111.72575144	0.66	665.922918731
0.17	2800.2082377	0.67	671.206163514
0.18	2538.32516881	0.68	677.078786984
0.19	2315.97691398	0.69	683.54034983
0.2	2125.53279388	0.7	690.592101962
0.21	1961.14085074	0.71	698.236656746
0.22	1818.25192649	0.72	706.477666004
0.23	1693.28533246	0.73	715.319509539
0.24	1583.39005453	0.74	724.767010551
0.25	1486.27165426	0.75	734.825184647
0.26	1400.06512807	0.76	745.499025293
0.27	1323.24041648	0.77	756.793322733
0.28	1254.53143165	0.78	768.71250702
0.29	1192.88223388	0.79	781.260499166
0.3	1137.40584729	0.8	794.44054813
0.31	1087.35247721	0.81	808.255025829
0.32	1042.08477553	0.82	822.705148392
0.33	1001.05842368	0.83	837.790589853
0.34	963.806748879	0.84	853.508955183
0.35	929.928411835	0.85	869.855083353
0.36	899.077442547	0.86	886.820158418
0.37	870.955077139	0.87	904.390617653
0.38	845.30298258	0.88	922.546860473
0.39	821.897557879	0.89	941.261780112
0.4	800.545078668	0.9	960.499161182
0.41	781.0775125	0.91	980.212009572
0.42	763.348878667	0.92	1000.34090515
0.43	747.232061602	0.93	1020.8124908
0.44	732.61601328	0.94	1041.53823066
0.45	719.403298867	0.95	1062.41358355
0.46	707.507952904	0.96	1083.31773992
0.47	696.853621564	0.97	1104.11406055
0.48	687.371971228	0.98	1124.65132745
0.49	679.001345811	0.99	1144.76587311
		1.0	1164.2845921

Table E.10: Rebalancing time constant, 5-cell case with modulated duty cycle

modulation index	$\tilde{\tau}_r$	modulation index	$\tilde{\tau}_r$
0.0	5139.63832758	0.5	1529.23223806
0.01	5133.09385748	0.51	1509.15633105
0.02	5113.56186571	0.52	1490.87532717
0.03	5081.34243098	0.53	1474.34888734
0.04	5036.92211717	0.54	1459.54259688
0.05	4980.95481856	0.55	1446.42720104
0.06	4914.23716584	0.56	1434.97785335
0.07	4837.68035424	0.57	1425.17339781
0.08	4752.28034808	0.58	1416.99570236
0.09	4659.08829541	0.59	1410.42905688
0.1	4559.18269539	0.6	1405.45964583
0.11	4453.64446488	0.61	1402.07510196
0.12	4343.5356159	0.62	1400.26414504
0.13	4229.88184306	0.63	1400.01630711
0.14	4113.65897458	0.64	1401.32174368
0.15	3995.78298597	0.65	1404.17112917
0.16	3877.10311992	0.66	1408.55563295
0.17	3758.397589	0.67	1414.46697135
0.18	3640.37134404	0.68	1421.89752919
0.19	3523.65544537	0.69	1430.84054272
0.2	3408.80765596	0.7	1441.29033311
0.21	3296.31396465	0.71	1453.24257728
0.22	3186.59082978	0.72	1466.69459903
0.23	3079.98799983	0.73	1481.64565963
0.24	2976.79181457	0.74	1498.09722306
0.25	2877.22891793	0.75	1516.05316636
0.26	2781.47032526	0.76	1535.51990158
0.27	2689.63578865	0.77	1556.5063719
0.28	2601.7983975	0.78	1579.02388115
0.29	2517.98934421	0.79	1603.08571419
0.3	2438.20277828	0.8	1628.70650416
0.31	2362.40066887	0.81	1655.90130378
0.32	2290.51759723	0.82	1684.68432008
0.33	2222.46540534	0.83	1715.06727676
0.34	2158.13763579	0.84	1747.05737579
0.35	2097.4137084	0.85	1780.65484016
0.36	2040.16279068	0.86	1815.85003406
0.37	1986.24733111	0.87	1852.62017535
0.38	1935.52623479	0.88	1890.9256792
0.39	1887.85767074	0.89	1930.70620166
0.4	1843.10150807	0.9	1971.87648808
0.41	1801.12138491	0.91	2014.32217366
0.42	1761.78641938	0.92	2057.89573027
0.43	1724.97257607	0.93	2102.41280325
0.44	1690.56370519	0.94	2147.64922888
0.45	1658.4522748	0.95	2193.33906214
0.46	1628.53981926	0.96	2239.17396673
0.47	1600.73712978	0.97	2284.80431575
0.48	1574.96421534	0.98	2329.84231255
0.49	1551.15006423	0.99	2373.8673596
		1.0	2416.43377454

Table E.11: Rebalancing time constant, 6-cell case with modulated duty cycle

modulation index	$\tilde{\tau}_r$	modulation index	$\tilde{\tau}_r$
0.0	∞	0.5	4305.81466591
0.01	1558413.93143	0.51	4182.9125392
0.02	390845.834976	0.52	4063.33824535
0.03	174630.490087	0.53	3948.25020955
0.04	98956.332834	0.54	3838.51726216
0.05	63931.4481559	0.55	3734.76790616
0.06	44907.2651051	0.56	3637.43613077
0.07	33438.2366076	0.57	3546.80154456
0.08	25996.6693175	0.58	3463.0231127
0.09	20897.4046658	0.59	3386.16671374
0.1	17253.022716	0.6	3316.22722047
0.11	14560.203417	0.61	3253.14599406
0.12	12516.3101794	0.62	3196.82467822
0.13	10930.59917	0.63	3147.13607804
0.14	9678.11281423	0.64	3103.93276809
0.15	8674.32196001	0.65	3067.05393325
0.16	7860.49363429	0.66	3036.33082513
0.17	7194.89614177	0.67	3011.59112388
0.18	6647.3227508	0.68	2992.66242875
0.19	6195.57328766	0.69	2979.37505782
0.2	5823.12741753	0.7	2971.56430913
0.21	5517.56178429	0.71	2969.07231691
0.22	5269.44034318	0.72	2971.74962014
0.23	5071.50955137	0.73	2979.45654336
0.24	4918.09174494	0.74	2992.06446663
0.25	4804.60916286	0.75	3009.45703247
0.26	4727.19728175	0.76	3031.53130153
0.27	4682.38415078	0.77	3058.19882664
0.28	4666.82438189	0.78	3089.38656862
0.29	4677.08357046	0.79	3125.03752913
0.3	4709.4727291	0.8	3165.11093003
0.31	4759.9348568	0.81	3209.58172722
0.32	4823.98866433	0.82	3258.43921422
0.33	4896.73771983	0.83	3311.68444947
0.34	4972.95486055	0.84	3369.3262337
0.35	5047.24862494	0.85	3431.37537275
0.36	5114.30855099	0.86	3497.83698872
0.37	5169.21000499	0.87	3568.70069224
0.38	5207.74084299	0.88	3643.92850501
0.39	5226.69847975	0.89	3723.44053256
0.4	5224.10371903	0.9	3807.09854019
0.41	5199.2903738	0.91	3894.68779139
0.42	5152.85475873	0.92	3985.89777531
0.43	5086.47867333	0.93	4080.30278183
0.44	5002.66379126	0.94	4177.34366893
0.45	4904.42738856	0.95	4276.31257985
0.46	4795.00747336	0.96	4376.34274922
0.47	4677.61311279	0.97	4476.40580183
0.48	4555.23907004	0.98	4575.31897848
0.49	4430.54829459	0.99	4671.76439449
		1.0	4764.32164267

Table E.12: Rebalancing time constant, 7-cell case with modulated duty cycle

modulation index	$\tilde{\tau}_r$	modulation index	$\tilde{\tau}_r$
0.0	40737.3233199	0.5	8154.11327543
0.01	40204.1795171	0.51	8005.43966697
0.02	38687.6343438	0.52	7845.30108486
0.03	36406.3597715	0.53	7677.00794148
0.04	33643.5224781	0.54	7503.67328929
0.05	30673.2162027	0.55	7328.13173626
0.06	27713.4482263	0.56	7152.89626872
0.07	24911.1622934	0.57	6980.14533615
0.08	22349.232281	0.58	6811.73166763
0.09	20062.6166221	0.59	6649.20488165
0.1	18054.9824766	0.6	6493.84137738
0.11	16311.9650227	0.61	6346.67671987
0.12	14810.3422184	0.62	6208.53738281
0.13	13523.772073	0.63	6080.07008375
0.14	12426.068206	0.64	5961.76796007
0.15	11492.8759264	0.65	5853.99349837
0.16	10702.3813267	0.66	5756.99850375
0.17	10035.4738573	0.67	5670.94155337
0.18	9475.62482725	0.68	5595.90339802
0.19	9008.63787703	0.69	5531.90071781
0.2	8622.35971256	0.7	5478.89855007
0.21	8306.39755349	0.71	5436.82161896
0.22	8051.86439213	0.72	5405.56472068
0.23	7851.15815065	0.73	5385.00226043
0.24	7697.77244838	0.74	5374.99699396
0.25	7586.1326943	0.75	5375.40799138
0.26	7511.45010162	0.76	5386.09780737
0.27	7469.5868631	0.77	5406.93880293
0.28	7456.92727498	0.78	5437.818516
0.29	7470.25147372	0.79	5478.64391974
0.3	7506.61034547	0.8	5529.34433872
0.31	7563.20200322	0.81	5589.87271739
0.32	7637.25205608	0.82	5660.20485789
0.33	7725.90179929	0.83	5740.33616989
0.34	7826.1104403	0.84	5830.27541329
0.35	7934.57939255	0.85	5930.03487173
0.36	8047.70815054	0.86	6039.61638324
0.37	8161.59172754	0.87	6158.99268581
0.38	8272.06837765	0.88	6288.08362906
0.39	8374.82269283	0.89	6426.72698039
0.4	8465.54289095	0.9	6574.64384606
0.41	8540.12264747	0.91	6731.39916633
0.42	8594.8885642	0.92	6896.35836525
0.43	8626.82655143	0.93	7068.642059
0.44	8633.77654881	0.94	7247.08175026
0.45	8614.56703402	0.95	7430.18059987
0.46	8569.06904401	0.96	7616.08454293
0.47	8498.16237908	0.97	7802.56997281
0.48	8403.62111042	0.98	7987.05463174
0.49	8287.93781359	0.99	8166.63783427
		1.0	8338.17435398

Table E.13: Rebalancing time constant, 8-cell case with modulated duty cycle

modulation index	$\tilde{\tau}_r$	modulation index	$\tilde{\tau}_r$
0.0	∞	0.5	13553.642937
0.01	2890253.77826	0.51	13595.3760988
0.02	725496.611229	0.52	13619.9217315
0.03	324628.407917	0.53	13619.2190488
0.04	184339.866978	0.54	13585.7251627
0.05	119423.544571	0.55	13513.4193761
0.06	84179.2066902	0.56	13398.6503897
0.07	62948.3571632	0.57	13240.6565302
0.08	49190.6274373	0.58	13041.6599583
0.09	39781.8846949	0.59	12806.5375665
0.1	33077.0892674	0.6	12542.1678452
0.11	28143.3653167	0.61	12256.611675
0.12	24419.9181771	0.62	11958.2918504
0.13	21553.3902865	0.63	11655.2995331
0.14	19312.3507883	0.64	11354.8978729
0.15	17540.2473999	0.65	11063.2365907
0.16	16128.2361943	0.66	10785.2509186
0.17	14998.8260926	0.67	10524.6980288
0.18	14095.6694524	0.68	10284.2805955
0.19	13376.9792767	0.69	10065.8140476
0.2	12811.1582152	0.7	9870.40534405
0.21	12373.8174731	0.71	9698.62255158
0.22	12045.6943066	0.72	9550.64396891
0.23	11811.1672109	0.73	9426.38233852
0.24	11657.1807169	0.74	9325.58400105
0.25	11572.4602236	0.75	9247.90521877
0.26	11546.9399522	0.76	9192.96891336
0.27	11571.3544095	0.77	9160.4052357
0.28	11636.9616292	0.78	9149.8790833
0.29	11735.3780781	0.79	9161.10715278
0.3	11858.5119346	0.8	9193.86651212
0.31	11998.5840967	0.81	9247.99608308
0.32	12148.2252026	0.82	9323.39187888
0.33	12300.6329243	0.83	9419.99636154
0.34	12449.7681737	0.84	9537.78187034
0.35	12590.5634741	0.85	9676.72772936
0.36	12719.1135651	0.86	9836.79037268
0.37	12832.818833	0.87	10017.865643
0.38	12930.4569154	0.88	10219.7423505
0.39	13012.1660756	0.89	10442.0462668
0.4	13079.3338953	0.9	10684.1740378
0.41	13134.3942351	0.91	10945.2171107
0.42	13180.5424624	0.92	11223.8767881
0.43	13221.3829468	0.93	11518.3730406
0.44	13260.5246295	0.94	11826.351804
0.45	13301.1422456	0.95	12144.7981476
0.46	13345.5252764	0.96	12469.9657713
0.47	13394.6460637	0.97	12797.3363773
0.48	13447.79268	0.98	13121.6248697
0.49	13502.32763	0.99	13436.8470421
		1.0	13736.4642038